A Measurement of the Spin-Dependent Asymmetry in Quasielastic Scattering of Polarized Electrons from Polarized ^{3}He

Thesis by
Cathleen Elaine Jones

In Partial Fulfillment of the Requirements
for the Degree of
Doctor of Philosophy

California Institute of Technology
Pasadena, California

1992
(August 22, 1991)

Acknowledgements

Many people were involved in this experiment during the development of the polarized target and the preparation and execution of the experiment. I would like to take this opportunity to thank all of them for their efforts. Several people deserve particular mention.

Firstly, I would like to thank my advisor, Bob McKeown, for giving me support and advice many times during my stay at Caltech. In particular, I appreciate the freedom he gave me in the design and operation of the target. I have had the pleasure of working with Richard Milner from whom I learned valuable lessons about being an experimentalist. The long hours spent in the Pelletron Lab would not have been nearly as productive or as enjoyable without the assistance and company of Bob Carr. During the experiment the aid of George Dodson, Karen Dow, Wolfgang Lorenzon, and Dan Tieger was invaluable. Betsy Beise listened patiently and gave sage advice many times during the data analysis.

My friends have been a source of entertainment, solace, inspiration, and joy to me through both the trials and successes that I have had in my graduate years.

Finally, I want to thank my parents, Eleanor and Martin Jones, for supporting me in my endeavors at all stages of my life.

Abstract

The results of a measurement of the spin-dependent asymmetry in inclusive quasielastic scattering of polarized electrons from polarized ^{3}He are reported. The experiment was run at the MIT-Bates Linear Accelerator Center using a beam of longitudinally polarized electrons at an incident energy of 574 MeV. Scattered electrons were detected independently in two spectrometers, with one measurement sensitive to the spin-dependent transverse quasielastic response function, $R_{T'}$, at $Q^2 = 0.20$ (GeV/c)^2 and the other sensitive to the spin-dependent interference response function, $R_{TL'}$, at $Q^2 = 0.16$ (GeV/c)^2. The asymmetry in the elastic kinematic region was also measured at a scattering angle of 44°. The target was gaseous ^{3}He polarized through optical pumping of metastable 2^3S atoms, with the polarization transferred to the ground state atoms through metastability exchange collisions. The target, the first of its kind to be used for an electron scattering experiment, is described in detail.

The analysis of the helicity dependent cross section data and the extraction of the quasielastic asymmetry are discussed. The measured quasielastic asymmetries are compared to theories that model the spin-dependent properties of ^{3}He as being dominated by the electromagnetic properties of the neutron, and are found to agree with the models. A value of the neutron electric form factor at $Q^2 = 0.16$ (GeV/c)^2 is extracted from the measured asymmetry sensitive to $R_{TL'}$, demonstrating a new technique for accessing information about the neutron.

Contents

Acknowledgements ii

Abstract iii

1 Introduction 1

2 Theory 6

2.1 Inclusive Scattering Formalism with Polarization 6

2.2 Extraction of Neutron Form Factors from the ^{3}He Quasielastic Asymmetry 13

2.2.1 Nucleon Form Factors 13

2.2.2 Models of the ^{3}He Asymmetry 15

3 The Experiment 22

3.1 Overview 22

3.2 Polarized Electron Beam 24

3.3 Møller Polarimeter 26

3.4 The Spectrometers 30

3.4.1 OHIPS 30

3.4.2 BIGBITE 32

3.5 Data Acquisition System 34

4 The Polarized ^{3}He Target 37

4.1 Optical Pumping of ^{3}He 39

4.2 Spin Relaxation Mechanisms 45

4.2.1 Magnetic Field Gradients 46

4.2.2 Surface Effects 47

4.2.3 Discharge Effects 48

4.2.4 Beam Effects 49

4.3 Polarized ^{3}He Target System 51

4.3.1 Prototype ^{3}He Systems 51

4.3.2 Polarized ^{3}He Target - Double-Cell System 55

4.3.3 Nd:YAP Laser System 65

4.3.4 Computer Control and Polarization Measurement System 70

4.4 Polarization and Relaxation Rate Measurements 71

4.4.1 Optical Polarization Measurement 72

4.4.2 Relaxation Rate Measurement 76

4.4.3 Determination of the Polarization in the Target Cell 84

4.4.4 Systematic Uncertainty in the Target Polarization 87

4.5 ^{3}He Target Depolarization Studies 88

4.5.1 Wall Coatings 88

4.5.2 Beam Effects 89

5 Data Analysis **96**

5.1 Experimental Cuts 96

5.2 Sources of Background 99

5.2.1 Empty Target Yield 99

5.2.2 Elastic Radiative Tail 104

5.2.3 Pions 105

5.3 Experimental Cross Section 107

5.3.1 OHIPS 107

5.3.2 BIGBITE 110

5.4 Calculation of the Experimental Asymmetry 116

5.4.1 Energy Binning 118
5.4.2 Target Spin Orientation and Polarization 118
5.5 Corrections to the Experimental Asymmetry 121
5.5.1 Empty Target Correction 123
5.5.2 Elastic Radiative Correction 125
5.5.3 Quasielastic Radiative Correction 127
5.5.4 Pion Correction 130
5.5.5 False Asymmetry Background from Helicity-correlated Beam Shifts . 131

6 Results **144**
6.1 OHIPS Asymmetry Results 145
6.2 BIGBITE Asymmetry Results 145
6.2.1 Quasielastic Asymmetry 145
6.2.2 Asymmetry in the Threshold-Elastic Region 148
6.3 Comparison with ^{3}He Models 151
6.3.1 OHIPS 152
6.3.2 BIGBITE 155
6.4 Determination of G_E^n 160
6.4.1 Extraction of G_E^n from the Quasielastic Asymmetry 160
6.4.2 Comparison with Previous Measurements 161

7 Conclusions **166**

A TURTLE Monte Carlo Input for Extended Targets **169**

B Cleaning the ^{3}He Target System **172**
B.1 Target Cell 172
B.2 Glassware 173

C Determination of the Volume of the Cells **174**

D Solutions to the Coupled Rate Equations for a Double-Cell System **177**

D.1 Solution to Relaxation Rate Equations 178

D.2 Solution to Pumping Rate Equations 184

E BIGBITE Experimental Asymmetries **191**

Bibliography **194**

List of Figures

2.1 Definition of target spin angles. 8

2.2 Calculation of ^{3}He quasielastic asymmetry, $A(\omega)$, split into contributions from the protons and neutrons 17

2.3 Calculation of ^{3}He quasielastic asymmetry, $A(\omega)$, split into contributions from the S state, S and S' states, and S and D states 18

2.4 Proton and neutron spin density matrix elements 20

3.1 Layout of the spectrometers for the experiment 23

3.2 Schematic drawing of the Møller polarimeter 27

3.3 OHIPS detector layout 31

3.4 BIGBITE momentum resolution for an extended target 33

3.5 OHIPS event trigger logic 34

3.6 BIGBITE event trigger logic 35

4.1 Level diagram for the 2^3S and 2^3P states of ^{3}He 41

4.2 Transition lines for $2^3S \rightarrow 2^3P$ states of ^{3}He 41

4.3 ^{3}He nuclear polarization vs. light intensity for the low pressure and high pressure limits 42

4.4 ^{3}He nuclear polarization vs. light intensity as a function of metastable population fraction within frequency bandwidth of the pumping light . . . 44

4.5 Isotope shift of the $2^3S \rightarrow 2^3P$ transition lines in helium 52

4.6 Room temperature prototype single-cell system 53

4.7 LN temperature prototype double-cell system 54

4.8 Top and side view of the layout of the target system 56

4.9 Polarized ^{3}He target double-cell system 57

4.10 Vacuum and gas-handling system for target 61

4.11 Scattering chamber. 64

4.12 Fluorescence spectra of YAP crystal. 66

4.13 Nd:YAP laser system 67

4.14 Optical polarimeter 73

4.15 Measurement of relaxation with discharge on 78

4.16 Measurement of polarization transfer 79

4.17 P_t/P_p as a function of the relaxation time in the target cell 85

4.18 Target cell relaxation times with and without an argon surface coating . . . 88

4.19 Measured P_t/P_p from electron beam depolarization test 90

4.20 Relaxation rates from the beam effects, as a function of beam current . . . 91

4.21 Measured P_t/P_p from data acquired during experiment 92

5.1 X1 vs. θ_l for target full and target empty 98

5.2 X1 vs. θ for target full runs with and without new scintillator cuts 100

5.3 OHIPS full vs. empty target yield 102

5.4 BIGBITE full vs. empty target yield 103

5.5 Elastic radiative tail 105

5.6 Pion cross section 106

5.7 OHIPS delay line efficiency and computer live time. 108

5.8 Calculated cross section at the OHIPS kinematics, with and without radiative corrections 110

5.9 BIGBITE wire chamber efficiency and computer live time. 111

5.10 BIGBITE solid angle acceptance 112

5.11 BIGBITE differential cross section 113

5.12 BIGBITE calculated ^{3}He quasielastic yield vs. experimental data 114

5.13 BIGBITE calculated total yield vs. experimental data 115

5.14 BIGBITE calculated ^{3}He elastic yield vs. experimental data 116

5.15 Target polarization during the experiment 120

5.16 BIGBITE asymmetry for net unpolarized data 124

5.17 OHIPS asymmetry in the elastic radiative tail 126

5.18 BIGBITE asymmetry in the elastic radiative tail 127

5.19 OHIPS quasielastic radiative correction to the asymmetry 129

5.20 BIGBITE quasielastic radiative correction to the asymmetry without momentum smearing 130

5.21 BIGBITE quasielastic radiative correction to the asymmetry with momentum smearing 131

5.22 Helicity-correlated beam position shift 134

5.23 Relative empty target background rates as a function of beam position . . . 137

5.24 Estimate of false asymmetry from x helicity-correlated beam position shift . 138

5.25 Estimate of false asymmetry from y helicity-correlated beam position shift . 139

5.26 BIGBITE experimental asymmetry vs. Δx and Δy for the threshold-elastic energy region 142

5.27 BIGBITE experimental asymmetry vs. Δx and Δy for the quasielastic energy region 143

6.1 BIGBITE quasielastic asymmetry, as a function of ω 147

6.2 BIGBITE asymmetry, as a function of ω, in the threshold-elastic region . . 150

6.3 Calculated quasielastic asymmetry as a function of ω for OHIPS kinematics 154

6.4 Calculated quasielastic asymmetry as a function of ω for BIGBITE kinematics 156

6.5 Comparison of the BIGBITE experimental asymmetry over the quasielastic peak with the calculated asymmetry 157

6.6 Calculated variation of the quasielastic asymmetry with scattering angle and spin angle at the BIGBITE kinematics 158

6.7 Quasielastic asymmetry as a function of G_E^n, calculated for the BIGBITE kinematics 161

6.8 Comparison of BIGBITE quasielastic asymmetry with the calculation using the best-fit value of G_E^n 162

6.9 G_E^n from Platchkov *et al.* 165

6.10 Model dependence of results of Platchkov *et al.* 165

C.1 Schematic of the volume measurement 175

D.1 Time evolution of the target and pumping cell polarizations during relaxation 181

D.2 Time evolution of the target and pumping cell polarizations during optical pumping 186

D.3 Equilibrium ratio of polarizations during optical pumping 187

D.4 Approach to equilibrium of the ratio of polarizations during optical pumping 188

D.5 Equilibrium pumping cell polarization during optical pumping vs. target relaxation time for different transfer time constants 189

D.6 Equilibrium pumping cell polarization during optical pumping vs. target relaxation time for different pumping time constants 190

List of Tables

2.1 Definition of kinematic variables 7
2.2 State probabilities of the ^{3}He wave function 16

3.1 Kinematics of OHIPS and BIGBITE measurements 24
3.2 Results of beam polarization measurements 30

4.1 Time constants of the target system 84
4.2 Expressions used to calculate the polarization of target nuclei 86
4.3 Target cell relaxation time as a function of beam current 91
4.4 Results of relaxation runs taken during the experiment 93

5.1 Target spin orientations 119
5.2 Empty target dilution factors and asymmetry for the net unpolarized data . 123
5.3 Helicity-correlated beam position shift for full data set 135
5.4 Helicity-correlated beam position shift for data set excluding runs with large Δx or Δy 140
5.5 Experimental asymmetry for full data set 141
5.6 Experimental asymmetry for data set excluding runs with large Δx or Δy . 141
5.7 Correlations between the experimental asymmetry and the helicity-correlated beam position shift 143

6.1 Results of the OHIPS asymmetry measurement 146

6.2 Contributions to the systematic uncertainty in the OHIPS quasielastic asymmetry measurement 146
6.3 BIGBITE quasielastic asymmetry, as a function of ω 148
6.4 Results of the BIGBITE quasielastic asymmetry measurement 149
6.5 Contributions to the systematic uncertainty for the BIGBITE quasielastic asymmetry measurement 149
6.6 Results of the BIGBITE asymmetry measurement in the threshold-elastic region 151
6.7 OHIPS quasielastic asymmetry – theory vs. experiment 153
6.8 Calculated OHIPS quasielastic asymmetry using theory of Friar *et al.*, separated into contributions from protons and neutrons 154
6.9 BIGBITE quasielastic asymmetry – theory vs. experiment 156
6.10 Calculated BIGBITE quasielastic asymmetry using theory of Friar *et al.*, separated into contributions from protons and neutrons 159

A.1 TURTLE deck for the OHIPS spectrometer with an extended target 170
A.2 TURTLE deck for the BIGBITE spectrometer with an extended target . . . 171

C.1 Table of measured parameters for volume determination 175
C.2 Fraction of atoms in the target cell as a function of the target temperature 176

E.1 BIGBITE experimental asymmetry as a function of ω in the quasielastic region 192
E.2 BIGBITE experimental asymmetry as a function of ω in the threshold-elastic region 193

Chapter 1

Introduction

Among the experimental techniques used to probe nuclear structure, lepton scattering stands out in terms of the quality of information it provides about the electromagnetic structure of nuclei and nucleons. The applicability of lepton scattering to studies of particle properties over a wide range of energy and distance scales has made it a popular tool of both nuclear and high energy physicists. One of the more dramatic examples of the power of the technique in probing fundamental properties of matter is that the parton structure of the nucleon was discovered in electron scattering experiments. For nuclear physics, detailed studies of the electromagnetic structure of nuclei ranging from helium to lead have refined much of our current understanding of nuclear structure.

After almost three decades of use, lepton scattering continues to be the reaction of choice for making detailed and precise measurements of properties that are difficult to extract from experiments using hadronic probes. One of the primary appeals of lepton scattering is the cleanliness of the reaction process. Unlike the case for hadron scattering where the interaction is not well understood and where there can be considerable uncertainty in separating effects caused by the beam from those that are due to the target, the basic reaction mechanism for electron scattering is well understood in terms of the theory of quantum electrodynamics. Therefore, electron scattering can be used to study the electromagnetic structure of hadronic targets. An additional advantage of electron scattering is the relative weakness of the interaction compared to the hadronic interaction. Because of this, a perturbative approach can be used to obtain an expression for the cross section, which includes only the first few terms in an expansion in the number of virtual photons exchanged in the interaction.

Among leptons, electrons are relatively easy particles to produce and to detect. The availability of high quality, intense, medium-energy electron beams makes electron scattering an attractive option for studying nuclear properties. Elastic scattering corresponds to the electron scattering from the entire nucleus, leaving it in the same internal configuration afterwards. At higher energy transfer, inelastic scattering occurs, and in the scattering cross section one finds a broad peak in the inelastic region, known as the quasielastic peak, at the energy corresponding to elastic scattering from a single nucleon within the nucleus. The peak is broadened by the Fermi momentum of the nucleons within the nucleus, and experiments using quasielastic scattering sample the nucleon properties within a nucleus. The scattering cross section can be expressed in terms of structure functions, also known as form factors for elastic scattering, which contain the information about the charge and current distribution of the target.

Of particular interest are the neutron electromagnetic form factors: G_E^n, the electric (or charge) form factor and G_M^n, the magnetic form factor. Although the electromagnetic properties of the proton have been studied for several decades, the neutron properties are much less well known since a free neutron beta decays with a half-life of about 10 minutes, so that neutrons cannot be made into a dense, stable target. Also, neutron beams are generally made by reactors and are limited to low energies, so scattering from polarized electron targets will not yield information that is accessed only at high momenta. Our current knowledge of the neutron electric form factor is rather limited. Only the slope of G_E^n at zero four-momentum-transferred ($Q^2{=}0$) is well determined, from measurements of neutron scattering from atomic electrons [1]. The bulk of our knowledge about the Q^2 dependence of G_E^n comes from measurements using deuterium targets. There is uncertainty in the values obtained from these studies because of the sensitivity to the deuteron wave function and the large size of the corrections for the proton contribution to the cross section. A new technique to measure G_E^n would be useful. One option is the use of inclusive quasielastic electron scattering from polarized ^{3}He described in this thesis.

Most of the electron scattering experiments done previously have used unpolarized beams and targets. Additional information can be obtained about nuclear properties through the use of polarization, and the fairly recent development of both polarized targets and beams has allowed more complete studies of electromagnetic structure than are possible with unpolarized reactions alone. The extraction of additional information is possible because the general expression for the spin-dependent cross section includes terms that depend upon structure functions that do not enter the spin-independent cross section, or that have a different dependence upon the electromagnetic amplitudes, making it easier to extract information about them from the experimental data.

The technique of using polarization to access new information about electromagnetic properties of the nucleon and nucleus offers great potential for expanding our understanding of nuclear structure. Although polarized electron sources have been available for decades, polarized targets capable of withstanding the beam currents encountered at electron accelerators have been unavailable until recently. The development of polarized targets for electron scattering experiments has been accompanied by a number of relatively recent papers that consider the theoretical framework of the reaction mechanism, including polarization. One example is the work by Donnelly and Raskin [2], which gives a general treatment of electron scattering for polarized beams, polarized targets, and detection of polarization in the final state.

Experiments using polarized targets and beams generally measure spin-dependent quantities, such as the asymmetry or the polarization of the recoil particles. The asymmetry is defined in terms of the helicity-dependent cross sections as

$$A = \frac{\sigma_+ - \sigma_-}{\sigma_+ + \sigma_-}, \tag{1.1}$$

where $+(-)$ refers to the helicity of the incident electron. ^{3}He is an interesting nucleus for polarization studies because in the quasielastic scattering region, the spin-dependent properties are dominated by the neutron within the nucleus, a phenomenon that occurs because the ^{3}He wave function is predominantly a spatially symmetric S-state, and antisymmetrization of the wave function requires that the protons occupy a spin-singlet state. If the ^{3}He ground state were entirely in a symmetric S-state, the spin of the nucleus would be carried solely by the unpaired neutron, and measurements of spin-dependent quantities in inclusive quasielastic scattering of polarized electrons from polarized ^{3}He would measure the neutron electromagnetic form factors directly. In short, electron scattering experiments with a polarized ^{3}He target can be used to obtain information about the neutron form factors. The experiment described here involved inclusive quasielastic scattering of polarized electrons from polarized ^{3}He, where the spin-dependent asymmetry was measured. The asymmetry depends upon quasielastic nuclear response functions of ^{3}He which contain information about the electromagnetic structure and which do not enter into the unpolarized cross section. During the experiment, data were collected in two spectrometers to obtain asymmetry measurements that depend upon different spin-dependent response functions of ^{3}He and contain complementary information about the neutron form factors.

The work presented here is one of the first to use both a polarized nuclear target and a polarized electron beam to measure spin-dependent, electromagnetic properties of the nucleus. The polarization is used to enhance the contribution to the cross section from the neutron electric form factor. Critical to the development of this new technique for obtaining information about the neutron were the design and construction of a polarized ^{3}He target of suitable polarization and thickness for electron scattering experiments. The target used for this experiment was developed at Caltech and used optical pumping of the metastable ^{3}He atoms to polarize the nucleus, a technique that was developed in the 1960's, but could not be applied to nuclear targets for electron scattering experiments until very recently because of the lack of intense sources of optical pumping light. The target described here is the first polarized ^{3}He target using the metastability-exchange, optical pumping technique developed for electron scattering experiments. A detailed description of the target and of the general technique of optical pumping as applied to ^{3}He is given in

Chapter 4.

The validity of the approximation that polarized ^{3}He is effectively a polarized neutron target is discussed in Chapter 2, along with a general treatment of the theory of polarized electron scattering and the dependence of the cross section upon the spin-dependent response functions. Chapter 3 contains a description of the experiment, which was performed at the MIT-Bates Linear Accelerator Center in March 1990 by a collaboration of Caltech and MIT. The data analysis is described in Chapter 5 and the results are presented in Chapter 6. In the latter chapter, the asymmetry results are given for the data collected in both spectrometers, and the extraction of G_E^n from the asymmetry is described. The results are compared with predictions of several models of ^{3}He , which suggest that the nuclear spin is carried primarily by the neutron within the ^{3}He nucleus. The extracted value of G_E^n is compared with previous measurements that used different techniques to obtain information about the neutron. Finally, the conclusions are presented in Chapter 7.

Chapter 2

Theory

2.1 Inclusive Scattering Formalism with Polarization

The formalism used to obtain an expression for the electron scattering cross section with the inclusion of polarization degrees of freedom is given in detail by Donnelly and Raskin in Reference [2]. That reference treats cases where the incident electrons are either polarized or unpolarized and the target is either initially polarized or the polarization is detected in the final state. Here, the results are presented for the particular case where the incident electrons are longitudinally polarized (the spin oriented along the momentum direction) and the target nuclei are initially polarized. Table 2.1 contains the definitions of the kinematic variables. The notation used by Donnelly and Raskin is followed for the most part, with exceptions noted in the text. The expressions are derived assuming that the Born plane-wave approximation for the incident electron, a single photon exchange interaction, and the extreme relativistic limit where the electron mass energy is negligible relative to its kinetic energy. Although the electron is assumed to be longitudinally polarized, the target spin can be oriented in any direction. The target spin direction is specified relative to the direction of the momentum transferred, $\vec{q}$, by the two Euler angles, θ^* and ϕ^*, as seen in Figure 2.1.

$K = (E, \vec{k})$	incident electron energy and momentum
$K' = (E', \vec{k}')$	final electron energy and momentum
$P_i = (E_i, \vec{p}_i)$	initial target energy and momentum
$P_f = (E_f, \vec{p}_f)$	final target energy and momentum
$(\omega, \vec{q})$	energy and momentum transferred from incident electron to target nucleus during main scattering event; $\omega = (E - E'), \vec{q} = (\vec{k} - \vec{k}')$
q, k, k'	magnitude of the 3-momentum transferred; $\lvert\vec{q}\rvert, \lvert\vec{k}\rvert, \lvert\vec{k}'\rvert$
Q^2	negative of the 4-momentum transferred, squared; $Q^2 = (q^2 - \omega^2) \geq 0$
θ	lab scattering angle of final electron
θ^*, ϕ^*	angles defining the target spin direction relative to $\vec{q}$
h	incident electron helicity; +1 (-1) for spin parallel (antiparallel) to $\vec{k}$

Table 2.1: Definition of kinematic variables.

The expression for the differential scattering cross section in the lab frame can be written as [3]

$$d\sigma = \frac{m_e}{k}\overline{\sum_{if}}|\mathcal{M}_{fi}|^2 \frac{m_e}{E'}\frac{d^3\vec{k}'}{(2\pi)^3}\frac{M_f}{E_f}\frac{d^3\vec{p}_f}{(2\pi)^3}(2\pi)^4\delta^{(4)}(K + P_i - K' - P_f), \tag{2.1}$$

where m_e is the electron mass and M_f is the mass of the final target system. $\overline{\sum}_{if}$ indicates an average over the initial states and a sum over the final states, where the polarizations determine the number of initial or final states. $\mathcal{M}_{fi}$ is the invariant matrix element and is defined in terms of the electron and nuclear electromagnetic currents. The relationship

$$\overline{\sum_{if}}|\mathcal{M}_{fi}|^2 = \frac{(4\pi\alpha)^2}{Q^4}\eta_{\mu\nu}W^{\mu\nu} \tag{2.2}$$

holds between the sum over the matrix elements squared and the electron and nuclear tensors, $\eta_{\mu\nu}$ and $W^{\mu\nu}$, assuming the first Born approximation. In this formula, α is the fine structure constant.

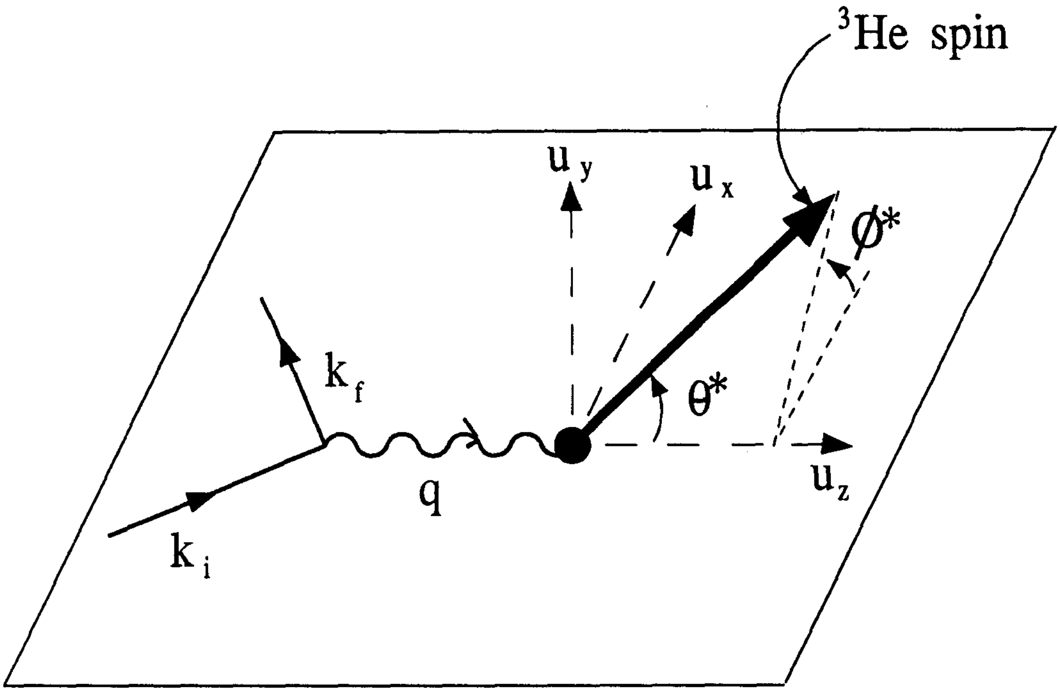

Figure 2.1: Definition of the target spin angles.

The electron tensor is

$$\eta_{\mu\nu} = \overline{\sum_{if}} [\bar{u}_f \gamma_\mu u_i]^* [\bar{u}_f \gamma_\nu u_i] \tag{2.3}$$

and the nuclear tensor is

$$W^{\mu\nu} = \overline{\sum_{if}} J^{\mu *}(Q) J^{\nu}(Q). \tag{2.4}$$

$J^\mu(Q)$ is the nuclear electromagnetic transition current in momentum space,

$$J^\mu(\vec{q}) = \int e^{i\vec{q}\cdot\vec{x}} < f|\hat{J}^\mu(\vec{x})|i > d^3\vec{x}, \tag{2.5}$$

defined in terms of the nuclear electromagnetic current density operator, $\hat{J}^\mu$. For longitudinally polarized electrons, the electron tensor can be written as[1]

$$\eta_{\mu\nu} = \frac{1}{4m_e^2}\left(K_\mu K'_\nu + K'_\mu K_\nu - \frac{1}{2}Q^2 g_{\mu\nu} - ih\epsilon_{\mu\nu\alpha\beta}K^\alpha K'^\beta\right). \tag{2.6}$$

---

[1] We use the definition $Q^2 \equiv (q^2 - \omega^2) \geq 0$, whereas Donnelly and Raskin define $Q^2 \equiv (\omega^2 - q^2) \leq 0$.

The metric is

$$g_{\mu\nu} = \begin{pmatrix} 1 & 0 & 0 & 0 \\ 0 & -1 & 0 & 0 \\ 0 & 0 & -1 & 0 \\ 0 & 0 & 0 & -1 \end{pmatrix}. \tag{2.7}$$

The differential cross section can be written as

$$\frac{d\sigma}{d\Omega} = \left(\frac{\alpha^2}{Q^4}\right) \frac{4m_e^2 k'}{k} f_{recoil}^{-1} \eta_{\mu\nu} W^{\mu\nu}, \tag{2.8}$$

where

$$f_{recoil} = 1 + \frac{k'E - kE'\cos\theta}{k'M_f}. \tag{2.9}$$

This can be rewritten as

$$\frac{d\sigma}{d\Omega} = \sigma_{Mott}\left[(v_L\mathcal{R}_L + v_T\mathcal{R}_T + v_{TT}\mathcal{R}_{TT} + v_{TL}\mathcal{R}_{TL}) + h\,(v_{T'}\mathcal{R}_{T'} + v_{TL'}\mathcal{R}_{TL'})\right] \tag{2.10}$$

$$\equiv \Sigma + h\Delta, \tag{2.11}$$

where

$$\sigma_{Mott} = \frac{\alpha^2\cos^2\frac{\theta}{2}}{4E^2\sin^4\frac{\theta}{2}}. \tag{2.12}$$

As can be seen from this expression, the cross section separates into a piece that is independent of the electron helicity, Σ, and a term that depends upon the helicity, $h\Delta$. If the electron spin polarization vector were transverse to the momentum direction, then Δ would be reduced by a factor of γ^{-1}, where γ is the relativistic factor, $\frac{E}{m_e}$. In expression 2.10, all the information about the nuclear electromagnetic structure is contained in the factors, $\mathcal{R}_K$. The v_K are kinematic factors defined as follows:

$$v_L = \left(\frac{Q^2}{q^2}\right)^2 \tag{2.13}$$

$$v_T = \frac{1}{2}\left(\frac{Q^2}{q^2}\right) + \tan^2\frac{\theta}{2} \tag{2.14}$$

$$v_{TT} = -\frac{1}{2}\left(\frac{Q^2}{q^2}\right) \tag{2.15}$$

$$v_{TL} = -\frac{1}{\sqrt{2}}\left(\frac{Q^2}{q^2}\right)\sqrt{\left(\frac{Q^2}{q^2}\right) + \tan^2\frac{\theta}{2}} \tag{2.16}$$

$$v_{T'}=\tan\frac{\theta}{2}\sqrt{\left(\frac{Q^2}{q^2}\right)+\tan^2\frac{\theta}{2}} \tag{2.17}$$

$$v_{TL'}=-\frac{1}{\sqrt{2}}\left(\frac{Q^2}{q^2}\right)\tan\frac{\theta}{2} \tag{2.18}$$

In these expressions, "L" and "T" refer to the longitudinal and transverse components of the virtual photon polarization, so the response functions are defined in terms of the electromagnetic current components specified with respect to the $\vec{q}$ direction. The primed terms indicate products of the symmetric terms in both the electron and the nuclear tensor, and the unprimed terms indicate products of the antisymmetric terms in both tensors.

The response functions, $\mathcal{R}_K$, depend upon the target spin direction. Since the spin direction can be varied experimentally, it is desirable to specify explicitly the functional dependence of the cross section upon θ^* and ϕ^*. This is done below in terms of Legendre functions.

$$\Sigma=\Sigma_0\left[1+\sum_{\mathcal{J}\geq 2}^{\mathcal{J}\text{ even}}\left(P_{\mathcal{J}}(\cos\theta^*)R^0_{\mathcal{J}}+P^1_{\mathcal{J}}(\cos\theta^*)\cos\phi^* R^1_{\mathcal{J}}+P^2_{\mathcal{J}}(\cos\theta^*)\cos 2\phi^* R^2_{\mathcal{J}}\right)\right] \tag{2.19}$$

$$\Delta=\Sigma_0\left[\sum_{\mathcal{J}\geq 1}^{\mathcal{J}\text{ odd}}\left(P_{\mathcal{J}}(\cos\theta^*)R^0_{\mathcal{J}}+P^1_{\mathcal{J}}(\cos\theta^*)\cos\phi^* R^1_{\mathcal{J}}\right)\right] \tag{2.20}$$

$$\Sigma_0 = 4\pi\sigma_{Mott}f^{-1}_{recoil}F^2 \tag{2.21}$$

F^2 and $R_{\mathcal{J}}$ are defined in terms of reduced response functions, $\mathcal{W}^K_{\mathcal{J}}$, which contain the information about the nuclear structure:

$$F^2 = f^{(i)}_0(v_L\mathcal{W}^L_0 + v_T\mathcal{W}^T_0) \tag{2.22}$$

In the expression above, $f^{(i)}_{\mathcal{J}}$ are Fano statistical tensors, which contain the information about the polarization of the initial state. For a 100% polarized target of spin J_i, the general formula for the Fano tensors is

$$f^{(i)}_{\mathcal{J}} = \frac{(2J_i)!\sqrt{2\mathcal{J}+1}}{\sqrt{(2J_i+\mathcal{J}+1)!(2J_i-\mathcal{J})!}}. \tag{2.23}$$

The $R_{\mathcal{J}}$ are defined separately for $\mathcal{J}$ even and for $\mathcal{J}$ odd, where $\mathcal{J}$ must satisfy the constraint $0\leq\mathcal{J}\leq 2J_i$. The special case of $\mathcal{J}=0$ has $R^0_0=1$.

$\mathcal{J}$ even:

$$R^0_{\mathcal{J}}=f^{(i)}_{\mathcal{J}}(v_L\mathcal{W}^L_{\mathcal{J}}+v_T\mathcal{W}^T_{\mathcal{J}})/F^2 \tag{2.24}$$

$$R^1_{\mathcal{J}}=f^{(i)}_{\mathcal{J}}(v_{TL}\mathcal{W}^{TL}_{\mathcal{J}})/F^2 \tag{2.25}$$

$$R^2_{\mathcal{J}}=f^{(i)}_{\mathcal{J}}(v_{TT}\mathcal{W}^{TT}_{\mathcal{J}})/F^2 \tag{2.26}$$

$\mathcal{J}$ odd:

$$R^0_{\mathcal{J}}=f^{(i)}_{\mathcal{J}}(v_{T'}\mathcal{W}^{T'}_{\mathcal{J}})/F^2 \tag{2.27}$$

$$R^1_{\mathcal{J}}=f^{(i)}_{\mathcal{J}}(v_{TL'}\mathcal{W}^{TL'}_{\mathcal{J}})/F^2 \tag{2.28}$$

The reduced response functions, $\mathcal{W}^K$, depend upon the electromagnetic matrix elements, $t_{\sigma J}$, where $\sigma = C, E, M$ for the Coulomb, electric, and magnetic matrix elements, respectively. They are defined in terms of the electromagnetic multipole operators as follows,

$$t_{CJ}(q)\equiv< J_f||\hat{M}_J(q)||J_i > \tag{2.29}$$

$$t_{EJ}(q)\equiv< J_f||\hat{T}^{el}_J(q)||J_i > \tag{2.30}$$

$$t_{MJ}(q)\equiv< J_f||i\hat{T}^{mag}_J(q)||J_i >, \tag{2.31}$$

where J_i and J_f denote the initial and final states by their spins. The reduced response functions are sums of products of two of the electromagnetic matrix elements, $t_{\sigma J}$. $\mathcal{W}^L$ contains products of two Coulomb matrix elements and may have interference terms from different multipoles, while $\mathcal{W}^T$, $\mathcal{W}^{TT}$, and $\mathcal{W}^{T'}$ contain transverse matrix elements only. The $\mathcal{W}^{TL}$ and $\mathcal{W}^{TL'}$ contain interference terms between transverse and Coulomb matrix elements.

For the general definition of the reduced response functions for arbitrary initial and final state, the reader is referred to Reference [2]. For now, we will consider the special case of initial and final spin-$\frac{1}{2}$ states, with parity conserved in the interaction. In this case

$$\Sigma = \Sigma_0, \tag{2.32}$$

so no new information is obtained from scattering experiments with unpolarized electrons where spin-$\frac{1}{2}$ nuclei are polarized, relative to that obtained from experiments using an unpolarized target. In order to have the reduced response functions, $\mathcal{W}^{TL}$ and $\mathcal{W}^{TT}$, enter the expression for the cross section for a polarized target, the spin of the polarized nucleus must be ≥ 1. For a spin-$\frac{1}{2}$ nucleus, the helicity-dependent term is

$$\Delta = \Sigma_0 \left[\cos\theta^* R_1^0 + \sin\theta^* \cos\phi^* R_1^1 \right]. \tag{2.33}$$

The reduced response functions are given in terms of the electromagnetic transition matrix elements as

$$\mathcal{W}_0^L = \frac{1}{\sqrt{2}}\, t_{C0}^2 \tag{2.34}$$

$$\mathcal{W}_0^T = \frac{1}{\sqrt{2}}\, t_{M1}^2 \tag{2.35}$$

$$\mathcal{W}_0^{T'} = -\frac{1}{\sqrt{2}}\, t_{M1}^2 \tag{2.36}$$

$$\mathcal{W}_0^T = -\frac{2}{\sqrt{2}}\, t_{C0} t_{M1}. \tag{2.37}$$

Now that the formalism for polarized electron scattering for polarized spin-$\frac{1}{2}$ targets has been developed, it is convenient to consider the case of inelastic scattering in the quasielastic kinematic region that is relevant to the experiment discussed here. We now modify the notation of Donnelly and Raskin slightly, and express the differential cross section in terms of quasielastic response functions, which depend upon Q^2 and ω.

$$\frac{d^2\sigma}{d\Omega dE} = \Sigma + h\Delta \tag{2.38}$$

$$\Sigma = \sigma_{Mott} \left(v_L R_L(Q^2,\omega) + v_T R_T(Q^2,\omega) \right) \tag{2.39}$$

$$\Delta = -\sigma_{Mott} \left(v_{T'} \cos\theta^* R_{T'}(Q^2,\omega) + 2 v_{TL'} \sin\theta^* \cos\phi^* R_{TL'}(Q^2,\omega) \right) \tag{2.40}$$

The quasielastic response functions can be written in terms of the nuclear electromagnetic matrix elements as

$$R_L(Q^2,\omega) = 2\pi \left| < \frac{1}{2} || \hat{M}_0(q) || \frac{1}{2} > \right|^2 \tag{2.41}$$

$$R_T(Q^2,\omega) = 2\pi \left| < \frac{1}{2} || i\hat{T}_1^{mag}(q) || \frac{1}{2} > \right|^2 \tag{2.42}$$

$$R_{T'}(Q^2,\omega)=2\pi|<\frac{1}{2}||i\hat{T}_1^{mag}(q)||\frac{1}{2}>|^2 \tag{2.43}$$

$$R_{TL'}(Q^2,\omega)=2\pi<\frac{1}{2}||\hat{M}_0(q)||\frac{1}{2}><\frac{1}{2}||i\hat{T}_1^{mag}(q)||\frac{1}{2}>. \tag{2.44}$$

The spin-dependent quasielastic asymmetry is

$$A=\frac{\left(\frac{d^2\sigma}{d\Omega dE}\right)_+-\left(\frac{d^2\sigma}{d\Omega dE}\right)_-}{\left(\frac{d^2\sigma}{d\Omega dE}\right)_++\left(\frac{d^2\sigma}{d\Omega dE}\right)_-}, \tag{2.45}$$

where +(-) denote the helicity of the incident electron. This can be rewritten as

$$A=\frac{\Delta(\theta^*,\phi^*)}{\Sigma}. \tag{2.46}$$

Therefore, the asymmetry is the ratio of the helicity-dependent term in the cross section to the helicity-independent term. Since $\Sigma = \Sigma_0$ for a spin-$\frac{1}{2}$ target, all of the dependence upon both the electron and nuclear spin is contained in Δ. Expressed in terms of the quasielastic response functions, the asymmetry is

$$A=-\frac{\cos\theta^* v_{T'}R_{T'}(Q^2,\omega)+2\sin\theta^*\cos\phi^* v_{TL'}R_{TL'}(Q^2,\omega)}{v_L R_L(Q^2,\omega)+v_T R_T(Q^2,\omega)}. \tag{2.47}$$

As can be seen from this equation, the sensitivity of A to the two spin-dependent response functions can be selected experimentally by varying θ^*, the angle between the nuclear spin and the 3-momentum transfer, $\vec{q}$. If $\cos\theta^* = 1$, then the asymmetry is maximally sensitive to $R_{T'}(Q^2,\omega)$, while if $\sin\theta^* = 1$, the asymmetry is maximally sensitive to $R_{TL'}(Q^2,\omega)$, the interference between the Coulomb and transverse response.

2.2 Extraction of Neutron Form Factors from the ^{3}He Quasielastic Asymmetry

2.2.1 Nucleon Form Factors

Before discussing the extraction of information about the neutron electromagnetic properties from the ^{3}He data, it is useful to present the expressions for the cross section and asymmetry in elastic electron scattering from a free nucleon. This is done within the context of the derivation given in the previous section, using the notation of Donnelly and

Raskin. In this case, expression 2.21 for the unpolarized cross section is written in terms of the longitudinal and transverse elastic form factors, F_L and F_T, where

$$F^2(Q^2) = v_L F_L^2(Q^2) + v_T F_T^2(Q^2). \tag{2.48}$$

The longitudinal and transverse form factors are related to the Sach's form factors, $G_E(Q^2)$, the electric (or more correctly, charge) nucleon form factor, and $G_M(Q^2)$, the magnetic nucleon form factor, by

$$\sqrt{4\pi}F_L = (1+\tau)G_E \tag{2.49}$$

$$\sqrt{4\pi}F_T = -\sqrt{2\tau(1+\tau)}G_M, \tag{2.50}$$

where $\tau \equiv Q^2/4m_n^2$.

The Sach's form factors have a simple, intuitive interpretation. In the nonrelativistic limit, they are related to the Fourier transform of the charge and current distribution within the nucleon, and in the $Q^2 = 0$ limits reduce to

$$G_E(Q^2 = 0) = q_N \tag{2.51}$$

$$G_M(Q^2 = 0) = \mu_N, \tag{2.52}$$

where q_N is the nucleon charge and μ_N is the magnetic moment of the nucleon. The unpolarized cross section is written in terms of G_E and G_M as

$$\frac{d\sigma}{d\Omega} = \sigma_{Mott} f_{recoil}^{-1}\left((1+\tau)^2 v_L G_E^2 + 2\tau(1+\tau)v_T G_M^2\right). \tag{2.53}$$

For the neutron, it is clear from this relationship that at low Q^2 the magnetic form factor dominates over the electric form factor. For this reason, it is difficult to extract G_E^n from unpolarized scattering data. If the neutron is polarized, then the spin-dependent part of the cross section, written as

$$\Delta = -\sigma_{Mott} f_{recoil}^{-1}\Big(2\tau(1+\tau)v_{T'}\cos\theta^* G_M^{n2}(Q^2) \tag{2.54}$$

$$-2(1+\tau)\sqrt{2\tau(1+\tau)}v_{TL'}\sin\theta^*\cos\phi^* G_M^n(Q^2)G_E^n(Q^2)\Big), \tag{2.55}$$

contains an interference term proportional to $G_E^n G_M^n$, so the spin-dependent asymmetry is more sensitive than the unpolarized cross section to the electric form factor of the neutron.

The spin-dependent asymmetry for the nucleon,

$$A = \frac{\left(\frac{d\sigma}{d\Omega}\right)_R - \left(\frac{d\sigma}{d\Omega}\right)_L}{\left(\frac{d\sigma}{d\Omega}\right)_R + \left(\frac{d\sigma}{d\Omega}\right)_L}, \tag{2.56}$$

is expressible in terms of the electric and magnetic form factors as

$$A_{\vec{e}\vec{N}} = -\frac{2\tau v_{T'} \cos\theta^* G_M^2(Q^2) - 2\sqrt{2\tau(1+\tau)} v_{TL'} \sin\theta^* \cos\phi^* G_M(Q^2) G_E(Q^2)}{(1+\tau) v_L G_E^2 + 2\tau v_T G_M^2}. \tag{2.57}$$

2.2.2 Models of the ^{3}He Asymmetry

Scattering experiments using polarized electrons and polarized ^{3}He are of particular interest because of the possibility of extracting information about the neutron electromagnetic form factors from the ^{3}He quasielastic asymmetry data. The ^{3}He wave function is dominated by the spatially symmetric $S-$state, in which the protons are paired off in a spin-singlet state so that the nuclear spin is carried by the neutron. If this were the only component to the ^{3}He wave function, then the quasielastic ^{3}He asymmetry would be directly proportional to the asymmetry for a free neutron, with the constant of proportionality the probability of scattering from a neutron in ^{3}He , σ_n/σ_{He}, where σ is used to denote the unpolarized scattering cross section. This is not the case, however, since there are small admixtures of other states in the ^{3}He wave function.

Model of Blankleider and Woloshyn

In Reference [4], Blankleider and Woloshyn estimate the effect of the other components of the wave function on the quasielastic asymmetry. They use the ^{3}He ground state wave function of Afnan and Birrell [5] obtained by solving the Faddeev equation using the Reid soft-core, nucleon-nucleon potential. The major components to the wave function are the spatially symmetric $S-$state, the mixed symmetry $S'-$state, and the $D-$state. The $P-$state probabilities are negligibly small. Table 2.2 shows the state probabilities calculated with this wave function.

Blankleider and Woloshyn model quasielastic electron scattering using the impulse approximation. They also use a closure approximation to sum over the final states so that

State	Probability (%)
S	88.6
S'	1.5
D	8.4

Table 2.2: ^{3}He wave function state probabilities, as given in [4], calculated using the wave function of Afnan and Birrell [5].

the ^{3}He structure functions used in the calculation depend only upon the ground state wave function. In this way, they calculate the spin-dependent asymmetry for quasielastic scattering and estimate the contributions to the asymmetry from the neutron and the protons in ^{3}He. The dependence of the asymmetry upon Q^2 and ω are calculable within their model. The results of their calculations indicate that at the center of the quasielastic peak, the asymmetry is dominated by the $S-$state with a small contribution from the $S'-$state, while in the tails of the quasielastic peak, the $D-$state component has a major impact upon the asymmetry. This means that near the maximum in the peak, the spin-dependent asymmetry is sensitive to the neutron properties. Figures 2.2 and 2.3 show the ^{3}He asymmetry as a function of ω for E = 574 MeV, θ = 44°, Q^2 = 0.158 (GeV/c)^2, calculated using Blankleider and Woloshyn's computer code. The asymmetry is plotted for both $\theta^* = 0°$ ($A \propto R_{T'}$), and $\theta^* = 90°$ ($A \propto R_{TL'}$). In Figure 2.2, the ^{3}He asymmetry is shown broken down into contributions from the protons and the neutron. The arrow indicates the position of the quasielastic peak, as calculated by the model. As one would expect, the contribution from the protons are less important for $A_{R_{T'}}$, which is dominated by the magnetic form factor of the neutron in the model of ^{3}He primarily as a polarized neutron. For $A_{R_{TL'}}$, the neutron contribution is comparable to the protons across a substantial portion of the quasielastic peak, while the proton contribution dominates in the tails of the quasielastic peak. In Figure 2.3 the asymmetry is broken into contributions from the S state, S and S' states, and S and D states. In the tails of the quasielastic peak, the contributions from the S' and D states become quite important, with the effects acting to cancel each other. The contribution from the D-state dominates, as is seen by

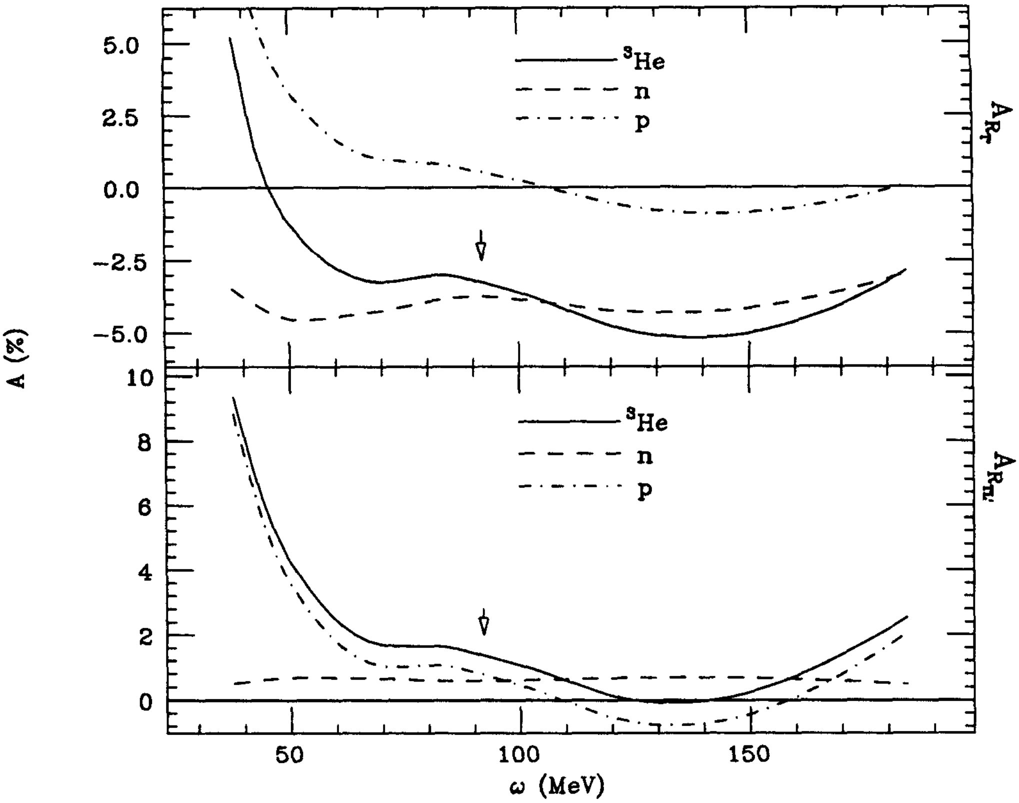

Figure 2.2: Calculation of ^{3}He asymmetry as a function of energy transfer, ω, for $E = 574$ MeV and $\theta = 44°$, using the computer code of Blankleider and Woloshyn [4]. The upper graph is the asymmetry for $\theta^* = 0°$ and the lower on is for $\theta^* = 90°$. The contributions from the protons and neutrons are shown. The arrow indicates the position of the quasielastic peak calculated from the model.

comparing the ^{3}He asymmetry with the asymmetries calculated using only a subset of the states in the wave function. Note that the asymmetries calculated for subsets of the wave function cannot be summed directly from the graph because the cross section varies with the number of states assumed to contribute to the scattering amplitude. Furthermore, it should be noted that the Blankleider and Woloshyn calculation may not be quantitatively accurate for the asymmetry in the tails of the peak, especially near the three-body threshold. Nonetheless, they provide a qualitative prediction that the D and S' states have large contributions to the ^{3}He asymmetry in the tails of the quasielastic peak, with a rough estimate of the size of the contributions.

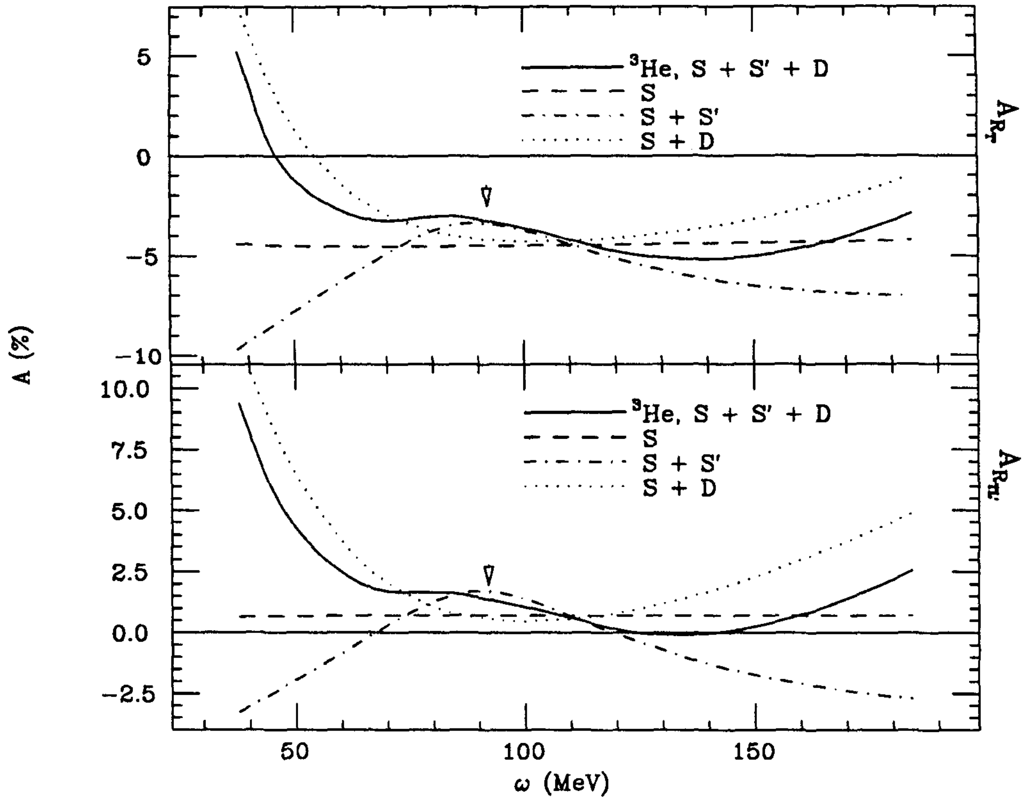

Figure 2.3: Calculation of ^{3}He asymmetry as a function of energy transfer, ω, for $E = 574$ MeV and $\theta = 44°$, using the computer code of Blankleider and Woloshyn [4]. The upper graph is the asymmetry for $\theta^* = 0°$ and the lower on is for $\theta^* = 90°$. The contributions from the S state, S and S' states, and S and D states are shown. The arrow indicates the position of the quasielastic peak calculated from the model.

Model of Friar *et al.*

Another calculation of the contribution of the neutron within ^{3}He to the spin-dependent asymmetry has been done by Friar *et al.* [6]. They use a simple model of the polarization of ^{3}He to estimate the degree of polarization of the neutron and the protons within a ^{3}He nuclei in the $+\frac{1}{2}$ magnetic substate. They calculate the polarization of the nucleons within a sample of 100% polarized ^{3}He by considering the matrix elements

$$P^{\pm}_{n,p} =< m = +1/2|\hat{P}^{\pm}_{n,p}|m = +1/2 >, \tag{2.58}$$

where

$$\hat{P}^{\pm}_{n} = \sum_{i} \frac{1-\tau_3(i)}{2}\frac{1 \pm \sigma_z(i)}{2}, \tag{2.59}$$

$$\hat{P}_p^{\pm} = \sum_i \frac{1+\tau_3(i)}{2}\frac{1 \pm \sigma_z(i)}{2}, \tag{2.60}$$

and τ and σ are the isospin and spin operators. The polarization of the neutron and protons can be represented by spin density matrices,

$$\rho_n = \begin{pmatrix} P_n^+ & 0 \\ 0 & P_n^- \end{pmatrix} = \begin{pmatrix} 1-\delta & 0 \\ 0 & \delta \end{pmatrix} \tag{2.61}$$

and

$$\rho_p = \begin{pmatrix} P_p^+ & 0 \\ 0 & P_p^- \end{pmatrix} = \begin{pmatrix} \frac{1}{2}-\delta' & 0 \\ 0 & \frac{1}{2}+\delta' \end{pmatrix}. \tag{2.62}$$

δ and δ' can be written in terms of the state probabilities of the ^{3}He ground state wave function:

$$\delta = \frac{(2\mathcal{P}(D) + \mathcal{P}(S'))}{3}, \tag{2.63}$$

$$\delta' = \frac{(\mathcal{P}(D) - \mathcal{P}(S'))}{6}. \tag{2.64}$$

The expressions for δ and δ' can be easily understood from a simple argument. Consider the $D-$state of ^{3}He . In this configuration, $L = 2$, and the three spins of the nucleons are aligned opposite to L to give a net spin $\frac{1}{2}$. This means that both the neutron and the proton spins are oriented opposite to the nuclear spin, and the $D-$state probabilities in δ and δ' enter into the spin density matrix element for the $+\frac{1}{2}$ spin state of both the neutron and the proton with a "$-$" sign. The $S'-$state, on the other hand, has a neutron and proton paired off to a spin-singlet state, while the other proton has its spin oriented along the direction of the nuclear spin. Therefore, the $S'-$state probabilities should enter the spin density matrix element for the $+\frac{1}{2}$ spin state with a "$-$" sign for the neutron and a "+" sign for the proton.

Unlike Blankleider and Woloshyn, who use a single model of the ^{3}He wave function to calculate the spin-dependent asymmetry in quasielastic scattering, Friar *et al.* estimate the quantities δ and δ' from a number of different nuclear potential models of the ground state wave function. They plot δ and δ' vs. the calculated binding energy for the different models and extract a best-fit value by choosing the value of the fit to the δ and δ' data

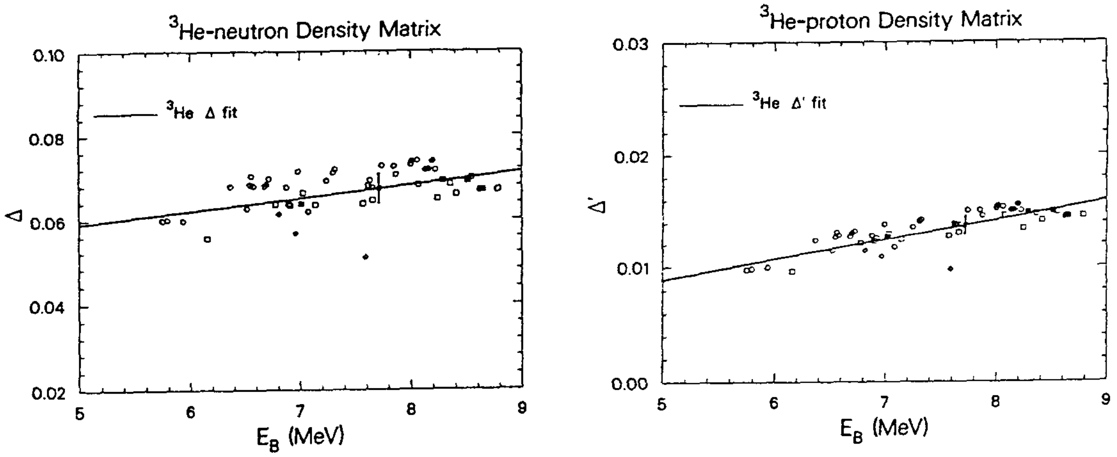

Figure 2.4: Calculated proton and neutron spin density matrix elements from Reference [6]. The points represent the matrix elements calculated from different nuclear models of ^{3}He and are plotted as a function of the calculated binding energy from the model. The line represents the best linear fit to the data, and the point with the error bar is the value for the matrix elements used by the authors.

points corresponding to the physical ^{3}He binding energy of 7.72 MeV. Figure 2.4 shows their results. They obtain the numbers

$$\delta \approx 0.07 \pm 0.01 \tag{2.65}$$

$$\delta' \approx 0.014 \pm 0.002, \tag{2.66}$$

where the error bars quoted are purely subjective and are taken as three times the average spread of the points about the best-fit straight line. This method of extracting the results is justified by the authors with the argument that δ and δ' are only weakly dependent upon the binding energy. Most of the models giving results with binding energies above 7 MeV include three body forces. The authors make no effort to single out a particular model as being better than the others for the calculation of the degree of polarization of the neutron in ^{3}He.

The simple argument given by this reference does not permit the calculation of the ω dependence of the asymmetry. The D and S' states are assumed to be equally sampled by all quasielastic scattering events, without taking into account the fact, for example, that the $D-$state component contributes more in the tails of the quasielastic peak than it does at the center. Therefore, this method of including the contributions from the protons can be used only in the calculation of the quasielastic asymmetry integrated over an ω range encompassing a significant fraction of the quasielastic peak. If this is done, however, then the asymmetry for scattering from polarized ^{3}He is simply related to the asymmetries for polarized electron scattering from a free polarized nucleon, given previously in Equation 2.57, by

$$A = (1 - 2\delta)\left(\frac{\sigma_n}{\sigma_{He}}\right) A_{\vec{e}\vec{n}} - 2\delta'\left(\frac{2\sigma_p}{\sigma_{He}}\right) A_{\vec{e}\vec{p}}. \tag{2.67}$$

This model provides a simple picture of the ^{3}He spin in terms of the nucleons, and is useful in understanding the contributions from the protons and neutrons to the ^{3}He quasielastic asymmetry. Because a large number of models are considered in determining δ and δ', it also provides information on the theoretical uncertainty in the extraction of information about the nucleons from the ^{3}He quasielastic asymmetry.

Chapter 3

The Experiment

3.1 Overview

The experiment to measure the quasielastic, spin-dependent asymmetry in the scattering of polarized electrons from polarized ^{3}He (MIT-Bates experiment 88-02) was proposed and carried out by a collaboration of Caltech and MIT. The experiment ran at the MIT-Bates Accelerator Center in March 1990 on beamline B in the South Experimental Hall. For the experiment, a beam of longitudinally polarized electrons was scattered from a polarized ^{3}He target, which was developed at Caltech. Because this was the first time a polarized target of this type was built, the target is described in extensive detail in a separate chapter. This chapter contains the description of the other experimental aspects.

A recirculated beam of 574 MeV incident energy was obtained from the polarized electron source, described in more detail in Section 3.2. The linac operated at 600 pulses per second with a typical peak current at the target of 1 mA and pulse length of 15 μsec.

The scattered electrons were detected in singles mode in two spectrometers, the One Hundred Inch Proton Spectrometer (OHIPS), and BIGBITE, named for its large momentum acceptance. Figure 3.1 is a schematic of the layout. OHIPS was located to the right of the beam direction ("beam right") at an angle of 51.1°. The central momentum of the spectrometer was set to correspond to the center of the quasielastic peak. The BIGBITE spectrometer was located to beam left at an angle of 44.0° and had a sufficiently large mo-

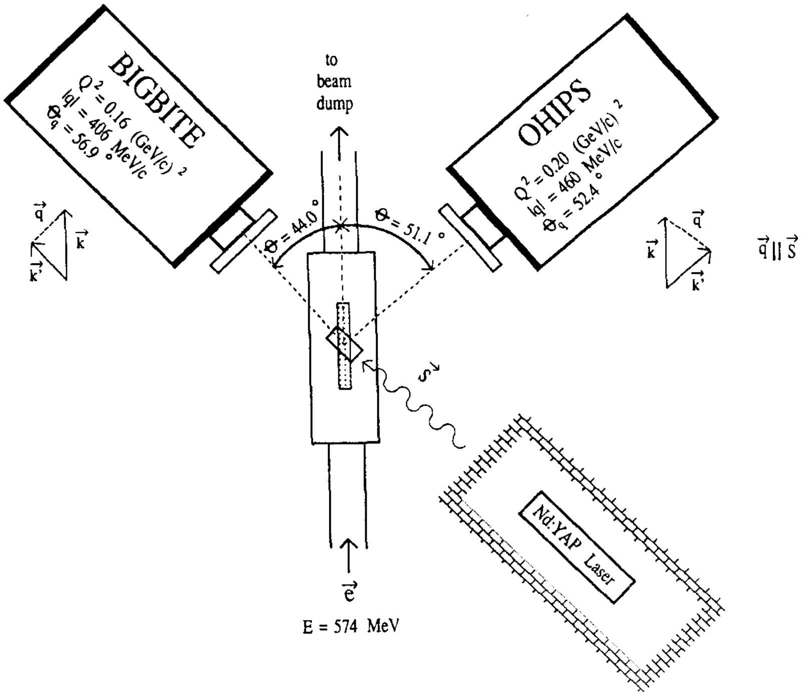

Figure 3.1: Layout of the spectrometers and the laser system for the experiment. The quasielastic kinematics of the events detected by each spectrometer is indicated on the schematic.

mentum acceptance to include both elastic and quasielastic events. The spectrometers will be described in more detail in Section 3.4. Table 3.1 contains a summary of the kinematics for the measurements.

The target spin was oriented in three different directions over the course of the experiment. Initially, the spin was oriented at an angle of 51.5°, beam left, relative to the incident electron momentum (runs 300-481). Next, it was rotated to 44.5° to improve the sensitivity of the quasielastic asymmetry measured with BIGBITE to the interference term, $R_{TL'}$ (runs 500-561). Finally, the spin orientation was reversed so that the spin angle was 135.5°, beam right (runs 562-659). For scattered electrons detected by OHIPS, this spin orientation corresponds to the angle between the target spin and the momentum transfer, defined in Chapter 2 as θ^*, being $\sim 0°$, so the quasielastic asymmetry measurement is very nearly maximally sensitive to $R_{T'}$. For quasielastic events in BIGBITE, θ^* was $\sim 75°$ so

	Q^2 $(\mathrm{GeV/c})^2$	θ (deg)	$\vec{q}$ (MeV/c)	$\theta_{\vec{q}}$ (deg)
OHIPS quasielastic	0.20	51.1	460.	-52.4
BIGBITE quasielastic	0.16	-44.0	406.	56.9
BIGBITE elastic	0.18	-44.0	420.	64.1

Table 3.1: Kinematics of the OHIPS and BIGBITE measurements. Positive angles indicate beam right and negative angles indicated beam left.

the quasielastic asymmetry is primarily sensitive to $R_{TL'}$.

3.2 Polarized Electron Beam

In the fall of 1989, the polarized source used at Bates was changed from a GaAs source designed at Yale to a GaAs source obtained from Chalk River, based upon the design from SLAC [7]. Although both sources use the same polarization technique, because the design of the SLAC-type source does not allow the crystal to become dirty as quickly, the lifetime of the GaAs source used for this experiment was much longer than that obtained for previous experiments at Bates. Under acceptable linac vacuum conditions, the new source operates with a mean lifetime of $\sim$ 120 hours and a quantum efficiency of $\sim$ 3%.

The principle of operation of the GaAs source is described in the general treatise on the subject of polarized electrons, Reference [8]. Basically, the source works through the photoemission of electrons that have been polarized through optical pumping. Electrons in the valence band of GaAs, a direct band gap crystal, absorb circularly polarized light and in the process are excited to the conduction band. A Pockels cell in the laser optics system that acts as a quarter wave plate determines the helicity of the optical pumping light and therefore, the polarization of the excited electrons. Once in the conduction band, the electrons diffuse to the surface, which has been treated with cesium to create a negative electron affinity, and are emitted and injected into the accelerator beam line. The source is located above the beamline so the electrons are bent through 90° for injection into the accelerator. Upon injection into the linac, the electrons have an energy of 380 keV and are longitudinally polarized.

The electron helicity was changed by varying the voltage on the Pockels cell in the polarized source laser optics. The helicity was selected randomly on a pulse by pulse basis. For operating the accelerator with the polarized source, the accelerator is phase-locked to the line frequency of 60 Hz. Actually, the helicity selection was done in a quasi-random fashion. For accelerator operation at a rep rate of 600 Hz, the helicity of the beam pulse is selected randomly in each of the first 10 pulses, then chosen to be the opposite helicity of those values for the next 10 pulses. For example, if the initial random order was

$$+ + + - + + - + - +,$$

then the next ten pulses would have the helicities

$$- - - + - - + - + - .$$

Varying the helicity in this quasi-random fashion allows the experimental data to be analyzed as ten separate asymmetry measurements, which have less noise than the full data set [11]. However, the data from this experiment were not analyzed in this manner, primarily because the ^{3}He quasielastic asymmetry was large enough that the noise did not present a problem.

For this experiment, the beam energy was chosen to provide longitudinally polarized electrons at the target after spin precession through the bending magnets along the beam transport line. Since this experiment used a recirculated beam, the spin precession came from the 360° bend of the recirculator and the 90° bend of the switching magnet that directed the beam into the B line of the South Hall. The precession angle with respect to the momentum of the electron spin for a given bend angle, θ_{bend}, is

$$\theta = \frac{g-2}{2}\gamma\theta_{bend}. \tag{3.1}$$

In this expression, γ is the relativistic factor, $\frac{E}{m_e}$, and g is the Landé g factor for the electron magnetic dipole moment. If the electron undergoes acceleration to an energy

$E_1 + E_0$ during the first pass through the linac, then gains an additional energy of E_1 during the second pass, the total spin precession is

$$\theta = 2\pi \frac{g-2}{2m_e} \left(\frac{E_{inc} + E_0}{2} \right) + \frac{\pi}{2} \frac{g-2}{2m_e} E_{inc} \tag{3.2}$$

where $E_{inc} = 2E_1 + E_0$ is the incident energy at the target. To obtain longitudinally polarized electrons at the target, one chooses the incident electron energy such that $\theta = n\pi$, where n is an integer. For $E_0 = 20$ MeV and $n = 2$, the "magic energy" that yields longitudinal polarization at the target is 574 MeV.

During the experiment the beam current at the target ranged up to 22 μA with an average current of 11 μA. Two beam toroids on the B-line, BT1 and BT2, were used to monitor the beam charge by measuring the induced current during the beam pulse. The energy-defining slits in the accelerator were set so that the spread in the beam energy was $\sim 0.6\%$ FWHM. The beam energy was determined using the dipole bending magnet (FB1) in the 14° line and the calibration from Reference [10] relating the nominal energy (MeV) to the true energy:

$$E = \frac{E_{nom}}{0.987 + E_{nom}(5.6 \times 10^{-5})}. \tag{3.3}$$

Using this formula the energy for this experiment is determined to be 574.3 MeV, an estimate that is valid at the 1% level in this energy range.

3.3 Møller Polarimeter

For this experiment, a Møller polarimeter was built and installed by a collaboration of Caltech, MIT, and NBS[9] in the north dump area, after the last bend from the beam switchyard into the B line, upstream of the polarized ^{3}He target. This section summarizes the design of the polarimeter and the beam polarization measurements done by the collaboration.

The polarimeter was set up to measure the spin-dependent asymmetry in polarized electron-electron scattering (Møller scattering) at a center-of-mass angle of 90° corresponding to a head-on collision between the two electrons. As one would expect from the Pauli

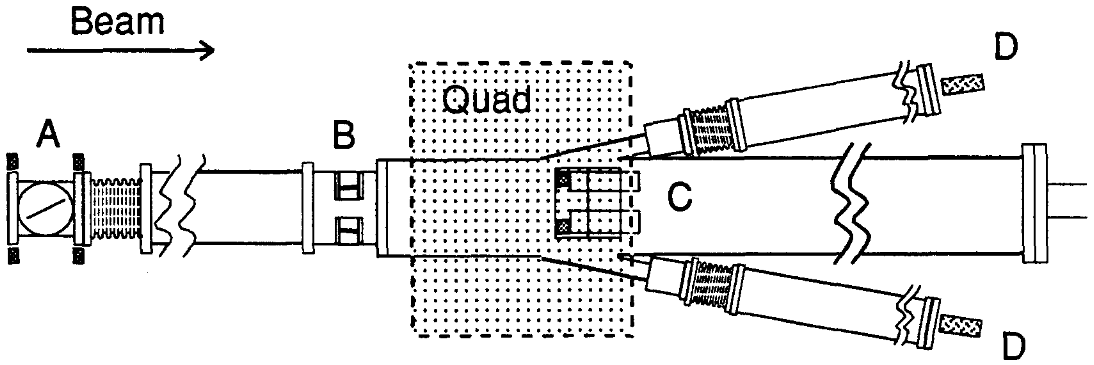

Figure 3.2: Schematic drawing of the Møller polarimeter. (A) target; (B) and (C) collimators; (D) detectors.

exclusion principle for identical fermions, the scattering cross section for the two electrons is much smaller if their spins are oriented in the same direction relative to having their spins in opposite directions. The spin-dependent asymmetry is maximum at 90° in the center-of-mass system and vanishes for scattering at 0° or 180°. The asymmetry can be written in the form

$$A_{Moeller} = \sum_{i,j=x,y,z} P_i^t P_j^b A_{ij}, \tag{3.4}$$

where P^t and P^b are the target and beam polarizations, respectively, and $\hat{z}$ is along the beam direction, $\hat{y}$ normal to the scattering plane in the direction of $\vec{k}_{inc} \times \vec{k}_{final}$, and $\hat{x}$ is along $\hat{y} \times \hat{z}$. For ultrarelativistic electrons and scattering at 90° in the center-of-mass frame, all A_{ij} vanish except $A_{yy} = -A_{xx} = \frac{1}{9}$ and $A_{zz} = -\frac{7}{9}$. Thus, the asymmetry for longitudinally polarized electrons scattering from a target of known polarization oriented along the $\hat{z}$ direction is quite sensitive to the beam polarization.

Figure 3.2 shows the layout of the Møller polarimeter. The apparatus consists of a target chamber surrounded by Helmholtz coils oriented with the $\vec{B}$ field along the beam direction, followed by a collimator that momentum-selects Møller scattered electrons in the horizontal plane at 90° in the center-of-mass system ($\theta_{lab} = 2.4°$). Downstream is a quadrupole magnet that defocuses the Møller electrons from the beam direction, bending them along side arms, where they are detected in aerogel Čerenkov counters. The polarimeter was set up to detect the scattered electrons from a beam of 574 MeV incident energy, although the polarimeter can be modified to work for any beam energy by placing the target chamber on a movable platform and installing a system of bellows before and after the target chamber.

The target chamber contained a movable target ladder with a BeO target for beam position monitoring and tuning to the Møller peak, an aluminum target for tuning, and two supermendur (49% Fe, 49% Co, 2% V) foil targets for the polarization measurements, one $\approx 25\mu$ thick and the other $\approx 13\mu$ thick. An empty frame was included for normal running on the polarized ^{3}He target. Only the thinner target was used for this experiment to limit the count rate and multiple scattering. The beam position was monitored during the data acquisition with a microwave cavity, beam position monitor upstream of the target chamber. During the Møller runs, a water-cooled beam dump in the form of slits was moved into the beam line to stop the scattered beam from hitting the ^{3}He target.

The supermendur foil was oriented at 30° to the beam direction, and a $\vec{B}$ field of 150 G from the Helmholtz coils was used to magnetize it. The field was sufficient to saturate the electron polarization in the ferromagnetic foil. The longitudinal polarization at saturation for a foil oriented at 30° to the beam direction is $P^t = 0.068$. The target polarization was determined by reversing the direction of the holding field while measuring the voltage induced in pickup coils enclosing the target foil. This was done during offline calibration runs, not during the experiment.

For Møller scattering at $\theta_{cm} = 90°$, both the beam electron and the atomic electron are scattered with equal energy in opposite directions. In principle, they can be detected either in coincidence or singly. For this experiment, all of the data collected for the beam polarization measurement were taken in singles mode, using only one of the Čerenkov detectors. This meant that the count rate was much higher than one would have achieved with a coincidence measurement, but the background was much worse. The system was designed to measure the electron polarization for beam energies ranging from 150 MeV to 1 GeV, so the background was worse than could be achieved for a single energy polarimeter simply because of collimating considerations. Another problem encountered was that during the experiment the background signal fluctuated on an intermediate timescale that was smaller than the time needed to complete a set of runs to determine the beam polarization ($\approx$ 30 minutes), but much longer than the beam pulse duration. This led to a background that varied between individual runs of a Møller measurement. The fluctuating background signal is probably a result of fluctuations in the beam position; the number of particles passing through the collimator and being bent into the side arms depends upon the position at which the incident beam hits the target foil.

For the asymmetry measurement, data were collected for 3072 beam pulses at a single field setting of the quadrupole magnet; then the magnetic field was changed and the process repeated. The signal from the Čerenkov detector was integrated over the beam pulse and normalized to the amount of charge in the pulse. The beam helicity during the Møller runs was varied randomly on a pulse-by-pulse basis. The field of the quadrupole magnet, B_Q, was varied from below the field that centered the Møller scattered events on the detector, B_Q^{peak}, to above the peak. The data from the scan showed the size of the background relative to the Møller peak. For the runs taken during this experiment, the signal-to-noise ratio was approximately 1:6. No spin-dependent asymmetry was observed in the background counts.

The beam polarization was measured four times over the course of the experiment, each measurement taking 30 minutes or more to complete. Table 3.2 shows the run numbers and the extracted longitudinal electron polarizations for the measurements. The polarization from the second run is $\approx$ 15% lower than the polarizations from the other three data

Run Number	P_e
330	$38.5 \pm 4.6\%$
509	$31.9 \pm 7.0\%$
536	$39.8 \pm 5.3\%$
650	$46.9 \pm 6.9\%$

Table 3.2: Values of the beam polarization measured during MøIler runs.

sets. It was discovered that the circular polarization of the laser light at the source was not maximized, leading to the decreased polarization of the electrons. The problem was corrected and another MøIler run was taken (the third set) afterwards to verify that the electron polarization returned to normal. It was determined that ^{3}He runs 500-524 were taken with the lower beam polarization. The experimental asymmetries for these runs are calculated assuming the beam polarization measured in the second MøIler run. The data from the other three runs are averaged to obtain $P_e = 40.8 \pm 4.1\%$ and are used for the extraction of the ^{3}He asymmetry for all other runs.

3.4 The Spectrometers

3.4.1 OHIPS

The OHIPS spectrometer consists of two quadrupole magnets and a 100″ radius dipole magnet, which bends particles in the vertical plane (QQD). For this experiment, the quadrupole magnets were operated in VH mode, where Q1 focused in the dispersive direction (x) and Q2 focused in the direction transverse to the bend plane (y). This configuration gives better angular acceptance for extended targets at the expense of the momentum resolution, a quantity that is less important for quasielastic scattering since the peak is already broadened significantly by Fermi motion. The spectrometer was moved as close to the pivot as possible, subject to contraints from the target geometry, in order to maximize the solid angle; the drift distance from the target center to the effective field of the first

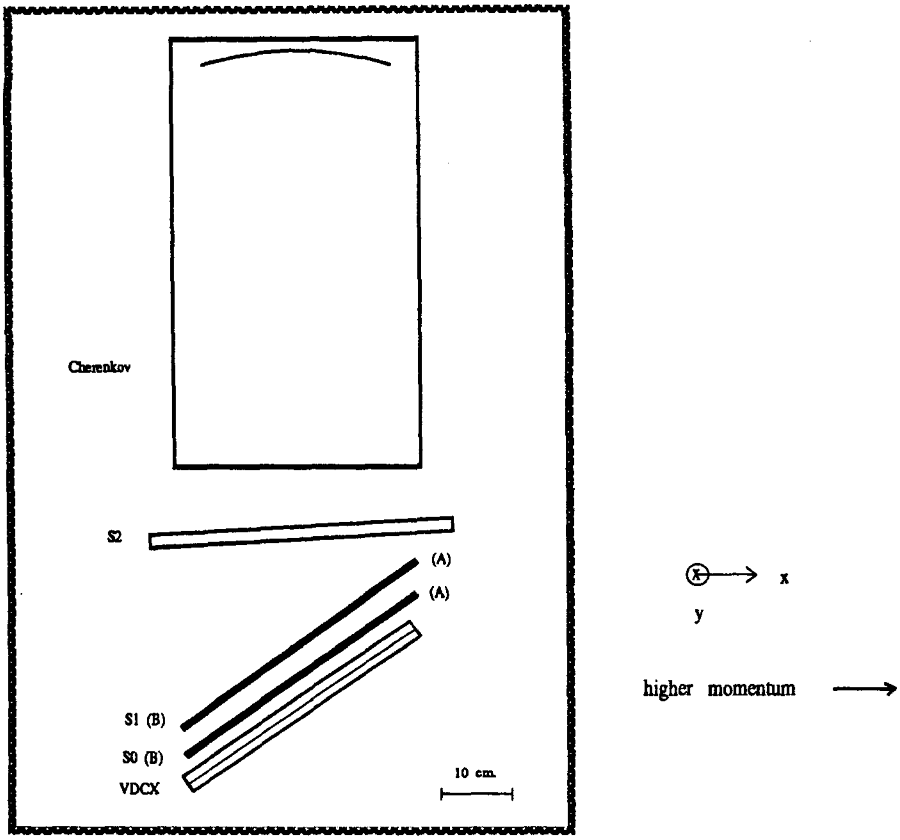

Figure 3.3: OHIPS detecter layout.

quadrupole was 93 cm. A 21 cm-thick lead collimator was attached in front of the first quadrupole to reduce background and define the solid angle acceptance. The collimator opening was 17.1 cm (x direction, upstream end) by 7.6 cm (y direction, upstream end).

The detectors used for OHIPS were a crossed-wire, vertical drift chamber (VDCX), and three plastic scintillators. A Čerenkov detector was also installed but did not provide much usable information because an electronics problem limited the high voltage that could be applied to the phototube without inducing noise in the drift chamber readout. Figure 3.3 shows the layout of the detectors. A detailed discussion of the VDCX and the electronic readout can be found in [14]. The scintillators were made of NE110 plastic; S0 and S1 were 0.48 cm thick, and S2 was 3.8 cm thick. The dipole magnet was set so that the central momentum of the spectrometer was 462 MeV.

3.4.2 BIGBITE

BIGBITE is a horizontal-bend spectrometer with two quadrupole magnets and a dipole magnet with a bend angle of 35°. The spectrometer was operated in the forward quad configuration [15], which gives a larger solid angle acceptance at the expense of momentum resolution and acceptance. The BIGBITE target slits are located inside the spectrometer vacuum window in front of the first quadrupole magnet. BIGBITE slit #1 (3.8 cm horizontal by 12.7 cm vertical, elliptical opening) was used for the experiment. The detector package consists of two wire chambers followed by two scintillators, all located inside a concrete hut. At the rear of the hut is a concrete block, which allows access to the detectors while reducing background radiation. Early in the experiment, shielding blocks were added between the beam dump and the hut to reduce the background rate. The number of ungated events per unit beam charge was reduced by approximately a factor of four with the shielding in place. A description of the multiwire proportional counters and the associated electronics readout system is given in Reference [16] and a description of the scintillators in Reference [15]. The scintillators were each arranged into three sections, labeled 1-3, where subsection 1 was on the high momentum side. Scintillator A was closer to the target.

Because events analyzed by the BIGBITE spectrometer are bent in the horizontal plane, for an extended target there is a correlation between the position along the target at which an event originates and the reconstructed momentum. This results in a decreased momentum resolution for extended targets. Figure 3.4 shows the momentum resolution for a 10 cm-long target viewed at a spectrometer angle of 44° in terms of $\delta \equiv \frac{\Delta p}{p_0}$, where p is the particle momentum and p_0 is the spectrometer central momentum, which was set to 517 MeV for this experiment. The spectrometer properties were calculated with a Monte Carlo program, which used rays generated by TURTLE [12]. The TURTLE deck used is given in Appendix A.

BIGBITE detected both elastically and quasielastically scattered electrons, with the quasielastic peak centered at $\delta \sim -5\%$ and the elastic peak at $\delta \sim +5\%$. The advantage

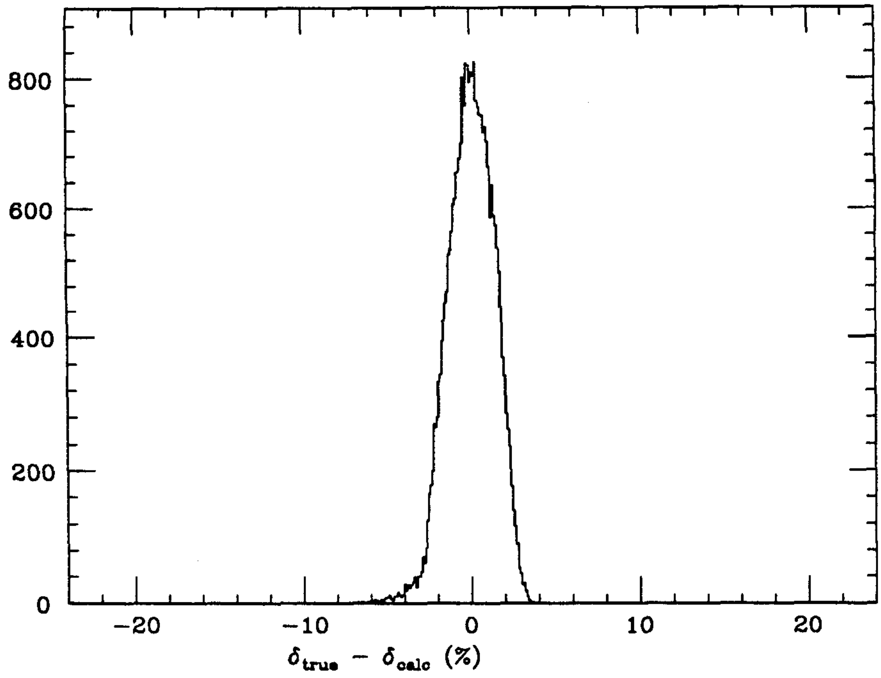

Figure 3.4: The momentum resolution of the BIGBITE spectrometer for an extended target of 10 cm length viewed at 44°. The momentum resolution is given in terms of $\delta \equiv \frac{p-p_0}{p_0}$, where p is the momentum of the scattered electron and p_0 is the central momentum of the spectrometer. The values plotted are the number of events vs. $(\delta_{true} - \delta_{calculated})$, and is generated by a TURTLE Monte Carlo calculation.

of this spectrometer is that the momentum acceptance is large enough to include both the elastic peak and a large portion of the quasielastic peak. The disadvantage is that the poor momentum resolution prohibited the clean separation of the elastic peak and the continuum threshold; thus, it was not possible to extract unambiguous information about the elastic asymmetry. The events in the quasielastic region could be extracted without this problem by restricting the analysis to regions around the quasielastic peak sufficiently far from the elastic and threshold regions.

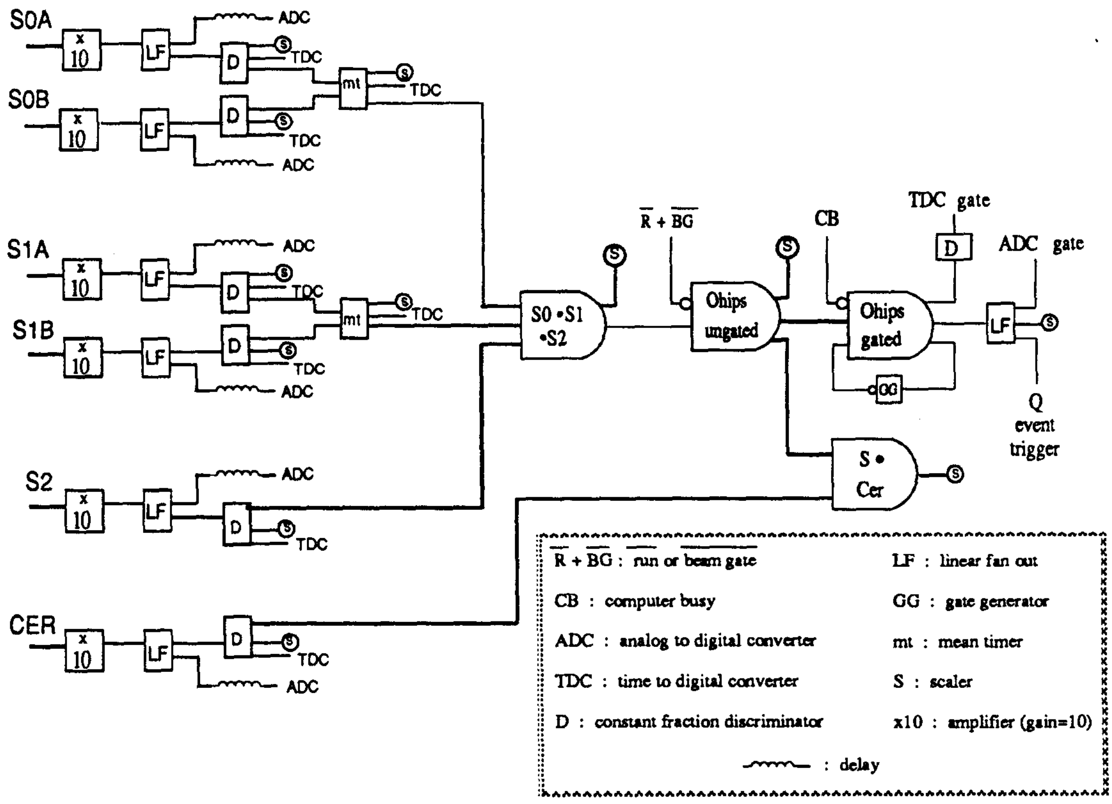

Figure 3.5: OHIPS event trigger logic.

3.5 Data Acquisition System

The data were acquired using the "Q" data acquisition program [17] running on a dedicated microVAX computer. The Q system was set up to trigger on each beam-burst and read the integrated charge, measured by toroidal magnets upstream of the target, and the electron helicity for the beam-burst. In this way, the charge was accurately accounted for each beam helicity. The Q system also read scalers and event data from both spectrometers. The target polarization information was acquired by an acquisition and control system running on a dedicated microVAX, described in Section 4.3.4. The information was passed to the main acquisition system each second through Camac event registers read in with the scalers by Q approximately every five seconds. Detailed information on the target polarization was stored separately by the target control system. The beam helicity information was included in the event stream for each spectrometer, in addition to being included in each

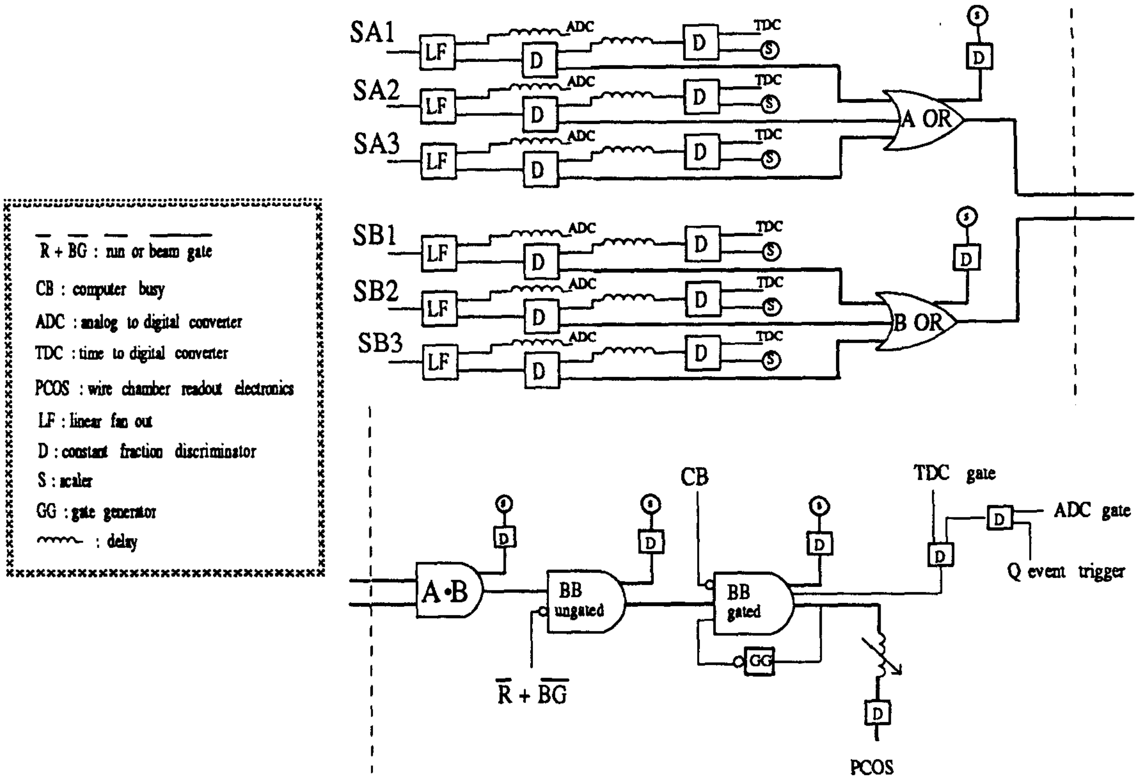

Figure 3.6: BIGBITE event trigger logic.

beam-burst event.

Standard, single-arm, data acquisition systems were used for both OHIPS and BIGBITE. The analog signals from the phototubes for the scintillators are used to form the trigger logic in addition to being sent through Analog to Digital Converters (ADC) and Time to Digital Convertors (TDC) for the spectrometer event data stream. The digitized information from the various detectors is buffered by the Microprogrammable Branch Driver (MBD), then transferred to the Q data acquisition system, which stores the events on magnetic tape and performs the online analysis.

Figure 3.5 shows the OHIPS event trigger logic. The ungated event trigger from OHIPS requires a signal from all three scintillators, with a veto for events outside the beam gate or when data acquisition is not requested through the Q system. The gated events are vetoed if the computer is busy and are limited to a single event per beam-burst.

Figure 3.6 is a diagram of the BIGBITE event trigger. At least one hit in each scintillator plane is required for the ungated event trigger. This requirement does not incorporate into the trigger the information about the particle momentum from the sectioning of each scintillator plane. This is done by software cuts to determine "good" events, a process discussed in Section 5.1. The gated event is limited to one event per beam-burst and is vetoed by a "computer busy" signal.

Chapter 4

The Polarized ^{3}He Target

In the early 1960s a technique to polarize ground state ^{3}He atoms through metastability-exchange collisions with optically pumped ^{3}He metastable atoms was developed at Rice University [18]. Since that time, the use of polarized ^{3}He in atomic and nuclear physics has generated much interest and activity in the community. For nuclear physics, polarized ^{3}He has been considered for both the target and the beam at a variety of facilities. An interesting collection of papers on polarized beams and targets, and on the physics possibilities for each, is found in the proceedings of the workshop on polarized ^{3}He in nuclear physics held at Princeton in 1985. [19].

The earliest attempts to build a polarized ^{3}He target were made at Rice University [20] [21]. The targets were designed for low-energy, nuclear structure experiments, several of which are described in [22] [23] and the references therein. The early targets operated at room temperature with pressures of $\sim$ 1 torr and were limited in polarization to $P_t \sim 10\%$ because they were optically pumped with ^{4}He arc lamps. They were designed to operate with low hadronic beam currents, $\sim$ 10$-$100 nA, where beam depolarization does not present a problem.

In 1968, a group at Toronto embarked on an ambitious project to construct a polarized ^{3}He target with high density and polarization [24][25]. Their goal was a target of 500 ml ^{3}He gas with a pressure of one atmosphere and 25% polarization, which they attempted to achieve by using a mercury Toeppler pump to compress ^{3}He which had been polarized in a separate cell through the metastability-exchange optical pumping technique. Ultimately they failed in their attempt, primarily because of the difficulty of working with the mercury compression pump and limitations in the pumping rate from ^{4}He arc lamps. However, much useful information about spin relaxation mechanisms was learned from their research.

The interest in polarized ^{3}He extends beyond low-energy nuclear structure physics. The development of lasers that operate at the frequency needed for optical pumping of the metastable ^{3}He atoms has opened new possibilities in research using polarized ^{3}He. A review of current research in atomic, condensed matter, and nuclear physics using polarized ^{3}He is found in [26]. One interesting research program being pursued at l'Ecole Normale in Paris is the study of the quantum statistics of spin-polarized liquid ^{3}He [27]. A current option for a high polarization electron source is the helium afterglow, or chemi-ionization, source, which uses polarized metastable ^{3}He to produce polarized electrons [28][29].

The development of the target described in this work became feasible when laser technology advanced to the point where intense sources of optical pumping light in the infrared, in particular at the wavelength of the $2^3S \rightarrow 2^3P$ transition in ^{3}He, $\lambda = 1.0834\mu$m, became commercially available. The increased optical pumping power meant that new targets could be developed with high polarization at densities suitable for electron scattering experiments. In the case of the target developed at Caltech, the higher density was achieved by optically pumping the ^{3}He in one cell at room temperature and using a second cell at $\sim$ 15 K, connected by diffusive transfer to the pumping cell, as the target cell. The project was started at Caltech in 1985 and involved a series of feasibility studies to assess the beam depolarization effects using a beam of protons from the Pelletron accelerator at Kellogg Radiation Lab on the Caltech campus. The polarized target for the MIT-Bates experiment was built in 1988, and a beam depolarization study was done with electrons at MIT-Bates in January 1989, a year before the experiment to measure the spin-dependent asymmetry ran.

In this chapter, the method of optical pumping and the relevant spin relaxation mechanisms are described in the first section. Next, a description of the design and operation of the ^{3}He polarized target, along with a brief outline of the early studies done at Caltech using prototype systems, is given. Then the polarization and relaxation time measurements are described, and lastly, details of the beam depolarization studies performed on the polarized ^{3}He target are presented.

4.1 Optical Pumping of ^{3}He

"Optical pumping" refers to a technique of transferring angular momentum from photons to atoms, creating a nonthermal population distribution of the magnetic substates through the absorption of radiation at an atomic transition frequency. The possibility of producing large atomic polarizations through the absorption of circularly polarized light in both ground state and excited state atoms was proposed by Kastler [30] in 1949. This suggestion led to the development of many different techniques for polarizing a variety of atoms. A review of the theory and application of the process, along with a discussion of the spin relaxation mechanisms, is found in Reference [31].

If the ground state of ^{3}He is polarized, then the nucleus is polarized because the atom is in a $J = 0$ state. Direct optical pumping of the ground state is not feasible because the transition frequency is in the ultraviolet. Two possibilities exist using optical pumping to polarize ^{3}He. The technique used for this target involves polarizing the 1^1S_0 ground state ^{3}He atoms through metastability-exchange collisions with optically pumped 2^3S_1 metastable atoms, a technique developed by Colegrove, Schearer, and Walters [18] at Rice University in the early 1960s. Another technique for polarizing ^{3}He involves spin-exchange with polarized alkali atoms; this technique was not used for the Caltech target and is not discussed here.

The metastability-exchange optical pumping procedure works as follows. The metastable 2^3S_1 population is established using a weak rf discharge in a cell of ^{3}He gas at a pressure of order 1 torr. The ratio of ground state atoms to 2^3S_1 atoms is $\sim 10^6 : 1$; the exact value depends upon the discharge level. The cell is placed in a homogeneous, magnetic field with the $\vec{B}$ field direction defining the spin quantization axis. Circularly polarized light at $\lambda = 1.0834\mu$m, the wavelength of the $2^3S_1 \rightarrow 2^3P_0$ atomic transition, incident upon the ^{3}He atoms, induces $\Delta m = +(-)1$ transitions for right-handed (left-handed) circularly polarized light, where m is the magnetic quantum number. (Note the use of the definition of right-handed circular polarized light conventional with atomic physicists as opposed to the definition given in the standard text on electromagnetism by Jackson [32].) The 2^3P_0 state decays through photon emission with equal probability to any accessible state with the electromagnetic transition rules, $\Delta L = 1$ and $\Delta m = 0, \pm 1$. Repeated absorption and emission build up a nonthermal population distribution in the magnetic substates of the metastable atoms: The metastable atoms become polarized. The polarization is transferred to the ground state atoms through collisions that do not alter the nuclear spins of the atoms involved but exchange the excitation of the electron clouds, known as "metastability-exchange" collisions. The collision process can be written schematically as

$$^3\overrightarrow{\mathrm{He}}(2^3S_1) \; + \; ^3\mathrm{He}(1^1S_0) \longrightarrow \; ^3\overrightarrow{\mathrm{He}}(1^1S_0) \; + \; ^3\mathrm{He}(2^3S_1).$$

The level diagram for atomic ^{3}He is shown in Figure 4.1. The nine lines that comprise the $2^3S \rightarrow 2^3P$ transition are designated by the notation C1-C9. Figure 4.2 shows the relative frequencies and intensities of the lines. Figure 4.3, taken from reference [33], shows the calculated, achievable, ground state polarization vs. the pumping light intensity for various transitions in two extreme cases, one the low pressure limit where there is no collisional depolarization of the 2^3P state and the other the high pressure limit where total collisional depolarization occurs. We operate the target at 2 torr, which is in the regime where collisional depolarization is important. Therefore, higher polarizations are achieved through optical pumping at the frequency of C8 or C9, rather than C5.

The relevant timescales for optical pumping are the pump-up time of the metastable atoms (τ_p), the relaxation times of the metastable (τ_r) and ground state (T_r) atoms, the timescales of the metastability exchange of the metastable (τ_e) and ground state (T_e) populations, the time for radiative decay through spontaneous emission of the 2^3P state (τ), and the timescale for the collisional mixing of the 2^3P atoms (τ_c). A discussion of the

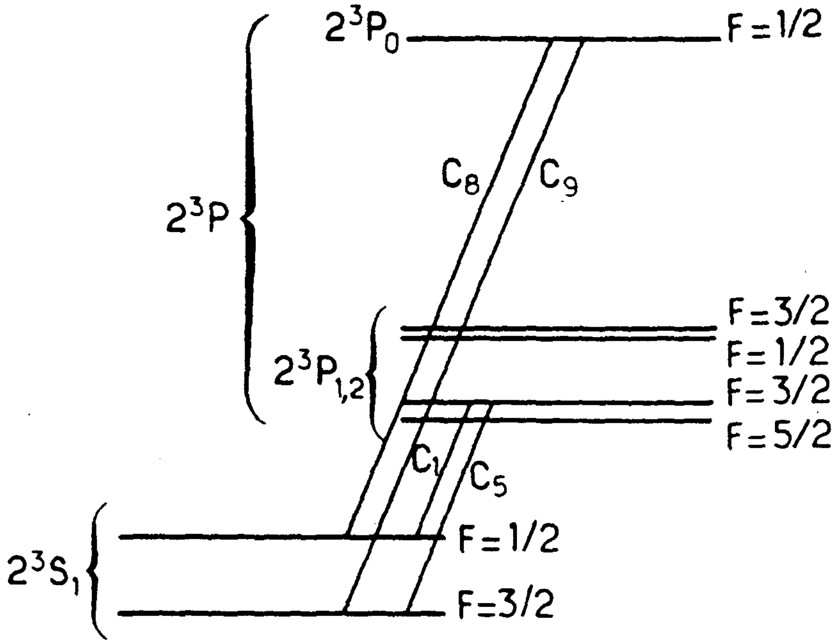

Figure 4.1: Level diagram for the 2^3S and 2^3P states of ^{3}He . [33]

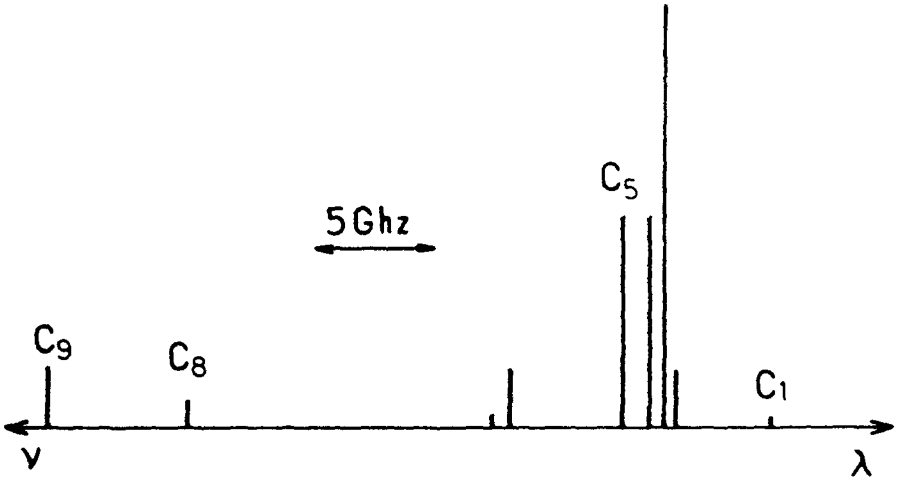

Figure 4.2: Relative strength and frequency of the transition lines for $2^3S \rightarrow 2^3P$ states of ^{3}He . [33]

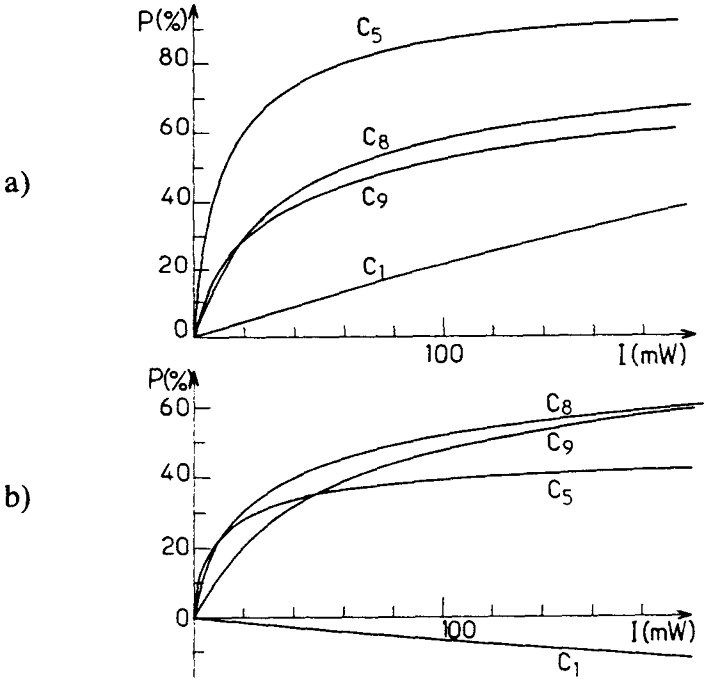

Figure 4.3: Calculated ^{3}He nuclear polarization vs. light intensity at a given transition frequency. a) No collisional mixing in the 2^3P state (low pressure limit). b) Complete collisional mixing in the 2^3P state (high pressure limit). The calculation assumes 0.3 torr ^{3}He gas pressure. Taken from Reference [33].

timescales is given in Reference [35]. We can assume that the target operates in a pressure regime where collisional mixing is significant ($\tau_c \leq \tau$; $\tau \sim 10^{-7}$ sec), so that the conditions for high pressure mentioned in the previous paragraph apply. To polarize the ground state efficiently, it is necessary that the timescale for the spin exchange between the two populations be much shorter than the spin relaxation times. The metastability-exchange rates can be written in terms of the metastability-exchange cross section as

$$\frac{1}{T_e} = \langle \sigma_e v \rangle n_m \tag{4.1}$$

$$\frac{1}{\tau_e} = \langle \sigma_e v \rangle N_g \tag{4.2}$$

where N_g and n_m are the ground state and metastable state number densities. For helium, σ_e is quite temperature-dependent [34] [35]; the cross section decreases roughly two orders of magnitude between 300 K and 4.2 K. To obtain efficient optical pumping, it is necessary to operate with the metastable atoms near room temperature, where $\tau_e \sim 10^{-6}$ sec and $T_e \sim 1$ sec. The nuclear polarization of the ground state atoms and the atomic orientation of the metastable atoms are destroyed by several mechanisms, which are described in Section 4.2. For now suffice it to say that the relaxation that is due to collisions with electrons, ions, and other states created by the discharge dominate in the pumping cell where the discharge must be maintained to create the metastable atoms. The relaxation times are dependent upon the exact conditions, but in general, $\tau_r \sim 10^{-4}$ sec and $T_r \sim 100$ sec. The metastable pumping rate depends upon the incident pumping light. Early work was done with ^{4}He discharge lamps for which $\tau_p \sim 10^{-4}$ sec. However, today laser sources provide much more intensity so that metastable pump-up times of order 10^{-7} sec are currently achieved.

The optical pumping technique described above is limited to relatively low pressures. The ^{3}He pressure range over which the technique works is approximately 0.1 torr to 10 torr. No other atomic species need be present for the optical pumping technique to work efficiently, so the gas can be pure ^{3}He. At low pressures the polarization is limited by collisions with the walls of the container, which cause spin relaxation, and at high pressures the lifetime of the metastable atoms limits the efficiency. Also, as a practical matter, it is difficult to maintain a uniform discharge in the ^{3}He gas as one goes to pressures above ~ 3 torr and to larger pumping cells.

^{3}He metastability-exchange optical pumping has benefited greatly from the development of lasers that operate in the infrared. The most convenient lasing materials are crystals similar to YAG, which use Nd^{3+} as the lasing centers. Two solid state crystals that can be made to lase at $\lambda = 1.0834\mu$m have become commercially available in the last five years. The first to become available in laser-quality crystals was neodymium-doped yttrium-aluminum-perovskite, YAlO$_3$, commonly known as YAP [36] [37]. The YAP crystal was used to pump optically the ^{3}He target developed for this experiment, primarily because it was the best intense source of polarized light available at the time. Section 4.3.3 contains a description of the laser used for the experiment. More recently,

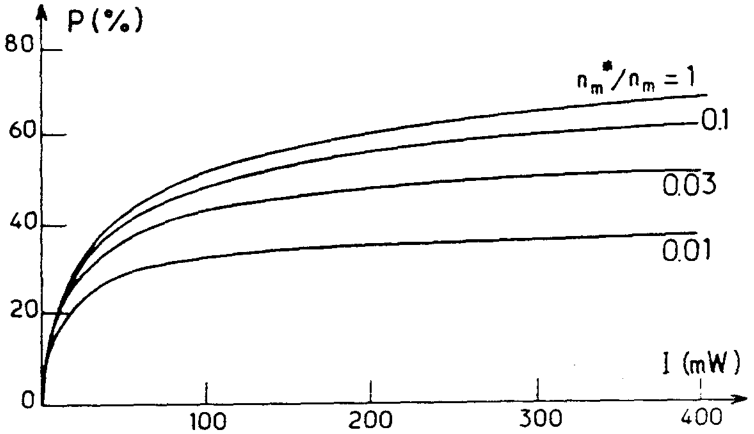

Figure 4.4: Calculated ^{3}He nuclear polarization vs. light intensity as a function of metastable population fraction within frequency bandwidth of the pumping light. Calculation assumes light at the frequency of the C9 transition and ^{3}He gas pressure of 0.3 torr. Taken from Reference [35].

a $La_{1-x}Nd_xMgAl_{11}O_{19}$ (LNA) crystal has become available [38] [39] [40] and offers much better frequency and stability characteristics than the YAP crystal. The continuing work at Caltech on the polarized ^{3}He target uses an LNA laser.

Reference [35] contains a detailed discussion of the influence of the pumping source characteristics (such as intensity, frequency, and polarization) upon the achievable nuclear polarizations with an emphasis on characteristics relevant to current laser light sources; a description of the calculation that generated the curves in Figure 4.3 is given in the reference. Also discussed are the effects of matching the frequency distribution of the optical pumping light with the Doppler distribution of velocities of the metastable atoms. The frequency matching has a significant effect upon the achievable nuclear polarization. Let n_m denote the total number of metastable atoms and n_m^* the number that are within the velocity class that can be optically pumped by the incident radiation. Figure 4.4, taken from Reference [35], shows the results of the calculation for different values of (n_m^*/n_m), assuming the pumping frequency of the C9 component to be at room temperature. As the graph shows, the achievable polarization depends strongly upon this parameter. The same reference indicates that $(n_m^*/n_m) \sim 0.05$ for standard multimode operation of their laser system with the ^{3}He atoms at room temperature. This is similar to the conditions for the laser used for the Caltech polarized target system.

The metastability-exchange technique for polarizing ^{3}He is a rapid process. In practical terms, net pumping rates of $10^{17} - 10^{18}$ polarized atoms per second can be achieved without difficulty using the lasers available at this time. This means that the target can be polarized on the order of minutes. The rapid polarization rate is a clear advantage of this polarization technique over the alternative of spin-exchange with polarized alkali atoms, a process that requires hours to polarize the ^{3}He atoms. An additional advantage is that the ^{3}He acts as its own buffer gas and the optical pumping is done directly on ^{3}He atoms. Therefore, there is no dilution of the ^{3}He that is due to other atomic species being present in the cell. This reduces the background, especially for experiments that study nucleon properties where buffer gases such as nitrogen contribute 28 nucleons per molecule relative to the 3 nucleons in ^{3}He. The background in experiments using pure ^{3}He as the target is substantially reduced from those that require other atomic species to be present.

4.2 Spin Relaxation Mechanisms

Spin relaxation can be broken into two very general categories: spin-spin relaxation, which involves the interaction of the dipole moments of neighboring atoms and spin-lattice relaxation, which couples the spins to external influences. Reference [41] indicates that the intrinsic relaxation time that is due to nuclear dipole-dipole interactions for ^{3}He is

$$T_{d-d} = 1.95 \times 10^8 \frac{\sqrt{T}}{p} \tag{4.3}$$

for a gaseous sample at temperature, T (K), and pressure, p (torr), which corresponds to an intrinsic relaxation time of order 10^9 sec for a 1 torr sample at room temperature. In any practical application as a nuclear target, the relaxation limitations arise from the spin-lattice interaction.

It is important to understand the mechanisms that contribute to the depolarization of the ^{3}He ground state atoms, especially those that affect the polarization of the nuclei in the target cell. In general, the spin relaxation is caused by magnetic field gradients and collisions, which tend to disorient the atoms. The collisions contributing to the depolarization involve interactions with electrons, ions, excited states, and impurities in the gas, and interactions with atoms at the surface of the container. For the treatment that follows, the depolarizing effects are broken into four categories: magnetic field gradients, surface effects, discharge effects, and beam effects. In this section a discussion of the relaxation mechanisms is given. The results of a quantitative assessment of the effects for the polarized target are given in Section 4.5.

4.2.1 Magnetic Field Gradients

The depolarization from magnetic field gradients arises because a spin will precess around a magnetic field. In a dc holding field, if a magnetic field gradient exists over the volume of a cell containing polarized atoms, then as the atoms diffuse through the volume, they will see an effective time-varying magnetic field, which tends to alter the direction of the orientation. By the very nature of Brownian motion, the diffusing atoms experience a randomly fluctuating magnetic field so that there are no coherent effects. Reference [42] deals with nuclear, spin-lattice relaxation from magnetic field gradients. A generalization of the treatment given in this reference finds that the relaxation rate that is due to small transverse gradients in a holding field that is principally along the $\hat{z}$ direction is

$$\frac{1}{t_g} \equiv \frac{\langle v^2 \rangle}{3} \frac{|\vec{\nabla} B_x|^2 + |\vec{\nabla} B_y|^2}{B_0^2} \left(\frac{\tau_c}{1 + \omega_0^2 \tau_c^2} \right) . \tag{4.4}$$

B_0 is the holding field, τ_c the mean time between atomic collisions, and $\omega_0 = \gamma B_0$ is the Larmor frequency for the magnetic field. For ^{3}He the gyromagnetic ratio, γ, is 3.24 kHz/G. Schearer and Walters [42] measured the mean collision rate as a function of pressure at 300° K and determined that $\tau_c = (2.2 \pm 0.2) \times 10^{-7} p^{-1}$sec, where p is the pressure in torr. $\langle v^2 \rangle = 3kT/m$ is the mean square thermal velocity of the atoms.

The relaxation rate from magnetic field gradients decreases as the temperature decreases since the atoms move more slowly and therefore experience smaller fluctuations in the field for a given amount of time. In a double-cell system such as the design used for the Caltech target where the target cell is cooled and the pumping cell is operated at room temperature, the effect of the field gradients is more important for the pumping cell.

4.2.2 Surface Effects

The ^{3}He nuclear polarization can be destroyed by interactions with atoms in the cell walls. This happens when the atoms diffuse to the walls, are absorbed or adsorbed onto the surface and interact with paramagnetic impurities there. Clearly, this effect depends strongly upon the properties of the specific surface chosen for the container. In general, the mechanism for the surface-induced relaxation is not well understood. Several studies have investigated the effects and measured the ^{3}He spin relaxation times for a variety of materials. References [43] and [44] deal with nuclear spin relaxation on different types of glass, while reference [41] extends the study to include both glass and metal surfaces.

The depolarization process for glass surfaces can be fairly well understood in terms of two competing processes, one that dominates at high temperatures and the other that dominates at low temperatures. At high temperatures the relaxation is primarily due to permeation of the ^{3}He atoms into the glass surface. This conclusion is supported by the empirical evidence that the surface-induced relaxation time, T_s, is much shorter for quartz and pyrex borosilicate glass than for Corning 1720 or 1723 aluminosilicate glass, which is highly impermeable to helium. At low temperatures the relaxation is dominated by adsorption onto the surface. The sticking time increases as $\tau_0 \exp(-E/kT)$, where E is the adsorption energy ($\sim$0.01 eV) and $\tau_0 \sim 10^{-13}$ sec [43], so as one goes to lower temperatures, this term rapidly becomes important. The relaxation time at a particular temperature is very sensitive to the exact properties of the surface. Large variations are observed between different samples of the same material, making it difficult to predict the effect of the surface interactions accurately. Reference [41] gives measured values of $T_s \sim 10^4$ sec for pyrex at room temperature, the glass used for the pumping cell in the target system.

For metal surfaces no relaxation effect from permeation should be seen. The depolarization is probably dominated by adsorptive effects, especially at low temperatures, although the surface-induced depolarization mechanism is not well understood. According to the study of surface-induced relaxation from various metals [41], the observed relaxation rates cannot be explained simply in terms of paramagnetic impurities. At room temperature the measured relaxation times for metals obtained from the study are of order $10^4 - 10^5$ sec.

Metastability-exchange optical pumping has a fast pumping rate, so in the pumping cell, maintained at room temperature, the surface effects are not very important, and pyrex can be used. For practical applications to nuclear targets, at room temperatures the surface-induced relaxation effects from pyrex surfaces are negligible compared to the depolarization from magnetic field gradients for an extended geometry such as that used for the double-cell target system. On the other hand, at low temperatures, $\leq 20K$, the surface effects become very important. One way to ameliorate the effects is to coat the cold metal surface with an inert substance. Substantial decreases in the relaxation rates can be achieved this way; the effects observed at Caltech for the polarized target are discussed in Section 4.5.1.

It is clear that the treatment of the surfaces of the cells that contain the polarized ^{3}He gas is very important. Achievable polarizations and relaxation rates depend critically upon the cleanliness of the surfaces with which the polarized gas comes in contact. A description of the procedure used to clean the target system is contained in Appendix B.

4.2.3 Discharge Effects

As was mentioned previously, a discharge must be maintained in the gas to create the metastable 2^3S atoms. The discharge is not selective, so many excited states, ions, and electrons are also present in the gas and collide with polarized ground state and metastable atoms, causing spin relaxation. A general discussion of the reactions occurring in a weak rf discharge is given in Reference [45]. In the cell where optical pumping is done, this is the dominant relaxation mechanism in all but the most extreme cases of gradient or surface effects. The optimum choice of the discharge level for a given situation is a competition between having a large enough metastable population and having a small enough population of undesirable states. For example, the optimal discharge level for a single pyrex cell may not be the same as the optimal for a double-cell system where a discharge is maintained in only one of the cells. Typically, the relaxation time in the pumping cell with the discharge on was $\sim 1 - 5$ minutes for the polarized target discussed here.

4.2.4 Beam Effects

The question of the effect of the beam on the nuclear polarization is very important when considering a polarized target for nuclear physics experiments using electron beams. Beam currents of $10 - 100$ μA represent a significant number of minimum ionizing particles, unlike the situation encountered with the early $^3\overrightarrow{\mathrm{He}}$ targets in low-energy, nuclear physics experiments. The study of beam effects was a substantial part of the early work in the development of the ^{3}He target at Caltech. Details of the results of the studies with the final target system are found in Section 4.5.2 and a brief summary of the early work using prototype systems is found in Section 4.3.1.

We consider two basic mechanisms that contribute to the spin relaxation. Firstly, the charged particle beam passing through the polarized gas generates a time-dependent magnetic field to which the nuclear spins can couple. The effect of this depends upon the current and pulse structure of the beam. For this experiment, the effect is negligible. Consider a beam pulse with peak current, I_p, and pulse length, τ. The Larmor precession frequency for an atom with gyromagnetic ratio, γ, in a magnetic field, B, is

$$\frac{d\theta}{dt} = 2\pi\gamma B. \tag{4.5}$$

The expression for the peak B field from the beam in cgs units is

$$B = \frac{2I_p}{cR}, \tag{4.6}$$

where I_p is in units of statamps ($1\text{A} = 3 \times 10^9$ statamps). For the Bates beam structure $I_p \sim 1$ mA and $\tau \sim 15\,\mu$sec. Assuming $R = 0.15$ cm, the spin precesses by $\sim$0.02°/pulse, a negligible amount compared to other sources of relaxation. The Bates accelerator operates at 600 Hz, so the pulses occur approximately every 1.7 msec. There is no coherent addition of the spin precession because of collisions and diffusion between the beam pulses.

The second spin relaxation mechanism to be discussed involves the creation of ions by the beam. This is the dominant beam depolarization mechanism for the ^{3}He target at the beam currents used in this experiment. References [47] and [48] present models of spin relaxation from the ionization of the beam. In general, the calculation of the specific effects depends upon characteristics such as the pressure and temperature, the geometry of the system, the magnitude of the holding magnetic field, and the purity of the gas. An outline of the depolarization process is given here. Reference [45] contains information about the reactions between ground state helium atoms and the atomic and molecular ions.

An ionizing beam will create $^3\mathrm{He}^+$ atomic ions in the target cell. The atomic ions are created by the beam and are destroyed by collisions with the wall or with impurities in the gas, recombination with electrons in the gas, and through incorporation into molecular ions. At pressures of $\geq$1 torr, the formation of molecular ions, $^3\mathrm{He}_2^+$, in three-body collisions becomes important.

$$\mathrm{He}^+ + 2\mathrm{He} \longrightarrow \mathrm{He}_2^+ + \mathrm{He}$$

The molecular ions are destroyed by collisions with the wall or with impurities and by recombination with electrons in the gas. At high pressures the recombination dominates the destruction of the molecular ions. At low pressures, the process is dominated by wall collisions; the molecular ions proceed by ambipolar diffusion to the wall where they are broken up.

Polarized ^{3}He atoms that are incorporated into molecular ions have their nuclear spins coupled to the rotational degrees of freedom and can be depolarized. The exchange process can be written schematically as

$$\mathrm{He}(1) + \mathrm{He}(2)\mathrm{He}^+(3) \longrightarrow \mathrm{He}(1)\mathrm{He}^+(2) + \mathrm{He}(3).$$

Also, the nuclei can be depolarized directly by the atomic ions, but for the pressures used for this target, the spin relaxation from molecular ions dominates. Reference [48] indicates that the number of ^{3}He depolarized per ^{3}He$^+$ ion produced by the beam is ≤ 1 for all pressures, while the number of ^{3}He depolarized per ^{3}He$_2^+$ is ≥ 1 for the pressures used for $^3\overrightarrow{\mathrm{He}}$ targets employing metastability-exchange optical pumping.

4.3 Polarized ^{3}He Target System

This section contains a physical description of the polarized ^{3}He target designed and built at Caltech. First, the prototype systems used for the initial beam depolarization studies are described. Next, the design of the double-cell target system is presented, and the laser and associated polarizing optics used for the optical pumping are described. Lastly, the electronics and the computer system for monitoring and controlling the target are discussed.

4.3.1 Prototype ^{3}He Systems

The development of the polarized ^{3}He target was done in three stages. The first studies were done on single cells of ^{3}He optically pumped by a ^{4}He discharge lamp. The next phase involved the construction of a double-cell system, optically pumped by a laser, with the target cell cooled by liquid nitrogen. The final phase was the development of the double-cell target used for the experiment at Bates. Many of the details of the setup are the same for all versions, so only a brief discussion of the prototype systems is given here, leaving the details to the section on the design of the final version.

Initially, solid state lasers were not available that operated at the frequency necessary to optically pump the metastable 2^3S atoms, although promising work was being done by the group in Paris headed by Michele Leduc to develop and test new materials. They had already studied metastability-exchange optical pumping, using a color-center laser [49]. Unfortunately, the system they used was expensive and cumbersome: The color-center laser was pumped by a dye laser which, in turn, was pumped by a Kr$^+$ laser. Therefore, the first studies done at Caltech relied on a ^{4}He discharge lamp to optically pump the ^{3}He. The motivation was to do preliminary studies of the beam effects at room temperature

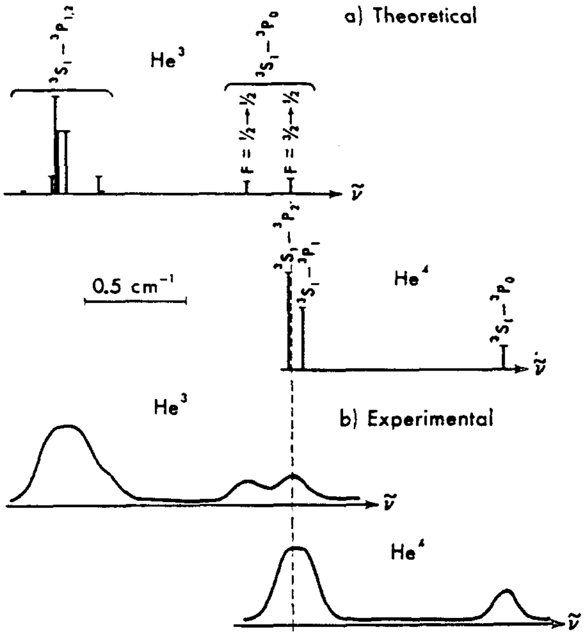

Figure 4.5: Isotope shift of the $2^3S \rightarrow 2^3P$ transition lines in helium. Taken from Reference [46].

and to build and test the equipment needed to measure the ^{3}He polarization.

Optical pumping with a ^{4}He discharge lamp takes advantage of the isotope shift in the helium spectral lines (Figure 4.5) to use the more intense output of the ^{4}He transition lines $2^3S_1 \rightarrow 2^3P_1$ and $2^3S_1 \rightarrow 2^3P_2$ to optically pump the $2^3S_1 \rightarrow 2^3P_0$ transition in ^{3}He . This provides higher polarization, as discussed in Section 4.1. Polarizations of $\sim$ 5% were achieved with the system.

Figure 4.6 shows the setup used for the first beam depolarization studies done at room temperature, the results of which are reported in Reference [47]. The tests used a beam of 3 MeV protons from the Caltech Pelletron accelerator at currents from 0.25 to 1 μA. In terms of ionization energy deposited in the gas, this is equivalent to 20 to 80 μA of minimum ionizing particles. Although it was difficult to extrapolate from measurements done at room temperature to the situation that would be encountered at low temperatures, the fact that the ^{3}He remained polarized with the beam in the cell, coupled with the availability of laser-grade crystals that provided $\sim$ 0.5 watt of power at 1.083 μm, was

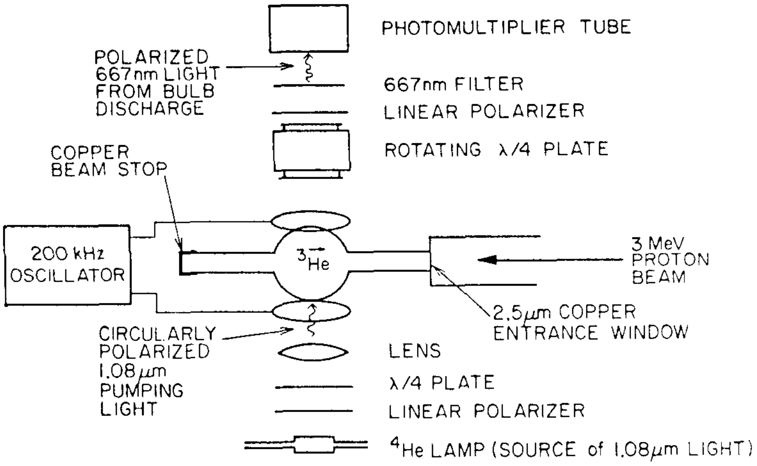

Figure 4.6: Room temperature prototype single-cell system.

sufficient motivation to proceed to the next phase of the development project.

The second phase involved building a prototype double-cell system that used a Nd:YAP laser for optical pumping. In this system the ^{3}He was optically pumped in a pyrex cell at room temperature, which was in diffusive contact through a pyrex transfer tube with a copper target cell cooled to liquid nitrogen temperature. The goal of the studies done with this system was to optically pump with the laser and to measure the polarization of the ^{3}He in the target cell as a function of beam current and target pressure. Figure 4.7 shows the double-cell prototype system. A detailed description of the apparatus and the beam depolarization studies done with it are found in Reference [50]. The prototype design had a pyrex pumping cell at room temperature connected by a pyrex capillary tube to a copper target cell. The target cell had 2.5 μm-thick copper foil windows attached by electron-beam welding to the body of the target cell. The cell was attached by braids to a cold finger in contact with a reservoir of liquid nitrogen. The target temperature was measured with a carbon resistor; the temperature measured at the target cell was ~85 K. With the laser used to optically pump the system, polarizations of ~25% were achieved at ^{3}He gas pressures of 1.0 to 3.5 torr. Beam depolarization studies were done at the Caltech Pelletron accelerator using 1 μA of 5 MeV protons, the equivalent of 40 μA of minimum

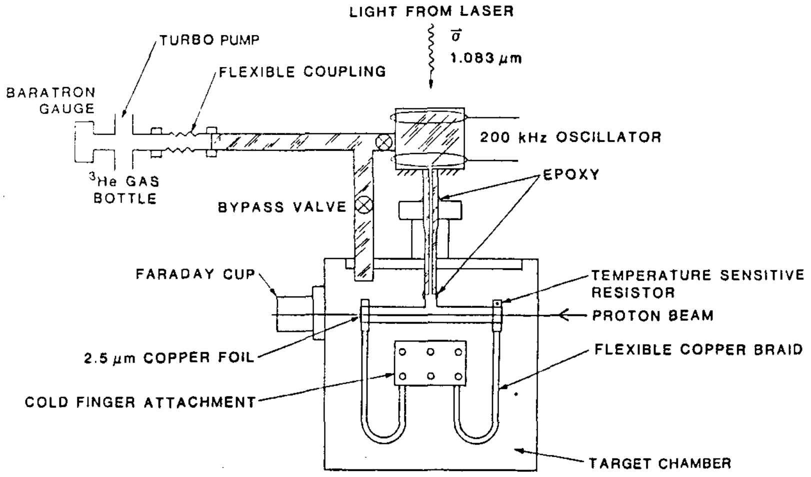

Figure 4.7: Liquid nitrogen temperature prototype double-cell system.

ionizing electrons. The polarization of the ^{3}He in the target cell was determined indirectly from the pumping cell polarization and the time constants of the double-cell system. The methods used to determine the target polarization in the prototype system are described in Reference [50]. The general method of polarization determination in a double-cell system is described in Section 4.4. The results of the studies done with the prototype double-cell system indicated that the ^{3}He polarization was maintained in the diffusion process even with the extended geometry of the double-cell design and that the beam depolarization was not so severe that the polarization could not be maintained in the target cell. The ratio of the polarization in the target cell to the polarization in the pumping cell, P_t/P_p, was consistent with 1.0 without the beam in the cell. With the beam on target, for both 2 torr and 4 torr, $P_t/P_p \sim 0.85 - 0.95$

With the double-cell prototype it was demonstrated that the target remained polarized in the presence of the beam for long periods of time without slow degradation of the polarization, a problem that had been encountered with the single-cell prototype. The characteristic signature of the problem was that the polarization declined over time as the relaxation time measured with the discharge turned on decreased drastically, even though the relaxation time constant measured with the discharge off remained long. A signature of this type indicates that the problem is a contaminant that interferes with the optical pumping of the metastable population, probably through collisions that decrease the lifetime or destroy the polarization, yet does not cause nuclear spin relaxation of the ground state atoms. The success in maintaining high polarizations for extended periods of time with the beam on target with the double-cell prototype, several hours in the case of this study, indicated that the problem probably was contaminants' being driven from the surfaces by the beam. The problem was eliminated when the target cell was cooled because the contaminants were frozen to the walls of the target cell instead of being available to interfere with the optical pumping of the metastable atoms. The results were quite encouraging about the prospects for building a target with a high enough luminosity for electron scattering experiments.

4.3.2 Polarized ^{3}He Target - Double-Cell System

The Caltech polarized ^{3}He target is designed as a two-cell system with a pumping cell at room temperature, upon which the optical pumping light is incident, connected via a transfer tube to a cooled target cell through which the beam passes. The target cell is enclosed in a scattering chamber with the pumping cell located above the top flange. Realistically, there is much more to the system that comprises the polarized target than merely the two cells containing the ^{3}He gas. In addition to the laser system, which is described in Section 4.3.3 and the electronics to control and measure the polarization, described in Section 4.3.4, there is the refrigerator system for cooling the target, the plumbing to the vacuum pumps and the gas-handling system, the scattering chamber, which encloses the target cell, devices to measure the temperature and pressure, and the Helmholtz coils, which provide the magnetic field for the polarized atoms. The layout of the system, as seen from the top and the side, is shown in Figure 4.8.

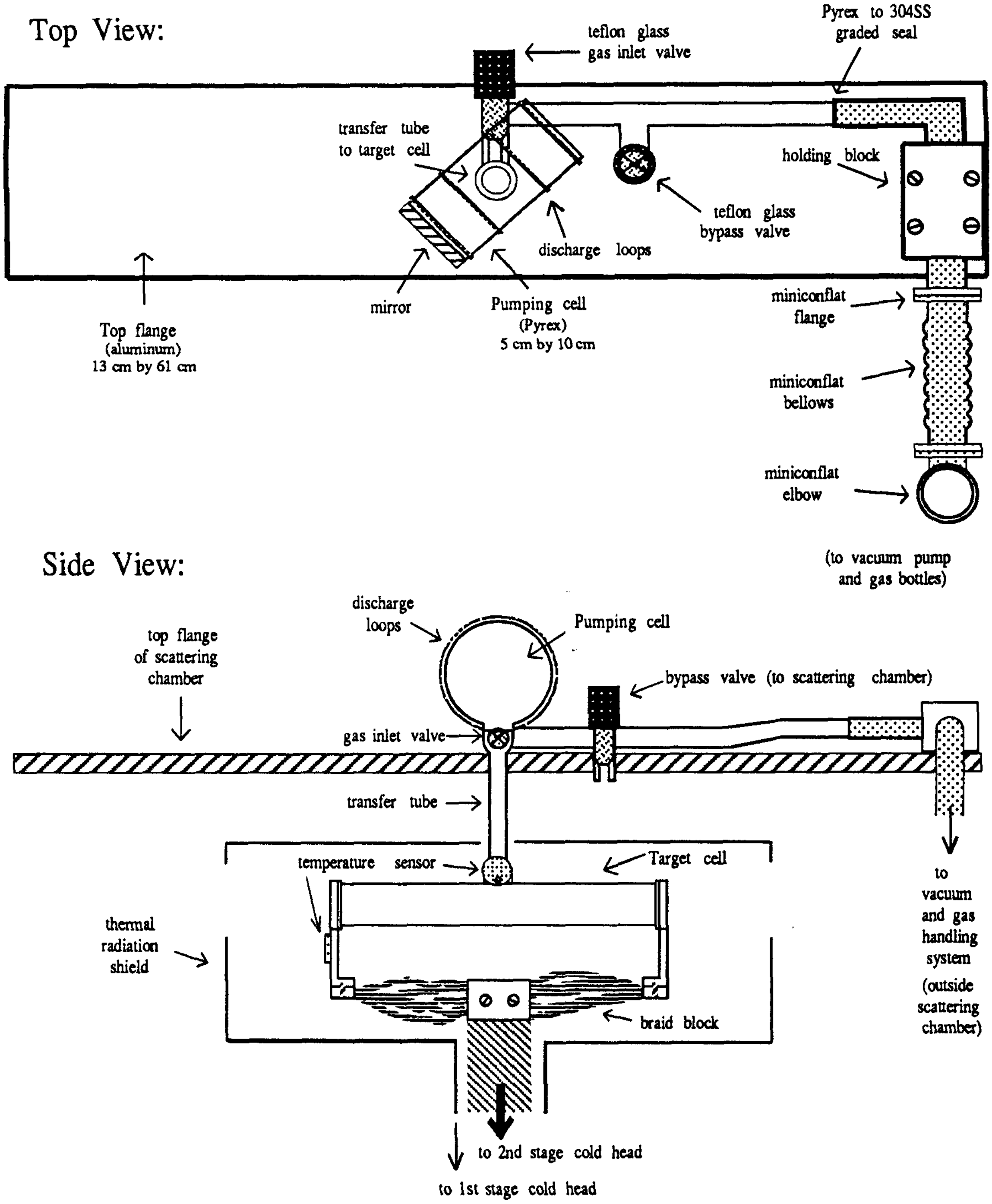

Figure 4.8: Top and side view of the general layout of the target system. In the top view the pumping cell and part of the plumbing can be seen. In the side view, both the pumping cell and the target cell are shown, along with the thermal radiation shield, the temperature sensors, and the braid block.

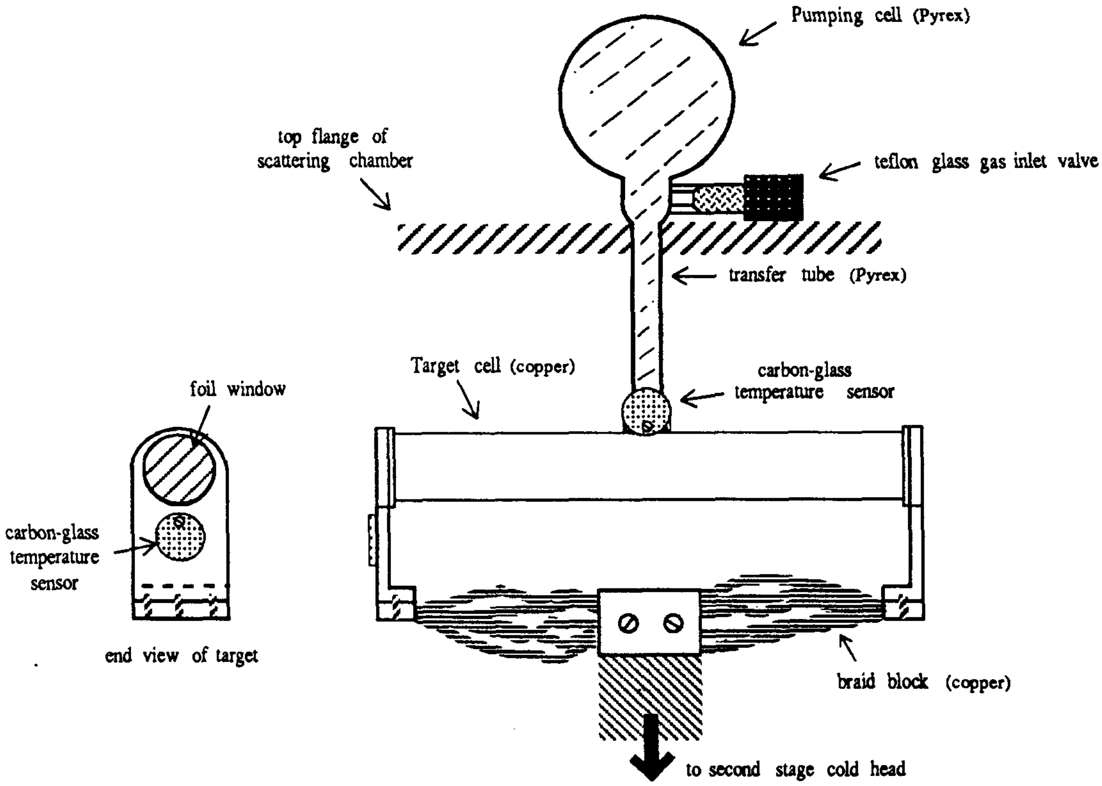

Figure 4.9: Schematic of the polarized ^{3}He target double-cell system. The relative positions of the pumping cell, transfer tube, and target cell are shown, in addition to the braid block, the temperature sensors, and the gas inlet valve.

Pumping and Target Cells

Figure 4.9 is a diagram of the target and pumping cells. The pumping cell, a pyrex cylinder 5 cm in diameter by 10 cm long, is located outside the scattering chamber which contains the target cell. The transfer tube is standard, medium-wall, half-inch pyrex tubing chosen to have an i.d. of 0.91-0.95 cm. It extends from the pumping cell through the top of the scattering chamber to the target cell, a distance of ~11 cm. The gas inlet valve joins to the transfer tube just below the pumping cell outside the scattering chamber. The target cell is a copper cylinder 16 cm long with 4.6 μm copper-foil windows. The body of the target cell is machined from a 2.54 cm i.d. OFHC copper tube, the exterior of which is turned by lathe to a thickness of 0.254 mm. The interior is not machined in order to avoid surface contamination from metallic bits of the machining tools. Since the copper is manufactured by rolling, it should be more free of magnetic contaminants than a machined surface unless special tools, such as ceramic drill bits, are used for machining. At the ends of the tube, for approximately the last 0.3 cm, the exterior wall is left 1 mm thick. Copper "feet" are used to provide thermal contact between the body of the target cell and the braid blocks that connect the target to the refrigerator. The feet are press-fit to the ends of the target cylinder.

Four discharge loops encircle the pumping cell to provide the weak discharge that creates the metastable atoms. The discharge operates at 200 kHz and the power is varied to select the brightness of the discharge. The level is chosen empirically depending upon the desired polarization and pump-up rate.

The copper-foil windows are made from the thinnest, rolled, pinhole-free copper-foil, readily available. It is difficult to find light-tight rolled foils of thickness ≤ 5 μm, so the foil is checked for pinholes using a floodlamp before individual target foil windows are cut. This way, small holes that can not be seen with normal room lights will show up. Foils manufactured by rolling are preferable to those made with evaporation techniques because the foil needs to be worked-hardened to withstand the pressure of the gas target.

Low-temperature epoxy, Emerson and Cumings Stycast 2850GT with catalyst LV24, (ratio of 100:7 by weight) is used to join the transfer tube to the target cell and to attach the foil windows to the main body of the target. Originally, electron-beam welding was used to attach the foils. However, the technique was unsatisfactory for the 2.5 cm diameter foils used in the final version of the target, and a leak tight seal could not be made. A 7 mm diameter hole located in the center of the top of the target cell is the opening for atoms transferring between the target and pumping cells. A copper stem, electron-beam-welded to the cylinder, surrounds the opening, protruding 0.7-1.0 cm above the target cell. The transfer tube attaches to the target cell by slipping over the stem and seating on a small copper block, which is silver-soldered to the outside of the stem.

The copper block serves as the contact point for one of two bobbin-mounted carbon-glass temperature sensors (Lakeshore Cryotronics), which monitor the temperature of the target. The sensor is mounted to the block using a copper screw. The second temperature sensor mounts to one of the feet just below the foil window, again using a copper screw to make a press-fit between the sensor and the target. Braid blocks made of copper wire connect the ends of the target cell to the second stage of the refrigerator. The braids not only provide the thermal connection but also serve to isolate mechanically the target cell, which is rigidly connected to the top of the scattering chamber by the pyrex transfer tube, from the refrigerator assembly, which contracts by approximately 2-3 mm during cooldown. Without the mechanical isolation the glass would break when the target was cooled.

The double-cell target system is assembled from the individual parts as follows. The foil windows are attached to the target cell after it has been cleaned but before it is fixed to the glassware. A thin layer of epoxy is used; it cures under a heat lamp in approximately one hour. An alignment jig is used to position the target correctly in the scattering chamber before epoxying the glass in place. The target is connected to the braid block, which attaches to the second-stage cold finger, using copper screws. Next an alignment jig is bolted to the top of the scattering chamber, replacing the top flange. On it, along the nominal beam axis, are mounted two cylinders, whose radii correspond to the curvature of the top of the target foot. Inserts with fixed cross hairs slip into the cylinders so that the alignment jig serves two purposes: the positioning of the target cell during assembly and the general alignment of the scattering chamber with respect to the beamline. The cylinders slide along the axis of their holders so that they can be moved in to touch the target or be moved out of the way. The position of the target is adjusted to match the alignment cylinders by adjusting the braids; then the jig is removed and a top flange, without glassware, is put on the scattering chamber. The glassware is constructed as one piece, consisting of the transfer tube, the pumping cell, the two glass valves, and the pyrex tube going from the pumping cell to the gas-flow system. The transfer tube of the glassware fits through a hole in the top flange and is positioned to slip over the copper stem and seat on the block. The system is epoxied in place at the copper-to-glass junction and at the hole through the top flange. Even with the mechanical isolation provided by the braids, the transfer tube must be positioned carefully so that it is within a few degrees of being normal to the top of the scattering chamber before epoxying it to the target cell, or it can easily break from the torque exerted during cooldown. The epoxy hardens under a heat lamp in 3-4 hours.

The double-cell system is connected to the vacuum and gas plumbing through a teflon glass valve located just below the pumping cell in the transfer section between the two cells. Being teflon, it outgasses and is difficult to clean, and therefore is not an optimal material to have in contact with the polarized gas. However, it is difficult to find valves that contain no magnetic material, and a material with any magnetic properties near the polarized gas causes substantial spin relaxation from magnetic field gradients. Even "nonmagnetic" stainless steel depolarizes the gas and cannot be used near the pumping or target cells. During operation of the target, the teflon glass valve is closed to seal the cells from the exterior plumbing.

At the end of the pyrex tubing leading from the pumping cell is a pyrex to 304 stainless steel, graded seal that connects the glassware to an elbow made of 304 SS with a 1.33″ miniconflat flange on the end. This provides the connection to the valves for the vacuum and gas-handling systems. The elbow fits through a block connected to the top flange, which holds the glassware securely in place so that the glass does not break during vacuum pumpdown of the system. Each target system consists of the target cell, the braid block, the glassware and a top flange with a holding block for the metal elbow, all as one integral unit.

As described in Appendix B, the copper cell is cleaned before the system is assembled and the surface of the glass is cleaned using a hot discharge and pumping after the cells are joined together. Pressures of $1 - 3 \times 10^{-7}$ torr are needed before optical pumping can be done. A separate cleaning station was set up to clean the systems under vacuum to free the scattering chamber for tests while cleaning new systems. Once cleaned, the targets and pumping cells were filled to atmospheric pressure with argon and stored with the gas

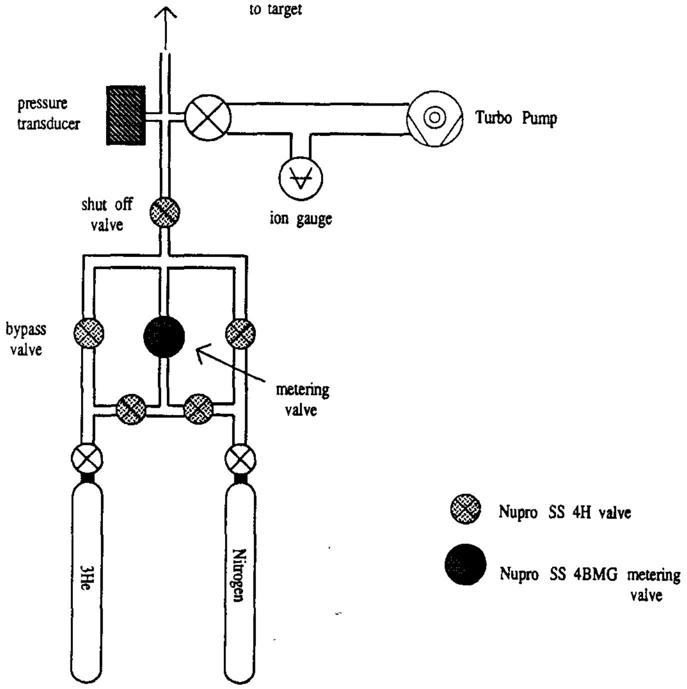

Figure 4.10: Vacuum and gas-handling system for the target.

inlet valve closed to isolate the system from water vapor. This kept the systems reasonably clean; systems stored this way took a day or so to clean once they were put in place in the scattering chamber instead of the five to seven days needed for the full cleaning cycle.

Vacuum and Gas-Handling System

Figure 4.10 shows the plumbing for the turbo pump connected to the target system and for the gas reservoirs. The cells connect to both ^{3}He and N_2 bottles; the N_2 serves as the wall coating for the target cell. The pyrex tubing from the pumping cell attaches to a junction with a baratron head (MKS Instruments Type 122A pressure transducer) to monitor the target pressure during filling or evacuation, a valve to the turbo pump, and a valve to the gas-handling system. The vacuum side of the plumbing is very straightforward. The valve connects the target system to a section with an ion gauge to monitor the pressure and a turbo pump. The rough pumping is done through a bypass valve to the scattering chamber and is described later.

The gas-handling system uses a total of eight valves to regulate the gas flow and to provide good vacuum pumping for this section of the plumbing. The valves directly on the gas bottles are crude and provide no regulation, so other valves are needed to make sure that the foils are not overpressurized. There is one metering valve (Nupro SS-4BMG) used for both gas bottles, a valve between the metering valve and each gas bottle, and a bypass valve to each bottle to provide good pumping conductance during the initial cleaning of the system when all the metal surfaces must be baked. The shut-off valve, located between the metering valve and the junction to the baratron head, is used to stop the gas flow when the target is not being filled. It is needed because metering valves are designed to limit the flow, not stop it completely, and therefore they will slowly leak. All valves but the metering valve and the valves directly on the gas bottles are Nupro SS-4H.

Care must be taken not to break the foil windows of the target when evacuating the system. The windows typically withstand 20-40 torr differential pressure. A bypass valve between the scattering chamber and the plumbing for the gas-handling system is used for this purpose. A teflon glass valve, connected to the pyrex tube that goes from the pumping cell to the vacuum valves, extends through the top of the scattering chamber. A roughing pump is connected to the scattering chamber, either through the beamline vacuum system when the chamber is connected to the beamline, or through one of the end flanges when the target system is tested alone. Both the valve into the scattering chamber and the valve to the pumping cell are left open during the initial pumpdown to prevent the foils from breaking.

Refrigerator System

A Cryomech GB04, closed-cycle, helium refrigerator is used to cool the target cell. In practice, temperatures of $\sim$15°K were obtained during the experiment without the beam on target. The power dissipated by the second stage of the refrigerator was $\sim$1-2 watts, depending upon the beam current.

Figure 4.8 shows how the refrigerator attaches to the target system. The second stage is connected to the target cell through a braid block and the first stage is connected to a thermal radiation shield that surrounds the target cell. The radiation shield is a nickel-coated copper box with the sides silver-soldered together. It attaches with copper screws to the first-stage cold finger. The box is built in two halves, with semicircular cutouts in each for the transfer tube (2 cm diameter) and the entrance and exit of the beam (3.8 cm diameter). Rectangular windows (3.8 cm high by 38 cm long) covered with 25 μm-thick aluminum foil run the length of the shield opposite the body of the target cell.

Scattering Chamber

The scattering chamber was made by Cryomech as part of the refrigerator system. A view of the cross section of the chamber is shown in Figure 4.11. It is machined from a 60 cm-long, round cylinder of aluminum with 16.5 cm i.d. and 21.6 cm o.d. Large, flat surfaces are machined on three sides to which the top and side flanges attach. These provide access into the chamber through large openings on three sides. The side flanges have 0.25 mm-thick aluminum windows to allow the scattered electrons to exit the chamber without significant energy loss. The top flange is 61 cm long by 13 cm wide. The side flanges are 61 cm long by 15 cm wide. The refrigerator is mounted to the bottom of the scattering chamber directly below the center of the target cell. The vacuum feedthrough for the signals from the temperature sensors also connects to the bottom of the scattering chamber.

Helmholtz Coils and Gradients

Encircling the scattering chamber are water-cooled Helmholz coils capable of operating at fields up to 200 Gauss, which provide the magnetic holding field for the nuclear spins. The axis of the pumping cell is oriented along the axis of the coils to an accuracy of ±5°. The coils were operated at 30 A during the experiment and did not require water cooling. This

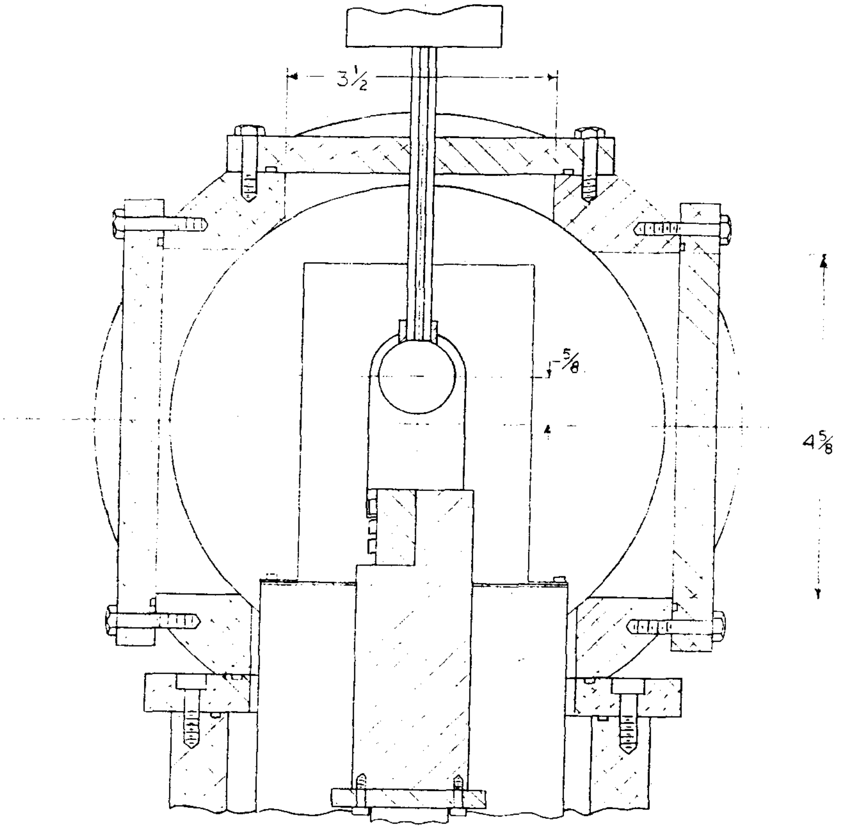

Figure 4.11: End view of the scattering chamber.

current provides an 18 G field at the center of the coils.

The coils are not quite an ideal Helmholz pair, which would have a diameter-to-coil separation ratio of 2:1. They are made of OFHC copper with a hollow, square cross section for the cooling water. Each coil is made of 24 turns of copper and has an i.d. of 71 cm, o.d. of 81 cm, and is 3.6 cm thick. The coil separation of 38 cm is adjustable by ±2 cm.

The magnetic field direction was measured by aligning a Brunton Classic compass along the beam direction using a transit, then reading the field direction from the compass. In this way the spin angle was measured to $\pm\frac{1}{2}^\circ$. The field direction was first measured with only the Helmholtz coils powered on; then the spectrometer magnets were run up to the current used for the experiment and the direction checked. The field direction changed by

-1° from the residual field at the pivot because of the spectrometer magnets.

The background magnetic field gradients were $\sim 5-10\times 10^{-3}$G/cm for the experiment. The center of the Helmholtz coils was set between the target and the pumping cells, with the pumping cell closer to the center to lessen the gradients in the cell which was maintained at room temperature where the effect of gradients are larger. Because of geometrical constraints, at the spin angle chosen for this experiment the center of the Helmholtz coils could not be moved closer than 7 cm to the center of the pumping cell.

4.3.3 Nd:YAP Laser System

Neodymium solid state lasers are a convenient intense source of infrared light. The neodymium ions, Nd^{3+}, which act as the lasing species are impurity ions imbedded in a glass or crystal. The crystal used as the optical pumping light source for the polarized target was Nd:YAP, an yttrium-aluminum-perovskite ($YAlO_3$) crystal, doped with 0.7% neodymium. The lasing medium is similar to YAG, which is $Y_3Al_5O_{12}$, in that the Nd^{3+} ions replace Y^{3+} ions in the lattice and the laser emission comes from $^4F_{3/2} \rightarrow {}^4I_{11/2}$ transitions. The characteristics of the emission differ from that of a YAG laser because of the different properties of the laser medium. The transitions in YAP are broader than those in YAG and the output light is polarized because of the orthorhombic structure of the YAP crystal. The crystal is cut with its a crystalline axis along the axis of the rod. Figure 4.12 shows the fluorescence spectra of YAP; the upper curve is for emission light polarized parallel to the c axis, and the lower curve is for light polarized parallel to the b axis. The primary peak is at 1.0795 μm and is polarized parallel to the c axis.

For optically pumping the ^{3}He metastable atoms, light at a wavelength of 1.0834 μm is needed. To obtain this, the laser is forced to lase on the 1.0845 μm secondary peak and from there it is tuned to 1.0834 μm. The components used to tune the laser are discussed below. For this crystal, the wavelength of 1.0834 μm is just above the lasing threshold, so although power output comparable to the YAG laser can be obtained at the primary peak, only 100 mW to 1 W are obtained at the optical pumping frequency.

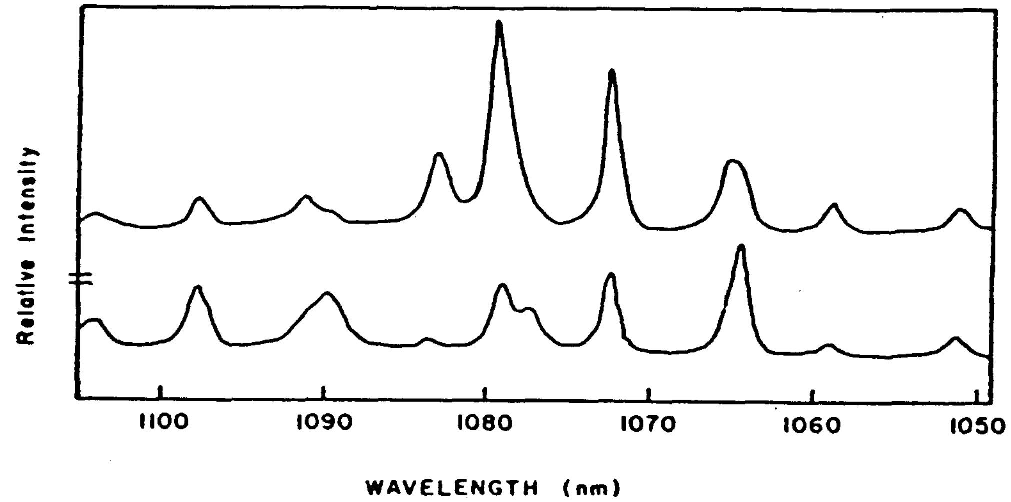

Figure 4.12: Fluorescence spectra of the YAP crystal cut with the *a* axis along the rod axis. The upper curve is for light polarized along the *c* axis and the lower curve is for light polarized along the *b* axis. Taken from Reference [36].

The fact that the laser operates so close to threshold means that the output is very sensitive to external conditions such as the cleanliness of the surfaces of the end mirrors and the tuning elements, the krypton lamp intensity, and the thickness and position of the tuning elements, which can change from thermal fluctuations. In addition, the YAP crystal has moderately bad thermal lensing, a property where the index of refraction varies as a function of temperature so that the laser crystal acts as a lens in addition to a light source. This means that the laser is sensitive to fluctuations in temperature which can arise from variations in the cooling water and from fluctuations in the power in the cavity. Obviously, this can become a serious feedback problem if the thermal lensing is severe. In our case it meant that the laser tune fluctuated, making it necessary to adjust the orientations of the tuning elements from time to time. The thermal lensing also had a benefit for this application: The light beam size had expanded to cover approximately half the surface area of the face of the pumping cell by the time it reached the cell. This made efficient use of the optical pumping light without the use of an expanding lens, which would have introduced more surface losses and reduced the power available for optical pumping.

A Nd:YAP rod, 4 mm diameter by 79 mm long, was purchased from Heraeus Indus-

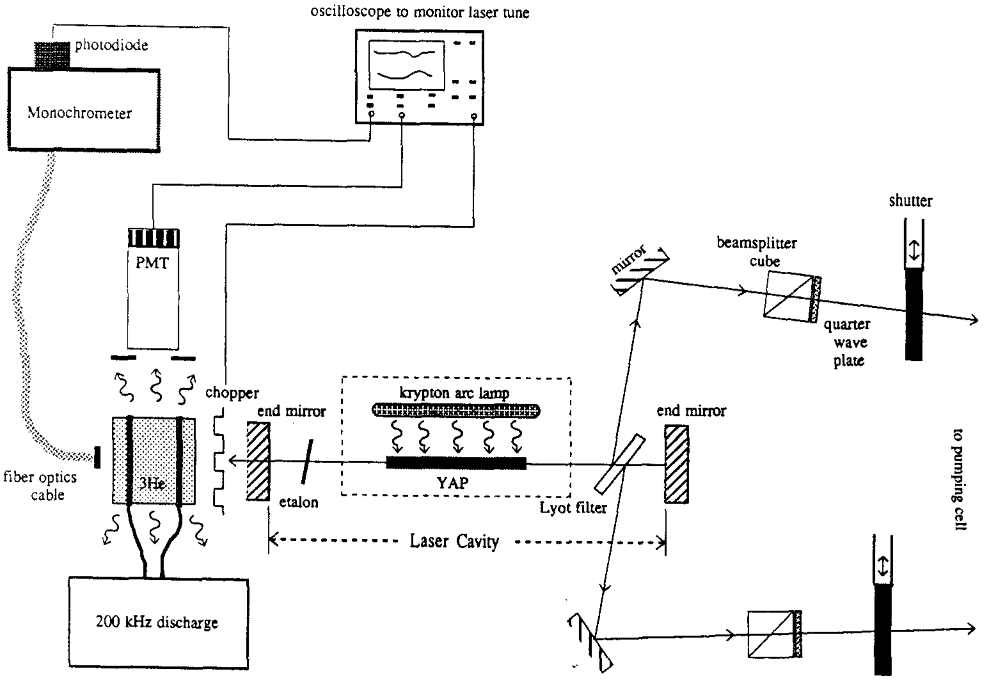

Figure 4.13: Nd:YAP laser system, polarizing optics, and laser tuning setup.

trielaser in Germany. The rod was inserted in a Model 9560 laser cavity purchased from Laser Applications of Winter Park, Florida.[1] The laser was operated in the CW mode to provide a continuous source of optical pumping light. The 9500 series lasers use a gold-plated elliptical cavity with the laser rod at one focus and a krypton arc lamp at the other focus. Model L-6052 krypton arc lamps, available from ILC, were used because they operated well under the conditions needed to pump the YAP crystal. They operated without breaking for typically 200 hours at a current of 31 A before the light output degraded seriously.

Figure 4.13 shows a schematic diagram of the laser and polarizing optics. The laser cavity contains elements to tune the frequency from the primary peak of the fluorescence spectrum to that needed for optical pumping. The laser cavity lies between two "totally" reflecting ($R \geq 99.9\%$) plane surface end mirrors. To ameliorate the effect of thermal lens-

---

[1] As of the time of writing, Laser Applications had filed bankrupcy proceedings.

ing, the laser cavity should be kept as short as possible. The cavity length used for the experiment was 40-45 cm. The cavity contains the YAP laser rod, a 0.25 mm-thick uncoated glass etalon, and a 5.3 mm-thick birefringent filter, also known as a Lyot filter, made of crystalline quartz. The Lyot filter is inserted in the cavity at the Brewster angle for light polarized parallel to the *c* axis (57.2°), so that the range of possible laser emission is similar to the upper curve in Figure 4.12. The Lyot filter acts as a crude frequency selector [51] [52] and is used to do the coarse tuning from the 1.0795 μm primary peak to the 1.0845 μm secondary peak. The fine tuning is accomplished by varying the angle of the etalon relative to the laser axis. Higher output power is obtained when the losses from the etalon are minimized by orienting it as close as possible to normal to the cavity axis. Both tuning elements are motorized with remote controls so that the laser could be tuned from the counting bay while the beam was in the experimental hall.

For tuning the laser, it is necessary to have some indication of the wavelength of the laser light. The small amount of light that leaks through one of the end mirrors is used for this purpose. A chopper is placed directly outside the end mirror; with the chopped signal it is easier to differentiate the signal from the background noise level. The coarse tuning from the primary peak to the secondary peak is monitored with a monochromator, which gives a rough measure of the wavelength. A photodiode at the rear of the monochromator is used to measure the intensity of the light passing through the device. The photodiode signal is viewed on an oscilloscope and is used to maximize the output at a particular wavelength.

To tune to the C8-9 transitions of ^{3}He requires a better monitor than the monochrometer. A sealed cell filled with 0.8 torr of ^{3}He is placed outside the laser cavity so that the light which comes through the end mirror passes through the cell. A weak discharge is maintained in the cell and a photomultiplier tube oriented perpendicular to the cavity axis monitors the fluorescence from the cell. A Hamamatsu R316-02 phototube, sensitive to 1.08 μm light, is used. A collimator is placed between the cell and the face of the phototube to reduce the amount of laser light directly scattered from the walls of the sealed cell into the phototube. The phototube output is monitored using an oscilloscope. When the frequency of the laser light corresponds to the $2^3S_1 \rightarrow 2^3P_0$ transition, the light is absorbed by the metastables and reemitted isotropically. This appears as a large signal from the phototube and is readily distinguished from background scattered light. The C1-5 transitions can be distinguished from the C8-9 transitions. Usually, the C8 and C9 transitions can also be differentiated from each other, although this depends upon characteristics of the laser tune and the tuning elements in the cavity.

The frequency width of the laser is $\sim$ 6 GHz with the 0.25 mm etalon in the cavity. The Doppler absorption width of the atoms is $\sim$ 1.8 GHz. Using this laser system, polarization pump-up rates of $\sim 2 \times 10^{17}$ atoms/sec are achieved.

For the YAP laser, because the laser operates very close to threshold at the optical pumping frequency, end mirrors that are nearly totally reflecting have to be used or else the power in the cavity is too low to stimulate emission. Therefore, for the experiment the output laser light used for optical pumping was the reflected losses off both surfaces of the Lyot filter. Mirrors were used to transport the light to the pumping cell. The number of mirrors used for this should be minimized since there are losses at each reflection, the size of which depends upon the quality of the surface. Also, the surface quality degrades over time, a process which is accelerated in a dusty environment. Between the last mirror and the pumping cell, each beam passed through a linear polarizer oriented for maximum transmission, then through a quarter wave plate whose optic axis was oriented at 45° to the polarization axis to polarize the light circularly. Electronically actuated, pneumatic shutters were placed between the polarizing optics and the pumping cell. The shutters could be remotely controlled to start or stop the optical pumping. This was very useful for the relaxation measurements, described in Section 4.4.2. A mirror was placed at the rear of the pumping cell to reflect the unabsorbed laser light back through the ^{3}He gas, so that it would interact with more velocity groups in the cell. A wratten filter (type 87B) to block visible light was placed in front of the mirror, preventing light from the discharge from also being reflected, something that could interfere with the polarization measurement.

To reverse the direction of the ^{3}He spin orientation, the sense of circular polarization of the light was reversed. This can be done by rotating the quarter wave plate by 90° relative to the direction of the linear polarization of the light. In practice, for the experiment this was done with two circular polarizers (beamsplitter cube and quarter-wave plate), one for each polarization sense, which were mounted on a movable slide. The slide mechanism was pneumatically actuated. A separate set of polarizing optics was used for each of the light beams from the laser.

The operation of the laser in the high radiation environment of the experimental hall required special precautions to prevent radiation damage of the crystal. The laser, the polarizing optics, and the electronics for the control and tuning of the laser were all enclosed in a lead shielding box. Additional lead shielding was stacked between the laser and the target. The light beams were offset above the height of the laser cavity using mirrors so that no direct line-of-sight opening existed between the target and the laser. Recall that the pumping cell was located above the beam height, so this was an additional precaution to allow more shielding at beam height. The shutters for the laser beams were mounted over the opening holes in the shielding box so that for safety reasons, the laser light would be entirely contained within the box when the shutters were closed.

4.3.4 Computer Control and Polarization Measurement System

A dedicated VAXstation II connected to a Camac crate monitored the target and performed control functions through a target data acquisition program especially developed for the Caltech polarized ^{3}He target. The computer monitored the voltage signals for the polarization (a procedure described in Section 4.4.1), read the target temperature from the temperature controller (Lakeshore DRC-82C), controlled the shutters to the laser, turned the discharge in the ^{3}He gas on and off, and performed automatically the measurements of the relaxation times described in Section 4.4.2. It calculated and plotted the polarization continuously as the data were acquired.

Using this system, the data acquisition could be done either continuously, in which case the polarization information was displayed to the screen but not saved, or for a specified length of time, in which case the data were both plotted and saved to a data file recorded on the hard disk. Relaxation studies were performed using a least-squares fit to determine time constants and polarizations. The functional forms for the fit were varied to select either a single-exponential or double-exponential decay expression, depending upon the temperature and transfer time between the two cells.

An output register was used to pass the polarization and temperature information to the Q data acquisition system for the experiment. The polarization was written to the register each time the signals were sampled, a time interval that was a variable input to the program. For the experiment, the polarization was typically sampled once per second. The target acquisition system does not require rapid data input since polarization variations occur on the timescale of seconds. The timing of the measurements is set with the internal clock of the computer so that no electronic interrupts are required from the Camac electronics.

The computer was located in the counting bay and the Camac crate on the South Hall floor. A Kinetic Systems 3952 L-2 crate controller was used. The electronics for the shutter, discharge, and control of the frequency generator (for the relaxation measurements) all used NIM standard signals to control their states. A BiRa 3251 Nim Out module was used to send the control signals from the computer to the electronics. A Kinetic Systems 3388 GPIB Interface was used to interface to the temperature controller and to the lockin amplifier, EG&G model 5210, which was used for the polarization measurement. The voltage signals for the polarization measurement were read through Kinetic Systems 3553 ADCs.

4.4 Polarization and Relaxation Rate Measurements

To extract the asymmetry from the measured cross section it is necessary to know the polarization of the atoms in the target cell during each asymmetry data run. For a double-cell system with the cells in diffusive contact so that the atoms pass back and forth between the two volumes, the target cell polarization can be determined indirectly from the polarization of the atoms in the pumping cell, which can be monitored continuously.

The discussion of the determination of the polarization is split into four sections. Section 4.4.1 describes the determination of the polarization in the pumping cell, which is done using an optical polarization detection technique. The measurement of the optical polarization of the light from the discharge in the pumping cell is described, and the method used to extract the nuclear polarization from the optical polarization is presented. From the information about the polarization of the pumping cell population, it is possible to determine the polarization of the target cell atoms. However, this requires additional information about the coupling of the two cells, such as the relative number of ^{3}He in each cell, the relaxation time of the system and the characteristic time for the exchange of atoms between the cells. The relaxation measurements used to determine the time constants for the double-cell system are described in Section 4.4.2, along with a detailed explanation of the extraction of the time constants from the relaxation data. Finally, the extraction of the polarization in the target cell from the data on the coupled-cell system is explained in Section 4.4.3, using results derived in Appendix D. A discussion of the systematic uncertainty in the target polarization is found in Section 4.4.4. The polarization values measured during the ^{3}He experiment are found in Section 5.4.2 of the chapter on the data analysis.

4.4.1 Optical Polarization Measurement

The optical technique for detecting the nuclear polarization of the ^{3}He in the pumping cell involves the measurement of the circular polarization of light emitted in the decay of an excited state of the ^{3}He atom created by the discharge. The excited state is polarized through the hyperfine interaction between the nucleus and the atomic electrons, so the circular polarization of the emitted light is related to the nuclear polarization. A detailed discussion of the technique is found in Reference [53]. It should be noted that the technique requires that the discharge be on during the measurement, or the excited state atoms will not be present.

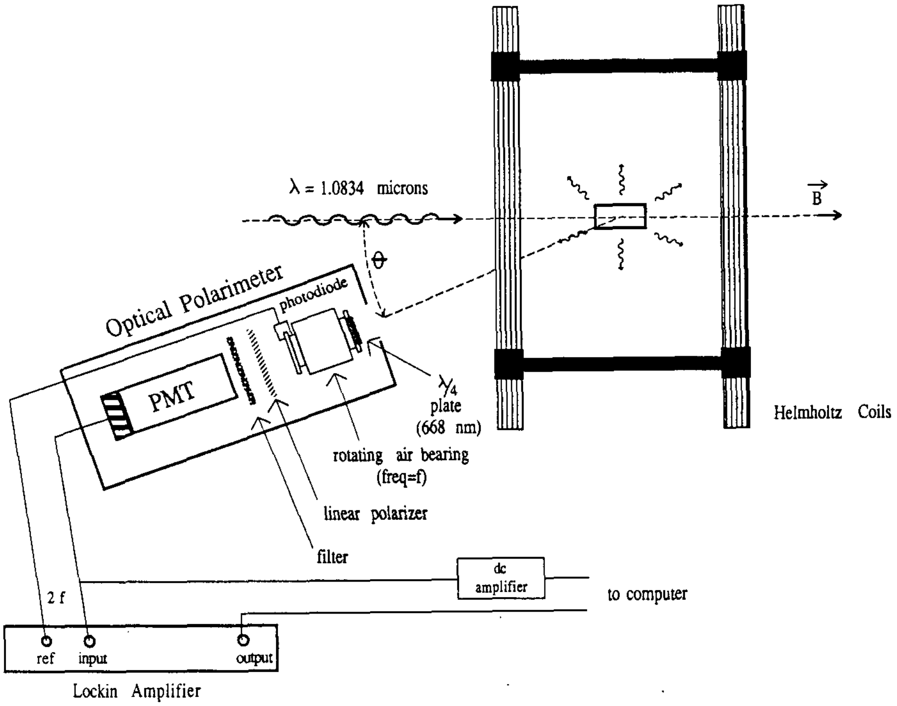

Figure 4.14: Optical polarimeter consisting of a rotating quarter wave plate, linear polarizer, filter, and photomultiplier tube. The phototube signal is sent to a lockin amplifier.

The emission from the $3^1D \rightarrow 2^1P$ transition, at $\lambda = 668$ nm, is used to determine the nuclear polarization. The light is detected and analyzed by an optical polarimeter, which views the pumping cell from outside the Helmholtz coils (see Figure 4.14). The optical analyzer consists of a rotating quarter-wave plate for 668 nm light, followed by a linear polarizer. The quarter-wave plate converts the circularly polarized light from the cell into linearly polarized light, which is maximally transmitted through the linear polarizer with a frequency of 2f, where f is the rotation frequency of the quarter-wave plate. Behind the linear polarizer is a filter that blocks light coming from other transitions, and an Amperex XP2023B phototube to measure the amplitude of the transmitted light. The output of the phototube is sent to a lockin amplifier to measure the ac component of the signal at the frequency 2f, and to a dc amplifier to amplify the dc signal. The output of each amplifier is sent to a Kinetic Systems 3553 ADC, which is read by the target acquisition program.

The ratio of the ac signal to the dc signal is proportional to the nuclear polarization. The relationship between the voltages and the polarization is

$$P_{nuc} = f_{pres} \frac{f_\theta}{\cos\theta} \frac{V_{li}}{V_{dc}}, \tag{4.7}$$

where V_{li} is the ac component of the signal from the phototube measured by the lockin amplifier, V_{dc} is the dc voltage from the phototube, θ is the angle of the optical polarimeter relative to the $\vec{B}$ field, f_{pres} is the pressure factor, and f_θ is the angle factor.

The factor, $f_\theta/\cos\theta$, is included to correct the measured circular polarization for changes introduced because the optical polarimeter views the cell from off-axis of the spin polarization direction. For the experiment, $\theta = 18°$ for the first target spin direction and $\theta = 25°$ for the other two spin directions. The $(\cos\theta)^{-1}$ dependence is a simple correction to account for the variation of the circular polarization of the emitted light with the angle between the axis of the analyzer and the spin quantization axis. The angle factor, f_θ, is a correction to account for the fact that the optical polarization measured at a large viewing angle is smaller than the value measured when the cell is viewed along the axis of the $\vec{B}$ field by a factor that cannot be accounted for by the $(\cos\theta)^{-1}$ dependence. The correction factor was determined empirically from measurements taken with an optical polarimeter at 5° and at larger angles. For $\theta = 18°$, $f_\theta = 1.064$, and for $\theta = 25°$, $f_\theta = 1.111$. The origin of the depolarization is not clearly determined, although it may be caused by reflections or refractions from the cell walls; light detected at small angles exits the cell through the flat front face of the cylinder, while light detected at larger angles exits through the curved side walls. The correction factor also depends upon the gas pressure, and is larger for 2 torr than for 0.8 torr. This is not surprising since the shape of the discharge is very different for the two pressures. At higher pressures the discharge is more localized than at lower pressures. The f_θ correction factor was measured at different discharge levels to verify that the effect is reproducible and does not depend upon the discharge level.

The pressure factor, f_{pres}, corrects for the depolarizing effects of collisions upon the electronic polarization of the excited 3^1D atoms. As mentioned previously, the collisions occur too rapidly to affect the nuclear polarization. However, collisions can alter the electronic alignment or orientation before the excited state decays. An equilibrium polarization is reached for the excited states with the discharge on and the atoms polarized. The pressure factor depends nonlinearly upon the gas pressure. The dependence was measured previously [54] by calibrating the optical detection technique against another indirect measurement of the nuclear polarization that used the absorption of the 1.0834 μm pumping light by the ^{3}He to infer the nuclear polarization. Ideally, one would calibrate the optical polarization against a direct measurement of the nuclear polarization, such as a nuclear magnetic resonance (NMR) measurement. This has been done recently at Caltech [55] and the results of the new calibration are used for the calculation of the nuclear polarization values presented in this thesis. The calibration factor used in this analysis for a pressure of 2 torr is $f_{pres} = 10.2$. The calibration factor depends upon the magnitude of the holding magnetic field since the electronic spins couple to the external field. The magnetic field dependence of the optical polarization was measured at Caltech and the pressure factor was corrected for the effect. For an 18 G field, the correction, included in f_{pres}, is -1.1% of the value.

In order to calculate f_{pres}, it is necessary to know the pressure in the target system. Since the target temperature varied as a function of the beam current, the ^{3}He gas pressure must be determined for each data run from the measurement of the temperature during the run. The pressure and temperature of the cell were recorded each time the target was filled. Once filled, the gas inlet valve was closed to seal the cell, so subsequent temperature variations gave rise to pressure variations. The temperature of the target cell was monitored continuously during each data run and the average temperature, combined with the information about the temperature and pressure of the gas when the system was filled, was used to calculate the correct pressure during the run. The procedure for determining the pressure is the following. Assume that the pumping cell has volume, V, and temperature, T, and that the two cells were originally filled with a pressure, p, of ^{3}He. When filled, the target cell, with volume, v, was at temperature, t. Later, the target temperature changed to t', causing the pressure to change to p'. The new pressure can be expressed in terms of known values as

$$p' = p \frac{(\frac{1}{T} + \frac{v}{V}\frac{1}{t})}{(\frac{1}{T} + \frac{v}{V}\frac{1}{t'})}. \tag{4.8}$$

The method used to determine the volume ratio is explained in Appendix C. It turns out that the correction to the pressure for the target temperature fluctuations had a negligible effect upon the pressure factor, which varies little for a pressure of ~ 2 torr. However, the correction to the number of nuclei in the interaction region was important for the cross section calculation discussed in Section 5.3.

The optical polarimeter must be calibrated so that the target acquisition program calculates 100% polarization for perfectly circularly polarized light passing through the optical analyzer. To do this, a sheet of circularly polarizing plastic was placed in front of the opening to the polarimeter and the amplification factor used by the target acquisition program to convert the the dc signal from the ADC to a voltage was adjusted to give a polarization of 99.7%. This was determined to be the degree of circular polarization of the light passing through the film to an accuracy of ±1.1%

4.4.2 Relaxation Rate Measurement

The expressions used to extract the target cell polarization from the measured polarization in the pumping cell depends strongly upon the time constants of the system. The measurements used to determine the time constants are described in this section. The relevant time constants are the relaxation times in the pumping cell and the target cell, and the time for atoms to tranfer between the two volumes.

The spin relaxation rate of the system is measured by shuttering the laser light so that the atoms are no longer being optically pumped and observing the decay of the polarization as a function of time. For a single cell, the polarization decays exponentially,

$$P(t) = P(0)\exp(-t/\tau), \tag{4.9}$$

with a single time constant, τ, parameterizing the rate. The time constant reflects the combination of all the effects contributing to the spin relaxation. For example, if there are two depolarization mechanisms contributing to the relaxation, which are individually characterized by the time constants τ_1 and τ_2, then the overall relaxation rate is

$$\frac{1}{\tau} = \frac{1}{\tau_1} + \frac{1}{\tau_2}. \tag{4.10}$$

The single exponential form of the expression for the spin relaxation process is altered for a system containing more than one cell. The time constants are defined in the relaxation rate equations for the coupled two-cell system.

$$\frac{dP_p}{dt} = \frac{-P_p}{\tau_p} + \frac{P_t - P_p}{t_p} \tag{4.11}$$

$$\frac{dP_t}{dt} = \frac{-P_t}{\tau_t} + \frac{P_p - P_t}{t_t} \tag{4.12}$$

The subscript 't'('p') refers to the target(pumping) cell. $\tau_{t(p)}$ is the relaxation time in the cell and $t_{t(p)}$ is the diffusion time for the population of atoms in the cell to transfer out. The transfer rate is defined in terms of a characteristic exchange time, t_{ex}, as

$$\frac{1}{t_{ex}} = \frac{1}{t_t} + \frac{1}{t_p}. \tag{4.13}$$

The derivation of the solution to the relaxation equations is given in Appendix D. For a double-cell system, the decay of the polarization is expressed as a sum of two exponentials. In a system designed so that the transfer rate between the two cells is much faster than the relaxation rate in either cell, the decay is made up of one exponential with a short time constant, which is approximately the transfer time between the two cells, t_{ex}, and a second exponential with a long time constant, which is approximately the weighted average of the relaxation time constants for the two cells, where the weighting factor is the fraction of the atoms in each cell. For the target system used for this experiment, the transfer time, $t_{ex} = 7.5 \pm 0.5$ sec, is much shorter than the relaxation time in either cell so this approximation is valid.

Three types of measurements were made to determine the relaxation times of the double-cell system. In the following discussions they are referred to as "relaxation with discharge on," "relaxation with discharge off," and "transfer" measurements. The combination of the measurements contains enough information to calculate the transfer time and the relaxation time in each cell.

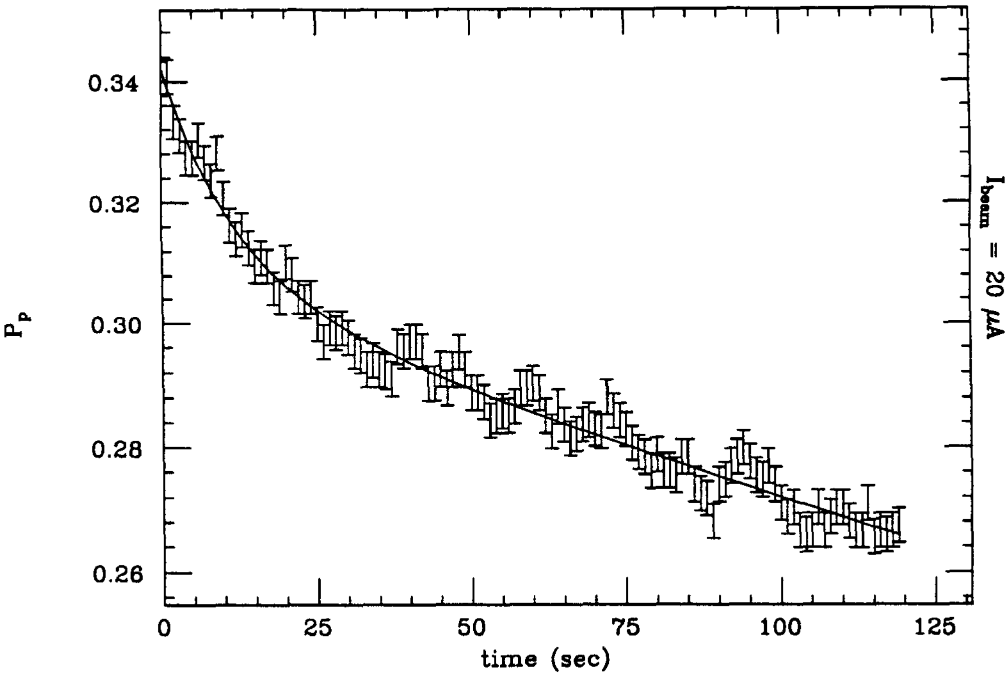

Figure 4.15: Example of a "relaxation with discharge on" measurement. The solid line is the fit to a sum of two exponentials. The data were taken with 20 μA of beam current on target.

The "relaxation with discharge on" measurement is performed by shuttering the laser light and measuring the polarization in the pumping cell as a function of time. The discharge is left on throughout the measurement. A fit to the data from this measurement yields four parameters: the two time constants for the double exponential decay and an amplitude multiplying each exponential.

$$P_p(t) = a_l e^{-t/\tau_l} + a_s e^{-t/\tau_s} \tag{4.14}$$

The subscript "p" on the above expression indicates that the polarization of the atoms in the pumping cell is measured. Figure 4.15 shows an example of this type of measurement, along with the double exponential fit to the decay.

The "transfer" measurement is a variation on the "relaxation with discharge on" measurement which gives a dramatic display of the polarization in the target cell. The meas-

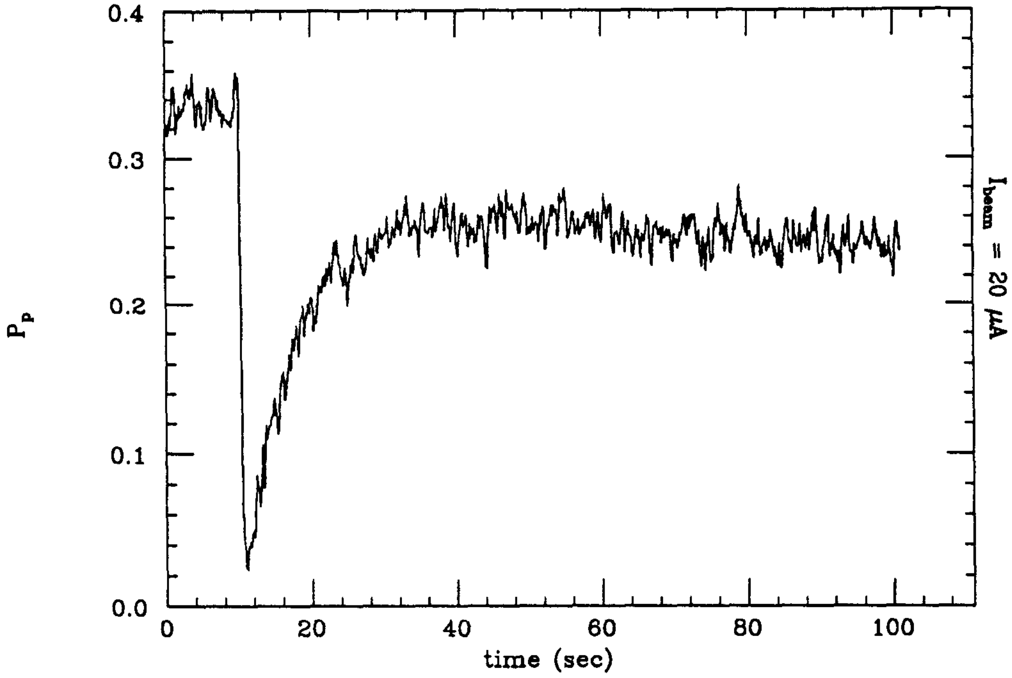

Figure 4.16: Example of a "transfer" measurement. The data were taken with 20 μA of beam current on target.

urement is done in the following sequence. After a stable equilibrium polarization has been reached by the atoms in the pumping cell, the laser light is shuttered at the same time as the polarization of the atoms in the pumping cell is destroyed. The repolarization is observed as polarized atoms transfer in from the target cell. Figure 4.16 shows an example of this type of measurement. The fit to the data is a double exponential, as for the previously described measurement, with the added constraint that $P_p(t_0) = 0$, where t_0 is the time at which the pumping cell atoms are depolarized.

$$P_p(t) \;=\; a_l\left(e^{-(t\,-\,t_0)/\tau_l} \;-\; e^{-(t\,-\,t_0)/\tau_s}\right) \tag{4.15}$$

The polarization of the atoms in the pumping cell is destroyed by applying a small transverse field at the Larmor frequency. This is done using small coils that surround the cell and are oriented transverse to the holding dc magnetic field. An HP 3325B function generator is used to generate the driving field. The correct frequency is set by hand using a very small amplitude signal and varying the frequency until the equilibrium polarization is minimized. It is necessary to reduce the driving field while setting the frequency because the atoms will depolarize in a time-varying magnetic field that is maintained for an extended period of time at frequencies close to the Larmor frequency. During the "transfer" measurement the field is pulsed on for ~0.1 sec at $t = t_0$, and the polarization in the pumping cell is sampled every 0.1 sec. The lockin amplifier integration time constant is set to 0.05 sec whereas normal polarization monitoring is done with an integration time of 1 sec to reduce the background variation of the signal.

The last type of relaxation measurement to be discussed is the "relaxation with discharge off" measurement. As was mentioned in the previous section, the optical detection technique employed to determine the polarization requires that a discharge be maintained in the pumping cell when the measurements are made, simply so that a population of the 3^1D excited state atoms exists in the cell. However, it is necessary to know the relaxation rate with the discharge off in order to extract the relaxation rates in the individual cells. Also, it is useful to know the relaxation rate with the discharge off since the discharge effects dominate the relaxation in the pumping cell and can mask problems with the magnetic field homogeneity or with the surfaces.

To minimize the impact of the discharge, it is turned on for only a short time during a polarization sample for the "relaxation with discharge off" measurements, and the polarization of the system is sampled at long intervals (~ 1-2 minutes). The discharge is turned on for two seconds and the polarization measured as rapidly as the computer system can handle while still being able to acknowledge an interrupt from the keyboard, a rate of ~50 Hz for the target acquisition system. The lockin amplifier takes time to settle when the discharge is turned on; for each sample the data taken in the first 1.3 sec are ignored and the data from the last 0.7 sec are averaged to obtain the polarization. The lockin amplifier is set on the 0.1 sec integration timescale for the "relaxation with discharge off" measurements. The polarization values are corrected for the influence of the discharge before extracting the relaxation time constant from the data. The nth sample polarization is corrected by

$$P_{corr} = P_{meas}e^{n\Delta t/t_d}, \tag{4.16}$$

where Δt is the amount of time that the discharge is on and t_d is the relaxation time constant that is due to the discharge. The corrected data from these measurements are fit with a single exponential to extract the long time constant of the system with the discharge off, $\tau_{l(off)}$. In cases where a double-exponential decay is expected, the first data point of the "relaxation with discharge off" measurement, taken just after the shutter is closed to block the laser light and just before the discharge is turned off the first time, is not included in the fit because the polarization of the system has not yet equilibrated through the transfer of atoms between the two cells. That point is used only to establish the initial polarization in the pumping cell.

It should be noted that in practice the relaxation time that is due solely to the discharge, t_d, is not actually measured, but instead, a time constant that is due to all depolarizing effects is extracted from the measurement with the discharge on. Although the time constant is dominated by the discharge relaxation, it does not solely reflect the discharge effect and only approximates t_d. However, limits can be set on $\tau_{l(off)}$; the long time constant is shorter than the value extracted assuming that $t_d = \infty$ and is longer than the time constant extracted assuming that $t_d = \tau_l$, where τ_l is the long time constant obtained from the fit to data taken with the discharge on, either in "relaxation with discharge on" or "transfer" runs. An iterative procedure can be used to obtain a better estimate of the long relaxation time constant of the system with the discharge off. Using the average of the two limits, $\overline{\tau_{l(off)}}$, a reasonable estimate of the time constant that is due to the discharge can be made:

$$\frac{1}{t_d} \approx \frac{1}{\tau_l} - \frac{1}{\overline{\tau_{l(off)}}}. \tag{4.17}$$

This value is then used to correct the data from the "relaxation with discharge off" measurement and a new value of the long time constant from effects other than the discharge, $\tau_{l(off)}$, is extracted.

Now that the relaxation measurements have been described, the extraction of the time constants of the system from the relaxation data can be explained. The relaxation rate equations for the two cells involve four time constants: the relaxation time in each cell, τ_p and τ_t, and the diffusion times, t_p and t_t. In addition, τ_p depends strongly upon the discharge, so the relaxation measurements taken with the discharge on yield a different contribution to the relaxation rate from the pumping cell than those taken with the discharge off. The two time constants for the pumping cell are denoted τ_p and $\tau_{p(off)}$ for the discharge on and off, respectively. It should be noted that the relaxation time relevant to the conditions under which data are acquired is the one where the discharge is on, τ_p, since the cell is being optically pumped continuously to maintain the ^{3}He polarization. The target cell relaxation rate is independent of the discharge. The diffusion times for the two cells are related to the transfer time, t_{ex}, as indicated in Equation 4.13. Because the system is sealed during optical pumping, detailed balance of the total number of atoms in the system requires that the relationship

$$\frac{N_p}{t_p} = \frac{N_t}{t_t} \tag{4.18}$$

hold for the diffusion times of the individual cells, where $N = N_t + N_p$ is the total number of atoms in the two-cell system. This relationship allows us to express both t_p and t_t in terms of t_{ex}, thereby reducing the number of time constants of the system to four. However, this is still too many to extract from one of the relaxation measurements, which gives two time constants from the fit done to the data with the discharge on, and one time constant for the data taken with the discharge off. Therefore, it is necessary to combine the information from a set of measurements to extract t_{ex}, τ_p, and τ_t.

The two time constants extracted from the fit to the data with the discharge on, τ_s and τ_l, are related to the parameters given above by the following formulas (see Appendix D).

$$\frac{1}{\tau_s} + \frac{1}{\tau_l} = \frac{1}{t_{ex}} + \frac{1}{\tau_p} + \frac{1}{\tau_t} \tag{4.19}$$

$$\frac{1}{\tau_l} \approx \frac{N_p}{N}\frac{1}{\tau_p} + \frac{N_t}{N}\frac{1}{\tau_t}. \tag{4.20}$$

The first expression is exact within the framework of the double-cell calculation, which does not consider the transfer tube as a separate volume, but splits it between a "cold" target and a "warm" pumping cell. The volume of the transfer tube is less than 5% of the volume of the pumping cell and only the bottom ~2 cm of it is cold, so it is a fair assumption to ignore it as a separate cell. The second expression is valid in the limit $t_{ex} \ll \tau_t, \tau_p$, where the transfer occurs much more rapidly than any other process in the system. In this case the long time constant comes from a weighted average of the relaxation rates of the atoms in the system. The fractions of the total number of atoms contained in each cell, N_p/N and N_t/N, are needed for the calculation. The method used to determine this number is explained in Appendix C. The measured ratio is $N_t/N = 0.890 \pm 0.005$.

The target cell relaxation time can be extracted from the long time constant of the "relaxation with discharge off" data, if we assume that the pumping cell relaxes at the same rate as a single sealed cell of 2.0 torr ^{3}He the size of the pumping cell at the same position within the Helmholtz coils. In this case, the pumping cell relaxation time with the discharge off, $\tau_{p(off)}$, is approximated by the single-cell relaxation time, $\tau_{sc} = 2900 \pm 700$ sec, which was measured with a field of 18 G from the Helmholtz coils and the spectrometer magnets on. The assumption is reasonable since spin relaxation from magnetic field gradients dominate in the pumping cell when the discharge is off. In this case,

$$\frac{1}{\tau_t} = \frac{N}{N_t}\left(\frac{1}{\tau_{l(off)}} - \frac{N_p}{N}\frac{1}{\tau_{sc}}\right) . \tag{4.21}$$

Using this value for the target cell relaxation rate, the pumping cell relaxation time, τ_p, can be extracted from the long time constant of the double exponential fit to the data taken with the discharge on.

$$\frac{1}{\tau_p} = \frac{N}{N_p}\left(\frac{1}{\tau_l} - \frac{N_t}{N}\frac{1}{\tau_t}\right) \tag{4.22}$$

Finally, the transfer time is obtained from both time constants of the double exponential fit to the data taken with the discharge on and the values calculated above.

$$\frac{1}{t_{ex}} = \frac{1}{\tau_s} + \frac{1}{\tau_l} - \frac{1}{\tau_p} - \frac{1}{\tau_t} \tag{4.23}$$

These results are summarized in Table 4.1.

Time Constants	
t_{ex}	transfer time
τ_t	relaxation time in target cell
τ_p	relaxation time in pumping cell (discharge on)
τ_{sc}	relaxation time of a sealed cell in position of the pumping cell (discharge off)

Type of Measurement	Fit Parameters	Relationship to Time Constants
"relaxation with discharge off"	$\tau_{l(off)}$	$\frac{1}{\tau_t} = \frac{N}{N_t}\left(\frac{1}{\tau_{l(off)}} - \frac{N_p}{N}\frac{1}{\tau_{sc}}\right)$
"relaxation with discharge on " and "transfer"	τ_s,τ_l,a_s,a_l	$\frac{1}{\tau_p} = \frac{N}{N_p}\left(\frac{1}{\tau_l} - \frac{N_t}{N}\frac{1}{\tau_t}\right)$ $\frac{1}{t_{ex}} = \frac{1}{\tau_s} + \frac{1}{\tau_l} - \frac{1}{\tau_p} - \frac{1}{\tau_t}$

Table 4.1: Time constants of the target system. Relationship between fit parameters from the relaxation data and the transfer time and relaxation times of the target and pumping cell.

4.4.3 Determination of the Polarization in the Target Cell

The polarization of the target atoms is inferred indirectly from the polarization measured in the pumping cell, the fraction of atoms in each cell, and the time constants of the system. Appendix D contains a derivation of the expressions relating the polarizations of the two cells. The appendix contains the exact expressions for the target and pumping cell polarizations during both relaxation and optical pumping, within the assumptions of the model, which are specified in the appendix.

Information from the charging curves is used to calculate the ratio of the polarizations in the two cells under equilibrium conditions, i.e., after the optical pumping light has been on the pumping cell for long enough that steady state conditions have been established in the cells. The premise underlying the use of the indirect measurement to determine the polarization of the target cell nuclei is that the pumping cell polarization relates to the target cell polarization in a straightforward manner. The equations derived in the appendix for the equilibrium polarizations of the two cells support this claim. The equilibrium ratio of the polarizations of the two cells, P_t/P_p, is found to depend only upon the relaxation

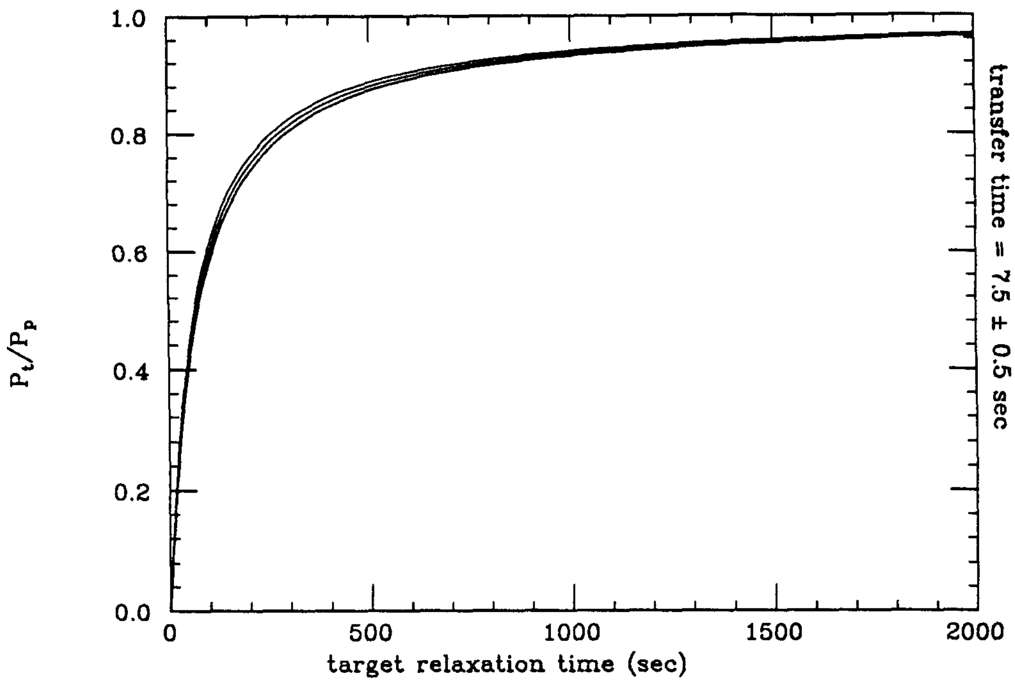

Figure 4.17: The calculated equilibrium polarization ratio, P_t/P_p, as a function of the relaxation time in the target cell, for transfer times of $t_{ex} = 7.5 \pm 0.5$ sec. The ratio becomes larger as the relaxation time gets longer and the transfer time gets shorter.

time in the target cell, the transfer time, and the fraction of atoms in each cell.

$$\frac{P_t}{P_p} = \frac{\left(\frac{N_p}{N}\right)\frac{1}{t_{ex}}}{\frac{1}{\tau_t} + \left(\frac{N_p}{N}\right)\frac{1}{t_{ex}}} = \frac{1}{1 + \frac{N}{N_p}\frac{t_{ex}}{\tau_t}} \tag{4.24}$$

Once these constants have been measured, the target cell polarization is simply calculable from the pumping cell polarization. One thing that should be noted is that the equilibrium condition between the two cells must be met before the simple ratio holds. For the target system developed at Caltech, equilibrium was established in about 8-10 minutes for pumping the system from an initially unpolarized state and much more quickly for changes in the relaxation time brought about by changes in the beam current. The approach to equilibrium is discussed in more detail in Appendix D.

Figure 4.17 shows the calculated equilibrium polarization ratio, P_t/P_p, plotted as a function of the relaxation time in the target cell for transfer times of 7.5 ± 0.5 sec. The

Type of Measurement	Fit Parameters	Target Polarization
"relaxation with discharge on"	τ_l,τ_s,a_l,a_s	$P_t = \left[1 + \tau_s \left(\frac{1}{\tau_p} - \frac{1}{\tau_t}\right)\right] a_l - \left(\frac{N_p}{N_t}\right) a_s$
"transfer"	τ_l,τ_s,a_l,a_s	$P_t = \left[\frac{N}{N_t} + \tau_s \left(\frac{1}{\tau_p} - \frac{1}{\tau_t}\right)\right] a_l$

Table 4.2: Relationship between the relaxation run fit parameters and the target cell polarization. The time constants are given in Table 4.1.

polarizations in the two cells become more nearly equal as the transfer time becomes shorter and as the relaxation time in the target cell gets longer. It is clear from Figure 4.17 that it is necessary to operate the target at $\tau_t \geq 300$ sec in the region where the ratio doesn't depend strongly upon the target cell relaxation, so that one can accurately infer the polarization in the target cell from the pumping cell polarization. Although the transfer time and the volumes are nearly constant throughout the experiment, the target cell relaxation time varies with the amount of beam current and with the quality of the wall coating. Therefore, the target cell relaxation time must be measured fairly often to monitor changes. The results of the measurements to determine the variation of the polarization ratio as a function of the beam current are given in Section 4.5.2.

To check the accuracy of the calculated ratio of the polarizations in the two cells, the target cell polarization was extracted from the information in the relaxation runs. Therefore, the relaxation data not only provided information about the time constants of the system but also about the polarization of the target cell. In Section 4.4.2 the relationships between the time constants of the fit and the transfer time and the relaxation time in the individual cells is given (Table 4.1). In Appendix D the relationship between the target cell polarization and the fit parameters is derived for the two different types of relaxation runs taken with the discharge on. They are summarized in Table 4.2. The ratio of the polarizations in the two cells was extracted from runs with different amounts of beam current on target and therefore, with different target cell relaxation times. The results are presented in the section on the beam depolarization studies (Section 4.5.2) and agree well with the calculated equilibrium ratio between the polarizations of the two cells during optical pumping shown in Figure 4.17.

4.4.4 Systematic Uncertainty in the Target Polarization

The factors contributing to the uncertainty in the target cell polarization come basically from two sources. The first is the uncertainty in the extraction of the nuclear polarization from the optical measurement used to determine the polarization in the pumping cell. The second is the uncertainty in the extraction of the target cell polarization from the pumping cell polarization. An uncertainty of $\Delta P_t/P_t = \pm 10\%$ is assigned to the target polarization.

The measured polarization of the pumping cell nuclei depends upon the pressure and temperature, the correction for the viewing angle of the optical polarimeter, the voltages from the optical polarimeter, V_{li} and V_{dc}, the optical calibration of the polarimeter using a circularly polarizing film, and the calibration of the optical measurement against the NMR measurement of the nuclear polarization. Of these factors, the uncertainties in the pressure and temperature have the smallest effect on the polarization value. The NMR calibration is valid to $\sim 3\%$. The main sources of uncertainty were the optical calibration, the correction for the polarimeter viewing angle, and the noise on the voltage signals from the phototube.

The extraction of the target cell polarization depends upon the transfer time and the relaxation time in the target cell. The transfer time is well determined because it does not vary significantly between measurements, depending only upon the temperature and pressure, which are held almost constant throughout the experiment. However, the target cell relaxation time depends upon the surface conditions and the amount of beam current, which change with time and need to be measured. The uncertainty in the relaxation time is a major source of uncertainty in the extraction of the target polarization. Also, there may be gradients in the ^{3}He polarization in the target cell because of beam effects, discussed more in Section 4.5.

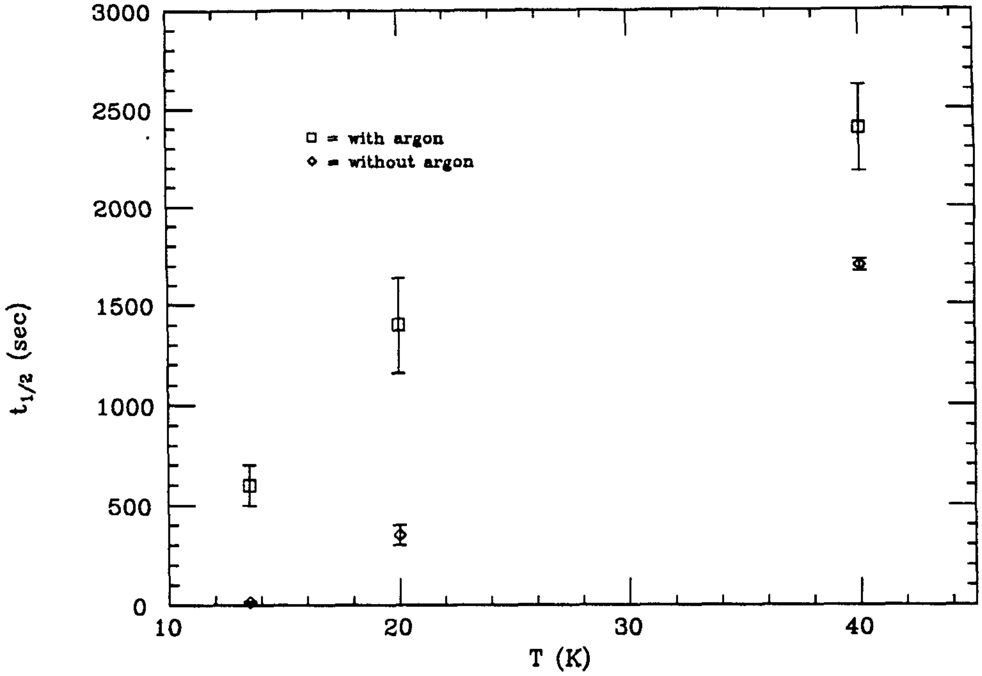

Figure 4.18: Target cell relaxation times with and without an argon surface coating.

4.5 ^{3}He Target Depolarization Studies

4.5.1 Wall Coatings

The surface of the target cell was coated with frozen nitrogen during the experiment to decrease the surface relaxation. Tests were done at Caltech to ascertain the effectiveness of different wall coatings. Gaseous argon, nitrogen, and krypton were frozen to the walls by cooling the cell below the freezing point of the gas after filling the volume with about 5-10 torr at a temperature of ~80 K. This corresponds to $\sim 3 \times 10^{20}$ atoms or molecules of the coating gas. The three wall coatings were found to work equally well, so nitrogen was chosen because of its ready availability. Figure 4.18 shows the spin relaxation half-life for the target system as a function of target cell temperature both with and without a wall coating of frozen argon. The wall coating decreases the surface relaxation effects substantially, especially at the lowest temperatures. The measured half-life at 13.5 K is increased by 1 – 2 orders of magnitude over what one could achieve without the wall coating. Without using this technique to decrease the relaxation from the surface effects, the target would not have operated at temperatures below 25 K.

4.5.2 Beam Effects

The initial beam depolarization studies for the target were done at the Pelletron accelerator at Kellogg Radiation Lab of Caltech using 0.25 – 1.0 nA of 5 MeV protons. This beam has an energy loss of $\frac{dE}{dx} = 106$ MeV/(g/cm^2), the equivalent of 10 – 40 μA of minimum ionizing particles. The target version used for these tests had a smaller diameter transfer tube than the final version used for the experiment, so the results are not directly comparable. However, the results of the proton studies indicated that the target remained polarized with $P_t/P_p \sim 0.85 - 0.95$ and target cell relaxation times of 500 – 1500 sec, depending upon the beam current.

In January 1989, a one-day test run to assess the depolarizing effects of an electron beam was performed at the MIT-Bates linear accelerator using a beam of 250 MeV unpolarized electrons. The target and laser systems were set up in the South Hall on the B-line. Relaxation measurements to determine P_t/P_p and τ_t were made at beam currents of 5.6, 11, 22, 33, and 44 μA. Figure 4.19 shows the measured ratio P_t/P_p as a function of the target cell relaxation time, which varies with the beam current. Table 4.3 summarizes the results, and lists the contribution to the relaxation times from beam effects, τ_{beam}, as a function of beam current. Figure 4.20 shows the relaxation rate that is due to the beam vs. the beam current. The rate varies roughly linearly with the beam current.

During the ^{3}He experiment, relaxation measurements to determine P_t/P_p and τ_t were made often, to monitor the relaxation time in the target cell so that the target cell polarization could be extracted for the asymmetry data runs. Figure 4.21 shows the results for the range of beam currents obtained during the experiment. Although the polarization ratios agree well with the prediction, the target cell relaxation times do not correlate as well with the beam current as the results from the test run. Also, for a given beam

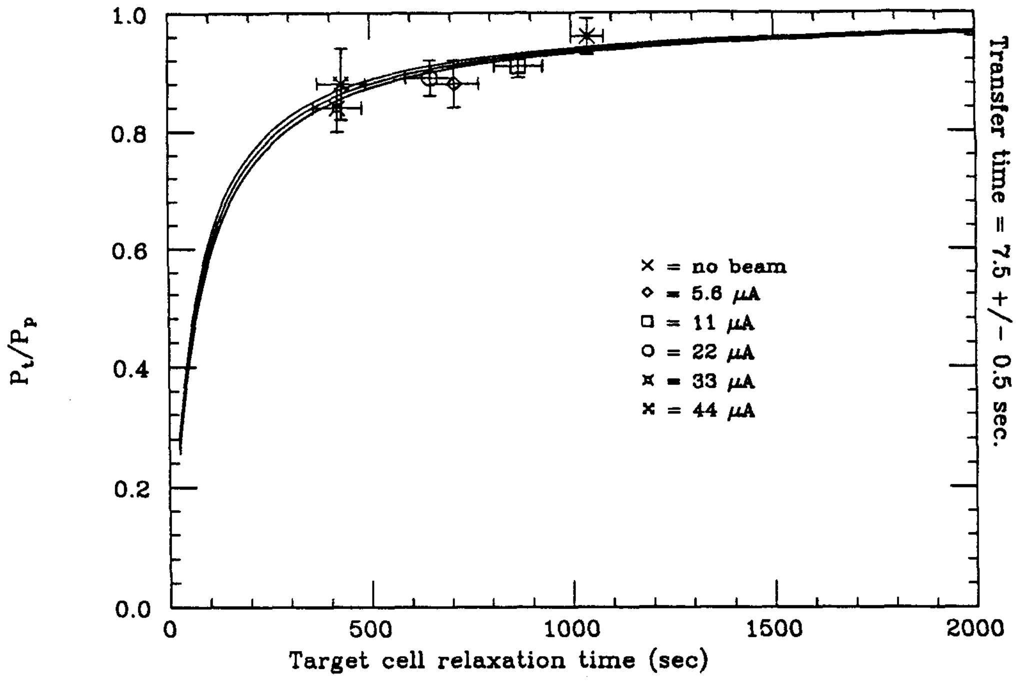

Figure 4.19: P_t/P_p as a function of the relaxation time in the target cell, for transfer times of $t_{ex} = 7.5 \pm 0.5$ sec, shown with the data from the study of beam depolarization with a minimum ionizing electron beam. The beam currents at which the data were taken are indicated.

current, the relaxation times observed during the experiment are shorter in most cases than those observed during the test run. This is because the surface conditions were not the same throughout the experiment, while they did not vary much during the test run, which lasted about 10 hours. The nitrogen wall coating appears to deteriorate with time, probably because it slowly evaporates from the area on the foil windows through which the beam enters and exits the cell, causing the relaxation time in the target cell to decline. This happens over the course of several days, and the effects can be substantially reduced by renewing the wall coating every day or two. In Figure 4.21 there are two data points for a beam current of 20 μA because the results were very different between two separate measurements, one taken at the beginning of the experiment and the other taken several weeks later. Table 4.4 gives the results of all the relaxation runs taken during the

I (μA)	P_t/P_p	τ_t (sec)	τ_{beam} (sec)
0	0.96 ± 0.03	1040 ± 40	-
5.6	0.88 ± 0.04	710 ± 60	2200 ± 600
11	0.91 ± 0.02	870 ± 60	5300 ± 2500
22	0.89 ± 0.03	650 ± 60	1700 ± 400
33	0.85 ± 0.04	420 ± 60	700 ± 170
44	0.88 ± 0.06	430 ± 60	730 ± 180

Table 4.3: Target cell relaxation time and polarization ratio vs. beam current. The contribution to the relaxation time from beam effects only, τ_{beam}, is indicated.

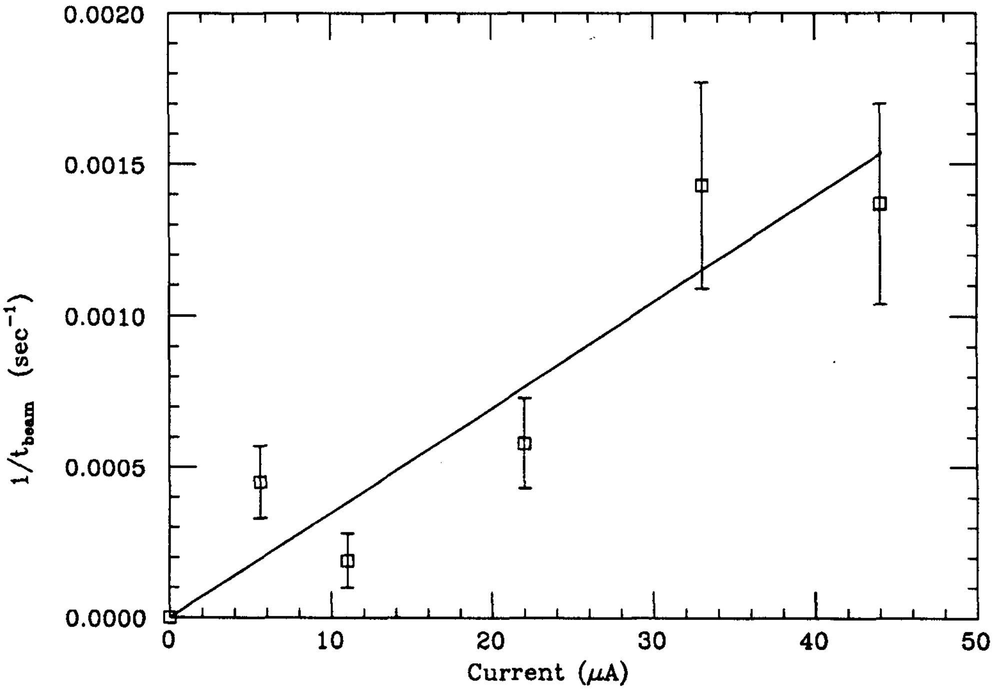

Figure 4.20: Relaxation rates from the beam effects, as a function of beam current.

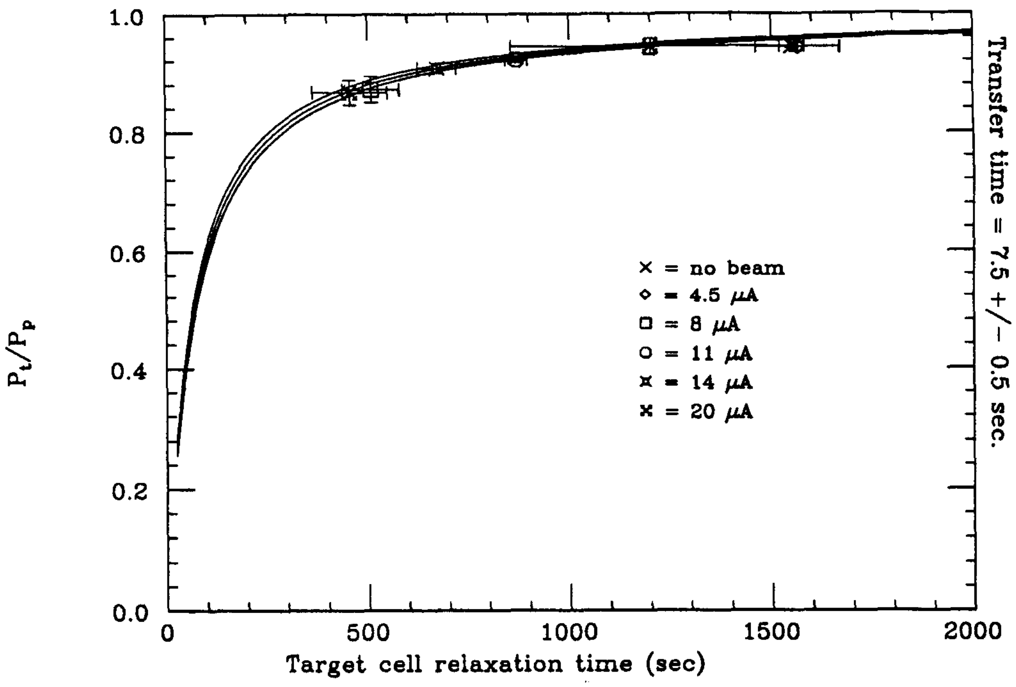

Figure 4.21: P_t/P_p as a function of the relaxation time in the target cell, for transfer times of $t_{ex} = 7.5 \pm 0.5$ sec, shown with the data from the experiment. The beam currents at which the data were taken are indicated.

experiment, both with and without beam on the target cell. For a given beam current the relaxation times before recoating the cell walls were sometimes substantially shorter than those obtained afterwards. For example, the data for 11 μA beam current show the dramatic difference caused by surface effects. The recoating process takes less than an hour, so the increased relaxation time after recoating comes from reduced surface effects because of the improved quality of the coating. The ratio, $P_t/P_p = 0.91$, is assumed for the extraction of the target polarization from the pumping cell polarizations measured during the experiment.

The similarity between the results obtained with the proton beam at Caltech and the electron beam at MIT-Bates supports the idea that the beam depolarization is dominated by the creation of ions in the gas. As was mentioned in Section 4.2.4, the atomic $^3He^+$ ions are created directly by the beam and the molecular ions are created in three-body

I (μA)	P_t/P_p	τ_t (sec)	type	Comments
0	0.951 ± 0.016	2130 ± 220	R	
0	0.992 ± 0.008	1880 ± 100	T	
0	0.940 ± 0.014	1880 ± 100	R	
0	0.896 ± 0.013	1770 ± 150	R	
0	0.953 ± 0.009	1770 ± 150	T	
0	0.892 ± 0.012	2130 ± 140	R	
0	0.970 ± 0.008	2130 ± 140	T	
0	0.973 ± 0.014	1720 ± 100	R	
0	1.001 ± 0.016	1720 ± 100	T	
0	0.941 ± 0.009	1650 ± 120	R	
0	0.968 ± 0.009	1650 ± 120	T	
0	0.943 ± 0.009	1810 ± 140	R	
0	0.973 ± 0.008	1810 ± 140	T	
0	0.946 ± 0.012	1210 ± 50	R	
0	0.955 ± 0.023	2350 ± 420	R	after recoating
0	0.911 ± 0.010	1460 ± 90	R	
0	0.906 ± 0.020	1380 ± 200	R	
0	0.909 ± 0.010	1860 ± 160	R	
0	0.912 ± 0.008	1590 ± 160	R	
0	0.914 ± 0.008	1670 ± 130	R	after recoating
4.5	0.935 ± 0.019	1570 ± 100	R	
4.5	0.945 ± 0.008	1570 ± 100	T	
8	1.049 ± 0.197	1580 ± 870	R	
8	0.870 ± 0.022	500 ± 70	R	
11	0.916 ± 0.010	850 ± 30	R	
11	0.912 ± 0.009	850 ± 30	T	
11	0.933 ± 0.011	920 ± 50	R	
11	0.930 ± 0.009	920 ± 50	T	
11	0.756 ± 0.069	270 ± 60	R	before recoating
14	0.878 ± 0.026	860 ± 190	R	
14	0.899 ± 0.055	860 ± 190	T	
14	0.873 ± 0.013	650 ± 50	R	
14	1.044 ± 0.016	650 ± 50	T	
14	0.865 ± 0.025	800 ± 190	R	
14	0.808 ± 0.023	800 ± 190	R	
20	0.922 ± 0.028	1200 ± 350	R	
20	0.952 ± 0.016	1200 ± 350	T	
20	0.847 ± 0.036	460 ± 90	R	before recoating
20	0.877 ± 0.025	460 ± 90	T	before recoating

Table 4.4: Results of relaxation runs taken during the experiment. The measurements for a given beam current are listed in the order taken during the experiment. "T" refers to "transfer" relaxation measurements and "R" refers to "relaxation with discharge on" measurements.

collisions with ground state atoms.

The energy needed to create an atomic ion is ~ 50 eV/ion, depending upon the purity of the gas. An ionizing beam of particles will create $^3\text{He}^+$ ions per unit volume at a rate, in cm^{-3}-sec^{-1}, of

$$S_1 = 6.1 \times 10^{12} \left(\frac{I\,p\,l}{V\,T}\right) \left(\frac{dE}{dx}\right), \tag{4.25}$$

where

I = beam current (μA)

p = pressure (torr)

l = target length (cm)

V = target volume (cm^3)

T = target temperature (K)

and

$\frac{dE}{dx}$ = stopping power ($\text{MeV}/(\text{g}/\text{cm}^2)$).

For minimum ionizing particles incident on ^{3}He, the stopping power is 2.6 $\text{MeV}/(\text{g}/\text{cm}^2)$. From this equation, it is estimated that $\sim 6 \times 10^{14}$ $^3\text{He}^+$ ions are formed per second for 20 μA of beam current. For this target, the $^3\text{He}^+$ atomic ions are converted into $^3\text{He}_2^+$ molecular ions very rapidly, within approximately 8 μsec. The conversion rate, in cm^{-3}-sec^{-1}, for the atomic ions to become incorporated into molecular ions, written in terms of the atomic ion concentration, $C1$, is [48]

$$S_2 = 8.8 \times 10^6 \left(\frac{p}{T}\right)^2 C1. \tag{4.26}$$

As mentioned in Section 4.2.4, interactions of the polarized nuclei with the molecular ions dominate the beam depolarization at the pressures used for the target. For the density used for the target, recombination with electrons is more significant than wall collisions in destroying the molecular ions, and the molecular ions are concentrated near the beam path. In this case, one must worry about a polarization gradient in the target cell, where the polarization of the ^{3}He in the beam path is different from the average polarization in the cell. It is possible to estimate the size of the effect from information about the diffusion time of the ^{3}He atoms in the target cell, and measured values of the relaxation rate that is due to the beam. The beam relaxation time for 20 μA of electrons, shown in Table 4.3, is $\sim$ 1700 sec, so the rate of depolarization of the ^{3}He nuclei in the target is roughly 1.6×10^{16}/sec. If the polarized ^{3}He did not diffuse out of the beam path, then they would depolarize in approximately 20 seconds. This is not the case, however. The atoms diffuse out of the beam path in $\sim 2-3$ beam-bursts and to the walls within approximately one second. Therefore, the gas in the target cell is mixed on a timescale much shorter than the time for depolarization. In this particular case, the atoms in the beam path may have a fractional polarization difference of $\sim$ -5% below the average in the target cell. During the experiment the average beam current was 11 μA, so the polarization in the beam path was probably even closer to the average. The target polarization was not corrected for the gradient in the data analysis. Rather, the effect was included in the uncertainty. For targets operating at higher beam currents or significantly larger densities, this effect should be considered in more detail.

Chapter 5

Data Analysis

The data analysis for this experiment involved the extraction of the electron helicity-dependent asymmetry, an operation performed separately on the data from each of the spectrometers. To obtain the asymmetry, the yield was calculated from events of each beam helicity, accounting for differences in charge between the two helicity states and making corrections for yield from background sources such as scattering from the target walls, pion production, and in the quasielastic region, events from the elastic radiative tail. The software cuts used to select good events are described in Section 5.1. Section 5.2 deals with the background sources that contribute to the total yield. The extraction of the unpolarized cross section for comparison with previous experimental data is described in Section 5.3, and the calculation of the experimental asymmetry is described in Section 5.4. Section 5.5 deals with the corrections made to the experimental asymmetry to extract the quasielastic, spin-dependent asymmetry for scattering from ^{3}He. The results of the experiment are given in Chapter 6.

5.1 Experimental Cuts

The OHIPS and BIGBITE event triggers described in Section 3.5 are sufficiently general to include not only the events of interest in the data saved to tape, but also many events from background radiation in the experimental hall. Further requirements are imposed in the software analysis to define "good" events, i.e., events that originate from (or near) the target. Of course, these events possibly include background which must be accounted for through measurements and calculations. This is discussed in Section 5.2. The software cuts used to define "good" events in OHIPS and BIGBITE are described here.

Since the hardware trigger for OHIPS requires a hit in each of the three scintillator planes, the cuts applied in software pertain to the information from the drift chambers. The VDCX is described briefly in Section 3.4.1, and the extraction of the track position and slope from the delay line information is given in detail in Reference [14]. There are four delay lines with 28 or 29 wires on each line. The wire number is determined from the time difference of signals from each end of the delay line. The test for an event to have "good" momentum information requires a signal from all four delay lines, with the wire numbers indicating that the signals are from neighboring wires. In addition, the slope of the track, calculated from the drift distance information, must be positive in both chambers. This eliminates data where two or more events occurred during the read out of the delay lines or when noise on the delay line interfered with the wire number determination, confusing the track reconstruction. The "good" events, stored in the Q histogram, OSDELG, are used in the calculation of the quasielastic asymmetry without further momentum cuts. For the cross section estimate, the yield was corrected to account for all events with four delay line signals, regardless of the ordering of the wires or the slope in the chambers. This was done because data collected during the optics study done in January 1990 [13] on the ^{12}C elastic scattering cross section indicate that the events eliminated by the more stringent test requirements for OSDELG are good events but without reliably reconstructable momenta. In general, approximately 10% of the data is eliminated by requiring the slope test and the neighboring wire test over the simpler requirement of signals from four delay lines.

For BIGBITE, the hardware trigger requires a hit from both scintillator planes. Although each plane is constructed in three separate segments with individual readouts, the trigger does not make use of the information from the segmentation to reduce the background rates. The software cuts for the "good" momentum events involve both the

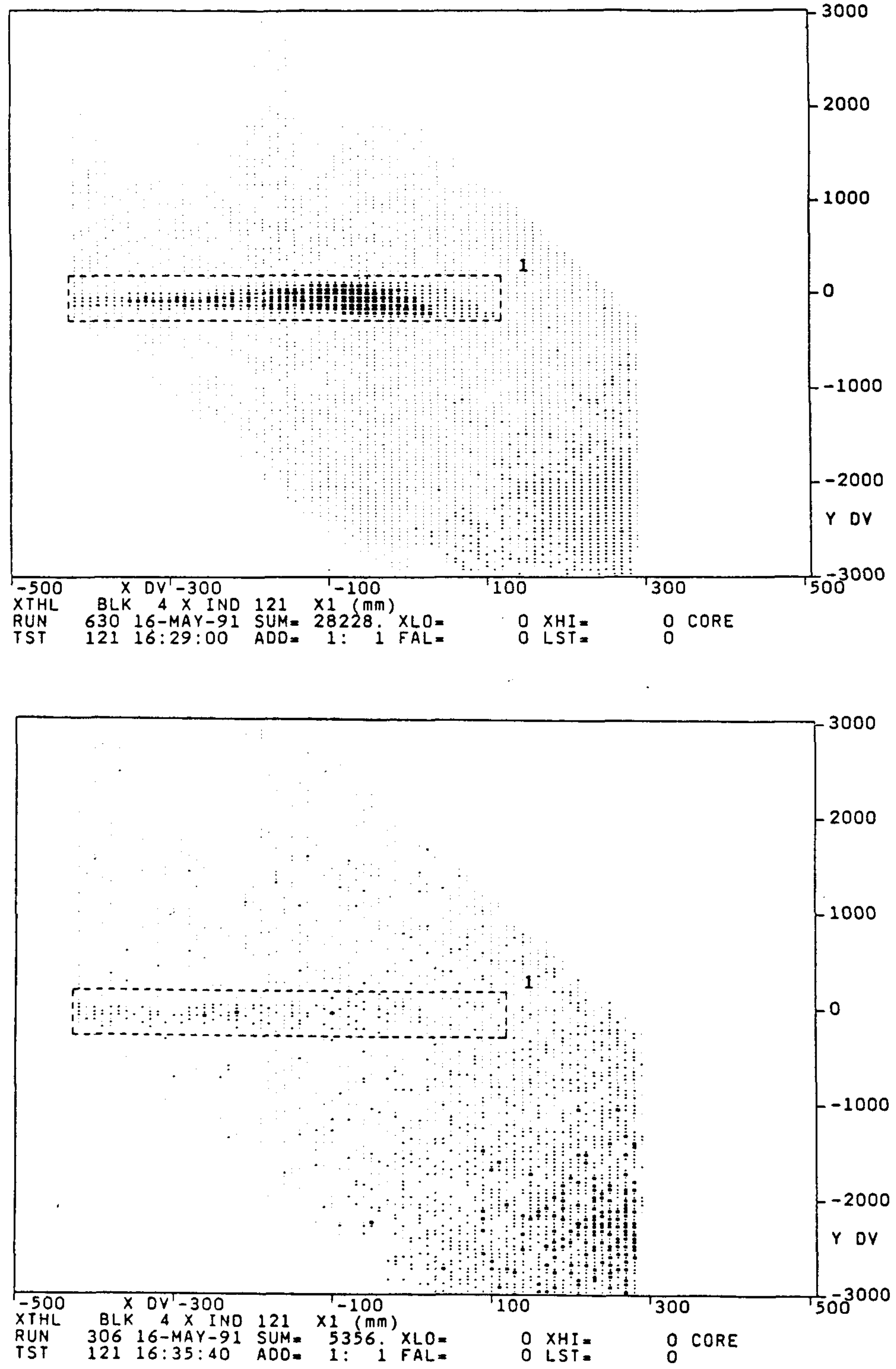

```
XTHL   BLK  4 X IND 121  X1 (mm)
RUN   630 16-MAY-91 SUM= 28228. XLO=      0 XHI=      0 CORE
TST   121 16:29:00  ADD=  1:  1 FAL=      0 LST=      0
```

```
XTHL   BLK  4 X IND 121  X1 (mm)
RUN   306 16-MAY-91 SUM=  5356. XLO=      0 XHI=      0 CORE
TST   121 16:35:40  ADD=  1:  1 FAL=      0 LST=      0
```

Figure 5.1: X1 vs. θ_l for target full (top) and target empty (bottom).

wire chambers and the scintillator information. The scintillator test imposed in software is that the scintillator segments firing in each plane be either in the same relative position or adjacent to each other. The wire chamber information consists of position data from two sets of X and Y chambers (labeled X1, Y1, X2, and Y2); the test requires a single hit in each plane. A tracking requirement is also imposed to determine whether the events originate from the general direction of the target. This corresponds to requiring that the scattering angle, θ, calculated from the X wire position information, be correlated with the X1 position. This cut is imposed by requiring that X1 and a linearized angle, $\theta_l \equiv 2.92(\mathrm{X1}) + 0.5(\theta)$, lie within a box in the two-dimensional histogram of X1 vs. θ_l. Figure 5.1 shows the graph for a run with the target full and for an empty target background run; the box indicates the cut used to determine good events. The efficiency of this cut is $\geq 98.8\%$. The "good" events are saved in the Q histogram, DELG.

Prior to this analysis, it was believed that the scintillator segments overlapped sufficiently and that the planes were aligned sufficiently well that only segments in the same relative position in each plane would fire for a good event, a more stringent requirement than is used in analyzing the data from this experiment. The requirements were relaxed after a hole was discovered in the X1 vs. θ spectrum for events in DELG, so that events firing adjacent segments in the two planes were accepted. Figure 5.2 shows the spectra of X1 vs. θ for "good" events with the old and the new cuts. The hole shows up at a position that corresponds to the junction between scintillator segments 1 and 2, on the high momentum side of the spectrometer. Changing the scintillator requirements eliminated the hole without significantly increasing the background counts.

5.2 Sources of Background

5.2.1 Empty Target Yield

Because the density of the target gas was low for a nuclear target ($\sim 1.2 \times 10^{18}/\mathrm{cm}^3$), the background from the target walls and the windows was potentially a serious problem. To

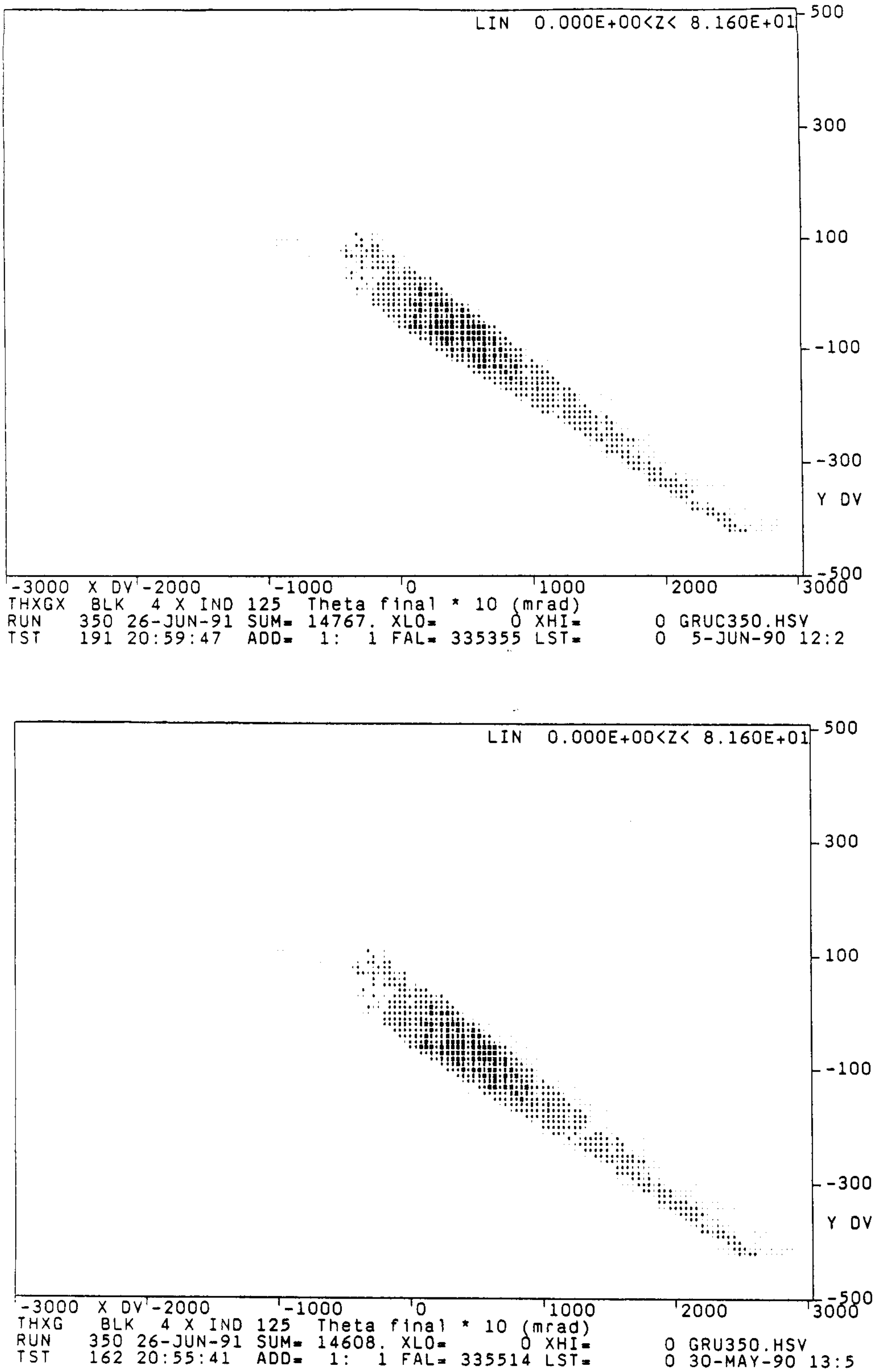

Figure 5.2: X1 vs. θ for target full runs with (bottom) and without (top) new scintillator cuts.

ensure that electrons scattered from the entrance and exit foil windows were not accepted by the spectrometers, 2.54 cm-thick tungsten collimators were used to restrict the effective target length seen by the spectrometers to 10 cm. The collimators were mounted outside the exit window on each side of the scattering chamber, between the scattering chamber and the spectrometer entrance window. The edges of the tungsten blocks were beveled at the spectrometer scattering angle and were held in place along a groove mounted to the support legs of the scattering chamber using set screws. The alignment of the collimators was done to a precision of 1 mm. The collimators effectively eliminated the background from the windows, so the main source of the empty target yield was particles in the beam halo scattering from the target walls. A phototube mounted to the outside of the beam line approximately one meter upstream of the target was used as a halo monitor; the beam was tuned to minimize the phototube signal.

The beam position was adjusted while viewing the fluorescence of a beryllium oxide (BeO) target upstream of the ^{3}He target. The beam position for the ^{3}He asymmetry runs was chosen to minimize the empty target yield. The position selected corresponded to an offset of $\sim$ 3 mm below and $\sim$ 3 mm to beam-left of the nominal beam center. The yield was smaller for the beam offset below the center because of the additional material of the transfer tube and the mounting block for the temperature sensor connected to the top of the target cell. The left-right position was selected off center not only because of indications that the rates were slightly smaller there, but also because of difficulties in steering the beam in the beam-right direction. In order to estimate empty target rate variations for left-right position fluctuations, it was better to choose the position away from the steering limits.

For the empty target runs, the ^{3}He gas was pumped out of the target cell. Since the target cell was not moved for the measurement, the geometry was exactly the same as with the target full. Runs were taken with the target empty several times over the course of the experiment. The empty target yield was measured at the beginning of the experiment (runs 302-314), after several days of running (runs 344-345), and again after an eleven-day

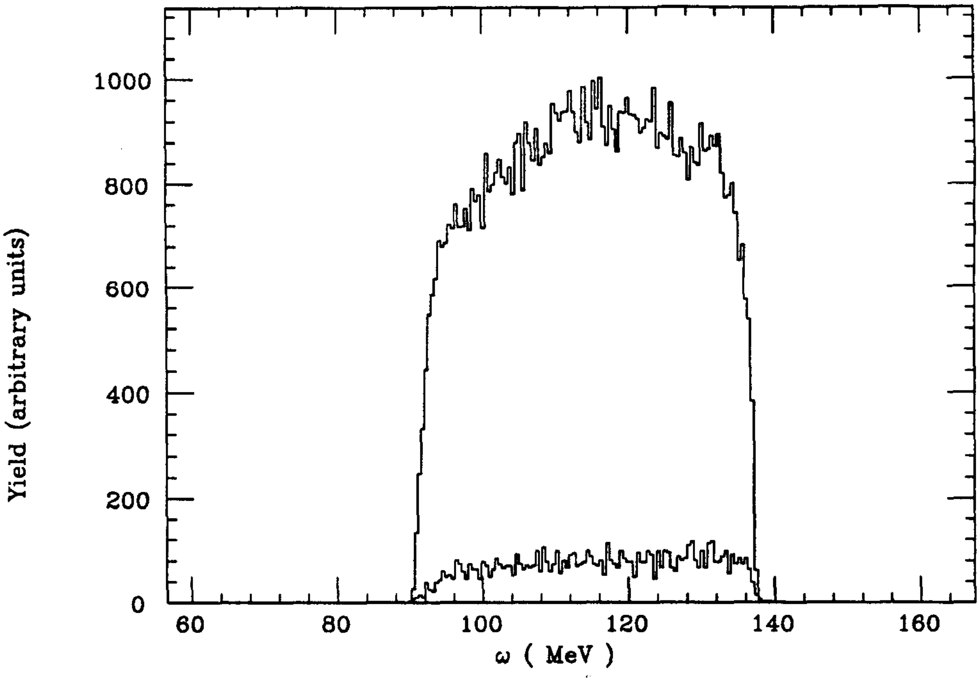

Figure 5.3: OHIPS full vs. empty target yield as a function of ω, the energy transfer.

shutdown (runs 500-508). Two of the sets of empty target data include measurements of the empty target yield as a function of beam position (runs 302-314 and 500-508). The position dependence of the rates extracted from these runs is used to estimate the size of the false asymmetry from a helicity-correlated beam position shift, a calculation described in Section 5.5.5.

Figures 5.3 and 5.4 show the empty and full target yields as a function of the energy transfer, ω, for OHIPS and BIGBITE, respectively. The values plotted are normalized to account for charge and efficiency differences between the empty and full target runs. The full target yield is calculated from the sum of all the ^{3}He asymmetry runs, and the empty target yield from the sum of all the empty target runs with the beam at the position used for the ^{3}He asymmetry runs. The empty target yield for OHIPS is $9.8 \pm 1.6\%$ of the full target yield, integrated across the momentum acceptance. The data for BIGBITE indicate that there is no yield from ^{3}He below $\omega = 11$ MeV. For BIGBITE, the empty target yield

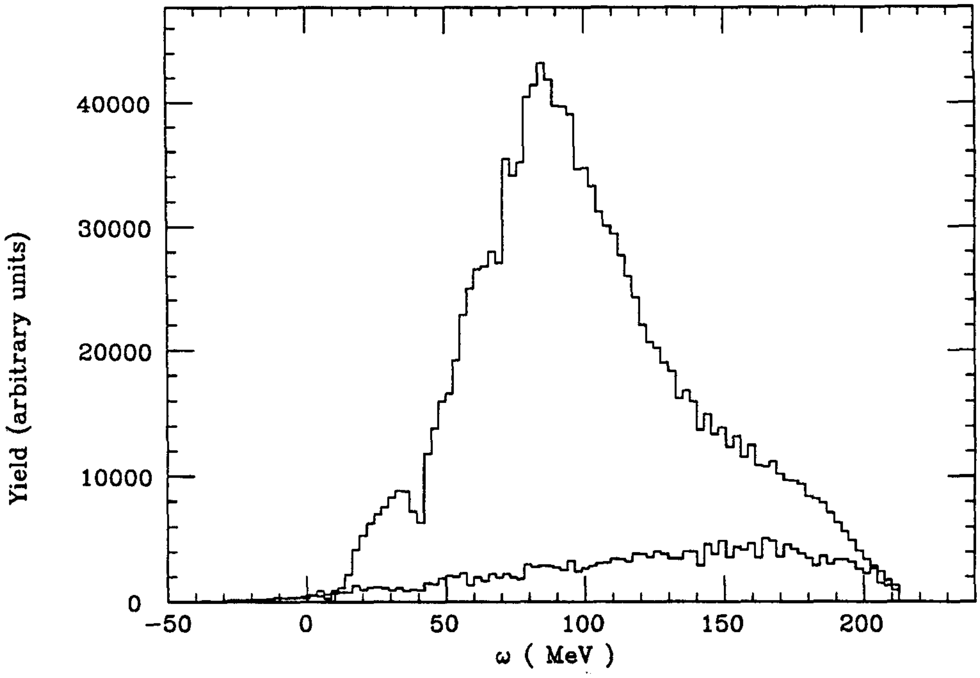

Figure 5.4: BIGBITE full vs. empty target yield as a function of ω, the energy transfer.

for 58 MeV $\leq \omega \leq$ 161 MeV, the region chosen for the quasielastic analysis, is $15 \pm 4\%$ of the total yield. In the region around the elastic peak, the relative yield from the empty target becomes more significant. For 11 MeV $\leq \omega \leq$ 37 MeV, the empty target accounts for $21\% \pm 3\%$ of the yield, while for 11 MeV $\leq \omega \leq$ 32 MeV it contributes $24\% \pm 4\%$.

The fluctuation in the charge-normalized yield from the individual empty target runs is larger than the statistical uncertainty, indicating that the beam position or the beam halo varied over the duration of the experiment. The correction for the empty target background is the average of the yield from the individual runs taken at the beam position chosen for the ^{3}He data collection. The systematic error assigned to the empty target correction corresponds to the root-mean-square deviation of the yield.

5.2.2 Elastic Radiative Tail

In the single photon exchange approximation the elastic peak appears as a delta function in the momentum spectrum, smeared by the beam energy width and the spectrometer resolution. In practice, however, energy straggling and bremsstrahlung give rise to elastically scattered electrons with lower final momenta than the value at the elastic peak. These events comprise the elastic radiative tail, a significant source of background in the quasielastic scattering region. The radiative corrections are classified as "internal" if they are due to radiation in the field of the primary target nuclei involved in the scattering, and "external" if they arise from interactions with other target nuclei or with nuclei in the entrance and exit material of the target system.

The paper by Mo and Tsai [56] contains a detailed description of the radiative correction process. For the calculation of the radiative tail for the polarized ^{3}He target system, the target thickness is assumed to be the thickness corresponding to the average target temperature and pressure. The entrance foil window was 4.6 μm copper foil and the exit material consisted of the 0.25 mm copper wall of the target cell, corrected for the scattering angle, and approximately 0.43 mm of aluminum in the scattering chamber windows and the first-stage, thermal radiation shield. Inclusion of additional material to account for the spectrometer windows has a negligible effect on the results.

Figure 5.5 shows the elastic radiative tail calculated for the kinematics of the OHIPS and the BIGBITE measurements. The BIGBITE elastic yield has been smeared roughly by the momentum resolution of the spectrometer to obtain a more realistic estimate of the elastic radiative tail contribution under the quasielastic peak. The elastic yield is estimated to contribute $1.1 \pm 0.1\%$ of the total yield in the OHIPS spectrometer and $3.9 \pm 0.4\%$ of the total yield in the energy region used for the quasielastic analysis of the BIGBITE data.

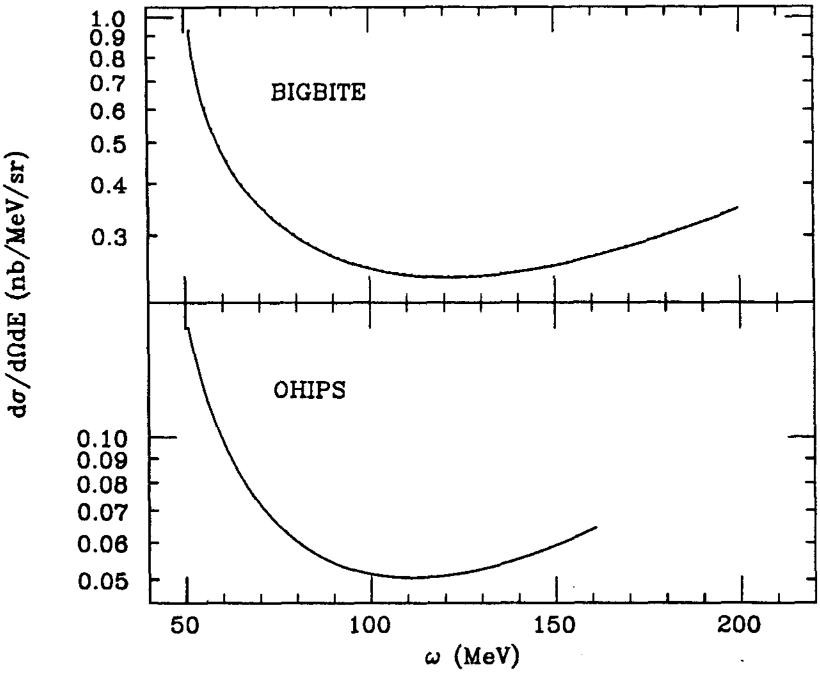

Figure 5.5: The elastic radiative tail as a function of ω, calculated for the kinematics of the BIGBITE and the OHIPS measurements. The BIGBITE cross section has been smeared by the spectrometer momentum resolution.

5.2.3 Pions

The pion cross section was calculated using the computer code of O'Connell and Lightbody [57]. The calculation accounts for the effect of the Fermi motion by including the nucleon momentum in the scattering process and transforming from the nucleon rest frame to the lab frame to calculate the cross section. A Monte Carlo routine is used to assign an initial momentum to the struck nucleon. The calculation indicates that the pions contribute 1.1% of the total yield in the OHIPS spectrometer and 1.7% of the total yield in the energy region used for the quasielastic asymmetry analysis of the BIGBITE data. As is done for the elastic radiative tail, the pion yield for BIGBITE is smeared over the momentum acceptance of the spectrometer before integration. Figure 5.6 shows the calculated pion cross section for the two spectrometers. The fractional uncertainty in the pion yield

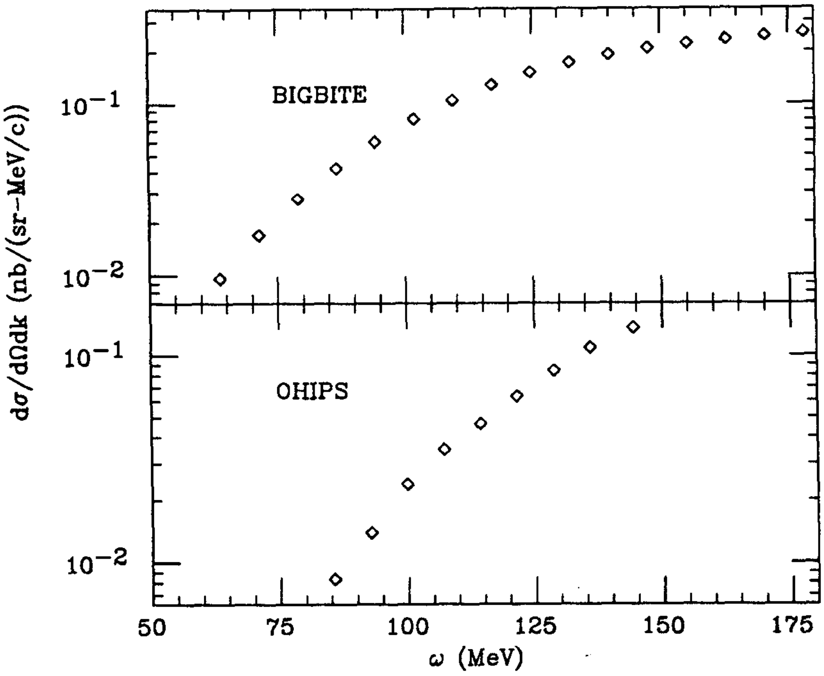

Figure 5.6: The pion cross section as a function of ω, calculated for the kinematics of the BIGBITE and the OHIPS measurements. The BIGBITE cross section has been smeared by the spectrometer momentum resolution.

is assumed to be 100%.

Since Bigbite was run without a Čerenkov detector, there is no experimental information on the pion yield in that spectrometer. As was mentioned in Section 3.4.1, a Čerenkov detector was mounted in OHIPS to provide information about the pion production. Unfortunately, problems with the phototube base caused noise to be introduced into the delay lines whenever the tube was run at high voltage. Some data were taken with the phototube operating at lower voltage than was normally used. The pion spectra from these runs show no sign of a statistically significant asymmetry, although the poor statistics on the measurement limit the usefulness of the information. Because of the limitations of the experimental data, all corrections for the pion contributions are based on the calculation of the pion yield.

5.3 Experimental Cross Section

5.3.1 OHIPS

The expression for the raw cross section in terms of experimental observables for the data collected in OHIPS is

$$\frac{d^2\sigma}{d\Omega dE} = \frac{N_{OSDELG}}{N_e N_t\, \epsilon\, \Delta E \Delta\Omega} \tag{5.1}$$

where

N_{OSDELG} = counts in OSDELG within a specified energy bin,

N_e = number of incident electrons,

N_t = number of target nuclei,

ϵ = delay line efficiency × computer live time × multiple hit correction,

ΔE = energy bin size,

and

$\Delta\Omega$ = solid angle.

The unpolarized cross section is calculated using the counts in OSDELG, which includes events of either electron helicity. Energy limits of 92 MeV $\leq \omega \leq$ 136 MeV are chosen so that the spectrometer momentum acceptance is flat in the region used for the cross section calculation. The beam charge in each beam pulse was measured with two beam toroids on the B line (BT1 and BT2) and recorded for each pulse. The charge measured by BT2, the beam toroid closer to the target, is used in the cross section calculation.

The ^{3}He asymmetry data were collected in individual runs of $\sim$ 10 μA-hrs integrated beam charge each. The number of target nuclei is calculated separately for each run, based upon the average temperature of the target during the run and the temperature and pressure of the ^{3}He gas when the target was filled. The calculation of the pressure of the double-cell system as a function of the target temperature is described in Section 4.4.1. The target thickness in nuclei/cm^2 is

$$N_t = 9.7 \times 10^{18} \left(\frac{p\,L}{T}\right) \tag{5.2}$$

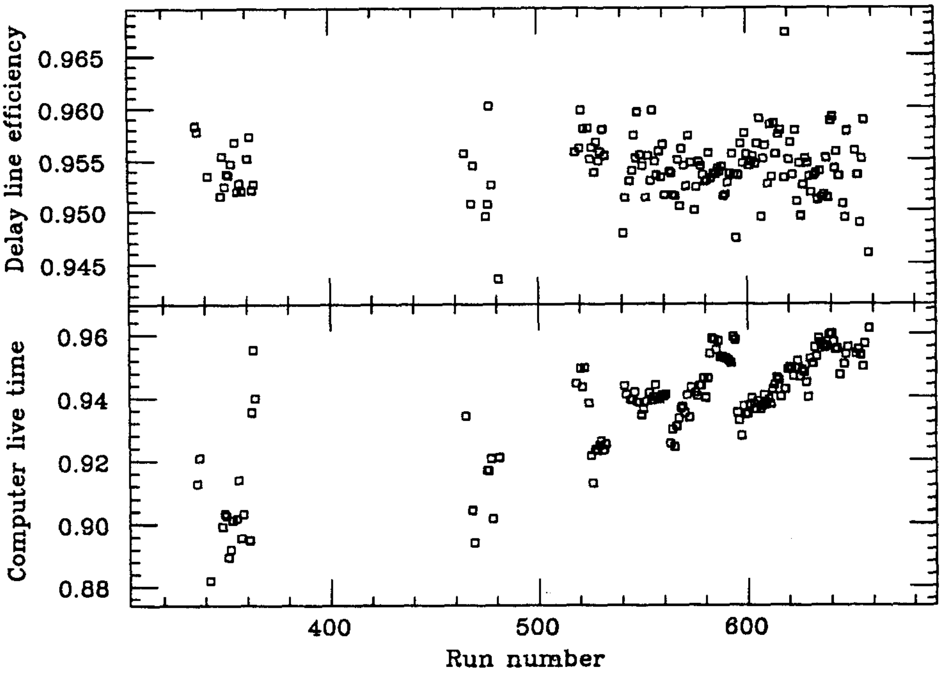

Figure 5.7: OHIPS delay line efficiency and computer live time, for each asymmetry run.

where p is the pressure (torr) of the double-cell system, L, the target length (10 cm), and T, the target temperature (K). The average target temperature and pressure during the asymmetry runs were 16.65 K and 2.09 torr, so the average target thickness was $1.2 \times 10^{19}/\mathrm{cm}^2$.

The multiple hit correction uses the slope test described in Section 5.1; the normalization accounts for events that do not satisfy the software requirements for reliably reconstructible momenta, yet originate from valid scattering events, which should be included in the cross section calculation. The efficiency also includes the computer live time, calculated as the ratio of gated-to-ungated OHIPS events, and the delay line efficiency of the VDCX. The overall delay line efficiency is calculated as the product of the individual delay line efficiencies for all eight delay lines. For the purpose of determining a single line efficiency, an event is judged "good" if it is registered as a hit on all the other delay lines;

i.e., the efficiency of the i$^{\text{th}}$ delay line is

$$\epsilon_i = \left(\frac{\mathcal{N}(\text{ hits on all delay lines })}{\mathcal{N}(\text{ hits on delay lines } j \neq i\ )} \right). \tag{5.3}$$

Figure 5.7 shows the delay line efficiency and the computer live time for the OHIPS runs taken with the target full. The average overall efficiency is 0.90. The runs missing from the figure correspond to empty target runs, Møller runs, set-up runs, or run numbers that were skipped.

A Monte Carlo calculation using the TURTLE [12] program to estimate the OHIPS angular acceptance indicates that the solid angle for a point target is 14.6 msr. Data taken during the optics study in January 1990 indicate that with the collimator used for this experiment the true solid angle is somewhat reduced (~6-10%) from the model's estimate [13]. Calculations for an extended target indicate that a solid angle of 12.2 msr is a reasonable estimate for the purpose of extracting the ^{3}He cross section from the data for comparison with previous experimental results.

The raw cross section calculated from the OHIPS data is 219 nb/sr. The value is reduced to 192 nb/sr when corrections are made for the empty target yield, the elastic radiative tail, and pion production. This value represents the ^{3}He quasielastic cross section, including radiative effects. For comparison with other data and with theoretical calculations, the quasielastic cross section must be corrected to represent a value independent of the target and detector properties. A calculation based upon the radiative correction formulas of Mo and Tsai [56] yields a value of 201 nb/sr for the unradiated ^{3}He quasielastic cross section. Figure 5.8 shows the calculated cross section at the OHIPS kinematics with and without radiative corrections. The systematic uncertainty on the cross section extracted from this analysis is 10%. The main source of uncertainty is the spectrometer acceptance. For comparison, previous ^{3}He quasielastic cross section data [58], scaled to the kinematics of this experiment using y-scaling [59], give a cross section of 210 nb/sr.

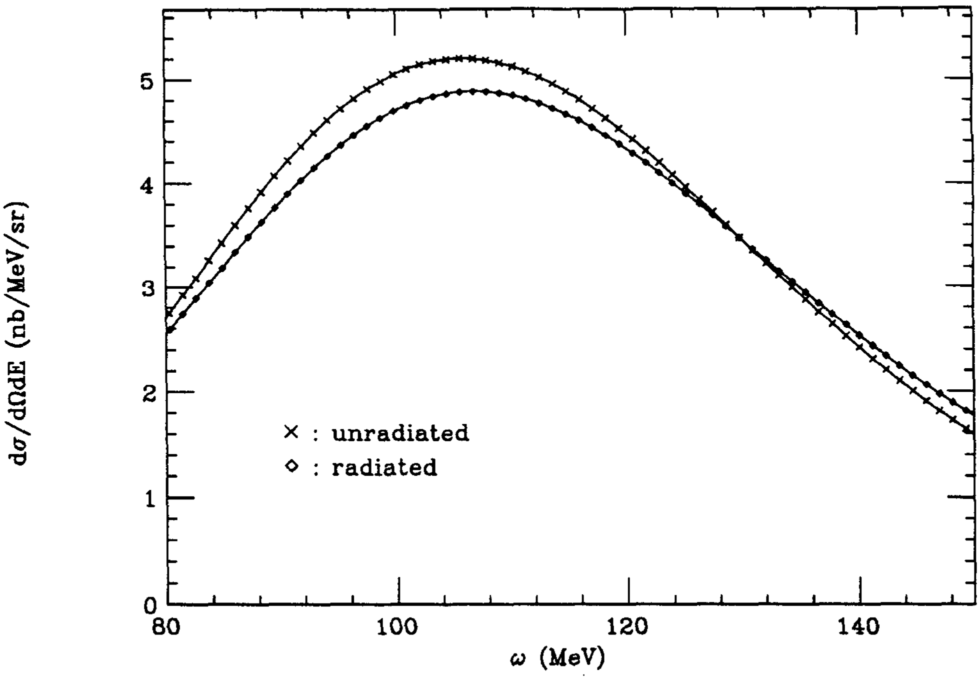

Figure 5.8: Calculated cross section at the OHIPS kinematics, with and without radiative corrections.

5.3.2 BIGBITE

For BIGBITE, the expression for the raw experimental cross section in terms of experimental observables is

$$\frac{d^2\sigma}{d\Omega dE} = \frac{N_{DELG}}{N_e N_t \, \epsilon \, \Delta E \Delta\Omega}, \tag{5.4}$$

where

N_{DELG} = counts in DELG within a specified energy bin,

N_e = number of incident electrons,

N_t = number of target nuclei,

ϵ = wire chamber efficiency × computer live time × multiple hit correction,

ΔE = energy bin size,

and

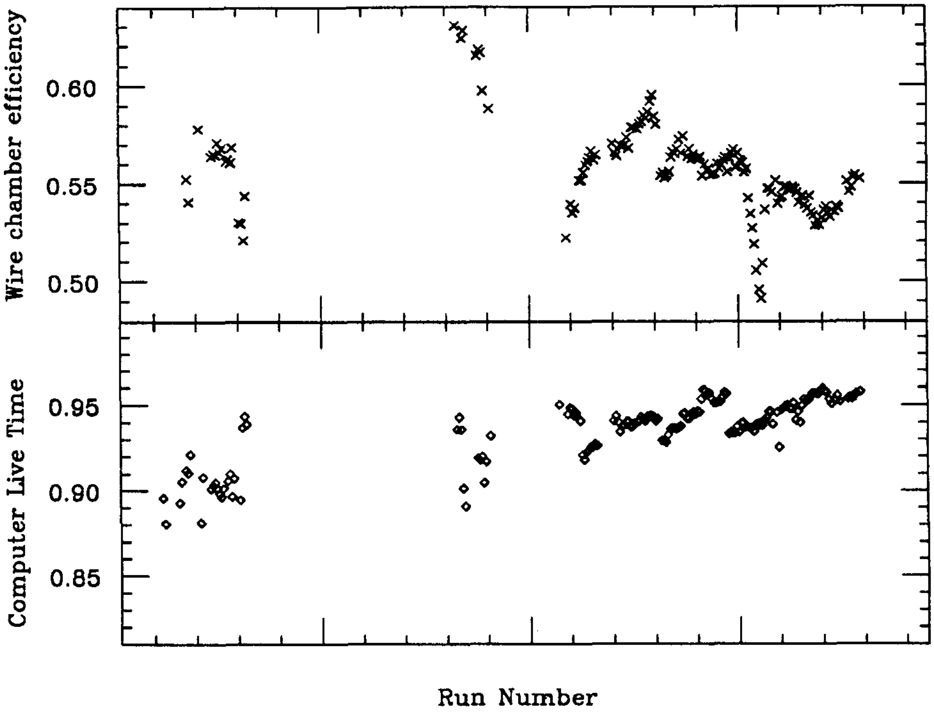

Figure 5.9: BIGBITE wire chamber efficiency and computer live time, for each asymmetry run. For the plot, the multiple hit correction is included in the wire chamber efficiency.

$\Delta\Omega$ = solid angle.

This expression represents the unpolarized cross section since DELG contains all events, regardless of beam helicity. The determination of N_e and N_t is described in the previous section. The efficiency is calculated as the product of the computer live time, which is the ratio of gated-to-ungated BIGBITE events, the wire chamber efficiency, and a correction to account for the fact that multiple hit events are not included in the criteria for good events described in Section 5.1. The efficiency is calculated as

$$\epsilon = \epsilon_{CPU}\, \epsilon_{mult} \prod_i \epsilon_{wc}(i), \tag{5.5}$$

where the efficiency of the i$^{\text{th}}$ plane of the wire chambers is defined by a redundancy argument similar to that used for the OHIPS delay line efficiency, as

$$\epsilon_{wc}(i) = \left(\frac{\mathcal{N}(\geq 1 \text{ hit in every plane})}{\mathcal{N}(\geq 1 \text{ hit in planes } j \neq i)} \right), \tag{5.6}$$

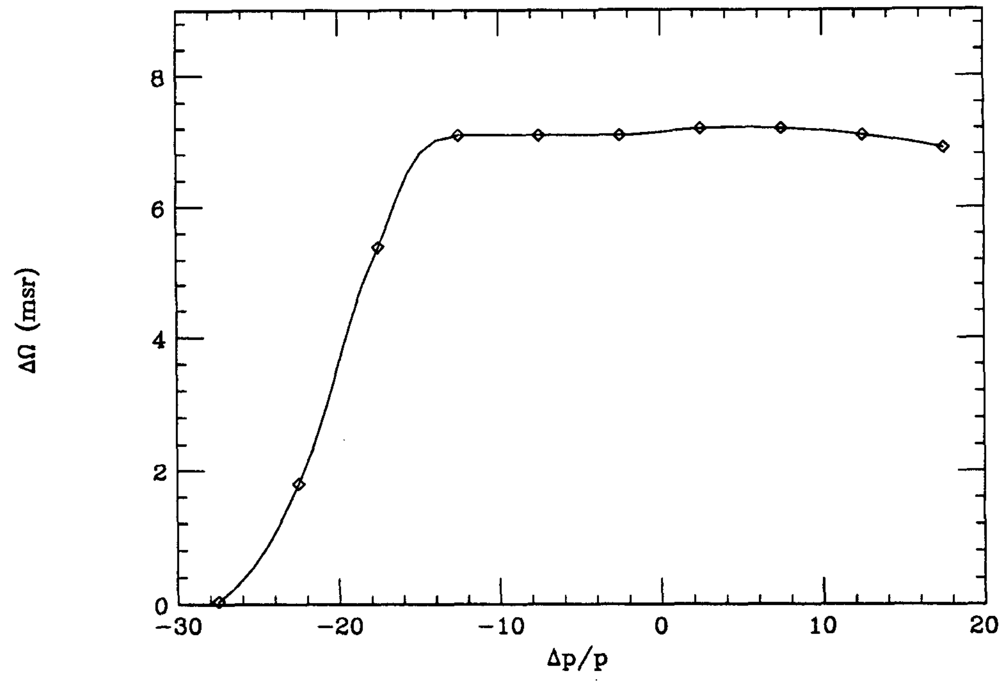

Figure 5.10: BIGBITE solid angle acceptance, from TURTLE calculation, plotted as a function of the percent deviation from the central momentum of the spectrometer.

and the multiple hit correction is

$$\epsilon_{mult} = \left(\frac{\mathcal{N}\,(\text{single hit in every plane})}{\mathcal{N}\,(\geq 1 \text{ hit in every plane})} \right). \tag{5.7}$$

Figure 5.9 shows the computer live time and wire chamber efficiencies for the BIGBITE asymmetry runs. The multiple hit correction has been included in the wire chamber efficiency for the plot. The average overall efficiency for BIGBITE asymmetry runs is 0.52.

The momentum acceptance of BIGBITE is quite large, $\left(\frac{\Delta p}{p_0}\right) \sim \pm 25\%$, and the angular acceptance varies over this momentum range. The solid angle as a function of the momentum of the scattered electron was calculated using the TURTLE Monte Carlo program, and the results are shown in Figure 5.10. The acceptance is relatively flat in the region -46 MeV $\leq \omega \leq 130$ MeV and falls precipitously above $\omega = 130$ MeV.

The doubly differential cross section for the BIGBITE data is shown in Figure 5.11. The raw cross section has been corrected for the empty target counts only. Because the

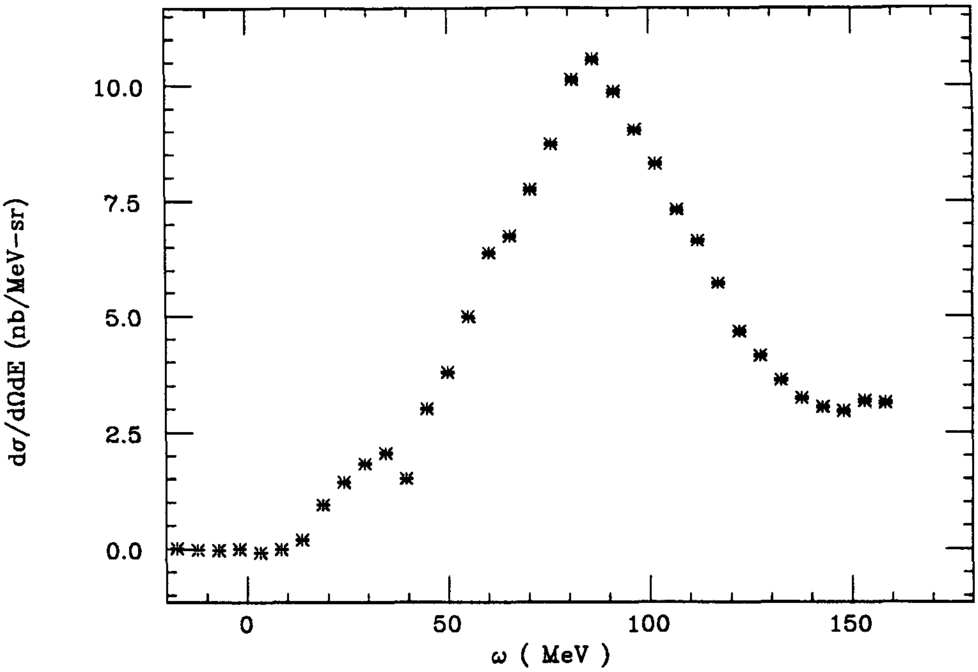

Figure 5.11: BIGBITE differential cross section, corrected for empty target yield only. The error bars are statistical only.

final momentum and the position along the target at which an event originated are correlated for this spectrometer (see Figure 3.4), which leads to poor momentum resolution, it is difficult to compare the cross section directly with calculations and previous measurements. Therefore, a TURTLE Monte Carlo program is used to simulate the yield from an extended target in both the quasielastic and elastic regions at the geometry and kinematics relevant to this measurement. The quasielastic yield is modeled from previous experimental data [58], y-scaled to the kinematics of this experiment. The cross section is radiated using the procedure of Mo and Tsai [56]. The calculation assumes no low ω cutoff; it is not expected to be valid in the region of the two- and three-body breakup. Figure 5.12 shows the calculated quasielastic yield and the experimental yield corrected for empty target background. The yield plotted here differs from the differential cross section only in that the momentum dependence of the solid angle has not been removed. To compare to the

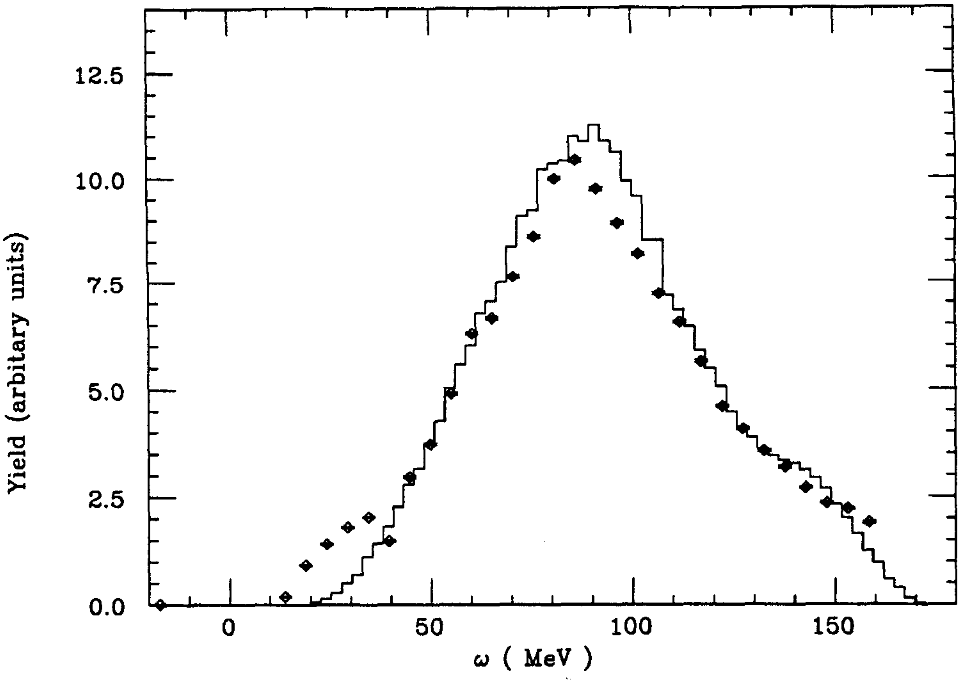

Figure 5.12: BIGBITE quasielastic yield, including radiative effects, calculated from a Monte Carlo routine. The diamonds are the experimentally measured data points. The calculation assumes no low ω cutoff.

data, the pion yield and the yield from the elastic radiative tail in the quasielastic region should also be included in the calculation. This is shown in Figure 5.13. The agreement is good, although the calculation slightly overestimates the yield. The histogram of the calculated yield is cut off on the low ω side of the quasielastic peak because the calculation of the elastic tail is not accurate near the center of the elastic peak.

The Monte Carlo calculation of the elastic yield assumes the ^{3}He charge and magnetic form factor parameterization of McCarthy, Sick, and Whitney [60]. Figure 5.14 shows the estimated elastic yield. The elastic peak is spread out over $\sim$ 35 MeV in ω, making a clean separation of the threshold and elastic events impossible. The yield excess in Figure 5.12 around $\sim$ 30 MeV is at a position corresponding to the elastic yield, according to the results of the Monte Carlo simulation of the elastic scattering events shown in Figure 5.14. One thing that should be noted is that the elastic yield generated by the program has

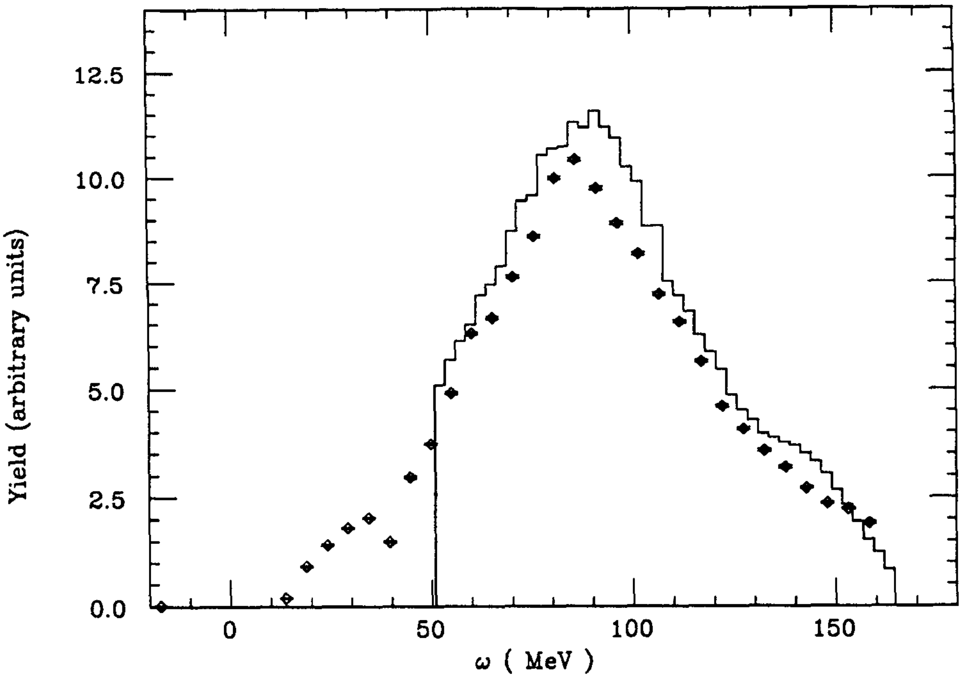

Figure 5.13: BIGBITE total yield, including the calculated quasielastic yield, pion production, and the elastic radiative tail. The diamonds are the experimentally measured data points. The quasielastic cross section was estimated from a Monte Carlo simulation of the spectrometer, assuming no low ω cutoff and including quasielastic radiative corrections. The histogram is terminated on the low ω side because of a lack of information about the elastic radiative tail near the center of the elastic peak.

not been radiated, primarily because of difficulties in matching the radiative tail to the radiatively corrected cross section at the elastic peak and because of the poor momentum resolution. The elastic radiative correction reduces the estimated peak cross section by ~25%, so the experimental yield is higher than predicted. There are several reasons why the yield in the region of the elastic peak may be overestimated. The poor momentum resolution of the spectrometer makes it impossible to separate the threshold strength from the elastic yield, so events from the two- and three-body threshold may be contributing in that region. Also, the elastic cross section changes rapidly with Q^2, so if the beam energy or the scattering angle differed from their assumed values, the elastic cross section could vary significantly. For example, a change of 1° in the scattering angle causes a change of

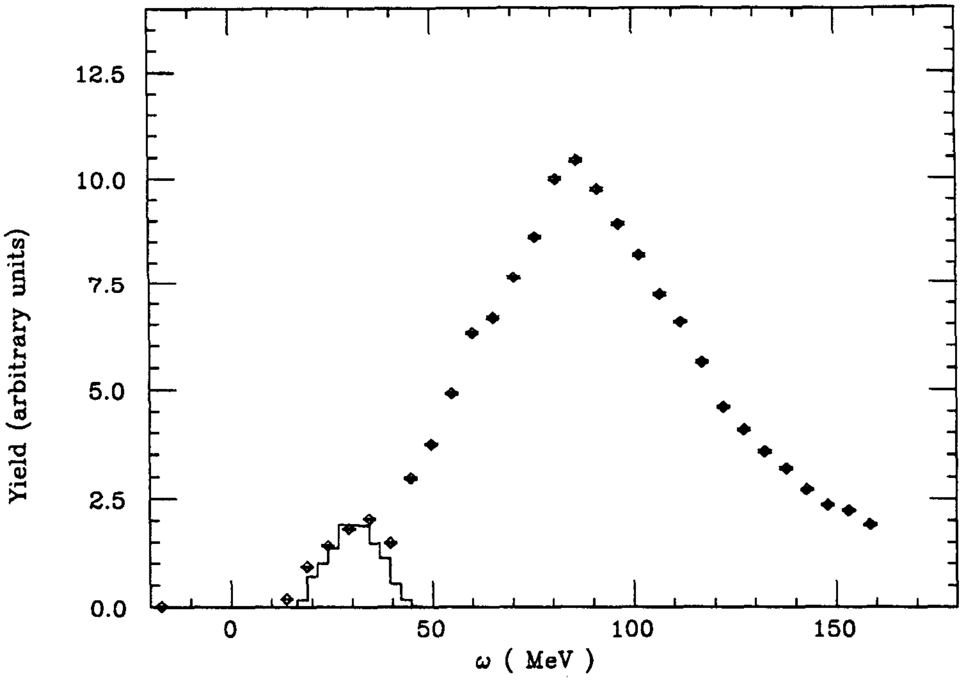

Figure 5.14: BIGBITE elastic yield calculated from a Monte Carlo routine. The diamonds are the experimentally measured data points. The calculation includes no radiative corrections.

~ 25% in the elastic cross section.

The fact that the quasielastic cross sections for both OHIPS and BIGBITE agree with the calculations, have much better statistics, and are not nearly as difficult to extract from the data lead us to conclude that the target density is accurately determined from the procedure used.

5.4 Calculation of the Experimental Asymmetry

The expression for the spin-dependent asymmetry defined in terms of the cross sections for the different helicity states of the beam, is

$$A = \frac{\left(\frac{d\sigma}{d\Omega}\right)_R - \left(\frac{d\sigma}{d\Omega}\right)_L}{\left(\frac{d\sigma}{d\Omega}\right)_R + \left(\frac{d\sigma}{d\Omega}\right)_L}. \tag{5.8}$$

This expression can be reduced by eliminating factors that do not depend upon the beam helicity. For example, the number of target nuclei is the same for either beam helicity, and since the two helicity states of the beam are at almost the same position within the target cell (see Section 5.5.5), the spectrometer solid angle does not depend upon the helicity. Also, the spectrometer efficiencies for electrons detected during beam pulses of different helicity are consistent within the statistical uncertainty of the efficiency measurement. Therefore, a simplified expression for the asymmetry in terms of measured quantities can be obtained. The expression for the charge-normalized raw asymmetry is

$$A_{raw} = \frac{(\frac{N_R}{c_R}) - (\frac{N_L}{c_L})}{(\frac{N_R}{c_R}) + (\frac{N_L}{c_L})}, \tag{5.9}$$

where

$N_{L(R)}$ = number of good events with left(right) helicity incident electrons

and

$c_{L(R)}$ = amount of left(right) helicity beam charge.

The asymmetry calculated from this expression is normalized to the charge in each helicity state of the beam, thereby eliminating false asymmetries arising from a helicity-correlated systematic variation in the beam charge. The expression is valid regardless of whether the events are summed over all or part of the momentum acceptance of the spectrometer.

The raw experimental asymmetry, which depends upon the target and beam polarization, is related to the physical asymmetry, A, which is normalized to unit polarizations, by

$$A_{raw} = P_t P_b A. \tag{5.10}$$

In order to compare the asymmetries of individual runs that may have different beam or target polarizations, the asymmetry of each run is normalized to 100% polarization for the target and the beam. The physical asymmetry is used in the discussions that follow. The beam polarization measurement is discussed in Section 3.2. More information about the target polarization is given in Section 5.4.2 below and in Chapter 4.

5.4.1 Energy Binning

For the purposes of obtaining the quasielastic asymmetry, energy cuts are imposed to limit the data to the region near the top of the quasielastic peak. This is trivial for the OHIPS data since the entire momentum acceptance of the spectrometer extends only $\left(\frac{\Delta p}{p_0}\right) \sim \pm 5\%$ around the maximum in the quasielastic peak. Therefore, for the OHIPS data the experimental asymmetry is calculated from the sum of all good events. No attempt is made to use finer energy bins because the statistical precision is sufficiently poor that useful information about the energy dependence of the quasielastic asymmetry cannot be obtained from the experimental data.

Unlike OHIPS, the BIGBITE spectrometer has a large momentum acceptance, so an energy cut of 58 MeV $\leq \omega \leq$ 161 MeV is used to restrict the events chosen for the asymmetry calculation to kinematics near the center of the quasielastic peak, at $\omega \sim 85$ MeV. The statistics are good enough for the asymmetry to be calculated for smaller energy bins so that the energy dependence of the quasielastic asymmetry results can be compared to theoretical predictions.

5.4.2 Target Spin Orientation and Polarization

The measurement of the target polarization is discussed in detail in Section 4.4; the measured values for the experimental runs are presented here. Over the course of the experiment the target spin direction, defined by β, the angle between the initial electron momentum and the target spin angle, was varied three times. Initially, the direction of the Helmholtz coils was set to optimize the measurement of G_M^n, using the OHIPS spectrometer, i.e., $\theta^* = 0°$ for electrons detected by OHIPS, but the fringe field from the spectrometers caused the $\vec{B}$ direction to rotate by $\sim 1°$, once the spectrometer magnets were powered up. After collecting several hundred microamp-hours of beam charge, with the accelerator reliability and beam quality very poor, the beam was turned off for approximately one week to work on the machine. During that time we rotated the spin direction a small amount to improve the sensitivity of the quasielastic data collected by the BIGBITE spectrometer to

Notation	β	OHIPS θ^*	OHIPS ϕ^*	BIGBITE θ^*	BIGBITE ϕ^*
L1	51.5° (l)	0.9°	0°	101.4°	0°
L2	44.5° (l)	7.9°	0°	108.4°	0°
R	135.5° (r)	172.1°	180°	78.6°	180°

Table 5.1: Target spin orientations. "l" and "r" refer to beam-left and beam-right directions, respectively. θ^* and ϕ^* define the angle between the target spin direction and the $\vec{q}$ direction for the quasielastic kinematics.

G_E^n. The direction was rotated by 7°, a change which, according to calculations based on the models discussed in Section 2.2.2, would have a small effect ($\frac{\Delta A}{A}$ ~6%) on the OHIPS asymmetry, yet would increase the contribution to the BIGBITE asymmetry from the term involving $R_{TL'}$ from 58% to 69%. After acquiring data at this orientation for a while, the spin direction was rotated by 180° to provide a rough check for systematic errors; the asymmetry sign should reverse when the target spin is reversed. The ^{3}He polarization reversal was verified by monitoring the polarization of a sealed cell of ^{3}He as the circular polarization of the optical pumping light was changed.

In the discussions that follow the asymmetry information is presented both for the full data set and for the different target spin directions. The notation used to designate the three data sets for the different target spin orientations are "L1", "L2" and "R." Table 5.1 contains a compilation of pertinent information about the target spin direction.

Figure 5.15 is a histogram of the target polarization for the ^{3}He asymmetry runs, weighted by the amount of charge in each run. The average polarization for the L1 data set is 26.6%, 22.0% for the L2 data set, and 21.5% for the R data set. The averages are calculated from the runs used to extract the quasielastic results. The polarization was much higher at the beginning of the experiment and before the asymmetry data acquisition began. For instance, polarizations in excess of 30% were maintained for ~ 100 hours in mid-February before usable beam was delivered. Unfortunately, the amount of beam delivered

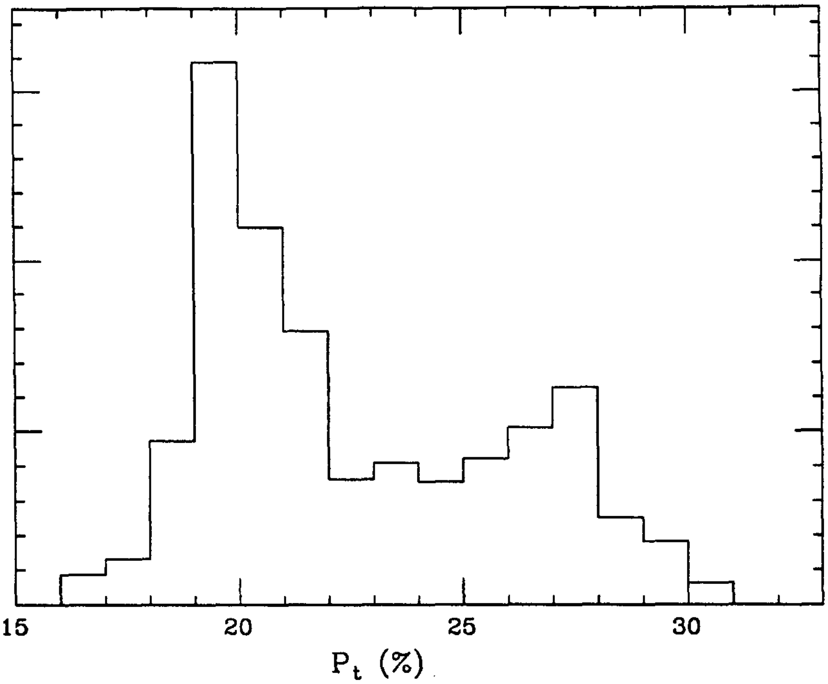

Figure 5.15: Histogram of the target polarization during the experiment. The histogram shows the average target polarization during the runs, weighted by the amount of beam charge in each run.

at the start of the experiment was much less than in the final days of running.

There are several factors that contributed to the decline in the target performance. Firstly, as discussed in Section 4.5.2, the nitrogen coating on the foil windows was slowly evaporated by the beam. When the cell was recoated with frozen nitrogen or when more nitrogen was added on top of the old layer, the target polarization improved markedly. For example, between runs 562 and 563, the cell was recoated with N_2, and the polarization rose from 11% to 28% with beam on target. Between runs 626 and 627 an additional layer of N_2 was added to the existing layer, and the polarization increased from 24% to 28%. Secondly, the spray from the beam during Møller runs probably caused contaminants to be released from the epoxy that was used to attach the entrance and exit windows to the target cell. In the pumping cell, the contaminants act to destroy the metastable atoms, decreasing the optical pumping efficiency. Although the target system was baked several times during the experiment, the system degraded with time because of repeated exposure to the beam spray. Once we realized the source of the problem, Møller measurements were limited to shorter running periods, usually less than an hour of beam on target, with the result that very rapid degradation of the polarization was prevented. Thirdly, the laser was exposed to an environment in the South Hall that was rather dusty because of the construction of the tunnel for the South Hall Ring, and the overall power output was reduced because of losses from imperfect surfaces. All of the problems mentioned above can be overcome. The target walls should be recoated with nitrogen every couple of days, possibly more often if electron currents of $\geq 40\mu$A are used. A better beam stop is needed for the Møller runs. Although precautions were taken to keep the laser clean, such as cleaning the optics thoroughly every couple of days and replacing the mirrors, more needs to be done. One possibility is to use a forced air system to blow dry nitrogen over the laser optics.

With regard to the target performance, we would like to note that the experiment was intended to run in only a few days. In fact, because of accelerator problems the experimental data were collected over a period of 35 days. In addition, the target was operating for over a month prior to that while waiting to obtain useful beam. Thus, the variation in the target polarization represents the performance over the course of a several-month period. This was the first time that the polarized target was operated continuously for an extended period of time, and much was learned about maintaining it in the environment of an electron accelerator during the experiment.

5.5 Corrections to the Experimental Asymmetry

The advantage of an asymmetry measurement over an absolute measurement of the cross section is that much of the dependence upon spectrometer and target properties are eliminated since the asymmetry is just a ratio of the spin-dependent part of the cross section to the spin-independent term. Thus, most uncertainties from the spectrometer acceptance and the target thickness are either significantly reduced or eliminated entirely. The disadvantage, however, is that not only does one have to correct for yield from sources other than the desired scattering process, but care must also be taken to avoid introducing false asymmetries into the measurement and to account for background asymmetries, corrections that one does not consider in standard cross section measurements. In general, the corrections to the asymmetry can be roughly split into two categories: those that arise from a dilution of the cross section from some sort of background and those that involve an asymmetry directly. Examples of the former type are the corrections for the empty target yield, the pion production, and the events from the elastic radiative tail under the quasielastic peak. These backgrounds are discussed in detail in Section 5.2. Basically the correction for these effects is a renormalization of the asymmetry:

$$A_{corrected} = f A_{exp}, \tag{5.11}$$

where f is the dilution factor for the cross section,

$$f \equiv \sigma_{total}/(\sigma_{total} - \sigma_{bkgrd}). \tag{5.12}$$

The latter type of correction involves the subtraction of an asymmetry from the experimental value to obtain the ^{3}He quasielastic asymmetry:

$$A_{corrected} = A_{exp} - \Delta A \tag{5.13}$$

Examples are the correction for the asymmetry of the events in the elastic tail and the quasielastic radiative correction.

The full expression used in this analysis to extract the ^{3}He quasielastic asymmetry from the experimental asymmetry is

$$\begin{aligned} A_{QE} = A_{exp} & \left(\frac{1}{1 - d_{empty} - d_{eltail} - d_{\pi}} \right) \\ & - A_{eltail} \left(\frac{d_{eltail}}{1 - d_{empty} - d_{eltail} - d_{\pi}} \right) \\ & - A_{\pi} \left(\frac{d_{\pi}}{1 - d_{empty} - d_{eltail} - d_{\pi}} \right) \\ & + \Delta A_{rad}, \end{aligned} \tag{5.14}$$

	ω limits (MeV)	A_{unpol} (%)	d_{empty}
BIGBITE	58 - 161	$+0.3 \pm 1.4$	0.15 ± 0.04
BIGBITE	11 - 37	-1.3 ± 5.2	0.21 ± 0.03
BIGBITE	11 - 32	-2.7 ± 6.2	0.25 ± 0.04
OHIPS	90 - 138	$+1.1 \pm 1.4$	0.096 ± 0.016

Table 5.2: Empty target dilution factors and the asymmetry for the net unpolarized data from each spectrometer.

where

$$d_{bkgrd} \equiv \frac{\sigma_{bkgrd}}{\sigma_{total}}. \tag{5.15}$$

The corrections to the BIGBITE asymmetry are applied on a bin-by-bin basis since the asymmetry is calculated in energy bins smaller than the full spectrometer acceptance. The OHIPS corrections are integrated over the spectrometer acceptance, as is the calculated asymmetry. In the sections that follow the terms in Equation 5.15 are discussed in detail.

5.5.1 Empty Target Correction

The empty target yield is discussed in Section 5.2.1. Table 5.2 contains the empty target dilution factors for different kinematic regions in the two spectrometers.

As can be seen from Equation 5.15 for the quasielastic asymmetry, the empty target background is assumed to have no inherent asymmetry. To check the validity of this claim, the data were examined for evidence of an asymmetry. Although the statistics on the empty target runs are sufficient to provide good information about the yield, the number of events collected is too small to provide significant information about a background asymmetry. Therefore, even though the asymmetries determined from the empty target data are consistent with zero, the statistical precision of the result is sufficiently poor that a different method of examination is warranted. One technique is the following. During the experiment the target spin direction was rotated by 180° when the sense of circular polarization of the incident optical pumping light from the laser was reversed. The optical

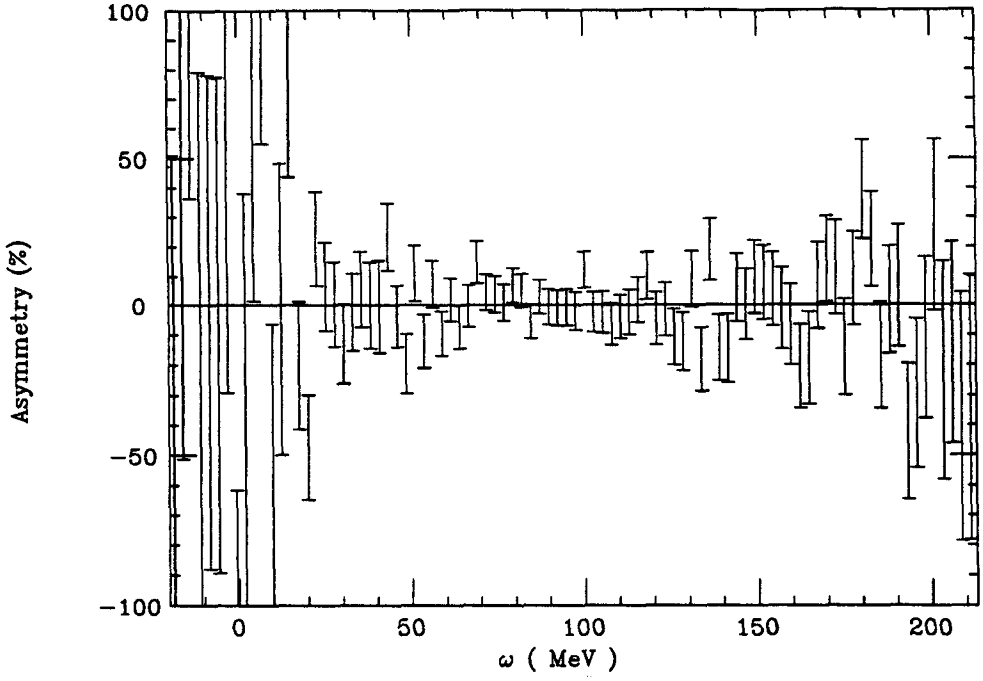

Figure 5.16: Asymmetry as a function of ω, for the full target runs summed in such a way as to yield net unpolarized data.

pumping light should affect only the polarization of the ^{3}He nuclei, so any background asymmetry would not reverse sign when this is done. Therefore, an inherent background asymmetry should show up in the experimental asymmetry for the full data set summed over the target spin orientations in such a way as to cancel the ^{3}He asymmetry. This is done using the BIGBITE asymmetry data. In Figure 5.16, it can be seen that $A_{unpol}(\omega)$ shows no evidence of an asymmetry. Table 5.2 gives the net asymmetry for the unpolarized spectrum summed between the ω limits in different energy ranges of the BIGBITE spectrometer. The net result for the OHIPS data is also listed in the table. In Section 5.5.5 a more detailed discussion of the search for a background asymmetry is presented.

5.5.2 Elastic Radiative Correction

The calculation of the elastic radiative tail is discussed in Section 5.2.2. To calculate the ratio, d_{eltail}, needed for the asymmetry correction, the measured cross section for the full target is used along with the calculated cross section in the radiative tail. For the OHIPS data, $d_{eltail} = 0.011 \pm 0.001$ and for the Bigbite energy region used for the quasielastic asymmetry analysis, $d_{eltail} = 0.039 \pm 0.004$.

In addition to the cross section dilution factor, the experimental asymmetry must be corrected for the asymmetry of the events in the elastic radiative tail. The elastic asymmetry can be expressed in terms of the charge and magnetic form factors for ^{3}He , F_c and F_m, as

$$A_{el} = \frac{\Delta}{\Sigma} = -\frac{2\tau\mu_A^2 v_{T'} \cos\theta^* F_m^2 + 2\sqrt{2\tau(1+\tau)}\mu_A Z v_{TL'} \sin\theta^* \cos\phi^* F_m F_c}{(1+\tau)Z^2 v_L F_c^2 + 2\tau\mu_A^2 v_T F_m^2} \tag{5.16}$$

where the form factors have been normalized to

$$F_c(Q^2 = 0) = F_m(Q^2 = 0) = 1. \tag{5.17}$$

In this formula Z is the nuclear charge, μ_A is defined in terms of the magnetic moment of ^{3}He as $(m_{\rm He}/m_n)\mu_{\rm He}$, and all other variables are defined in Chapter 2.

In general, if there is an asymmetry in the elastic peak, then there will also be an asymmetry in the radiative tail, although the value will be different from the peak value because of the spread in energies of the incident and scattered particles contributing to the tail. To calculate the asymmetry in the elastic radiative tail, first the elastic radiative tail cross section is calculated separately for the left and right helicity electrons using the full expression, including both spin-dependent and spin-independent terms for the elastic cross section in the calculation. Then the asymmetry is calculated in the normal manner:

$$A_{eltail} = \frac{\left(\frac{d^2\sigma}{d\Omega dE}\right)_{eltail_R} - \left(\frac{d^2\sigma}{d\Omega dE}\right)_{eltail_L}}{\left(\frac{d^2\sigma}{d\Omega dE}\right)_{eltail_R} + \left(\frac{d^2\sigma}{d\Omega dE}\right)_{eltail_L}}. \tag{5.18}$$

For the kinematics of the OHIPS measurement, the elastic asymmetry was substantially different for the two target spin directions, L1 and L2. (We omit R, for which the asymmetry just reverses sign from the value calculated for L2.) For $\beta = 51.5°$, $A_{el} = -3.9\%$, and

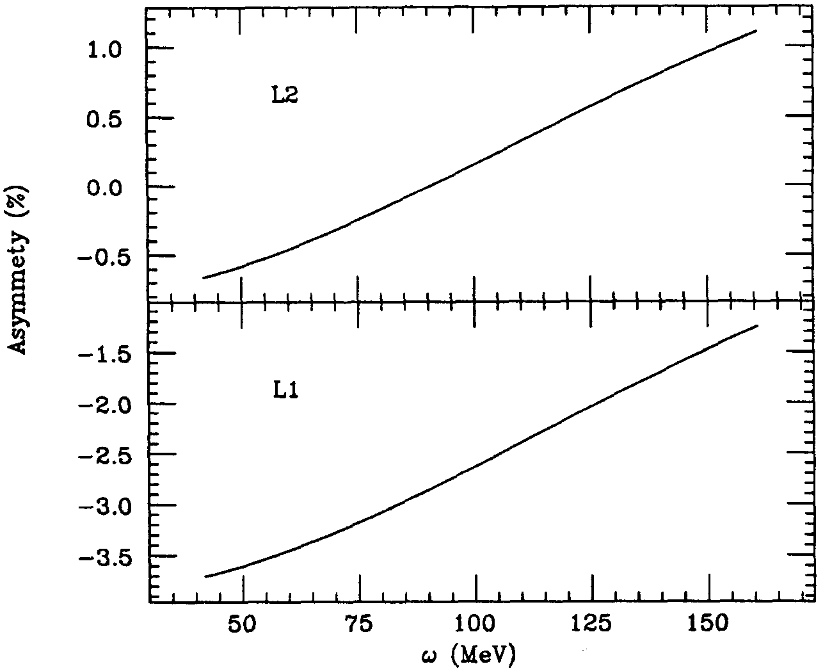

Figure 5.17: OHIPS asymmetry in the elastic radiative tail, shown for the target spin orientations L1 and L2. The asymmetry for the R spin orientation is the negative of the asymmetry for the L2 orientation.

for $\beta = 44.5^\circ$, $A_{el} = -0.7\%$. In both cases the elastic asymmetry is sufficiently small as to have a minimal impact on the extracted quasielastic asymmetry. For the sake of completeness, however, they are included in the analysis. Figure 5.17 shows the asymmetry in the elastic tail for the OHIPS kinematics. The average asymmetry, weighted by the cross section over the momentum acceptance of the spectrometer, is $A_{eltail} = -2.3\%$ for the L1 data set and $A_{eltail} = +0.4\%$ for the L2 data set. A 10% fractional uncertainty is assigned to the calculated asymmetry in the elastic radiative tail.

At the kinematics of the Bigbite measurement, the elastic asymmetry is not significantly different for the two target spin directions. In both cases $A_{el} \sim 18\%$, so the elastic radiative tail asymmetry is calculated for one orientation only. Figure 5.18 shows the asymmetry for the BIGBITE kinematics. A weighted average over the energy range used for the quasielastic analysis gives $A_{eltail} = 16.8\%$. As for the OHIPS data, a 10% frac-

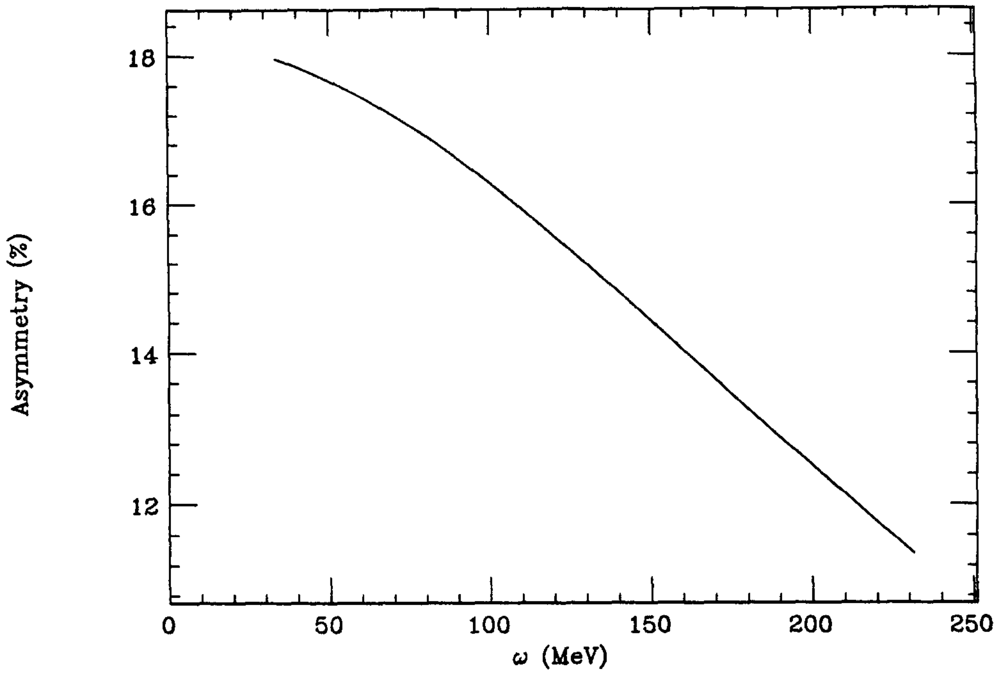

Figure 5.18: BIGBITE asymmetry in the elastic radiative tail, shown for the target spin orientations L1 and L2. The asymmetry for the R spin orientation is the negative of the plotted asymmetry.

tional uncertainty is assigned to the calculated asymmetry in the elastic radiative tail for BIGBITE.

5.5.3 Quasielastic Radiative Correction

Theoretical calculations of the helicity-dependent cross section for quasielastic scattering, from which the quasielastic asymmetry is obtained, assume single photon exchange in the scattering process. In practice, the measured cross section includes effects from higher order processes such as bremsstrahlung and energy straggling. Just as radiative corrections have to be applied to the measured cross section for comparision with theoretical calculations, so must the measured quasielastic asymmetry be corrected for radiative effects.

In the following expressions for the radiative correction to the quasielastic asymmetry we will use the shorthand notation, σ_{rad}, to denote the quasielastic cross section including radiative effects, and σ to denote the cross section, assuming single photon exchange. As usual, +(−) refers to right(left) helicity electrons. The calculated asymmetry to which we wish to compare the experimental results involves single photon exchange,

$$A = \frac{\sigma_+ - \sigma_-}{\sigma_+ + \sigma_-}, \tag{5.19}$$

and the quasielastic asymmetry including radiative effects is

$$A_{rad} = \frac{\sigma_{rad+} - \sigma_{rad-}}{\sigma_{rad+} + \sigma_{rad-}}. \tag{5.20}$$

We can write

$$A = \frac{R_+\sigma_{rad+} - R_-\sigma_{rad-}}{R_+\sigma_{rad+} + R_-\sigma_{rad-}}, \tag{5.21}$$

where

$$R_{+(-)} \equiv \frac{\sigma_{+(-)}}{\sigma_{rad+(-)}}. \tag{5.22}$$

In the limit where $A \ll 1$ and the radiative correction is small, the quasielastic asymmetry can be written as

$$A = A_{rad} + \Delta A_{rad}, \tag{5.23}$$

where the asymmetry correction is

$$\Delta A_{rad} \approx \frac{1}{2}\left(\frac{R_+ - R_-}{R_+}\right). \tag{5.24}$$

The correction factors, R_+ and R_-, are calculated using the procedure of Mo and Tsai [56] for inelastic scattering.

Figure 5.19 shows the results for the OHIPS kinematics. The difference between the results for the two spin directions, L1 and L2, is negligible. This is as expected since the asymmetry is insensitive to the small changes in Q^2 at kinematics where it is dominated by G_M^n. The correction, integrated over the energy acceptance of the spectrometer, is −0.08%. Sources of systematic uncertainty are the spin angle, scattering angle, beam energy, cross section and asymmetry. A fractional uncertainty of 36% is assigned to the quasielastic radiative correction for the OHIPS data.

The correction for the BIGBITE data depends strongly upon the target spin direction because the asymmetry varies quite a bit as a function of Q^2 at the kinematics sensitive to

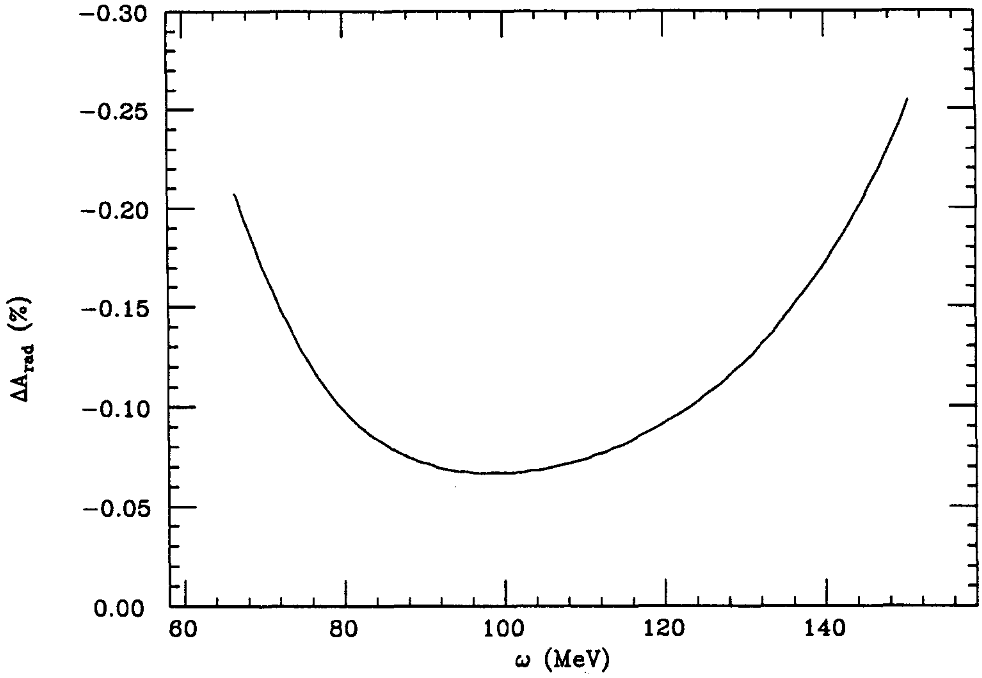

Figure 5.19: OHIPS quasielastic radiative correction to the asymmetry, shown for the target spin orientation L1 or L2. The asymmetry for the R spin orientation is the negative of the plotted asymmetry.

G_E^n. Figure 5.20 shows the correction factors for the target spin directions L1 and L2. The asymmetry correction is smaller for the target spin at the more forward angle where the asymmetry is smaller and more sensitive to G_E^n. In general terms, the correction is sensitive to θ^*, the angle between $\vec{q}$ and β. Because of the extended target geometry, the electron scattering angle varies by $\sim \pm 2.5°$ about the central angle of 44°, so a simple calculation does not account for the spread in θ^* of the events. Therefore, the Monte Carlo program that models the yield in BIGBITE is used to generate a correction factor appropriately smeared by the spectrometer acceptance and weighted by the yield. Figure 5.21 shows the results obtained with the simulation. A fractional uncertainty of 55% is assigned to the quasielastic radiative correction for the BIGBITE data. This correction is applied to the raw asymmetry data, binned by 1% in $\left(\frac{\Delta p}{p_0}\right)$.

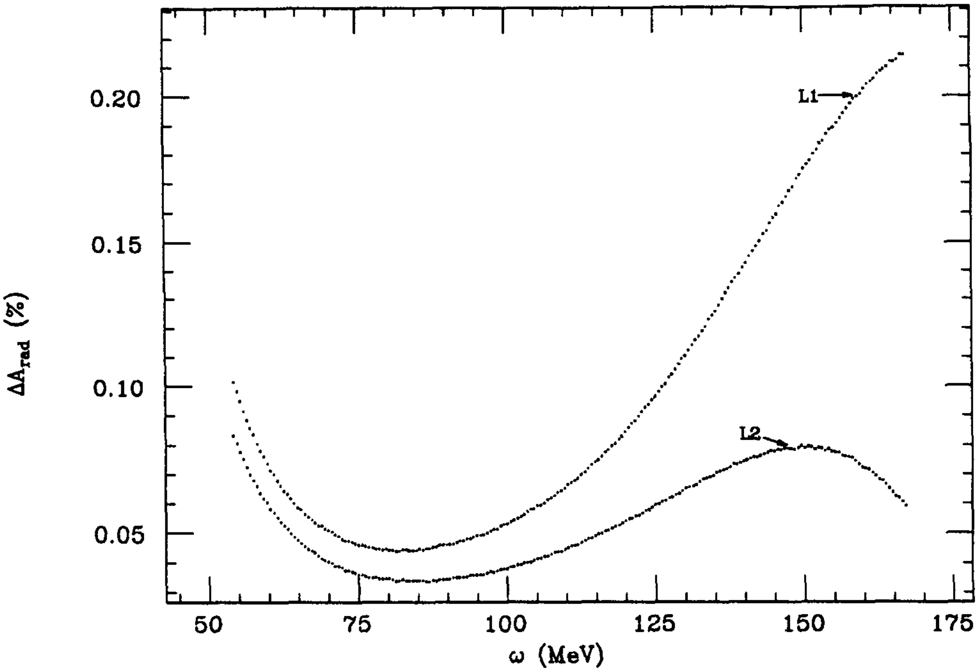

Figure 5.20: BIGBITE quasielastic radiative correction to the asymmetry calculated without taking into account the momentum resolution of the spectrometer. The correction is plotted for the target spin orientations L1 and L2. The asymmetry for the R spin orientation is the negative of the L2 value.

5.5.4 Pion Correction

The pion correction term involves both an asymmetry and a cross section dilution term. The calculation of the pion yield is described in Section 5.2.3; for OHIPS, $d_\pi = 1.1 \pm 1.1\%$ and for BIGBITE, $d_\pi = 2.2 \pm 2.2\%$. Although this process may exhibit a helicity-dependent asymmetry, no experimental data exist in this region. Therefore, the pion asymmetry is assumed to be zero in the extraction of the quasielastic asymmetry and a systematic uncertainty of ±10% in $\left(\frac{\Delta A}{A}\right)$ is included to reflect our lack of knowledge about its value.

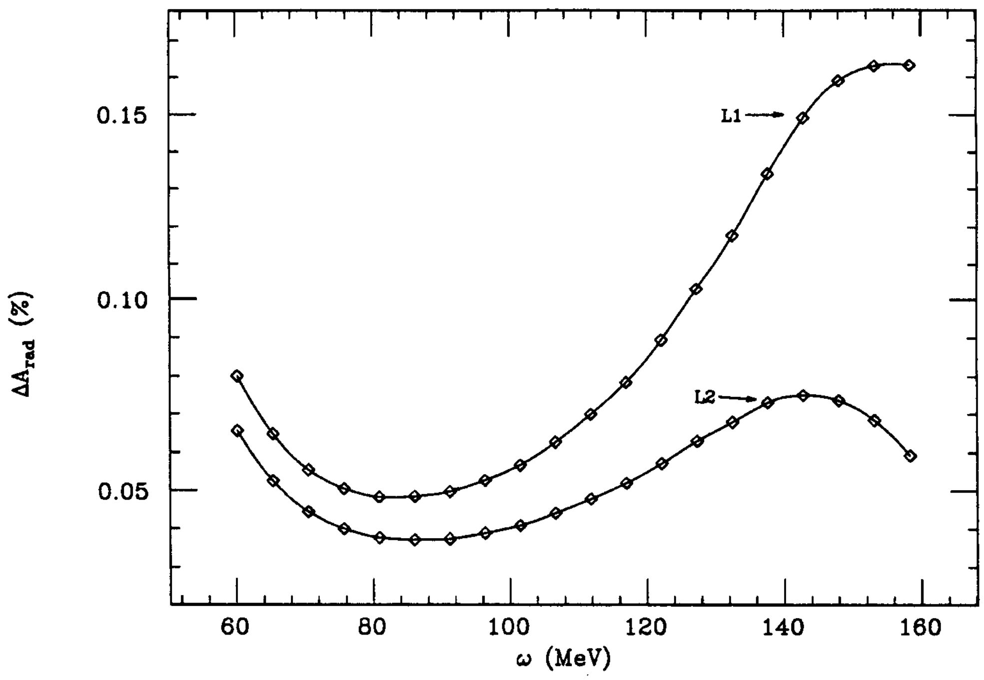

Figure 5.21: BIGBITE quasielastic radiative correction to the asymmetry including momentum smearing to account for the momentum resolution of the spectrometer. The correction is plotted for the target spin orientations L1 and L2. The asymmetry for the R spin orientation is the negative of the L2 value.

5.5.5 False Asymmetry Background from Helicity-correlated Beam Shifts

In extracting an asymmetry from experimental data, it is important to understand and account for false asymmetries. One source of false asymmetries is helicity-correlated variations in properties of the beam. In this section the size of the background false asymmetry from helicity-correlated variations in the beam properties is estimated. The two types of variations considered are a beam energy shift and a beam position shift. The contribution from the energy shift is discussed first, followed by a discussion of the false asymmetry from a helicity-correlated beam position shift. The discussion of the position shift includes the calculation of the helicity-correlated beam position shift from the beam position monitor data, an estimation of the background false asymmetry from the empty target rates, and a discussion of the impact of an induced false asymmetry from this source.

In the analysis that follows, the asymmetries quoted are the raw asymmetries corrected only for the empty target count rates and normalized to $P_t = P_b = 100\%$.

Helicity-correlated beam energy shift

False asymmetries can result when a shift in the beam energy correlated with the electron helicity gives rise to different count rates for the two helicity states because of the energy dependence of the cross section. The beam energy obtained from an accelerator varies slightly with the intensity of the beam pulse, a phenomenon known as beam loading. The loading is a machine-dependent characteristic, for the Bates machine $\frac{dE}{dI} \sim 2.3$ MeV/mA for single-pass beam and $\frac{dE}{dI} \sim 9.2$ MeV/mA for recirculated beam [61]. If beam pulses of different helicity carry slightly different amounts of charge, then the beam energy will be helicity-dependent and a false asymmetry can arise. To estimate the size of this effect, the charge difference

$$\Delta I = \left(\frac{\text{charge}}{\text{beam} - \text{burst}}\right)_R - \left(\frac{\text{charge}}{\text{beam} - \text{burst}}\right)_L \tag{5.25}$$

was calculated for all runs. The average difference is $\sim 1 \times 10^{-4}$ mA. The contribution from this effect is negligible; the estimated false asymmetry is approximately three orders of magnitude smaller than the measured asymmetry.

Helicity-correlated beam position shift

A helicity-correlated beam position shift can give rise to a false asymmetry if there is a position dependence to the background rates from the empty target. The procedure for estimating the magnitude of the false asymmetry from a beam position shift is the following. Firstly, the size of the helicity-correlated position shift is determined from the beam position monitor data for each run where information is available. Next, the false asymmetry arising from the position dependence of the empty target background rates is calculated from data taken with the target empty, where the beam position was varied about the central position used for the asymmetry measurements. This provides an estimate of the size of the false asymmetry expected, given the position shifts observed. Based upon the measured helicity-correlated beam position shifts, runs with large shifts are eliminated from the data set used to calculate the ^{3}He asymmetry. The experimental asymmetry is reported for the full data set and for the subset that excludes runs with large helicity-correlated shifts in the beam position. The systematic uncertainty in the ^{3}He asymmetry that is due to the false asymmetry is calculated. As an alternate technique for assessing the impact of the false asymmetry from the helicity-correlated beam position shift, in the last part of this section, an analysis is performed to look for a correlation between the experimental asymmetry during a particular run and the size of the helicity-correlated position shift observed during the run.

The helicity-correlated beam position shift is calculated using the beam x and y position information from the BIGBITE data set. The beam position was recorded in the event data stream for every BIGBITE trigger. However, the histograms used for this analysis are generated using only those events that satisfy the criteria that there be a single hit in every wire chamber plane. The beam position spectra generated from the good OHIPS events are qualitatively the same as for the BIGBITE data.

The beam position is specified in terms of the x and y directions; the x direction corresponds to beam right/left, the y direction to up/down. Data from the beam position monitor are histogrammed separately for the two beam helicity states and a relative shift between the peak centroids is calculated for each run. Although y position data are available for all runs, x position data is not available for the first nine data runs. In cases where only part of the peak is within the histogram limits, which are the ADC limits for the BPM signal, the beam position shift is calculated from the centroid difference of the available data.

The position shift, calculated in the number of channels in the histogram, is converted to a distance shift, using the data from the beam position monitor calibration done during the experiment. For the x direction the conversion factor is $+110$ channels/mm, and for the y direction the factor is -56 channels/mm. Centroid shifts are typically less than one

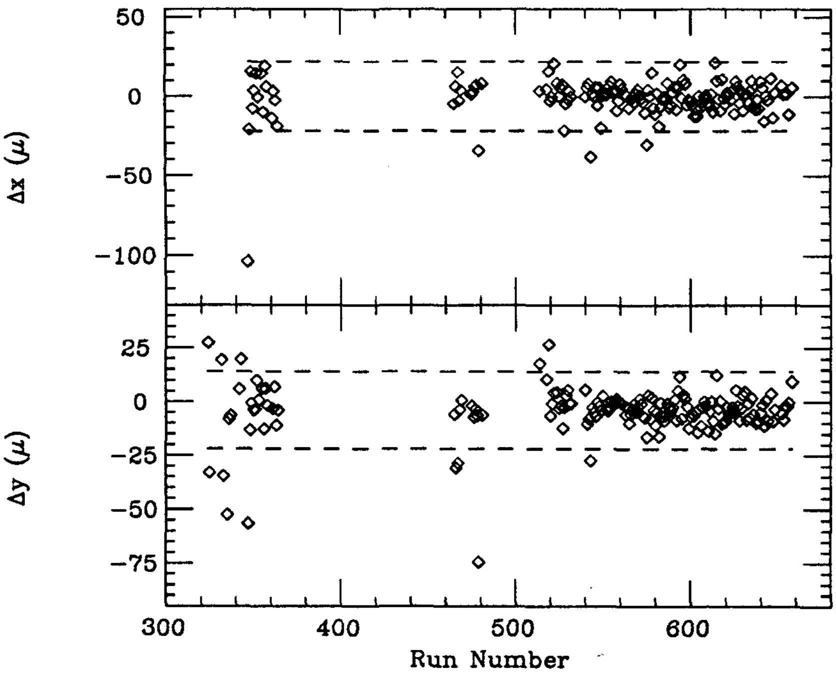

Figure 5.22: Helicity-correlated beam position shift, calculated from the beam position monitor information in the BIGBITE event data. y position information is available for all runs, but x information is unavailable for the first nine runs in the data set. The dashed lines correspond to two standard deviations from the average shifts: $\overline{\Delta x} = -0.8$ μm and $\overline{\Delta y} = -4.3$ μm.

channel. Figure 5.22 shows the x and y helicity-correlated position shifts for all available runs. The beam position monitor was not stable during the experiment, so the absolute position calculated from the BPM information cannot be trusted. However, the relative positions are valid because the drift occurred on a much longer timescale than the timescale for the helicity reversal.

Table 5.3 contains the average helicity-correlated beam shifts. The values are calculated using all asymmetry runs for which BPM data are available, with each run being given equal weighting. The shifts for three different target spin orientation data sets are also given. All Δx shifts are consistent with zero. This is not true for Δy, however; the helicity-correlated shift in the y direction of -3.9 ± 0.6 μm during the acquisition of the R data is

	Δl_{all} (μm)	Δl_{L1} (μm)	Δl_{L2} (μm)	Δl_R (μm)
X	-0.8 ± 1.0	-3.3 ± 4.5	0.9 ± 1.7	-0.8 ± 0.8
Y	-4.3 ± 0.9	-8.6 ± 3.5	-0.7 ± 1.4	-3.9 ± 0.6

Table 5.3: Average x and y helicity-correlated beam position shifts, in microns, calculated from the full set of asymmetry runs. The values are given averaged over all the runs in the data set and averaged over the subsets for the different target spin orientations.

more than 6σ from zero.

Intuitively, one would expect that an offset in the x direction could arise in the accelerator because that direction lies in the bending plane. In fact, there is some $x - y$ coupling in the magnetic optics of the machine, so an offset in the y direction can also be generated. However, the offset in the y direction is more likely to originate in the electron source, before injection into the linac. The most likely source of the helicity-correlated shift in the y direction is the Pockels cell in the source optics which is used to vary the circular polarization of the optical pumping light for the GaAs crystal. In addition to acting as a quarter-wave plate, the Pockels cell acts as a lens, so if the light incident on the cell is not exactly along the axis, the different helicity light beams will exit the cell at different angles. This translates into the electrons' being emitted from the GaAs crytal at slightly different positions for the two beam helicity states. This is a plausible source of the helicity-correlated position shift in the y direction. Reference [11] contains more details about this phenomenon.

Calculation of the false asymmetry from empty target runs

If the background count rate varies with beam position, as is likely because of asymmetries in the target system geometry, then a helicity-correlated shift in the beam position will give rise to a false asymmetry. Let $R(x, y)$ denote the empty target rate as a function of beam position. The false asymmetry can be expressed in terms of the left and right helicity beam positions as

$$A_{\text{false}} = \frac{R(x_R, y_R) - R(x_L, y_L)}{R(x_R, y_R) + R(x_L, y_L)}. \tag{5.26}$$

In order to calculate the expected contribution to the asymmetry, one needs an estimate of the variation of the empty target rate with beam position. Two sets of empty target runs were made during the experiment, one at the very start and another between the acquisition of the L1 and L2 data. The beam position was set visually using a BeO target upstream of the ^{3}He target. The cross section is calculated for each run using Equation 5.4. The number of target nuclei with the target empty and the solid angle do not vary from run to run, so in the discussion that follows, the relative rates calculated at the different beam positions do not include these factors.

The data for all empty target runs have been combined in the following analysis and the rates are calculated separately for the quasielastic region (58 MeV $\leq \omega \leq$ 161 MeV) and in the elastic-threshold region (11 MeV $\leq \omega \leq$ 37 MeV). Figure 5.23 is a graph of $R(x,y)$ for the two ω ranges considered. The quoted uncertainties in the rates reflect the statistics of the combined runs only. Systematic variations of 20-25% are typical for the empty target runs.

The rates are fit with linear or parabolic functional forms, depending upon the shape of the distribution. If one assumes that

$$R(x_L) = R(x_R) + \frac{dR}{dx}\Delta x + \frac{d^2R}{dx^2}\Delta x^2 + ..., \tag{5.27}$$

then the false asymmetry for a given rate distribution, $R(x)$ (or $R(y)$ for the y direction), and helicity-correlated beam position shift, Δx, can be written to second order as

$$A_{false} = \frac{d_{empty}}{P_t P_b}\left(\frac{(\frac{dR}{dx})\Delta x + (\frac{d^2R}{dx^2})\Delta x^2}{2R(0)}\right), \tag{5.28}$$

where d_{empty} is given in Table 5.2. The false asymmetry is normalized by the average target and beam polarizations since it is unaffected by the target and beam polarizations, yet the physical asymmetry used in the calculation for ^{3}He has been normalized to 100% polarization. In the case of the data shown in Figure 5.23, the second order terms are $\geq 10^3$ smaller than the first order terms, so they are ignored in the calculations that follow.

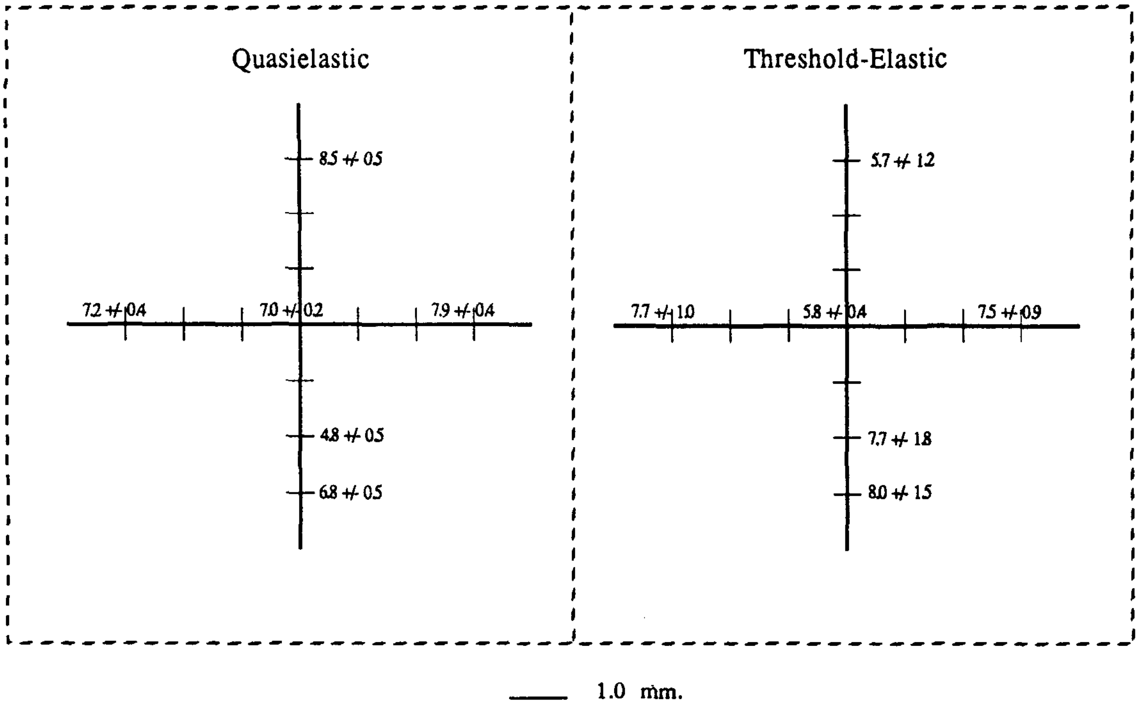

Figure 5.23: Relative background rates from the empty target as a function of beam position. The values are calculated from the BIGBITE data and are graphed for the quasielastic energy range, 58 MeV $\leq \omega \leq$ 161 MeV, and the threshold-elastic region, 11 MeV $\leq \omega \leq$ 37 MeV.

A parabolic fit is used to determine $R(x)$ for both ω regions. Figure 5.24 shows the calculated false asymmetry, A_x, for the two energy ranges. For 11 MeV $\leq \omega \leq$ 37 MeV the average value for the false asymmetry is

$$A_x = -6 \pm 8 \times 10^{-4}\ \%,$$

where the error bar reflects the scatter in the data about the mean divided by the square root of the number of runs in the sample. For the quasielastic region the calculated false asymmetry is

$$A_x = -1.1 \pm 1.4 \times 10^{-3}\ \%.$$

Both linear and parabolic fits are used to determine $R(y)$ in the threshold-elastic region, while only a linear fit is made to the rate data in the quasielastic region. The results are

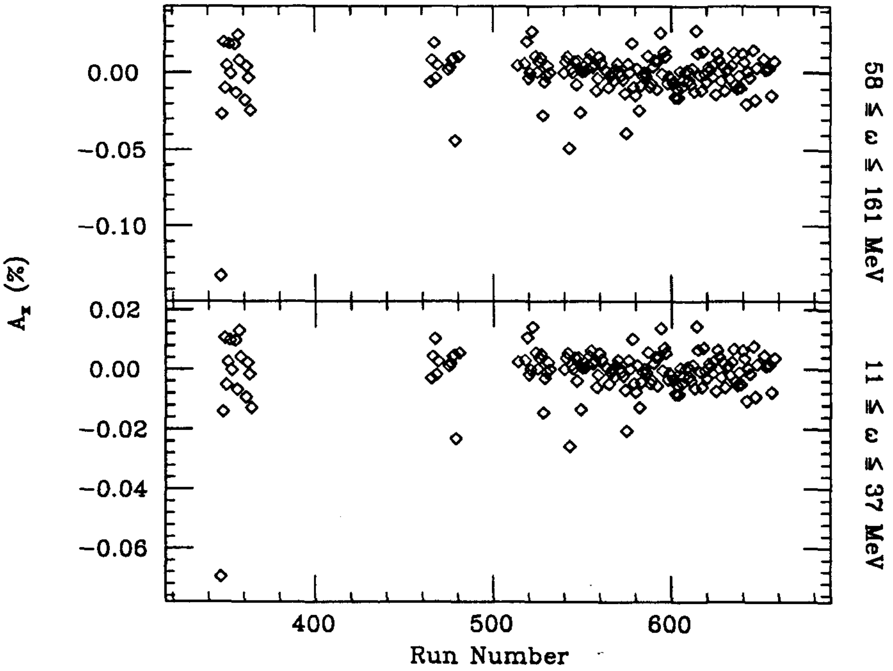

Figure 5.24: False asymmetry from the x helicity-correlated beam position shift, plotted for all asymmetry runs and for the two energy ranges, 11 MeV $\leq \omega \leq$ 37 MeV in the threshold-elastic region and 58 MeV $\leq \omega \leq$ 161 MeV in the quasielastic region.

shown in Figure 5.25. For the energy range in the threshold-elastic region the average false asymmetry is

$$A_y = 3.1 \pm 0.7 \times 10^{-2}\ \%.$$

In the quasielastic region the average is

$$A_y = -2.1 \pm 0.5 \times 10^{-2}\ \%.$$

Even though on the average the false asymmetry may contribute only a few percent uncertainty to the experimental value, since the measured asymmetry in the quasielastic region is only $\sim$ 0.3% without polarization normalization, one must take care to eliminate runs that may have a substantial false asymmetry contribution. The average asymmetries given above include all runs, even those with large helicity-correlated beam position shifts.

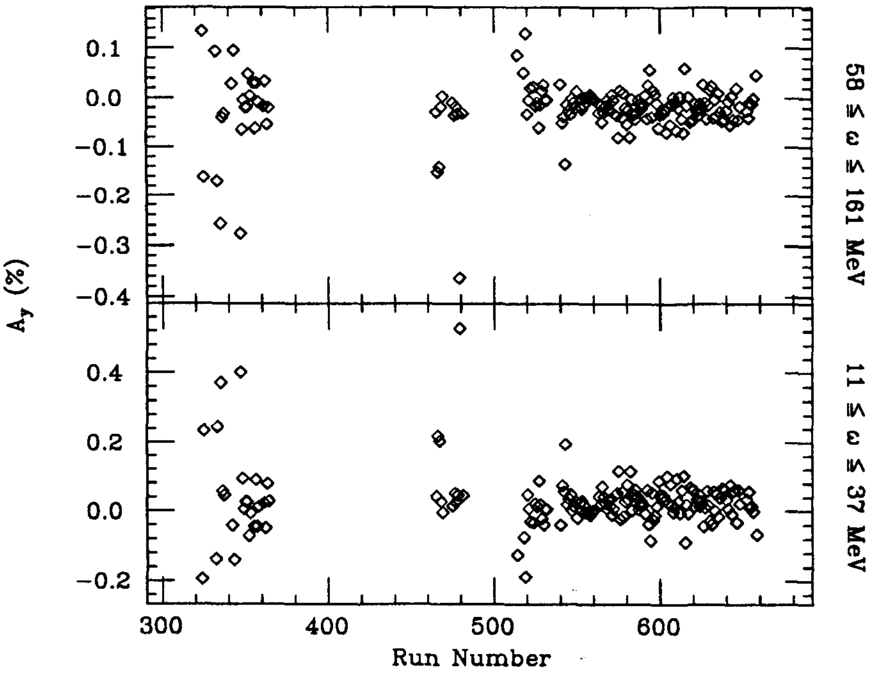

Figure 5.25: False asymmetry from the y helicity-correlated beam position shift, plotted for all asymmetry runs and for the two energy ranges, 11 MeV $\leq \omega \leq$ 37 MeV in the threshold-elastic region and 58 MeV $\leq \omega \leq$ 161 MeV in the quasielastic region.

Calculation of the asymmetry excluding runs with large helicity-correlated beam position shifts

To ensure that a false asymmetry is not introduced into the data from helicity-correlated shifts in the beam position, runs are eliminated from the data set used to calculate the ^{3}He asymmetry if they have helicity-correlated shifts in either the x or y direction more than 2σ from the average value for the entire data set, where σ is the standard deviation of the data. The same runs are excluded from both the BIGBITE and the OHIPS data sets. In general, the overlap of runs with large position shifts in the x direction with runs with large shifts in the y direction is quite high. The acceptance criteria are $-22\ \mu\text{m} \leq \Delta x \leq +22\ \mu\text{m}$ and -22μ m $\leq \Delta y \leq +14\ \mu\text{m}$. The dotted lines in Figure 5.22 demarcate the boundary between the runs included and excluded from the data set.

	Δl_{all} (μm)	Δl_{L1} (μm)	Δl_{L2} (μm)	Δl_R (μm)
X	0.3 ± 0.7	1.2 ± 2.2	1.5 ± 1.3	-0.4 ± 0.8
Y	-3.0 ± 0.6	-2.6 ± 1.2	-1.2 ± 0.8	-3.7 ± 0.6

Table 5.4: Average x and y helicity-correlated beam position shifts, in microns, calculated from the set of runs with shifts in both x and y directions within 2σ of the average. The values are given averaged over all the runs in the data set and averaged over the subsets of data for different target spin orientations.

In all, 5.5% of the data (80 μA-hr of charge) is excluded by this cut. The majority of the runs with large helicity-correlated beam position shifts occurred during acquisition of the L1 data. A total of 52 μA-hr of charge is eliminated from the L1 data set. This constitutes 19% of the total charge in the set. The other data sets lost 3.4% (L2) and 2% (R) of the charge in the full data set. Table 5.4 shows the average helicity-correlated beam position shifts calculated using the reduced data set. The scatter in the position shifts are reduced approximately a factor of two for the L1 data set by excluding the runs with large shifts.

It is now possible to estimate a systematic error associated with the helicity-correlated beam position shift from the values in Table 5.4 and the fits to $R(x,y)$, by following the procedure outlined above, which uses the empty target rate information to estimate the false asymmetry for a given position shift.

$$|A_{\text{false}}| \leq \pm 2.2 \times 10^{-2}\ \% \qquad 58\ \text{MeV} \leq \omega \leq 161\ \text{MeV}$$

$$|A_{\text{false}}| \leq \pm 1.5 \times 10^{-2}\ \% \qquad 11\ \text{MeV} \leq \omega \leq 37\ \text{MeV}$$

To assess the effect of the helicity-correlated beam position shifts upon the measured asymmetry, the BIGBITE asymmetry in both energy regions chosen for this analysis is calculated from the set of "good" position shift runs and compared to the values calculated from the set of all runs. Table 5.5 contains the experimental asymmetries for the different target spin orientations using the full data set, and Table 5.6 contains the asymmetries calculated from the set excluding those runs with large position shifts. The differences

ω limits (MeV)	A_{L1} (%)	A_{L2} (%)	A_R (%)	A_{all} (%)
11 - 37	$+37 \pm 10$	19 ± 11	-23 ± 7	25.5 ± 5.0
58 - 161	$+2.5 \pm 2.4$	$+3.0 \pm 2.5$	-2.1 ± 1.6	2.38 ± 1.18

Table 5.5: BIGBITE experimental asymmetry for the full data set, calculated for the different target spin orientations.

ω limits (MeV)	A_{L1} (%)	A_{L2} (%)	A_R (%)	A_{all} (%)
11 - 37	$+32 \pm 11$	19 ± 11	-24 ± 7	24.6 ± 5.2
58 - 161	$+3.7 \pm 2.6$	$+3.4 \pm 2.5$	-2.5 ± 1.6	2.97 ± 1.21

Table 5.6: BIGBITE experimental asymmetry for the data set excluding runs with large Δx or Δy, calculated for the different target spin orientations.

between the values for the two data sets are consistent within the statistical precision of the measurement. False asymmetries of the size estimated above present no problem for this experiment.

Search for correlations between the experimental asymmetry and the helicity-correlated beam position shift

Another technique can be used to estimate the impact of a false asymmetry arising from a helicity-correlated beam position shift. If the helicity-correlated position shifts were causing large asymmetries, then a scatter plot of A_{exp} vs. Δx or Δy could reveal the trend. Assume that the measured asymmetry is made up of two parts, one the asymmetry of the ^{3}He, A_{He}, and the other a false asymmetry proportional to the helicity-correlated position shift, $A_{false} = k\Delta x$. Although A_{He} reverses sign when the target spin orientation is reversed, the background asymmetry should not change sign. Therefore, a linear fit to A_{exp} vs. Δx and Δy (L1 and L2) and $-A_{exp}$ vs. Δx and Δy (R) can determine the correlation factor, k.

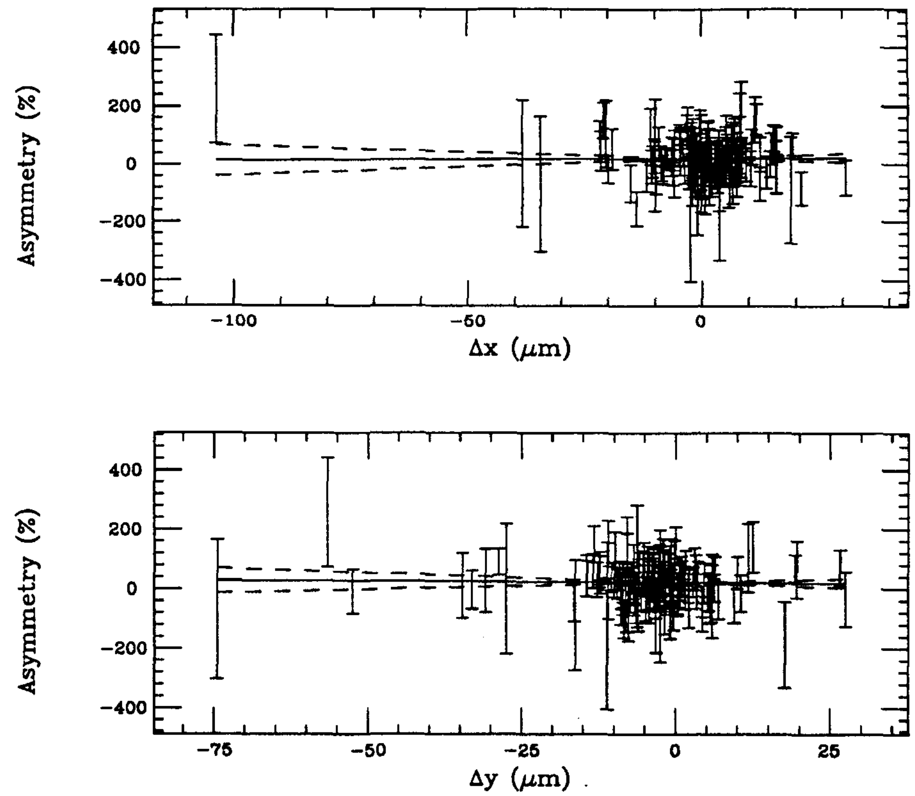

Figure 5.26: BIGBITE experimental asymmetry vs. Δx and Δy for the energy range 11 MeV $\leq \omega \leq$ 37 MeV in the threshold-elastic region.

Figures 5.26 and 5.27 display scatter plots for the two energy ranges, 11 MeV $\leq \omega \leq$ 37 MeV and 58 MeV $\leq \omega \leq$ 161 MeV. The solid lines are the best linear fits to the data weighted by the statistical error bars of the experimental asymmetries. The dashed lines show the uncertainty in the slope. No correlation can be distinguished within the statistical fluctuation of the sample. Table 5.7 contains the correlation factors and the false asymmetries calculated from the Δx and Δy values given in Table 5.3, assuming the linear correlation between the measured asymmetry and the helicity-correlated beam position shift. This method of estimating the magnitude of the contribution from a false asymmetry gives asymmetry results that are consistent with zero.

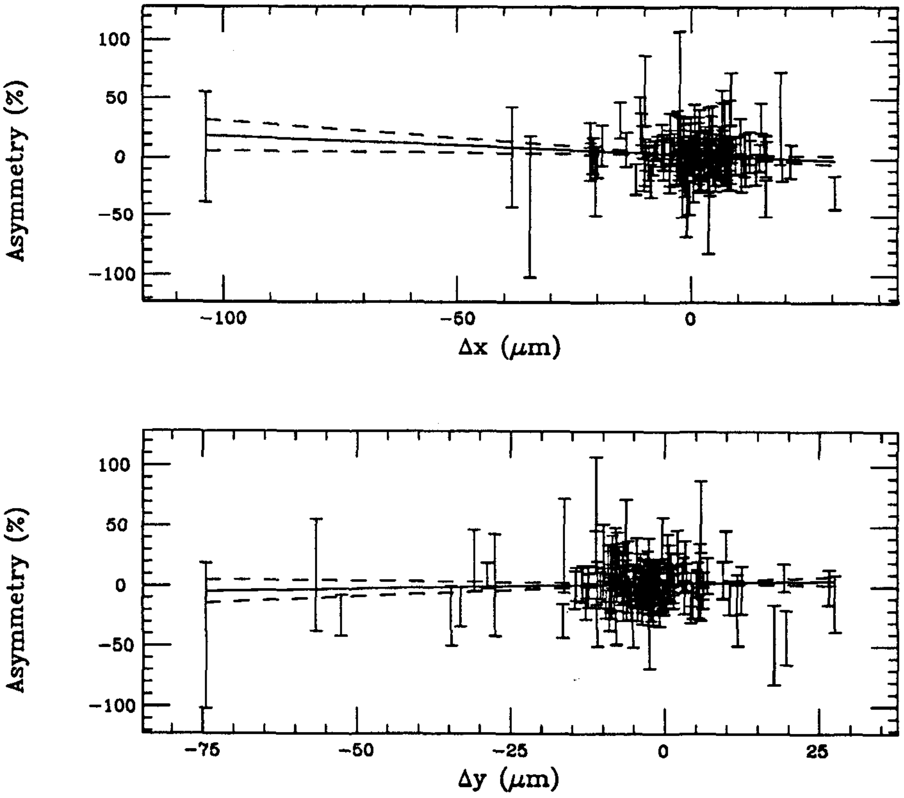

Figure 5.27: BIGBITE experimental asymmetry vs. Δx and Δy for the energy range 58 MeV $\leq \omega \leq$ 161 MeV in the quasielastic region.

δ limits (%)	$\frac{dA}{d(\Delta x)}$ $(\frac{\%}{\mu m})$	$\frac{dA}{d(\Delta y)}$ $(\frac{\%}{\mu m})$	A_x $(10^{-2}\%)$	A_y $(10^{-2}\%)$
$-20 - 0$	-0.15 ± 0.13	-0.09 ± 0.13	-4 ± 3	-27 ± 40
$4 - 9$	$+0.06 \pm 0.52$	-0.10 ± 0.55	$+30 \pm 165$	$+1.5 \pm 13$

Table 5.7: Results of the search for a linear correlation between the measured asymmetry and the helicity-correlated beam position shift.

Chapter 6

Results

Before proceeding with the discussion of the results, it should be mentioned that the analysis of the experimental data included no final state corrections or corrections for meson exchange effects. Since this was an inclusive measurement, the final state interactions are much less important than when a hadron is detected in the final state, and given the uncertainty on the measured asymmetry, this correction can be neglected. As for the meson exchange effects, the pion exchange contribution to the magnetic moment of ^{3}He is estimated to be $\sim 17\%$ [6]. However, as there is no theoretical calculation of the effect of meson exchange currents on the ^{3}He quasielastic asymmetry, meson exchange corrections are not applied to the data from this experiment.

In this chapter, the results of the spin-dependent quasielastic asymmetry measurements in OHIPS and BIGBITE are presented in Sections 6.1 and 6.2, respectively. Section 6.2 also contains a discussion of the asymmetry in the threshold-elastic region measured with BIGBITE. In Section 6.3, the results are compared with the predictions of the ^{3}He models of Blankleider and Woloshyn [4] and Friar *et al.* [6], introduced in Section 2.2.2. The extraction of G_E^n from the quasielastic asymmetry measured in BIGBITE, along with a comparison to previously measured values obtained from different experimental techniques, is discussed in Section 6.4.

6.1 OHIPS Asymmetry Results

A preliminary analysis of the OHIPS results has already been published elsewhere [62]; a more detailed analysis is given in this thesis. The difference between the values presented in the reference and those presented here reflects minor changes in the analysis.

The OHIPS asymmetry is calculated from the events within the energy acceptance of the spectrometer, 90 MeV $\leq \omega \leq$ 138 MeV, using Equation 5.15 which relates the experimental asymmetry to the quasielastic asymmetry. Table 6.1 shows the results for the data taken with different target spin orientations and for the sum of all the data. The results for the individual data sets are consistent, and the asymmetry changes sign between the "L" and "R" spin orientations, as one would expect when the direction of the nuclear spin is reversed.

Table 6.2 shows the individual contributions to the systematic uncertainty from the various sources of error. The dominant sources of uncertainty are the target and beam polarizations and the asymmetry in the pion background. The helicity-correlated variation in the detector efficiency is less than the uncertainty on the determination of the efficiency for events collected with different beam helicity states. The average efficiency difference for the ^{3}He asymmetry runs is used to estimate the systematic uncertainty.

6.2 BIGBITE Asymmetry Results

6.2.1 Quasielastic Asymmetry

The results of the BIGBITE quasielastic analysis has been published [63], with only small changes between the reported results and those presented here. The BIGBITE quasielastic asymmetry is calculated using Equation 5.15. The statistics of the BIGBITE measurement are sufficient for the asymmetry to be determined as a function of ω for comparison with theoretical predictions of the energy dependence of the quasielastic asymmetry. In general, the corrections to the asymmetry are energy-dependent also, so they are applied to the raw asymmetry data on a bin-by-bin basis. Figure 6.1 shows the asymmetry for 58 MeV $\leq$

	A_{QE} (%)	charge (μA-hr)	P_t (%)
L1:	-3.8 ± 3.0	239	26.6
L2:	-2.5 ± 2.9	333	22.0
R:	$+4.4 \pm 2.8$	808	21.5
combined:	$-3.79 \pm 1.37 \pm 0.67$	1381	22.5

Table 6.1: Results of the OHIPS asymmetry measurement for each of the target spin orientations and for the combined data set. The asymmetry error specified for the individual data sets are statistical only, while the two errors on the final result are statistical and systematic, respectively. The amount of charge in each set and the average target polarization for the ^{3}He runs are also indicated.

Systematic Uncertainty:	$\frac{\Delta A}{A}$
beam polarization:	0.105
target polarization:	0.100
pion asymmetry:	0.100
empty target subtraction:	0.018
pion subtraction:	0.012
helicity-correlated efficiency variations:	0.012
helicity-correlated beam shifts:	0.010
quasielastic radiative corrections:	0.008
elastic radiative corrections:	0.001

Table 6.2: Contributions to the systematic uncertainty in the OHIPS quasielastic asymmetry from the individual error sources.

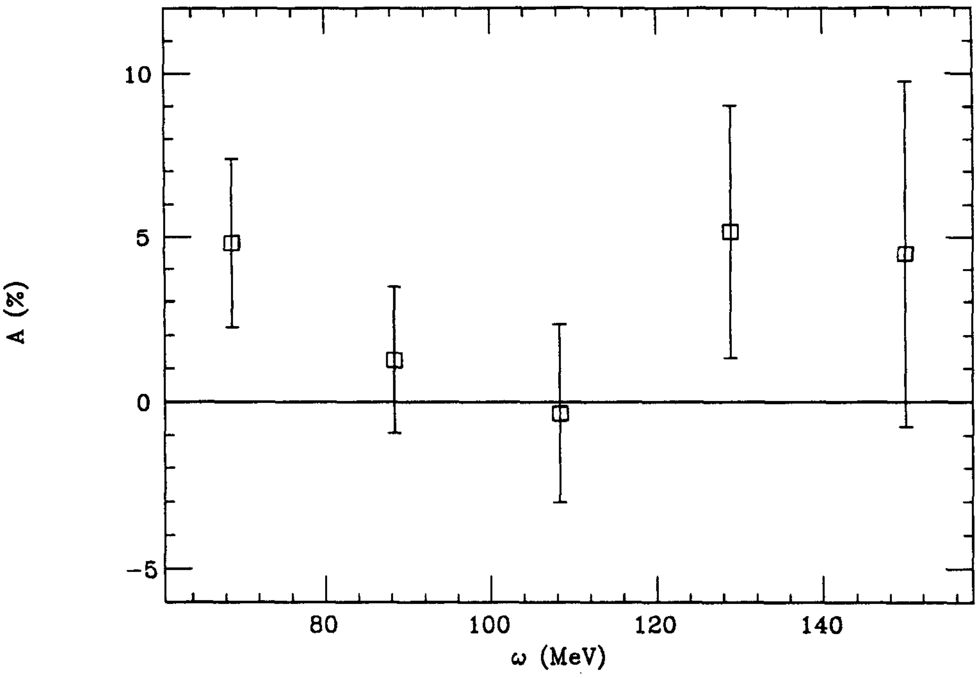

Figure 6.1: BIGBITE quasielastic asymmetry as a function of ω. All corrections have been made to the experimental values. The error bars reflect the statistical uncertainty. The systematic uncertainty, $\frac{\Delta A}{A} = 21\%$, is nearly independent of the energy transfer for this energy range.

$\omega \leq 161$ MeV, the region selected for the calculation of the quasielastic asymmetry. The error bars are the statistical uncertainties only. The values of the quasielastic asymmetry as a function of ω are tabulated in Table 6.3.

The asymmetry results, integrated across the quasielastic energy region, 58 MeV $\leq \omega \leq$ 161 MeV, are given in Table 6.4. They are separated into the results for the data taken at the different target spin orientations and for the full data set. The results are consistent for the data sets, and the asymmetry changed sign when the target spin direction was reversed. The individual contributions to the systematic uncertainty are shown in Table 6.5. The dominant sources of uncertainty are the target and beam polarizations and the asymmetry in the pion background. The systematic uncertainty from helicity-correlated variations in the efficiency is ±9%. For every run, the wire chamber efficiency is calculated from

ω	A_{QE}
68.8	4.8 ± 2.6
88.3	1.3 ± 2.2
108.3	-0.3 ± 2.7
128.9	5.2 ± 3.8
149.9	4.5 ± 5.3

Table 6.3: Tabulated values of the BIGBITE quasielastic asymmetry as a function of ω. All corrections have been made to the experimental values. The error bars reflect the statistical uncertainty. The systematic uncertainty, $\frac{\Delta A}{A} = 21\%$, is nearly independent of the energy transfer for this energy range.

events with a single hit in each plane for each beam helicity. The systematic uncertainty is calculated from the average efficiency difference between the detector efficiencies calculated using events of each beam helicity state. The results obtained this way for a number of runs spread throughout the experiment were checked against the helicity-correlated efficiency difference calculated with the expression from the wire chamber efficiency given in Section 5.3.2. Both calculations yield results consistent with zero. The helicity-correlated variation in the detector efficiency is less than the uncertainty on the determination of the efficiency. The average efficiency difference for the ^{3}He asymmetry runs is used to estimate the systematic uncertainty.

The raw asymmetries for the BIGBITE measurement are tabulated in Appendix E.

6.2.2 Asymmetry in the Threshold-Elastic Region

Since the momentum acceptance of BIGBITE is $\sim \pm 25\%$, quasielastic and elastic events were collected simultaneously. Because of the poor momentum resolution of the BIGBITE spectrometer ($3.5\% \frac{\Delta p}{p_0}$ FWHM), it is impossible to separate the events in the elastic peak, centered at $\omega \sim 30$ Mev, from events near the inelastic two- and three-body thresholds at 5.5 MeV and 7.7 MeV below the elastic peak, respectively. Nonetheless, the elastic asymmetry is estimated to be large ($\sim +18\%$), and the asymmetry in the threshold region may also be large. The threshold cross section and asymmetry are not known well enough

	A_{QE} (%)	charge (μA-hr)	P_t (%)
L1:	$+3.2 \pm 2.7$	228	26.6
L2:	$+2.9 \pm 2.7$	336	22.0
R:	-1.9 ± 1.7	808	21.5
combined:	$2.41 \pm 1.29 \pm 0.51$	1372	22.5

Table 6.4: Results of the BIGBITE quasielastic asymmetry measurement for each of the target spin orientations and for the combined data set. The uncertainty specified for the individual data sets is statistical only, while the two errors on the final result are statistical and systematic, respectively. The amount of charge in each set and the average target polarization for the asymmetry runs are also indicated.

Systematic Uncertainty:	$\frac{\Delta A}{A}$
beam polarization:	0.105
target polarization:	0.100
pion asymmetry:	0.100
helicity-correlated efficiency variations:	0.090
empty target subtraction:	0.050
elastic radiative corrections:	0.046
pion subtraction:	0.021
quasielastic radiative corrections:	0.012
helicity-correlated beam shifts:	0.010

Table 6.5: Contributions to the systematic uncertainty in the BIGBITE quasielastic asymmetry from the individual error sources.

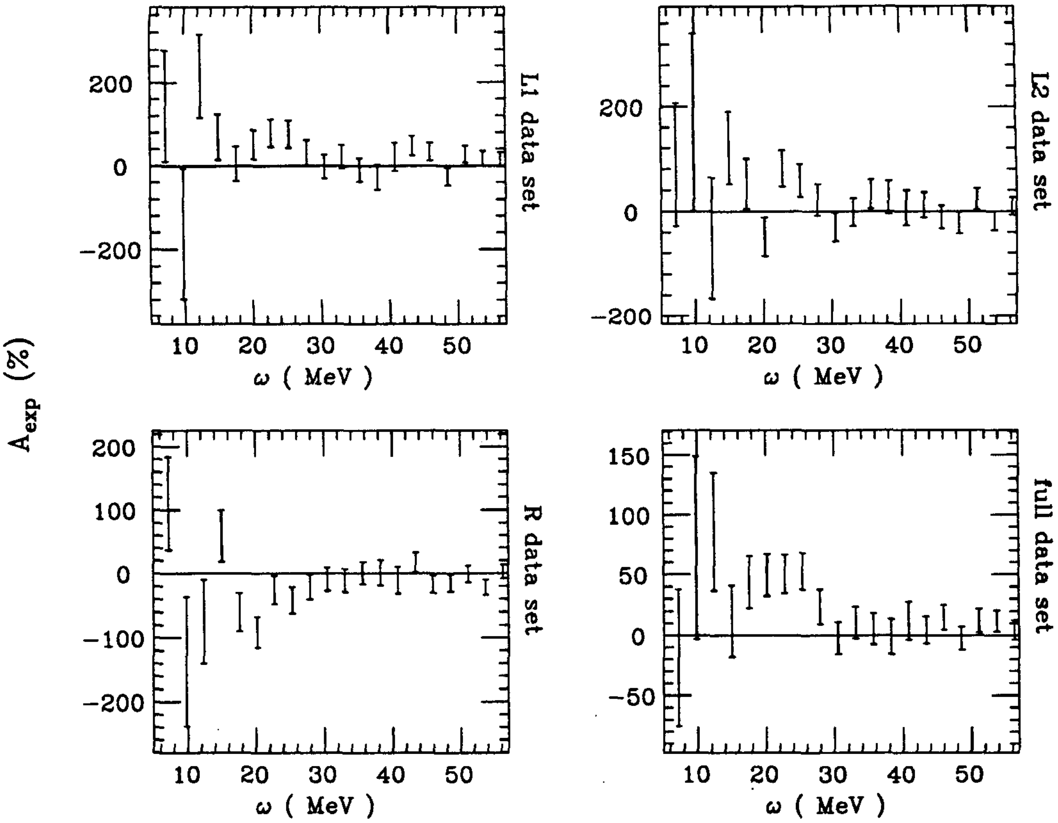

Figure 6.2: BIGBITE asymmetry, as a function of ω, in the threshold-elastic region. The asymmetry includes only empty target corrections. The error bars reflect the statistical uncertainty. The asymmetries are given for each spin orientation and for the full data set. The elastic peak is centered at $\omega = 30 \pm 5$ MeV, and has a FWHM of $\sim$ 35 MeV because of the spectrometer momentum resolution for an extended target.

to model the threshold region with sufficient accuracy to extract the elastic asymmetry from the experimental data.

Because the BIGBITE asymmetry at the quasielastic peak is roughly an order of magnitude smaller than the elastic asymmetry, it is useful to measure the asymmetry in the threshold-elastic region. The measurement can be used to verify that the target is polarized and to obtain an estimate of the product of the beam and target polarizations. In the case of this measurement, the spectrometer resolution was too poor and the elastic cross section too small for the elastic asymmetry to be useful as anything but a very crude polarization monitor.

The Monte Carlo estimate of the elastic yield is shown in Figure 5.14. The elastic

ω limits	A_{exp} [all] (%)	A_{exp} [L1] (%)	A_{exp} [L2] (%)	A_{exp} [R] (%)
11 MeV $\leq \omega \leq$ 37 MeV	$+24.6 \pm 5.2$	$+32.3 \pm 10.8$	$+19.1 \pm 10.9$	-23.7 ± 7.0
11 MeV $\leq \omega \leq$ 32 MeV	$+32.4 \pm 6.2$	$+43.9 \pm 12.9$	$+21.0 \pm 13.2$	-32.1 ± 8.4

Table 6.6: BIGBITE experimental asymmetry in the threshold-elastic region for different ω limits. The experimental asymmetry is corrected for the empty target background and normalized to $P_t = 100\%$ and $P_b = 100\%$. The integrated asymmetry is given for each of the target spin orientations and for the combined data set. The uncertainty is statistical only.

strength is centered at approximately $\omega = 30$ MeV, and is spread over ~ 35 MeV FWHM. Since the beam energy is determined to only ~ 1%, the elastic peak position is known to only 5 MeV. Figure 6.2 shows the experimental asymmetry, corrected for empty target background, in the threshold-elastic region. The plots show $A_{exp}(\omega)$ for the three different target spin orientations and for the full data set. The asymmetry changes sign between the "L" and "R" target spin directions, and is fairly large in this region. Table 6.6 shows the integrated experimental asymmetry with empty target corrections for different ω limits. The results are very sensitive to the selection of the energy limits. It is difficult to make quantitative statements about the results in this region, but the measured asymmetry has the expected sign and magnitude of the ^{3}He elastic asymmetry. Unfortunately, not much else can be concluded from the results in the threshold-elastic region.

The raw asymmetries for the threshold-elastic region are tabulated in Appendix E.

6.3 Comparison with ^{3}He Models

The predictions of two models of the ^{3}He quasielastic asymmetry, presented in Section 2.2.2, are compared to the experimental results. Both models suggest that the quasielastic asymmetry of ^{3}He is sensitive to the neutron form factors.

For the purposes of comparing the results to theory, previously determined parameterizations of the nucleon form factors are used. In Section 6.4 this requirement is relaxed and the quasielastic asymmetry measured with BIGBITE is used to obtain a best-fit value of G_E^n at $Q^2 = 0.16$ (GeV/c)^2 for comparison with previous measurements. Before presenting the predictions for the kinematics of this experiment, some of the assumptions of the calculations are discussed.

The computer code of Blankleider and Woloshyn is used to calculate the quasielastic asymmetry as a function of ω for the kinematics of the OHIPS and the BIGBITE measurement. The wave function used is discussed in Section 2.2.2 and in Reference [4]. The code uses the dipole form for the proton form factors and the neutron magnetic form factor,

$$G_E^p(Q^2) = \left(1 + \frac{Q^2}{0.71}\right)^{-2}, \tag{6.1}$$

$$G_M^p(Q^2) = \mu_p G_E^p, \tag{6.2}$$

$$G_M^n(Q^2) = \mu_n G_E^p, \tag{6.3}$$

where Q^2 is given in (GeV/c)^2 and the nucleon magnetic moments are

$$\mu_p = +2.793\,\mu_N, \tag{6.4}$$

$$\mu_n = -1.913\,\mu_N. \tag{6.5}$$

For the neutron electric form factor, the Galster parameterization [64] is used:

$$G_E^n(Q^2) = \frac{-\tau G_M^n}{1 + 5.6\tau}. \tag{6.6}$$

Equation 2.67, from the model of Friar *et al.*, gives the ^{3}He quasielastic asymmetry in terms of the free nucleon asymmetries. The calculation of the quasielastic asymmetry from this formula uses the Höhler [65] form factors for the proton form factors and for G_M^n, and the Galster parameterization for G_E^n. The deviation of the Höhler form factors from the dipole form is negligible at the kinematics of this experiment.

6.3.1 OHIPS

The quasielastic asymmetry measured with the OHIPS spectrometer is primarily sensitive to the transverse spin-dependent response function, $R_{T'}$, at $Q^2 = 0.20$ (GeV/c)^2. As Table 5.1 shows, $\theta^* \approx 0°$, so the contribution from the interference response function, $R_{TL'}$, should be negligible.

	A_{QE} (%)	$A_{(BW)}$ (%)	$A_{(F)}$ (%)
L1:	-3.8 ± 3.0	-4.7	-4.4
L2:	-2.5 ± 2.9	-4.5	-4.1
R:	$+4.4 \pm 1.8$	$+4.5$	$+4.1$
combined:	$-3.79 \pm 1.37 \pm 0.67$	-4.5	-4.2

Table 6.7: Calculated values of the OHIPS quasielastic asymmetry vs. experimental results for the different target spin orientations and for the full data set. The data are integrated over the range, 90 MeV $\leq \omega \leq$ 138 MeV. The predictions of the models of Blankleider and Woloshyn, $A_{(BW)}$, and of Friar *et al.*, $A_{(F)}$, are shown.

Blankleider and Woloshyn

Figure 6.3 shows the ω dependence of the quasielastic asymmetry at the kinematics of the OHIPS measurement, calculated within the model of Blankleider and Woloshyn. The contributions from the proton and neutron are indicated on the plot. The asymmetry is reasonably flat in the region within the spectrometer acceptance, 90 MeV $\leq \omega \leq$ 138 MeV, and the neutron contribution dominates in this region. The average asymmetry, weighted by the cross section, is given in Table 6.7 for each target spin orientation. The agreement with the experimental data is quite reasonable.

Friar *et al.*

The calculated ^{3}He asymmetry using the model of Friar *et al.* for each of the target spin orientations is shown in Table 6.7. The experimental data agree well with the calculation from this model.

Although the calculation of Friar *et al.* is less sophisticated than that of Blankleider and Woloshyn, because a large number of different nuclear models are used to determine the polarization of the nucleons within ^{3}He, it gives an indication of the uncertainty in the calculated asymmetry coming from nuclear structure effects. For the OHIPS measurement, the uncertainty given in Section 2.2.2 for the polarizations of the protons and neutrons

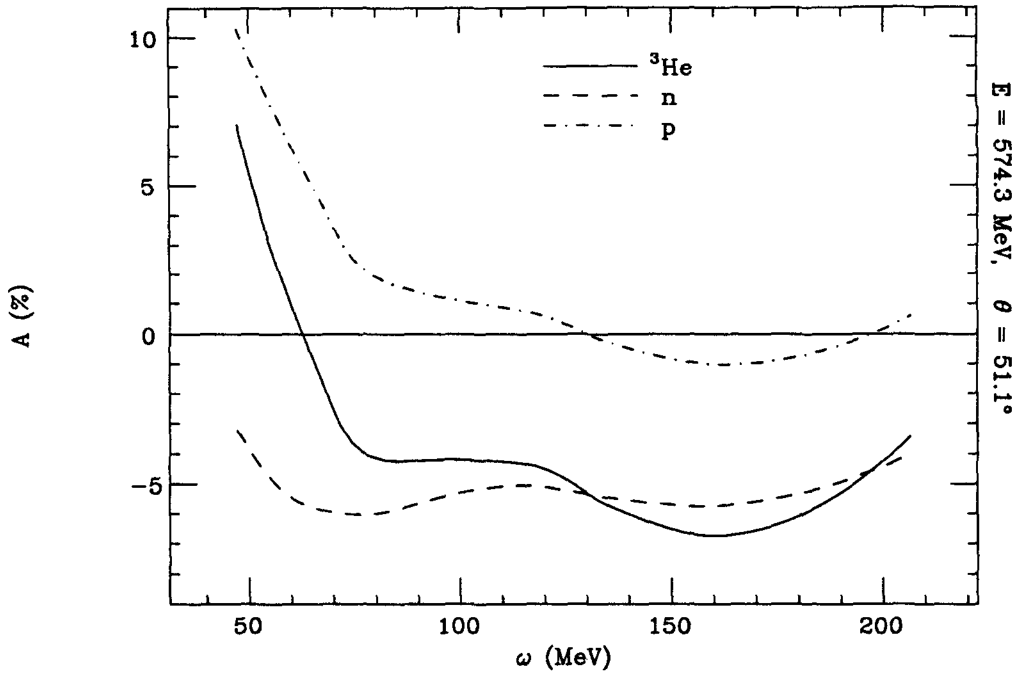

Figure 6.3: Calculated quasielastic asymmetry as a function of ω for OHIPS kinematics using the model of Blankleider and Woloshyn. The contributions from the protons and the neutron in ^{3}He are shown. The energy range, 90 MeV $\leq \omega \leq$ 138 MeV, is used to calculate the quasielastic asymmetry from the experimental data.

		$A_{G_M^2}$ (%)	$A_{G_E G_M}$ (%)
L1	^{3}He	−4.43	+0.030
	neutron	−5.20	+0.014
	proton	+0.76	+0.016
L2	^{3}He	−4.39	+0.26
	neutron	−5.15	+0.12
	proton	+0.75	+0.14

Table 6.8: Calculated OHIPS quasielastic asymmetry for L1 and L2 target spin orientations using the theoretical predictions of Friar *et al.*. The asymmetry is separated into contributions from each type of nucleon. The sensitivity to the transverse and interference terms are indicated. The results for the R data set are the negative of the L2 results.

within a sample of polarized ^{3}He indicates that the fractional uncertainty in the calculated asymmetry, $\frac{\Delta A}{A}$, which is due to nuclear structure effects is $\sim 4\%$.

The model of Friar *et al.* allows the ^{3}He quasielastic asymmetry to be easily separated into the contributions from each of the nucleon form factors. Equation 2.67 can be rewritten as

$$A_{He} = A_{G_M^2} + A_{G_E G_M} \tag{6.7}$$

$$= (1-2\delta)A_n - 2\delta' A_p \tag{6.8}$$

where $A_{G_M^2}$ ($A_{G_E G_M}$) contains contributions from the terms involving G_M^2 ($G_E G_M$) for both the proton and the neutron. Similarly, the contributions from the neutron and protons, $(1-2\delta)A_n$ and $-2\delta' A_p$, respectively, can be separated into transverse and interference parts. Using this model, for a particular set of experimental conditions, the influence of each nucleon form factor upon the spin-dependent ^{3}He asymmetry can be calculated quite simply. Table 6.8 shows the individual contributions for each of the target spin orientations. The dominant contribution is from the asymmetry term proportional to $(G_M^n)^2$.

6.3.2 BIGBITE

At the BIGBITE kinematics and spin angle, the quasielastic asymmetry is sensitive to G_E^n. Although the BIGBITE measurement depends primarily upon the interference response function, $R_{TL'}$, there is a nonnegligible contribution from $R_{T'}$. In fact, the contribution from $R_{T'}$ is predicted to be over a third of the total asymmetry. Furthermore, since the neutron electric form factor is relatively small for $Q^2 = 0.16(\mathrm{GeV/c})^2$ compared to the proton electric form factor, the contribution to the interference term from the proton is significant.

Blankleider and Woloshyn

Figure 6.4 shows the energy dependence of the quasielastic asymmetry at the kinematics of the BIGBITE measurement. The data points from this experiment, including all

	A_{QE} (%)	$A_{(BW)}$ (%)	$A_{(F)}$ (%)
L1:	$+3.2 \pm 2.7$	2.3	2.5
L2:	$+2.9 \pm 2.7$	1.9	2.1
R:	-1.9 ± 1.7	-1.9	-2.1
combined:	$2.41 \pm 1.29 \pm 0.51$	2.0	2.2

Table 6.9: Calculated values of the BIGBITE quasielastic asymmetry vs. experimental results for the different target spin orientations and for the full data set. The data are integrated over the energy range 58 MeV $\leq \omega \leq$ 161 MeV. The predictions of the models of Blankleider and Woloshyn, $A_{(BW)}$, and of Friar *et al.*, $A_{(F)}$, are shown.

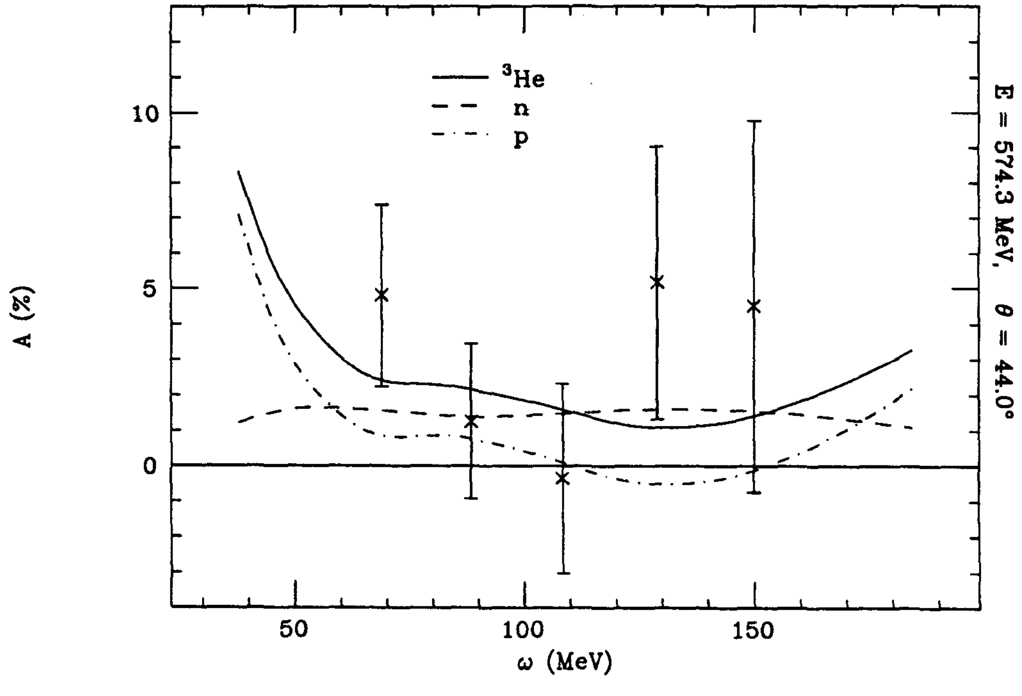

Figure 6.4: Calculated quasielastic asymmetry as a function of ω for BIGBITE kinematics, using the model of Blankleider and Woloshyn. The contributions from the protons and the neutron in ^{3}He are shown. The measured quasielastic asymmetries are shown for the energy range, 58 MeV $\leq \omega \leq$ 161 MeV. The error bars reflect the statistical uncertainty.

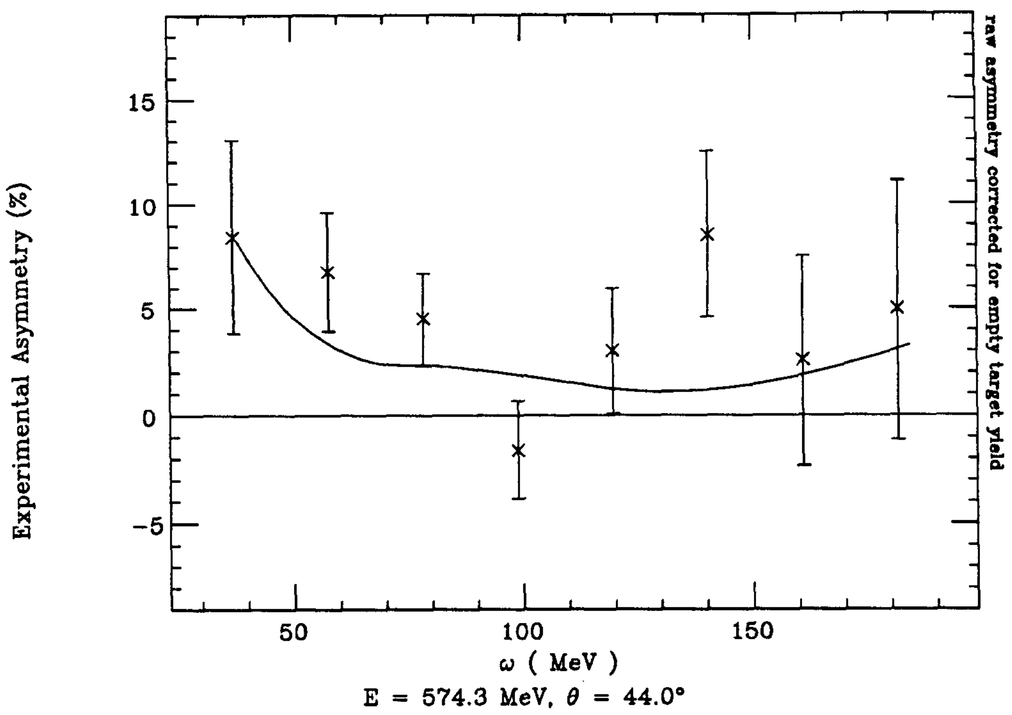

Figure 6.5: Comparison of the experimental asymmetry in the energy range, 47 MeV $\leq \omega \leq$ 213 MeV, with a calculation using the model of Blankleider and Woloshyn. The measured asymmetries are corrected for the empty target counts only. The graph shows the ^{3}He asymmetry across most of the quasielastic peak. The error bars are the statistical uncertainty.

corrections, are shown along with a calculation using the computer code of Blankleider and Woloshyn. The estimated contributions of the protons and neutron are indicated on the plot. The error bars on the data points include only the statistical uncertainty. The calculation indicates that the asymmetry is reasonably flat in the region used for the extraction of the quasielastic asymmetry and that although the neutron contribution dominates, the proton contributes significantly to the asymmetry. The average asymmetry for 58 MeV $\leq \omega \leq$ 161 MeV is given in Table 6.9 for each target spin orientation. The agreement with the experimental data is quite reasonable.

The contribution to the asymmetry from the D and S' states may be large in the tails of the quasielastic peak. The ω range used for the calculation of the quasielastic asymmetry

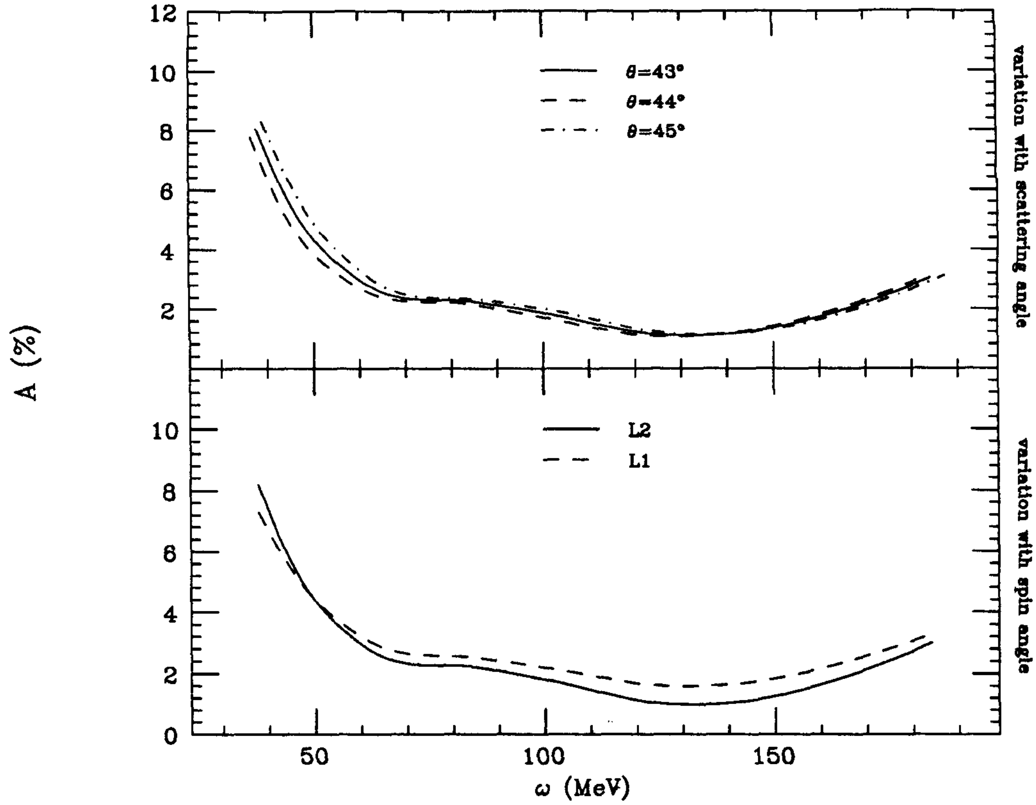

Figure 6.6: Calculated variation of the quasielastic asymmetry with scattering angle and spin angle at the kinematics of the BIGBITE measurement. The upper graph shows the variation with scattering angle. The lower graph indicates the variation with spin angle, and shows $A(\omega)$ for the two different spin directions used during the experiment.

was chosen to avoid large contributions from the tails. However, since it is useful to compare the energy dependence of the measured asymmetry to the prediction of Blankleider and Woloshyn over a larger range of energy transfer than is used for the extraction of the quasielastic asymmetry, the calculated $A(\omega)$ along with the experimental asymmetries for a large part of the quasielastic peak, calculated from the raw asymmetry and corrected only for the empty target background, is shown in Figure 6.5. The experimental asymmetries plotted are each averaged over 21 MeV in ω.

The Blankleider and Woloshyn calculation can be used to check the sensitivity of the ^{3}He asymmetry to variations in the scattering angle and the target spin direction. Figure 6.6 shows the calculated $A(\omega)$ for the two different spin directions chosen during the experiment and for different electron scattering angles. The dependence on the spin

		$A_{G_M^2}$ (%)	$A_{G_E G_M}$ (%)
L1	^{3}He	1.04	1.43
	neutron	1.21	0.60
	proton	-0.18	0.83
L2	^{3}He	0.65	1.48
	neutron	0.76	0.62
	proton	-0.11	0.85

Table 6.10: Calculated BIGBITE quasielastic asymmetry for L1 and L2 target spin orientations using the theoretical predictions of Friar *et al.*. The asymmetry is separated into contributions from each type of nucleon. The sensitivity to the transverse and interference terms are indicated. The results for the R data set are the negative of the L2 results.

and scattering angle is relatively weak and does not pose a problem for the experimental measurement reported here.

Friar *et al.*

The ^{3}He asymmetry for each of the target spin orientations in the energy range, 58 MeV $\leq \omega \leq$ 161 MeV, calculated using the model of Friar *et al.*, is shown in Table 6.9. The experimental data agree well with the calculation. The model of Friar *et al.* can be used to estimate the uncertainty that is due to nuclear structure effects in the calculated ^{3}He quasielastic asymmetry. If we assume the uncertainties on the S' and D states, reflected in the uncertainties quoted for the values of δ and δ', then the fractional uncertainty in the calculated asymmetry, $\frac{\Delta A}{A}$, coming from nuclear structure effects is 13% for the BIGBITE asymmetry.

Table 6.10 shows the individual contributions of the neutron and protons, calculated for each of the target spin orientations. The contributions from the transverse and interference terms in the asymmetry are also shown. The model predicts that the quasielastic ^{3}He asymmetry is dominated by the interference term. However, at these spin orientations, the contribution from the transverse term is substantial and cannot be ignored. Also, according to this model, the proton contribution to the interference term is larger than the neutron contribution for this value of Q^2. Clearly, an experiment designed to make a high-precision measurement of G_E^n, using this experimental technique, should optimize the sensitivity to G_E^n by orienting the nuclear spin perpendicular to the 3-momentum transfer. Also, at higher Q^2, the contribution from the neutron to the interference term should become more significant, according to current models of the neutron electric form factor.

6.4 Determination of G_E^n

6.4.1 Extraction of G_E^n from the Quasielastic Asymmetry

The best-fit value of G_E^n is obtained from the BIGBITE quasielastic asymmetry using the computer code of Blankleider and Woloshyn to model the contribution from the neutron for different values of the neutron electric form factor. The integrated quasielastic asymmetry, averaged over the values for the different spin orientations weighted by the amount of beam charge collected during each data set, is calculated for different values of G_E^n. The results are shown in Figure 6.7. A linear fit to the calculated points gives

$$G_E^n \; = \; -0.119 \; + \; (0.0791) \, A_{BW}. \tag{6.9}$$

For our results, this corresponds to

$$G_E^n(Q^2 = 0.16(\mathrm{GeV/c})^2) = +0.072 \pm 0.102 \pm 0.040, \tag{6.10}$$

where the error bars correspond to the statistical and systematic uncertainties of the measured asymmetry. The experimental data, along with the asymmetry calculated with the best-fit value of G_E^n, is shown in Figure 6.8.

The model of Friar *et al.* gives a value of 0.067 for G_E^n. The estimated systematic uncertainty associated with the nuclear structure effects for the extraction of G_E^n from the quasielastic asymmetry data is 13%. Although it has been suggested that the neutron electric form factor is modified within the nuclear medium [66], with the measured form

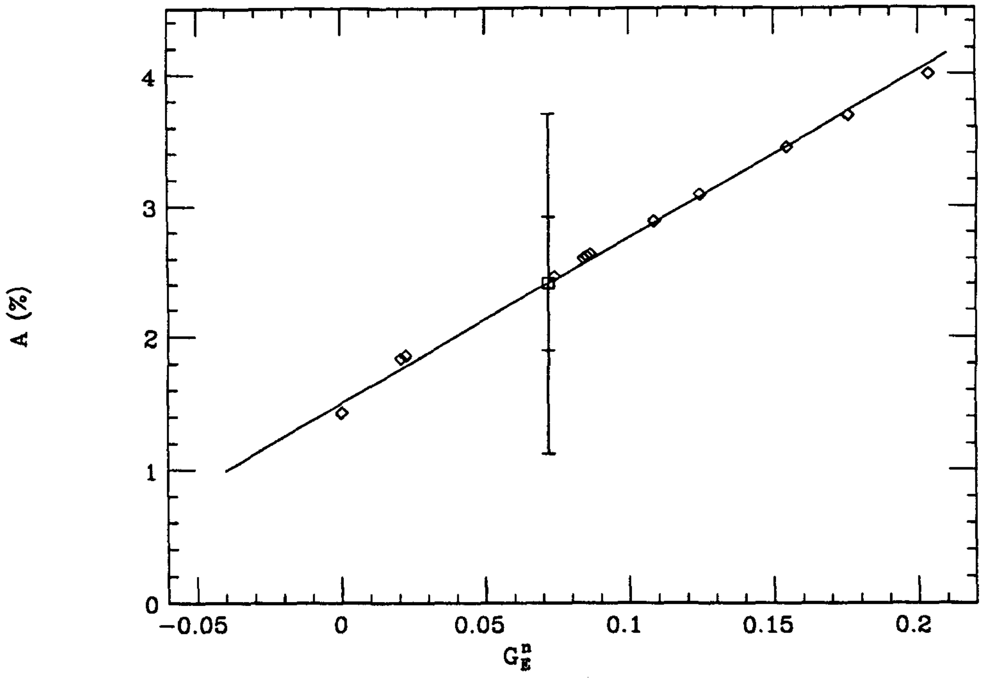

Figure 6.7: Calculation of the quasielastic asymmetry for the BIGBITE kinematics for different values of G_E^n using the computer code of Blankleider and Woloshyn. The calculated asymmetry is integrated over 58 MeV $\leq \omega \leq$ 161 MeV, weighted by the cross section. The solid line is the best linear fit to the calculated values. The data point is the measured quasielastic asymmetry with statistical (larger) and systematic error bars.

factor reduced over its free nucleon value, for $Q^2 \leq 0.4$ (GeV/c)^2, the effect is predicted to be negligible.

6.4.2 Comparison with Previous Measurements

Measurements of the electromagnetic form factors of the nucleons have been pursued for a number of years. Studies of the neutron electric form factor have primarily used electron scattering from a deuterium target, although other options such as unpolarized scattering from tritium and ^{3}He have also been considered [67]. In fact, the slope of G_E^n at $Q^2 = 0$ was determined by measurements of the scattering amplitudes of slow neutrons

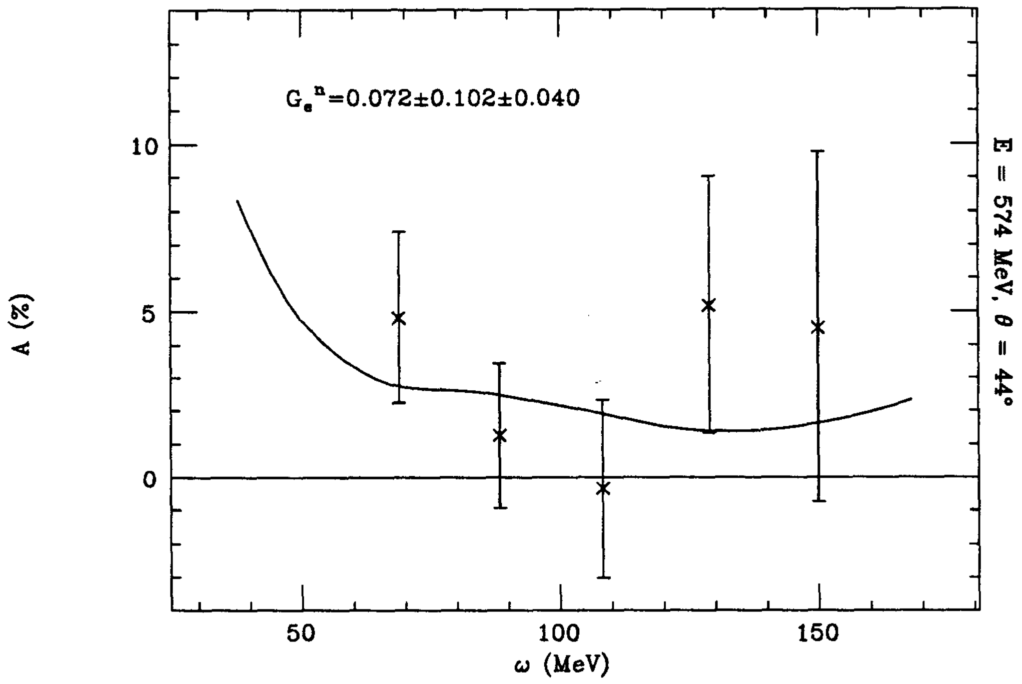

Figure 6.8: The quasielastic asymmetry as a function of ω for the BIGBITE kinematics calculated using the best-fit value of G_E^n, $G_E^n(Q^2 = 0.16(\mathrm{GeV/c})^2) = +0.072\pm0.102\pm0.040$. The measured data points with statistical error bars are shown.

from electrons [1]. The value,

$$\frac{dG_E^n(0)}{dQ^2} = 0.0199 \pm 0.0003\,\mathrm{fm}^2, \tag{6.11}$$

is our most accurate experimental information about G_E^n.

Our current information about the Q^2 dependence in the range relevant to this experiment comes primarily from electron-deuteron elastic scattering. Here, we consider the work of Galster *et al.* [64] and Platchkov *et al.* [68]. Both experiments measured the electric structure function, $A(Q^2)$, where the unpolarized scattering cross section involves two structure functions, A and B:

$$\frac{d\sigma}{d\Omega} = \sigma_{Mott}\left[A(Q^2) + \tan^2\frac{\theta}{2}B(Q^2)\right]. \tag{6.12}$$

Although the scattering cross section for this experiment is sensitive to G_E^n, the extraction of the value from the experimental data depends upon the wave function used for the deuteron. The fits to G_E^n obtained from the data of Galster *et al.* indicate that the nuclear structure uncertainty is approximately 100%. The broad range of Q^2 covered by the data of Galster *et al.* allows the values of G_E^n to be fit to an analytic expression. The best fit is obtained with the Feshbach-Lomon deuteron wave function and the one-parameter analytic expression, known as the Galster parameterization,

$$G_E^n(Q^2) = \frac{-\tau}{1+p\tau}G_M^n;\ p = 5.6. \tag{6.13}$$

It should be emphasized that the analytic form chosen for G_E^n is arbitrary and was picked to provide the best fit to the experimental data. A number of other functional forms have been suggested [65][69][70]. The Galster parameterization yields $G_E^n(Q^2 = 0.16(\mathrm{GeV/c})^2) = 0.046$.

The experiment of Platchkov *et al.* is similar to that of Galster *et al.*, but with improved systematic uncertainty. Figure 6.9 shows the extracted values of G_E^n from the experimental data using the Paris potential to calculate the deuteron wave function. The best fit was obtained using a two-parameter fit to the analytic expression

$$G_E^n(Q^2) = \frac{-a\tau G_M^n}{1+b\tau} \tag{6.14}$$

where the two fit parameters, a and b, are 1.25±0.13 and 18.3±3.4, respectively. This yields $G_E^n(Q^2 = 0.16(\mathrm{GeV/c})^2) = 0.040$. Figure 6.10 shows the model dependence of their result, using deuteron wave functions calculated from the Paris, Reid soft-core, Argonne V14, and Nijmegen potentials. For the Q^2 of this experiment ($4\ \mathrm{fm}^{-2}$), the nuclear structure uncertainty for the potentials shown is $\sim \pm 40\%$.

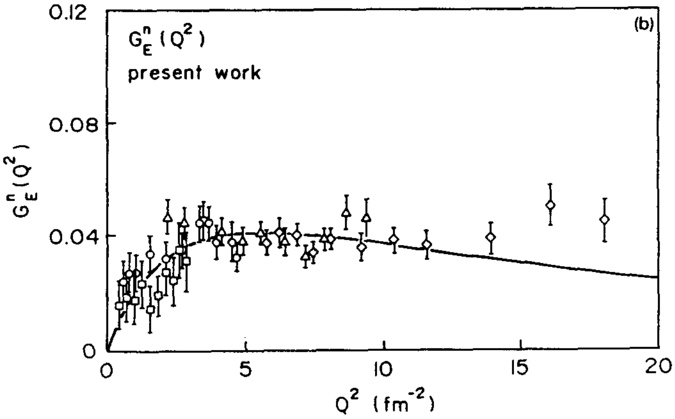

Figure 6.9: G_E^n from data of Platchkov *et al.*, extracted using the Paris potential for the deuteron wave function. The solid line is the best two-parameter fit to G_E^n. Taken from Reference [68].

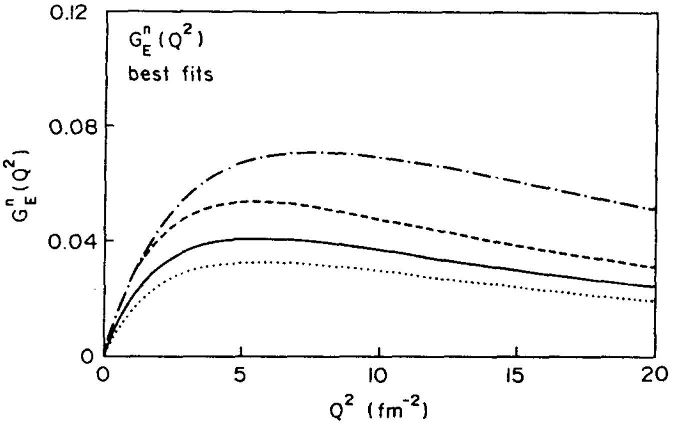

Figure 6.10: Model dependence of results of Platchkov *et al.* for best-fit values of G_E^n extracted from the experimental data using different nuclear potentials: Paris (solid), Reid soft-core (dotted), Argonne V14 (dashed), Nijmegen (dot-dash). Taken from Reference [68].

Chapter 7

Conclusions

The results reported here were obtained in the first test of a metastability-exchange polarized ^{3}He target in an electron scattering experiment. The spin-dependent asymmetry was measured using inclusive scattering in the quasielastic kinematic region. Data were collected in two spectrometers: The measurement made with OHIPS is maximally sensitive to the transverse spin-dependent response function, while the asymmetry measured with BIGBITE is more sensitive to the spin-dependent response function arising from the interference between the charge and magnetic multipoles. The results are consistent with the models of Friar *et al.* and of Blankleider and Woloshyn, both of which predict that the ^{3}He quasielastic asymmetry is sensitive to the neutron form factors.

In addition to reporting the results and describing the data analysis, a discussion of the polarized target is included in this work. Since this is the first target of its type, a description of the optical pumping technique used to polarize the ^{3}He is given along with the details of the design, construction, testing, and operation of the target. The results of beam depolarization studies and the effects of surface coatings are included. They indicate that the target operates well at temperatures below 20 K as long as a surface coating is used, in this case frozen nitrogen or argon. The target was shown to maintain a significant polarization in beam currents of 44 μA of minimum ionizing particles, making it suitable for a variety of facilities. Perhaps more important than its use as an external target, though, is that the optical pumping technique used for this target makes it the optimal choice for internal polarized ^{3}He targets where fast feed rates of the polarized atoms are vital.

The experiment discussed here has generated much interest in the nuclear physics community. The polarized ^{3}He target developed for this experiment can be used for a variety of nuclear and high energy physics experiments, and the results presented here are important as a test of the target. Although the uncertainties on the measured asymmetries are large, they are the first reported values of the spin-dependent asymmetry for a $^3\overrightarrow{\mathrm{He}}(\vec{e},e')$ experiment, and the results support the theoretical prediction that experiments using polarized electrons and polarized ^{3}He are sensitive to the neutron properties. The extracted value of G_E^n obtained from this experiment, although certainly not of comparable precision to the current measurements using elastic $d(e,e')$ experiments, is obtained from a completely different experimental technique and hence, is not sensitive to quite the same systematic errors as the deuterium experiments. It should be noted that the experiment reported here was not designed to measure G_E^n at all, and the amount of beam current delivered to the target was much less than would be required for a high-precision measurement of G_E^n. Rather, the results presented here are significant because they show the potential of this technique as a way to measure G_E^n over the broad range of Q^2 accessible at electron accelerators.

As with any new experimental technique and first attempt at an experiment, there is plenty of room for improvement. Although the metastability-exchange polarized ^{3}He target has very little background since only ^{3}He gas is present in the target, a denser target of this type with higher polarization is desired. Current technology makes such a target feasible. A laser with an LNA crystal can optically pump ^{3}He more quickly and to higher polarization and operates more reliably than the YAP laser used for this experiment. A liquid ^{3}He refrigerator can cool the gas in the target to 4 K, for increased target thickness. As more electron accelerators provide high-current polarized electron beams, precision measurements at high luminosity using the polarized ^{3}He target will become more feasible.

In addition to experimental improvements, more theoretical calculations are needed. Experiments using polarized ^{3}He would benefit from calculations using full spectral functions for ^{3}He, instead of the closure approximation made by Blankleider and Woloshyn. Also, a calculation of the meson exchange effects is badly needed. A number of facilities have currently approved experiments that will use polarized ^{3}He targets, and many facilities plan to have active physics programs using polarized ^{3}He in the near future. An estimation of the size of meson exchange current corrections is important for the analysis of the experimental data from those experiments, and as higher precision measurements are made, understanding the corrections will become crucial.

The use of polarization observables to access new information about the electromagnetic structure of nuclei and nucleons offers great potential for electromagnetic nuclear physics. This is a relatively new field of nuclear physics, and polarized ^{3}He targets will play an important role in polarization studies in the near future. The results of this experiment show the usefulness of the experimental technique of polarized electron scattering from polarized ^{3}He as a tool for electromagnetic studies.

Appendix A

TURTLE Monte Carlo Input for Extended Targets

The optics for both OHIPS and BIGBITE are modeled using a standard magnetic transport Monte Carlo program, known as TURTLE [12]. The input decks for the 10 cm-long target and the spectrometer configuration used during this experiment are given in Table A.1 for OHIPS and Table A.2 for BIGBITE.

```
OHIPS 0.929 meter drift VH focus"
50000
  1. 0.1  400. 3.5  250.  0.  2.5 0.462   "beam" ;
 55.1;
 17.                                      "SEC " ;
 13.  10.                                 "aper" ;
  3.0   0.474                             "d0  " ;
  6.0 1 8.5725                            "clxu" ;
  6.0 3 3.81                              "clyu" ;
  3.0   0.21                              "d1  " ;
  6.0 1 9.76                              "clxd" ;
  6.0 3 4.21                              "clyd" ;
  3.0   .245                              "d0.1" ;
  6.   1.  14.6   3.  14.6                "pipe";
  5.    .7080 +5.62576   15.24            "Q1  " ;
  3.   0.1307                             "DR2 " ;
  6.   1.  14.6   3.  14.6                "pipe";
  5.    .7080 -4.10906  15.24             "Q2  " ;
  6.   1.  14.6   3.  14.6                "pipe";
  6.0 1 20.3                              "pipe" ;
  6.0 3 12.4                               "pipe" ;
  3.   0.513                              "DR3 " ;
  6.0 1 20.3                              "pipe" ;
  6.0 3 8.9                               "pipe" ;
 16.   4.      20.320                     "vGAP" ;
 16.   5.       9.480                     "hGAP" ;
 16.   7.        .7                       "K1  " ;
 16.   8.       4.4                       "K2  " ;
  2.   0.                                        ;
  4.   1.      6.5661   0.00              "B1a " ;
  4.   1.      6.5661   0.00              "B1b " ;
  4.   1.      6.5661   0.00              "B1c " ;
  6.0 1 20.3                              "pipe" ;
  6.0 3 8.9                               "pipe" ;
 16.   7.        .4                       "K1  " ;
  4.    .9898 6.5661   0.00               "B1d " ;
  2.   0.                                        ;
  6.0 1 20.3                              "pipe" ;
  6.0 3 8.9                               "pipe" ;
(  3.0  1.626                              "DR4 " ;)
  3.0 0.534                               "DR4a";
  6.0 1 38.1                              "pipe" ;
  6.0 3 8.6                               "pipe" ;
  3.0 0.457                               "DR4b";
  6.0 1 38.1                              "pipe" ;
  6.0 3 15.3                               "pipe" ;
  3.0 0.635                               "DR4c";
  6.0 1 22.45                             "VDCX" ;
  6.0 3 8.89                              "VDCY" ;
 20.0 +35.26                              "ROT1" ;
  6.0 1 18.88                             "EDG1" ;
 20.0 -70.52                              "ROT2" ;
  6.0 1 18.88                             "EDG2" ;
 20.0 +35.26                              "ROT1" ;
 55.1                                            ;
 53.1                                     "flag" ;
SENTINEL
SENTINEL
```

Table A.1: TURTLE deck for the OHIPS spectrometer with an extended target.

```
BIGBITE QQD -- 10/90, 88-02'
500000
 1. 3.5 160. 0.1 200.0 0. 2.5 0.5167 ;
 17. 'SEC' ;
 7 0.0 0.0 0.0 0.0 0.0 -27.5 'Poff';
 16. 5. 12.7 ;
 16. 7. 0.7 ;
 16. 8. 4.4 ;
 55.1  ;
  3.0 0.656 'DR0' ;
 6.0  1. 1.85  3.  6.35 'SLIT' ;
 3.0 0.189 'DR1' ;
 13. 10. 'APER';
6. 1. 9.8425 3. 9.8425   'PIPE';
 5.00 .11525 -6.88677 10.20 'Q1A' ;
6. 1. 9.8425 3. 9.8425   'PIPE';
 5.00 .11525 -6.88677 10.20 'Q1B' ;
6. 1. 9.8425 3. 9.8425   'PIPE';
 5.00 .11525 -6.88677 10.20 'Q1C' ;
6. 1. 9.8425 3. 9.8425   'PIPE';
 5.00 .11525 -6.88677 10.20 'Q1D' ;
6. 1. 9.8425 3. 9.8425   'PIPE';
 3.0 0.3368 'DR2' ;
6. 1. 9.8425 3. 9.8425   'PIPE';
 5.00 .11625 5.16495 10.20 'Q2A' ;
6. 1. 9.8425 3. 9.8425   'PIPE';
 5.00 .11625 5.16495 10.20 'Q2B' ;
6. 1. 9.8425 3. 9.8425   'PIPE';
 5.00 .11625 5.16495 10.20 'Q2C' ;
6. 1. 9.8425 3. 9.8425   'PIPE';
 5.00 .11625 5.16495 10.20 'Q2D' ;
6. 1. 9.8425 3. 9.8425   'PIPE';
 3.0 0.7961 'DR3' ;
 20. 180. 'LFT' ;
 2.0 20. 'PFR' ;
 4.000 0.411 8.3968 0. 'BD1' ;
 4.000 0.411 8.3968 0. 'BD1' ;
 4.000 0.411 8.3968 0. 'BD2' ;
 2.0 15. 'PFR' ;
 20. -180. 'RGT';
 3.0 1.0902 'WC1' ;
 7. 7.4 0. 0. 0. 0. 0. ;
 6. 1. 35.6 ;
 7. -7.4 0. 0. 0. 0. 0. ;
 6. 3. 17.0 ;
 55.1     ;
 3.0 0.9603 'WC2' ;
 7. 15.1 0. 0. 0. 0. 0. ;
 6. 1. 55.9 ;
 7. -15.1 0. 0. 0. 0. 0. ;
 6. 3. 17.5 ;
( 55.1     ;)
 53.1           ;
(3.0 0.500 'Cer' ;)
SENTINEL
SENTINEL
```

Table A.2: TURTLE deck for the BIGBITE spectrometer with an extended target.

Appendix B

Cleaning the ^{3}He Target System

It is necessary to clean carefully all surfaces of the target system that come in contact with polarized ^{3}He atoms in order to reduce the depolarization from surface effects and to reduce the amount of impurities given off from the surface, which collect in the gas. The procedures used to clean the glassware and the target cell are described below.

B.1 Target Cell

The copper target cell was cleaned before being joined with epoxy to the glassware. The cleaning procedure is the following.

1. Soak the copper cell in a 15% solution of hydrofluoric acid for 30 minutes, making sure the inner surface of the target cell is totally immersed.
2. Remove from solution. Dip in large flask of distilled water to clean the acid off the surface.
3. Immerse in acetone to remove the water.
4. Clean surfaces with a tissue.

After being cleaned, the target was heated under vacuum in a bell jar to drive off the water. The cell was placed in the bell jar and the system roughed out; then the cell was heated to 120° C and maintained at this temperature under vacuum for an hour. After the heating element was turned off, the target was allowed to come to room temperature under vacuum before being removed from the bell jar.

B.2 Glassware

The glassware was cleaned after the target cell was epoxied in place. The cleaning procedure involved cycles of baking the glassware under vacuum and using a hot discharge to drive impurities from the cell walls. Initially, the scattering chamber and target system were pumped out using a roughing pump. Once the pressure was low enough, the valve between the gas plumbing for the target system and the scattering chamber was closed and the plumbing and target systems were opened to a turbo pump. The pumping cell was covered with a heating mantle and heated to $\sim 300 - 400°$ C. After baking for $24 - 48$ hours, the regimen of running hot discharges in the cell was started. The target system was filled with $0.8 - 1.0$ torr of ^{3}He, the gas inlet valve to the cells was closed, and a 20 MHz discharge was lit in the cell. The discharge is a pink color when the gas is clean and a bluish or purple color when the gas is dirty. The discharge was maintained until the gas looked dirty; then the gas was pumped out of the system, fresh gas was put in, and the procedure repeated. Initially, the gas turned a bluish color after only $5 - 10$ minutes, but after the system became cleaner it would remain pink for over an hour.

A vacuum of $\sim 1 \times 10^{-7}$ torr is needed before optical pumping should be started. Whenever the system was not used for an extended period of time, the pumping cell was left baking under vacuum. However, when the target cell was cold, the system was not baked and the gas inlet valve was kept shut to prevent contaminants from the rest of the plumbing and oil from the vacuum pumps from collecting on the cell walls.

Appendix C

Determination of the Volume of the Cells

The ratio of the volumes of the target and pumping cells is determined by measuring the change in pressure for two different target temperatures when a known amount of gas is let into the two cells through the gas inlet valve. A schematic of the system is shown in Figure C.1. The three different volumes involved in the measurement are the volume of the plumbing outside the cells between the gas inlet valve to the target system and the shutoff valve for the gas plumbing, the volume of the target cell, v, and the volume of the pumping cell, V. The pumping cell temperature, T, is approximately constant and the target cell temperature, t, can be varied by cooling the target with the refrigerator. The volume of the transfer tube between the two cells is naturally split by this measurement into a "cold" volume associated with the target and a "warm" volume associated with the pumping cell. The outside volume is filled to pressure, p, with the gas inlet valve closed. The inlet valve is opened and the pressure decreases to p'. Let t_1 and t_2 denote the two target temperatures at which the measurements are made, and define the quantity

$$f_i \equiv \left(\frac{p}{p'} - 1\right)_i^{-1} \tag{C.1}$$

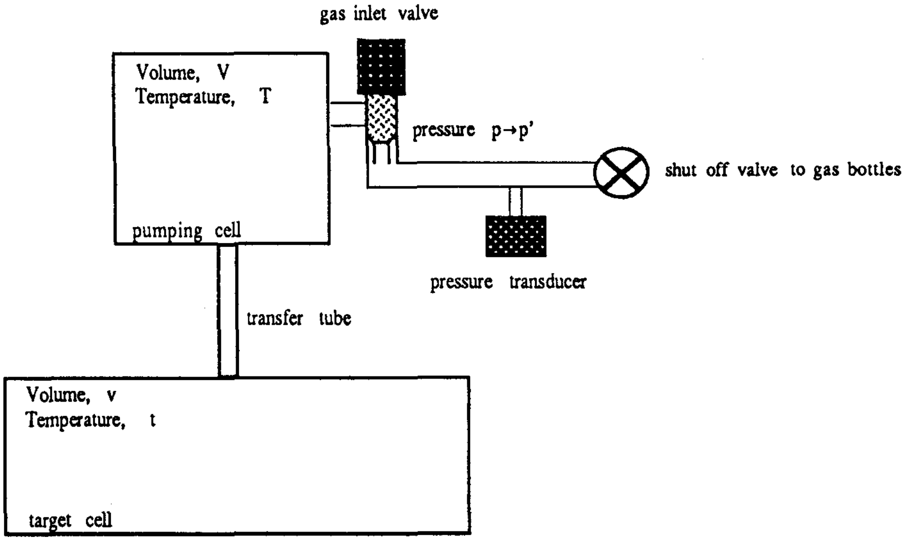

Figure C.1: Schematic of the volume measurement. The three relevant volumes are the pumping cell, the target cell, and the region outside the two cells between the gas inlet valve and the shutoff valve to the gas bottles.

in terms of the measured pressures at target temperature t_i. Then the ratio of the volumes of the two cells is

$$\frac{v}{V} = \left(\frac{t_1}{T}\right)\left(\frac{f_1 - f_2}{f_2(t_1/t_2) - f_1}\right). \tag{C.2}$$

Table C.1 contains the measured values of the pressure and temperature. The volume ratio extracted from these numbers is $\frac{v}{V} = 0.461$.

From the volume ratio, the fraction of atoms in each cell can be calculated as a

T (K)	t (K)	p (torr)	p' (torr)
295	295	2.68	1.26
295	17.3	10.19	1.30

Table C.1: Table of measured parameters for volume determination.

t	N_t/N
16.0	0.894
16.5	0.892
17.0	0.889
17.5	0.886

Table C.2: Fraction of atoms in target cell as a function of target temperature.

function of the target temperature. The values are shown in Table C.2. The ratio $N_t/N = 0.890 \pm 0.005$ is used for the calculation of the target polarization and target density.

Appendix D

Solutions to the Coupled Rate Equations for a Double-Cell System

Equations describing the time evolution of the polarizations in both cells of a coupled double-cell system can be obtained from the solutions to the rate equations for the polarization in each cell. The derivation of the solution for both conditions under which the polarization is relaxing and conditions under which the atoms are being optically pumped is presented in this appendix. In the discussion that follows, a design like the one used for the polarized ^{3}He target is assumed: The atoms are optically pumping in one cell, referred to as the pumping cell, and are in diffusive contact with a second cell, referred to as the target cell. The equations assume that the transfer tube has negligible volume and that there is no time lag between the time when the atoms leave one cell and enter the other. The volume of the transfer tube for the polarized ^{3}He target is approximately 5% of the volume of the pumping cell, so it is valid to ignore it in this calculation. Also, since the polarization evolves on the timescale of seconds, which is much longer than the time spent in the transfer tube, the delay in transferring between the cells can be ignored.

D.1 Solution to Relaxation Rate Equations

The relaxation rate equations for a double-cell system are

$$\frac{dP_p(t)}{dt} = -\frac{P_p(t)}{\tau_p} + \frac{P_t(t) - P_p(t)}{t_p} \tag{D.1}$$

$$\frac{dP_t(t)}{dt} = -\frac{P_t(t)}{\tau_t} + \frac{P_p(t) - P_t(t)}{t_t} \tag{D.2}$$

where the first term accounts for the spin relaxation in the cell and the second accounts for the exchange of polarization between the two cells. The terms in the equations are defined as

$P_{p(t)}$ = pumping (target) cell polarization

$\tau_{p(t)}$ = relaxation time in pumping (target) cell

and

$t_{p(t)}$ = diffusion time for pumping (target) cell atoms

Consider the exchange terms is Equations D.1 and D.2. Atoms diffuse out of the pumping cell carrying polarization away from the cell at a rate $\frac{1}{t_p}$ and out of the target cell carrying polarization away at a rate $\frac{1}{t_t}$. However, the polarization is defined in terms of the number of atoms in the cell from which the atoms diffuse and must be corrected by the number of atoms in the cell which they enter in order to reflect correctly the amount of polarization contributed.

$$P \equiv \frac{N_+ - N_-}{N_+ + N_-} \tag{D.3}$$

Since the cells are sealed, there are a fixed number of atoms in the system. Therefore, detailed balance requires that the number of atoms leaving one cell equals the number of atoms entering the other so that a constant pressure is maintained in the system.

$$\frac{N_p}{t_p} = \frac{N_t}{t_t} \tag{D.4}$$

Because of this relationship, both polarizations in the exchange term for a given cell enter with the same diffusion time constant. The equations can be further simplified because the transfer rate that is measured is the sum of the rates from the two cells,

$$\frac{1}{t_{ex}} = \frac{1}{t_p} + \frac{1}{t_t}. \tag{D.5}$$

Using Equations D.4 and D.5, the relaxation rate equations can be rewritten in matrix form as

$$\begin{pmatrix} \frac{dP_p(t)}{dt} \\ \frac{dP_t(t)}{dt} \end{pmatrix} = \begin{pmatrix} -\left(\frac{1}{\tau_p} + \left(\frac{N_t}{N}\right)\frac{1}{t_{ex}}\right) & \left(\frac{N_t}{N}\right)\frac{1}{t_{ex}} \\ \left(\frac{N_p}{N}\right)\frac{1}{t_{ex}} & -\left(\frac{1}{\tau_t} + \left(\frac{N_p}{N}\right)\frac{1}{t_{ex}}\right) \end{pmatrix} \begin{pmatrix} P_p(t) \\ P_t(t) \end{pmatrix}. \tag{D.6}$$

To find the solutions to Equation D.6, the 2 × 2 matrix needs to be diagonalized. The following shorthand notation will be used in the analysis that follows.

$$a \equiv -\left(\frac{1}{\tau_p} + \left(\frac{N_t}{N}\right)\frac{1}{t_{ex}}\right) \tag{D.7}$$

$$b \equiv \left(\frac{N_t}{N}\right)\frac{1}{t_{ex}} \tag{D.8}$$

$$c \equiv \left(\frac{N_p}{N}\right)\frac{1}{t_{ex}} \tag{D.9}$$

$$d \equiv -\left(\frac{1}{\tau_t} + \left(\frac{N_p}{N}\right)\frac{1}{t_{ex}}\right) \tag{D.10}$$

The eigenvalues are

$$\lambda_\pm = \frac{a+d}{2} \pm \sqrt{\left(\frac{a+d}{2}\right)^2 - (ad - bc)} \tag{D.11}$$

and the eigenvectors can be written as

$$\vec{v} = \begin{pmatrix} 1 \\ \alpha_\pm \end{pmatrix}, \tag{D.12}$$

where

$$\alpha_\pm \equiv \frac{a - c - \lambda_\pm}{d - b - \lambda_\pm}. \tag{D.13}$$

The transformation matrix is

$$\mathbf{T} = \begin{pmatrix} 1 & 1 \\ \alpha_- & \alpha_+ \end{pmatrix} \tag{D.14}$$

and the inverse transformation matrix is

$$\mathbf{T}^{-1} = \frac{1}{\Delta\alpha} \begin{pmatrix} \alpha_+ & -1 \\ -\alpha_- & 1 \end{pmatrix}, \tag{D.15}$$

where

$$\Delta\alpha = \alpha_+ - \alpha_-. \tag{D.16}$$

The rate equations can now be expressed in terms of two new polarization variables, $P_1(t)$ and $P_2(t)$, which are independent of each other and obey the rate equations

$$\begin{pmatrix} \frac{dP_1(t)}{dt} \\ \frac{dP_2(t)}{dt} \end{pmatrix} = \begin{pmatrix} \lambda_- P_1(t) \\ \lambda_+ P_2(t) \end{pmatrix}. \tag{D.17}$$

The solutions to these equations are subject to the constraints that the polarizations goes to zero as $t \to \infty$ and that

$$\begin{pmatrix} P_1(0) \\ P_2(0) \end{pmatrix} = \mathbf{T}^{-1} \begin{pmatrix} P_p(0) \\ P_t(0) \end{pmatrix} = \frac{1}{\Delta\alpha} \begin{pmatrix} \alpha_+ P_p(0) - P_t(0) \\ -\alpha_- P_p(0) + P_t(0) \end{pmatrix}. \tag{D.18}$$

The independent polarization solutions are then

$$\begin{pmatrix} P_1(t) \\ P_2(t) \end{pmatrix} = \frac{1}{\Delta\alpha} \begin{pmatrix} (\alpha_+ P_p(0) - P_t(0)) e^{\lambda_- t} \\ (P_t(0) - \alpha_- P_p(0)) e^{\lambda_+ t} \end{pmatrix}. \tag{D.19}$$

If we define two new time constants that characterize the decay of the two independent exponentials,

$$-\frac{1}{\tau_l} \equiv \lambda_+ \tag{D.20}$$

and

$$-\frac{1}{\tau_s} \equiv \lambda_-, \tag{D.21}$$

then the polarizations of the pumping and target cell can be expressed as a sum of two exponentials with these time constants.

$$\begin{pmatrix} P_p(t) \\ P_t(t) \end{pmatrix} = \frac{1}{\Delta\alpha} \begin{pmatrix} (\alpha_+ P_p(0) - P_t(0)) e^{-t/\tau_s} + (P_t(0) - \alpha_- P_p(0)) e^{-t/\tau_l} \\ \alpha_-(\alpha_+ P_p(0) - P_t(0)) e^{-t/\tau_s} + \alpha_+(P_t(0) - \alpha_- P_p(0)) e^{-t/\tau_l} \end{pmatrix} \tag{D.22}$$

The time evolution of the polarizations in the target and pumping cell can now be calculated exactly, assuming that the initial polarizations and time constants of the two cells are known. Figure D.1 shows the relaxation of the polarization in the two cells, normalized to the initial polarization of the pumping cell. For the calculation, $P_t(0)/P_p(0) = 0.90$, $\tau_t = 700$ sec, $\tau_p = 200$ sec, $t_{ex} = 7.5$ sec, and $\left(\frac{N_t}{N}\right) = 0.89$. For this example, $\tau_l = 552$ sec and $\tau_s = 7.3$ sec. The double-exponential form of the decay is clear from the graph.

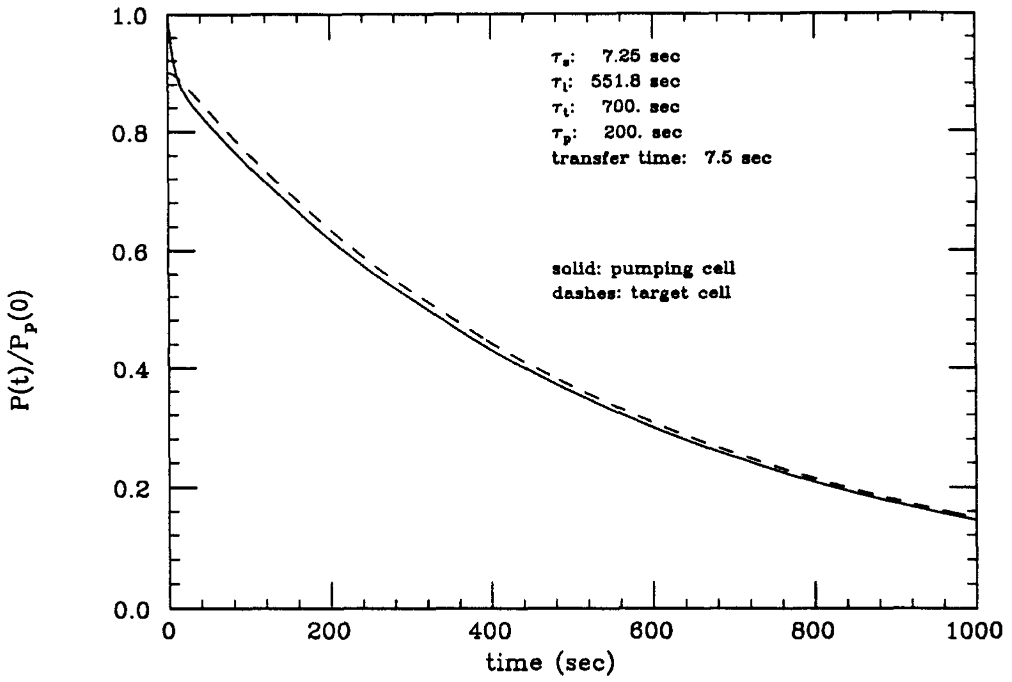

Figure D.1: Time evolution of the target and pumping cell polarizations during relaxation. For the calculation τ_t = 700 sec, τ_p = 200 sec, t_{ex} = 7.5 sec, $\left(\frac{N_t}{N}\right) = 0.89$, and $P_t(0)/P_p(0) = 0.90$. The long time constant of the decay, τ_l, is 552 sec and the short time constant, τ_s, is 7.3 sec.

In practice, one may not initially know the time constants of the system, τ_p, τ_t, and t_{ex}. In this case, the pumping cell polarization can be measured as a function of time during the polarization relaxation process, and information about the time constants and the target polarization can be inferred from a fit of a sum of two exponentials to the data. The parameters of the fit are two time constants and two amplitudes multiplying the exponentials.

$$P_p(t) = a_s e^{-t/\tau_s} + a_l e^{-t/\tau_l} \tag{D.23}$$

From the time constants of the fit, τ_l and τ_s, information about the time constants of the system can be extracted. The fit time constants can be expressed in terms of the parameters of the system as

$$\frac{1}{\tau_s}=\frac{1}{2}\left(\frac{1}{\tau_p}+\frac{1}{\tau_t}+\frac{1}{t_{ex}}\right)+\frac{1}{2}\sqrt{\frac{1}{t_{ex}^2}+\left(\frac{1}{\tau_p}-\frac{1}{\tau_t}\right)^2+\frac{2}{t_{ex}}\left(\frac{N_t-N_p}{N}\right)\left(\frac{1}{\tau_p}-\frac{1}{\tau_t}\right)} \tag{D.24}$$

and

$$\frac{1}{\tau_l}=\frac{1}{2}\left(\frac{1}{\tau_p}+\frac{1}{\tau_t}+\frac{1}{t_{ex}}\right)-\frac{1}{2}\sqrt{\frac{1}{t_{ex}^2}+\left(\frac{1}{\tau_p}-\frac{1}{\tau_t}\right)^2+\frac{2}{t_{ex}}\left(\frac{N_t-N_p}{N}\right)\left(\frac{1}{\tau_p}-\frac{1}{\tau_t}\right)}. \tag{D.25}$$

From these relationships, the exact expression

$$\frac{1}{\tau_s}+\frac{1}{\tau_l}=\frac{1}{t_{ex}}+\frac{1}{\tau_p}+\frac{1}{\tau_t} \tag{D.26}$$

can easily be obtained. In the case where the transfer time, t_{ex}, is much shorter than the relaxation time in either cell, the short time constant, τ_s, approximates the transfer time. Under these conditions, an approximate expression can be derived for the long time constant, τ_l, which depends only upon the relaxation times and the fraction of atoms in each cell.

$$\frac{1}{\tau_l}\approx\left(\frac{N_p}{N}\right)\frac{1}{\tau_p}+\left(\frac{N_t}{N}\right)\frac{1}{\tau_t} \tag{D.27}$$

This expression indicates that in the limit of fast transfer between the cells the rate of decay of the combined system is the average of the decay rates in each cell weighted by the number of atoms in the cell.

It is useful to determine the initial polarizations in the two cells so that the ratio, $P_t(0)/P_p(0)$, can be obtained. From the initial polarization ratio, the equilibrium polarization ratio during optical pumping can be determined, assuming that the relaxation measurement is not started until equilibrium has been reached. The polarization in the pumping cell is measured directly, and the initial polarization in the target cell can be obtained from the fit amplitudes. Using Equation D.22, one can express the initial target cell polarization, $P_t(0)$, in terms of the fit parameters and the initial polarization in the pumping cell. First, a comparison of Equation D.22 and D.23 tells us that

$$a_s=\frac{1}{\Delta\alpha}\left(\alpha_+P_p(0)-P_t(0)\right) \tag{D.28}$$

and

$$a_l = \frac{1}{\Delta\alpha}\left(P_t(0) - \alpha_- P_p(0)\right). \tag{D.29}$$

From Equations D.13, D.20, and D.21 we know that

$$\alpha_+ = \frac{\frac{1}{\tau_p} + \frac{1}{t_{ex}} - \frac{1}{\tau_l}}{\frac{1}{\tau_t} + \frac{1}{t_{ex}} - \frac{1}{\tau_l}} \tag{D.30}$$

and

$$\alpha_- = \frac{\frac{1}{\tau_p} + \frac{1}{t_{ex}} - \frac{1}{\tau_s}}{\frac{1}{\tau_t} + \frac{1}{t_{ex}} - \frac{1}{\tau_s}}. \tag{D.31}$$

In the limit that $t_{ex} \ll \tau_p, \tau_t$, these reduce to

$$\alpha_+ \approx 1 + \tau_s\left(\frac{1}{\tau_p} - \frac{1}{\tau_t}\right) \tag{D.32}$$

$$\alpha_- \approx -\left(\frac{N_p}{N_t}\right). \tag{D.33}$$

For a "relaxation with discharge on" measurement where the four fit parameters, a_l, a_s, τ_l and τ_s are extracted from the data (refer to Section 4.4.2 for a description of the relaxation measurements), the initial polarizations in the two cells can be written as

$$P_p(0) = a_l + a_s, \tag{D.34}$$

$$P_t(0) \approx \left[1 + \tau_s\left(\frac{1}{\tau_p} - \frac{1}{\tau_t}\right)\right] a_l - \left[\frac{N_p}{N_t}\right] a_s. \tag{D.35}$$

For a "transfer" relaxation measurement, the pumping cell polarization is zeroed initially, so the additional constraint that

$$a_s = -a_l \tag{D.36}$$

holds. Therefore, for this type of measurement,

$$P_t(0) \approx \left[\left(\frac{N}{N_t}\right) + \tau_s\left(\frac{1}{\tau_p} - \frac{1}{\tau_t}\right)\right] a_l. \tag{D.37}$$

For the "transfer" measurement, the pumping cell polarization is measured before being zeroed to determine the equilibrium value of the pumping cell polarization during optical pumping.

D.2 Solution to Pumping Rate Equations

For a single cell, the pumping rate equation is

$$\frac{dP}{dt} = \frac{P_0 - P(t)}{T} - \frac{P(t)}{\tau_p}, \tag{D.38}$$

where the first term reflects the pumping and the second term the relaxation. P_0 is the polarization achievable in the limit of no relaxation. The solution to this equation is

$$P(t) = \frac{P_0}{1 + \frac{T}{\tau_p}} \left(1 - e^{-t\left(\frac{1}{T} + \frac{1}{\tau_p}\right)}\right). \tag{D.39}$$

From this equation, it is clear that the achievable polarization in a single cell,

$$P_s \equiv \frac{P_0}{1 + \frac{T}{\tau_p}}, \tag{D.40}$$

decreases as the relaxation time gets longer for a given pumping time constant, T. The rate equation for a single cell can be rewritten in terms of P_s as

$$\frac{dP}{dt} = \left(\frac{1}{T} + \frac{1}{\tau_p}\right)(P_s - P(t)). \tag{D.41}$$

For the polarized ^{3}He target using the YAP laser, the pumping time constant was $\sim 20-30$ sec.

For a coupled two cell system with optical pumping of one cell only, the coupled rate equations are written in matrix form as

$$\begin{pmatrix} \frac{dP_p(t)}{dt} \\ \frac{dP_t(t)}{dt} \end{pmatrix} = \begin{pmatrix} \left(\frac{1}{T} + \frac{1}{\tau_p}\right) P_s \\ 0 \end{pmatrix} + \begin{pmatrix} -\left(\frac{1}{T} + \frac{1}{\tau_p} + \left(\frac{N_t}{N}\right)\frac{1}{t_{ex}}\right) & \left(\frac{N_t}{N}\right)\frac{1}{t_{ex}} \\ \left(\frac{N_p}{N}\right)\frac{1}{t_{ex}} & -\left(\frac{1}{\tau_t} + \left(\frac{N_p}{N}\right)\frac{1}{t_{ex}}\right) \end{pmatrix} \begin{pmatrix} P_p(t) \\ P_t(t) \end{pmatrix}, \tag{D.42}$$

where P_s is the polarization achievable in a single cell with pumping time constant, T, and relaxation time, τ_p. The eigenvalues for the 2×2 matrix are

$$\lambda_\pm \equiv \frac{a+d}{2} \pm \sqrt{\left(\frac{a+d}{2}\right)^2 - (ad - bc)} \tag{D.43}$$

where

$$a \equiv -\left(\frac{1}{T} + \frac{1}{\tau_p} + \left(\frac{N_t}{N}\right)\frac{1}{t_{ex}}\right) \tag{D.44}$$

$$b \equiv \left(\frac{N_t}{N}\right)\frac{1}{t_{ex}} \tag{D.45}$$

$$c \equiv \left(\frac{N_p}{N}\right)\frac{1}{t_{ex}} \tag{D.46}$$

$$d \equiv -\left(\frac{1}{\tau_t} + \left(\frac{N_p}{N}\right)\frac{1}{t_{ex}}\right). \tag{D.47}$$

The transformation matrix is

$$\mathbf{T} = \begin{pmatrix} 1 & 1 \\ \alpha_- & \alpha_+ \end{pmatrix}, \tag{D.48}$$

where

$$\alpha_\pm = \frac{a - c - \lambda_\pm}{d - b - \lambda_\pm}. \tag{D.49}$$

Following the same procedure as outlined in the previous section on the solution to the relaxation rate equations, the two independent exponential solutions are found to be

$$\begin{pmatrix} P_1(t) \\ P_2(t) \end{pmatrix} = \begin{pmatrix} \gamma_+\tau_s\left(1 - e^{-t/\tau_s}\right) \\ \gamma_-\tau_l\left(1 - e^{-t/\tau_l}\right) \end{pmatrix}, \tag{D.50}$$

where

$$\gamma_\pm \equiv \frac{\pm\alpha_\pm}{\Delta\alpha}\left(\frac{1}{T} + \frac{1}{\tau_p}\right)P_s \tag{D.51}$$

$$-\frac{1}{\tau_l} \equiv \lambda_+ \tag{D.52}$$

$$-\frac{1}{\tau_s} \equiv \lambda_-. \tag{D.53}$$

The pumping and target cell polarizations can now be written in terms of the time constants of the system and the polarization limit for a single cell as

$$\begin{pmatrix} P_p(t) \\ P_t(t) \end{pmatrix} = \frac{P_s}{\Delta\alpha}\left(\frac{1}{T} + \frac{1}{\tau_p}\right)\begin{pmatrix} (\alpha_+\tau_s - \alpha_-\tau_l) + \alpha_-\tau_l e^{-t/\tau_l} - \alpha_+\tau_s e^{-t/\tau_s} \\ \alpha_+\alpha_-\left[(\tau_s - \tau_l) + \tau_l e^{-t/\tau_l} - \tau_s e^{-t/\tau_s}\right] \end{pmatrix}. \tag{D.54}$$

An exact relationship between the fit time constants of the pumping data and the time constants of the system exists:

$$\frac{1}{\tau_s} + \frac{1}{\tau_l} = \frac{1}{T} + \frac{1}{\tau_p} + \frac{1}{\tau_t} + \frac{1}{t_{ex}}. \tag{D.55}$$

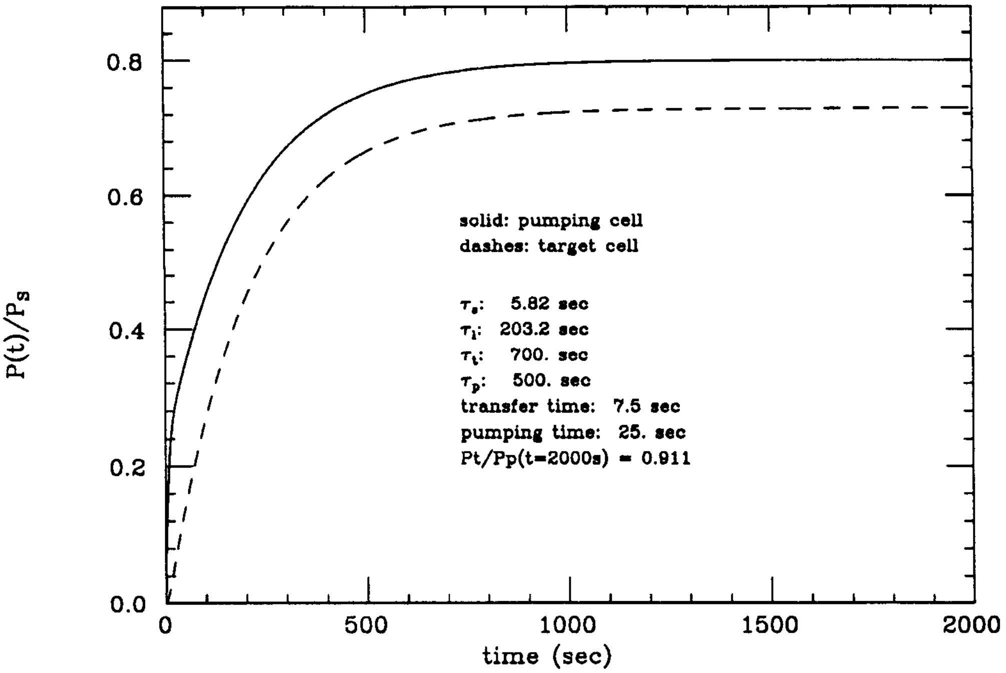

Figure D.2: Time evolution of the target and pumping cell polarizations during optical pumping. For the calculation, τ_t = 700 sec, τ_p = 200 sec, t_{ex} = 7.5 sec, T = 25 sec, and $\left(\frac{N_t}{N}\right) = 0.89$. The long time constant of the charging curve, τ_l, is 203 sec. and the short time constant, τ_s, is 5.8 sec.

The fit time constants can be written as

$$\frac{1}{\tau_l} = \frac{1}{2}\left(\frac{1}{T} + \frac{1}{\tau_p} + \frac{1}{\tau_t} + \frac{1}{t_{ex}}\right) - \frac{1}{2}\sqrt{\frac{1}{t_{ex}^2} + \left(\frac{1}{T} + \frac{1}{\tau_p} - \frac{1}{\tau_t}\right)^2 + \frac{2}{t_{ex}}\left(\frac{N_t - N_p}{N}\right)\left(\frac{1}{T} + \frac{1}{\tau_p} - \frac{1}{\tau_t}\right)} \tag{D.56}$$

and

$$\frac{1}{\tau_s} = \frac{1}{2}\left(\frac{1}{T} + \frac{1}{\tau_p} + \frac{1}{\tau_t} + \frac{1}{t_{ex}}\right) + \frac{1}{2}\sqrt{\frac{1}{t_{ex}^2} + \left(\frac{1}{T} + \frac{1}{\tau_p} - \frac{1}{\tau_t}\right)^2 + \frac{2}{t_{ex}}\left(\frac{N_t - N_p}{N}\right)\left(\frac{1}{T} + \frac{1}{\tau_p} - \frac{1}{\tau_t}\right)} \tag{D.57}$$

Figure D.2 shows the polarizations in the two cells as a function of time, for τ_t = 700 sec, τ_p = 200 sec, t_{ex} = 7.5 sec, T = 25 sec and $\left(\frac{N_t}{N}\right) = 0.89$.

Although the expressions derived above give the solution for the time evolution of the polarizations during optical pumping, in general we are interested only in the equilibrium

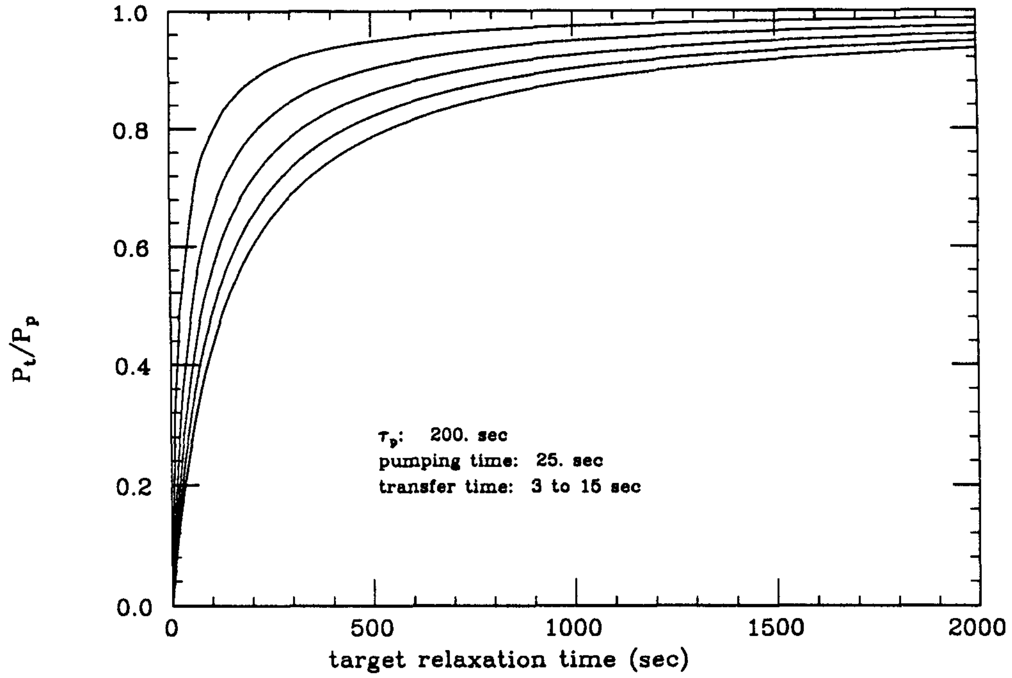

Figure D.3: Equilibrium ratio of target cell polarization to pumping cell polarization during optical pumping. For the calculation, τ_p = 200 sec, T = 25 sec, and $\left(\frac{N_t}{N}\right)$ = 0.89. The curves are for transfer times of 3, 6, 9, 12, and 15 sec. The ratio increases as the transfer time decreases.

polarization reached in the two cells after the system has been pumping for a while. The solution to this is much simpler than the formalism for the full solution, since it requires only that

$$\begin{pmatrix} \frac{dP_p(t)}{dt} \\ \frac{dP_t(t)}{dt} \end{pmatrix} = \begin{pmatrix} 0 \\ 0 \end{pmatrix} = \begin{pmatrix} \left(\frac{1}{T} + \frac{1}{\tau_p}\right) P_s - \left(\frac{1}{T} + \frac{1}{\tau_p} + \left(\frac{N_t}{N}\right) \frac{1}{t_{ex}}\right) P_p(t) + \left(\frac{N_t}{N}\right) \frac{1}{t_{ex}} P_t(t) \\ \left(\frac{N_p}{N}\right) \frac{1}{t_{ex}} P_p(t) - \left(\frac{1}{\tau_t} + \left(\frac{N_p}{N}\right) \frac{1}{t_{ex}}\right) P_t(t) \end{pmatrix}. \tag{D.58}$$

From these equations, the equilibrium ratio of the target to pumping cell polarizations,

$$\frac{P_t}{P_p} = \frac{\left(\frac{N_p}{N}\right) \frac{1}{t_{ex}}}{\frac{1}{\tau_t} + \left(\frac{N_p}{N}\right) \frac{1}{t_{ex}}} = \frac{1}{1 + \left(\frac{N}{N_p}\right) \frac{t_{ex}}{\tau_t}}, \tag{D.59}$$

is obtained. From this expression it is clear that the equilibrium ratio depends only upon the transfer time, the relaxation time in the target cell, and the fraction of atoms in each

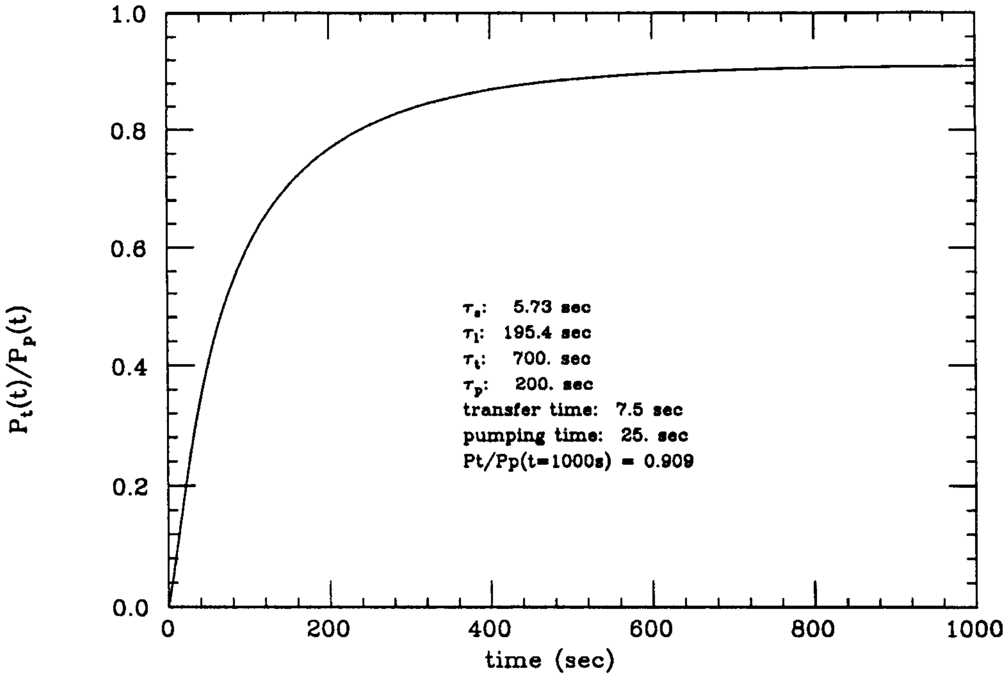

Figure D.4: Approach to equilibrium of the ratio of polarizations in target to pumping cell during optical pumping. For the calculation, τ_t = 700 sec, τ_p = 200 sec, t_{ex} = 7.5 sec, T = 25 sec, and $\left(\frac{N_t}{N}\right) = 0.89$.

cell. Figure D.3 shows the equilibrium ratio of polarizations in the two cells as a function to τ_t for different values of the transfer time. The target cell polarization approaches that in the pumping cell as the target cell relaxation time gets longer and as the transfer time gets shorter.

In order to use the information from the equilibrium polarization ratio to infer the target cell polarization from a measurement of the pumping cell polarization, it is necessary to understand the evolution of the polarization in the two cells to determine how long the system takes to reach equilibrium. Figure D.4 is a graph of $P_t(t)/P_p(t)$, showing how quickly the system approaches equilibrium for values of the time constants similar to those for the ^{3}He target. Equilibrium is reached after $\sim$ 600 sec.

The equilibrium ratio of the pumping cell polarization to that obtainable with a single

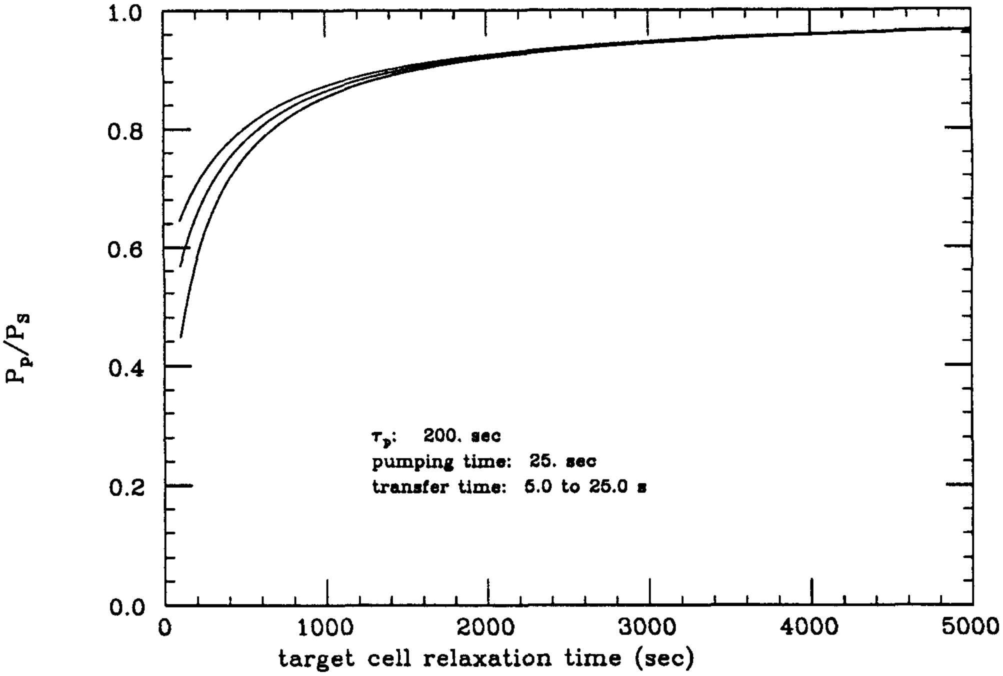

Figure D.5: Equilibrium pumping cell polarization during optical pumping relative to the polarization attainable with a single cell as a function of the target cell relaxation time and the transfer time, for transfer times of of 5, 15 and 25 sec. The ratio is smaller for shorter transfer times.

cell, P_p/P_s, can also be extracted from Equation D.56.

$$\frac{P_p}{P_s} = \frac{\left(\frac{1}{T} + \frac{1}{\tau_p}\right)\left(\frac{1}{\tau_t} + \left(\frac{N_p}{N}\right)\frac{1}{t_{ex}}\right)}{\left(\frac{1}{T} + \frac{1}{\tau_p}\right)\left(\frac{1}{\tau_t} + \left(\frac{N_p}{N}\right)\frac{1}{t_{ex}}\right) + \left(\frac{N_t}{N}\right)\frac{1}{t_{ex}}\frac{1}{\tau_t}} \tag{D.60}$$

If we define an effective pumping time, T_{eff}, by

$$\frac{1}{T_{eff}} \equiv \frac{1}{T} + \frac{1}{\tau_p}, \tag{D.61}$$

then the equation for the achievable pumping cell polarization in the double-cell system can be rewritten as

$$\frac{P_p}{P_s} = \frac{1}{1 + \left(\frac{N_t}{N_p}\frac{T_{eff}}{\tau_t}/1 + \frac{N}{N_p}\frac{t_{ex}}{\tau_t}\right)}. \tag{D.62}$$

Figure D.5 shows the equilibrium pumping cell polarization as a function of the target cell relaxation time, for different values of the transfer time. Figure D.6 shows the dependence upon the pumping time constant. For relaxation times typical of the polarized

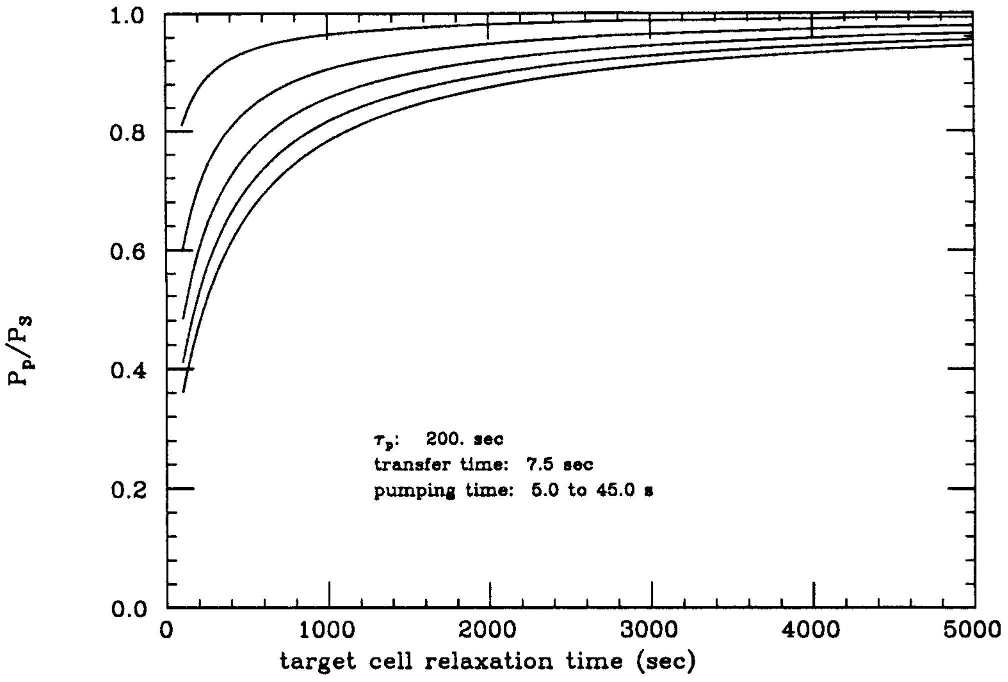

Figure D.6: Equilibrium pumping cell polarization during optical pumping relative to the polarization attainable with a single cell as a function of the target cell relaxation time and the pumping time, for pumping times of 5, 15, 25, 35, and 45 sec. The ratio is larger for shorter pumping times.

^{3}He target, τ_t = 500 – 1500 sec, ~ 75 – 90% of the polarization attained with a single cell is achievable in the pumping cell of a double-cell target system. Since the target cell polarization is reduced by ~ 5 – 10% from the pumping cell polarization, as is shown in Figure D.3, the target polarization is ~ 65 – 85% of what is achievable with a single cell for the polarized ^{3}He target used in the experiment.

Appendix E

BIGBITE Experimental Asymmetries

The experimental asymmetries measured with the BIGBITE spectrometer, corrected only for empty target background, are given in this appendix. For reference, Figures 5.12 and 5.14 show the experimental data and the estimated yield for quasielastic and elastic scattering, respectively. The asymmetries in the energy range 47 MeV $\leq \omega \leq$ 213 MeV are given in Table E.1. This range encompasses the region used for the quasielastic analysis. The asymmetries are specified for the full data set and for each of the target spin orientations. The error bars are statistical only. The values in the threshold-elastic kinematic region, -4 MeV $\leq \omega \leq$ 47 MeV, are given in Table E.2. As shown in Figure 5.4, for $\omega \leq$ 10 MeV, the events in the energy spectrum are consistent with the counts coming from the empty target, indicating that little or no ^{3}He scattering events contribute below this energy transfer.

ω	A_{exp} [all]	A_{exp} [L1]	A_{exp} [L2]	A_{exp} [R]
210.	−8.8 ± 32.1	−89.0 ± 66.5	29.3 ± 68.7	−10.0 ± 43.3
205.	−25.1 ± 25.9	6.3 ± 57.8	−106.0 ± 55.1	5.2 ± 34.1
200.	31.8 ± 20.3	32.6 ± 42.5	44.4 ± 44.1	−26.6 ± 27.2
195.	−26.5 ± 17.0	−85.6 ± 36.8	−58.1 ± 37.0	−6.9 ± 22.4
189.	14.4 ± 13.9	−15.4 ± 29.7	55.4 ± 29.8	−10.0 ± 18.6
184.	12.7 ± 12.2	16.1 ± 26.2	23.5 ± 26.3	−7.3 ± 16.1
179.	−11.2 ± 11.7	−1.2 ± 25.7	28.3 ± 24.8	30.2 ± 15.4
174.	7.4 ± 11.5	12.1 ± 24.7	5.0 ± 24.8	−6.6 ± 15.2
169.	1.6 ± 10.5	−2.3 ± 22.4	33.4 ± 22.6	9.0 ± 14.0
164.	12.6 ± 10.4	−3.9 ± 22.7	−9.5 ± 22.6	−26.9 ± 13.8
158.	3.2 ± 9.7	−26.2 ± 21.0	22.6 ± 20.5	−6.8 ± 13.0
153.	−4.8 ± 9.1	17.3 ± 19.7	−13.3 ± 19.2	9.7 ± 12.0
148.	6.5 ± 8.8	5.5 ± 19.2	19.4 ± 18.6	−1.7 ± 11.7
143.	12.9 ± 8.2	29.6 ± 17.3	−10.2 ± 17.5	−15.2 ± 11.1
138.	7.9 ± 7.6	24.2 ± 16.3	0.2 ± 15.9	−4.7 ± 10.3
133.	7.1 ± 7.2	−13.5 ± 15.2	20.7 ± 14.9	−9.8 ± 9.7
127.	3.3 ± 6.7	−4.4 ± 14.5	−13.6 ± 13.9	−13.5 ± 9.0
122.	4.6 ± 6.3	−1.8 ± 13.3	5.2 ± 13.1	−7.0 ± 8.5
117.	5.4 ± 5.7	11.1 ± 12.0	13.4 ± 11.8	0.2 ± 7.7
112.	−0.3 ± 5.2	−5.4 ± 11.2	−2.5 ± 10.8	−2.6 ± 7.1
107.	−7.4 ± 5.0	−9.5 ± 10.6	−16.3 ± 10.3	2.8 ± 6.7
102.	3.7 ± 4.6	4.4 ± 9.9	14.5 ± 9.6	1.2 ± 6.3
96.	−1.8 ± 4.4	−6.6 ± 9.4	−0.5 ± 9.1	0.4 ± 6.0
91.	−1.7 ± 4.2	−7.9 ± 9.1	2.3 ± 8.7	0.9 ± 5.7
86.	4.0 ± 4.1	−0.2 ± 8.7	5.8 ± 8.5	−4.9 ± 5.5
81.	5.4 ± 4.2	17.6 ± 8.8	7.0 ± 8.7	0.3 ± 5.7
76.	8.7 ± 4.5	20.0 ± 9.4	4.0 ± 9.4	−5.8 ± 6.1
71.	−0.6 ± 4.8	7.8 ± 9.9	10.4 ± 10.0	8.9 ± 6.5
65.	3.3 ± 5.1	2.7 ± 10.4	−3.7 ± 10.7	−6.6 ± 7.0
60.	10.5 ± 5.2	10.0 ± 10.8	5.1 ± 11.1	−13.0 ± 7.1
55.	7.9 ± 6.0	16.3 ± 12.4	−2.9 ± 12.5	−8.8 ± 8.2
50.	5.3 ± 6.9	1.0 ± 14.4	1.6 ± 14.5	−8.7 ± 9.4

Table E.1: BIGBITE experimental asymmetry as a function of ω, corrected for empty target yield, for the energy range, 47 MeV $\leq \omega \leq$ 213 MeV. The region selected for the analysis of the quasielastic asymmetry is 58 MeV $\leq \omega \leq$ 161 MeV. The asymmetries are shown for the full data set and for each of the target spin orientations. The experimental asymmetries have been normalized to P_t = 100% and P_b = 100%. The statistical uncertainties on the asymmetry values are given.

ω	A_{exp} [all]	A_{exp} [L1]	A_{exp} [L2]	A_{exp} [R]
46.0	14.9 ± 10.3	34.2 ± 21.4	-10.9 ± 22.1	-16.9 ± 13.9
43.4	4.3 ± 11.4	48.5 ± 23.6	11.8 ± 24.1	17.5 ± 15.4
40.8	12.1 ± 15.7	21.3 ± 33.7	5.8 ± 33.7	-11.0 ± 21.0
38.2	-0.9 ± 14.6	-26.3 ± 30.4	26.5 ± 31.4	1.0 ± 19.6
35.6	5.2 ± 12.9	-10.0 ± 27.6	33.2 ± 27.1	0.3 ± 17.3
33.1	10.3 ± 13.1	21.1 ± 28.2	-1.9 ± 26.6	-11.5 ± 17.8
30.5	-2.2 ± 13.3	-2.3 ± 28.7	-30.4 ± 27.7	-9.5 ± 17.8
27.9	23.5 ± 14.4	31.7 ± 30.3	21.8 ± 30.4	-20.9 ± 19.4
25.3	52.9 ± 15.2	75.7 ± 32.8	58.2 ± 31.6	-41.9 ± 20.4
22.7	50.5 ± 16.1	78.7 ± 33.0	81.5 ± 34.4	-25.6 ± 21.8
20.1	49.5 ± 17.4	50.3 ± 35.3	-48.9 ± 36.6	-91.3 ± 23.9
17.6	43.9 ± 21.3	4.9 ± 41.3	52.4 ± 47.4	-60.4 ± 29.3
15.0	11.4 ± 29.6	69.4 ± 54.8	121.2 ± 69.0	58.8 ± 40.7
12.4	86.0 ± 49.2	216.0 ± 100.2	-51.5 ± 114.8	-75.3 ± 64.8
9.8	72.9 ± 75.9	-162.5 ± 155.7	170.6 ± 170.2	-137.7 ± 101.2
7.2	-19.0 ± 56.5	144.5 ± 133.9	89.2 ± 117.8	110.2 ± 73.4
4.6	130.3 ± 99.5	76.3 ± 213.0	429.1 ± 207.1	-26.8 ± 133.9
2.1	-38.5 ± 78.7	-178.9 ± 166.6	1.6 ± 174.9	-1.8 ± 103.8
-0.5	112.3 ± 68.9	-9.0 ± 139.2	-39.8 ± 165.5	-208.7 ± 90.3
-3.1	66.5 ± 79.0	185.8 ± 140.9	-0.9 ± 181.1	-16.7 ± 112.3

Table E.2: BIGBITE experimental asymmetry in the threshold-elastic region, -4 MeV $\leq \omega \leq 47$ MeV, corrected for empty target yield. The experimental asymmetries have been normalized to $P_t = 100\%$ and $P_b = 100\%$. The asymmetries are shown for the full data set and for each of the target spin orientations. The statistical uncertainty is indicated for the asymmetry values.

Bibliography

[1] L. Koester, W. Nistler and W. Waschkowki, Phys. Rev. Lett. **36**, 1021 (1976).

[2] T. W. Donnelly and A. S. Raskin, Ann. Phys. **169**, 247 (Academic Press, New York, 1986).

[3] J. D. Bjorken and S. D. Drell *Relativistic Quantum Mechanics* (McGraw-Hill, New York, 1964).

[4] B. Blankleider and R. M. Woloshyn, Phys. Rev. C **29**, 538 (1984).

[5] I. R. Afnan and N. D. Birrell, Phys. Rev. C **16**, 823 (1977).

[6] J. L. Friar, B. F. Gibson, G. L. Payne, A. M. Bernstein, and T. E. Chupp, Phys. Rev. C **42**, 2310 (1990).

[7] C. Y. Prescott *et al.*, Phys. Lett. **B77**, 347 (1978).

[8] J. Kessler, *Polarized Electrons*, 2nd edition (Springer-Verlag, Berlin, 1985).

[9] J. Arrington *et al.*, Nucl. Instrum. and Meth. (submitted, 1991).

[10] D. H. Beck, Ph.D. thesis, Massachusetts Institute of Technology (unpublished, 1986).

[11] R. W. Michaels, Ph.D. thesis, Yale University (unpublished, 1988).

[12] D. C. Carey, K. L. Brown and C. Iselin, *Decay TURTLE, A Computer Program For Simulating Charged Particle Beam Transport Systems, Including Decay Calculations*, SLAC-246, (March 1982).

[13] D. Tieger, private communication.

[14] R. S. Turley, Ph.D. thesis, Massachusetts Institute of Technology (unpublished, 1984).

[15] E. J. Beise and D. R. Tieger, *BIGBITE Optics in the Forward Quad Configuration*, Bates Internal Report 89-02.

[16] L. D. Pham, Ph.D. thesis, Massachusetts Institute of Technology (unpublished, 1989).

[17] MP-1 Group, *Introduction to Q*, LAMPF Document MP-1-3401-3 (1985).

[18] F. D. Colegrove, L. D. Schearer, and G. K. Walters, Phys. Rev. **132**, 2561 (1963).

[19] *Workshop on Polarized ^{3}He Beams and Targets*, edited by R. W. Dunford and F. P. Calaprice (American Institute of Physics, New York, 1985).

[20] G. C. Phillips *et al.*, Phys. Rev. Lett. **9**, 502 (1962).

[21] D. M. Hardy, S. D. Baker, and W. R. Boykin, Nucl. Instrum. Meth. **98**, 141 (1972).

[22] S. D. Baker, D. H. McSherry, and D. O. Findley, Phys. Rev. **178**, 1616 (1969).

[23] D. M. Hardy *et al.*, Nucl. Phys. **A195**, 250 (1972).

[24] J. M. Daniels in *Workshop on Polarized ^{3}He Beams and Targets*, edited by R. W. Dunford and F. P. Calaprice (American Institute of Physics, New York, 1985), pp. 134-137.

[25] R. S. Timsit, *et al.*, Can. J. Phy. **49**, 509 (1971).

[26] M. Leduc, in *Paris 90 - Proceedings of the 7th International Conference on Polarization Phenomena in Nuclear Physics*, edited by A. Boudard and Y. Terrien (Les Editions de Physique, Paris, 1990), pp. 317-331.

[27] G. Tastevin *et al.*, J. Phys. France **49**, 1 (1988).

[28] M. V. McCusker, L. L. Hatfield, and G. K. Walters, Phys. Rev. A **5**, 177 (1972).

[29] L. G. Gray *et al.*, Rev. Sci. Instrum. **54**, 271 (1983).

[30] A. Kastler, J. Phys. Radium **11**, 225 (1950).

[31] W. Happer, Rev. Mod. Phys. **44**, 169 (1972).

[32] J. D. Jackson, *Classical Electrodynamics*, 2nd edition (John Wiley & Sons, New York, 1975).

[33] D. S. Betts and M. Leduc, Ann. Phys. Fr. **11**, 267 (1986).

[34] F. D. Colegrove, L. D. Schearer, and G. K. Walters, Phys. Rev. **135**, A353 (1964).

[35] P. J. Nacher and M. Leduc, J. Physique **44**, 2057 (1985).

[36] L. Schearer and M. Leduc, IEEE J. Quant. Electronics **QE22**, 756 (1986).

[37] C. L. Bohler *et al.*, J. Appl. Phys. **63**, 2497 (1988).

[38] J. M. Daniels, L. D. Schearer, M. Leduc, and P. J. Nacher, J. Opt. Soc. Am. **4**, 1133 (1987).

[39] C. G. Aminoff, C. Larat, M. Leduc, and F. Laloë, Revue Phys. Appl. **24**, 827 (1989).

[40] P. Tin and L. D. Schearer, J. Appl. Phys. **68**, 950 (1990).

[41] R. S. Timsit, J. M. Daniels, and A. D. May, Can. J. Phys. **49**, 560 (1971).

[42] L. D. Schearer and G. K. Walters, Phys. Rev. **139**, A1398 (1965).

[43] W. A. Fitzsimmons and G. K. Walters, Phys. Rev. Lett. **19** 943 (1967).

[44] W. A. Fitzsimmons, L. L. Tankersley, and G. K. Walters, Phys. Rev. **179**, 156 (1969).

[45] R. Byerly, Jr., Ph.D. thesis, Rice University (unpublished, 1967).

[46] R. C. Greenhow, Phys. Rev **136**, A660 (1964).

[47] R. G. Milner, R. D. McKeown, and C. E. Woodward[†], Nucl. Instrum. Meth. **A257**, 286 (1987).

[†] Published by C. E. Jones under former name.

[48] K. D. Bonin, T. G. Walker, and W. Happer, Phys. Rev. A **37**, 3270 (1988).

[49] M. Leduc, S. B. Crampton, P. J. Nacher, and F. Laloë, Nucl. Sci. Appl. **2**, 1 (1984).

[50] R. G. Milner, R. D. McKeown, and C. E. Woodward†, Nucl. Instrum. Meth. **A274**, 56 (1989).

[51] J. W. Evans, J. Opt. Soc. Am. **39**, 229 (1949).

[52] D. R. Preuss and J. L. Gole, Appl. Opt. **19**, 702 (1980).

[53] M. Pavlovic and F. Laloë, J. Phys. **31**, 173 (1970).

[54] M. Pinard and J. Van Der Linde, Can. J. Phys. **52**, 1615 (1974).

[55] H. Gao, T. Gentile and W. Lorenzon, to be published.

[56] L. W. Mo and Y.-S. Tsai, Rev. Mod. Phy. **41**, 205 (1969).

[57] J. S. O'Connell and J. W. Lightbody, Jr., program EPCB, (1987).

[58] K. A. Dow, Ph.D. thesis, Massachusetts Institute of Technology (unpublished, 1987).

[59] G. B. West, Phys. Rep. **18C**, 264 (1975).

[60] J. S. McCarthy, I. Sick, and R. R. Whitney, Phys. Rev. C **15**, 1396 (1977).

[61] Proposal for the Pulse Stretcher Ring, MIT-Bates Linear Accelerator Center (unpublished, 1984).

[62] C. E. Woodward† *et al.*, Phys. Rev. Lett. **65**, 698 (1990).

[63] C. E. Jones-Woodward *et al.*, Phys. Rev. C **44**, R571 (1991).

[64] S. Galster, H. Klein, J. Moritz, K. H. Schmidt, D. Wegener and J. Bleckwenn, Nucl. Phys. **B32**, 221 (1971).

[65] G. Höhler *et al.*, Nucl. Phys. **B114**, 505 (1976).

---

†Published by C. E. Jones under former name.

[66] U.-G. Meissner, Phys. Rev. Lett. **62**, 1013 (1989).

[67] E. B. Hughes, M. R. Yearian, and R. Hofstadter, Phys. Rev. **151**, 841 (1966).

[68] S. Platchkov *et al.*, Nucl. Phys. **A510**, 740 (1990).

[69] M. Gari and W. Krümpelmann, Phys. Lett **B173**, 10 (1986).

[70] F. Iachello, A. D. Jackson and A. Lande, Phys. Lett. **B43**, 191 (1973).